ALMA MATER STUDIORUM
UNIVERSITÀ DI BOLOGNA

Dipartimento di Fisica e Astronomia

DOTTORATO DI RICERCA IN
ASTROFISICA

Ciclo XXXV

Tesi di Dottorato

On the role of AGN feedback in shaping galaxies across cosmic time

Presentata da: **Elena Bertola**

Coordinatore Dottorato:
Chiar.mo Prof. **Andrea Miglio**

Supervisore:
Chiar.mo Prof. **Cristian Vignali**

Co-supervisori:
Dr. **Mauro Dadina**
Dr. **Massimo Cappi**

Esame finale anno 2023

Settore Concorsuale: 02/C1 – Astronomia, Astrofisica, Fisica della Terra e dei Pianeti
Settore Scientifico Disciplinare: FIS/05 – Astronomia e Astrofisica

A papà.

"Former chubby girls-
We're made of steel.
And Splenda.
We survive."
Bride wars (2009)

Contents

Abstract

Understanding how Active Galactic Nuclei (AGN) shape galaxy evolution is a key challenge of modern astronomy. In the framework where black hole (BH) and galaxy growth are linked, AGN feedback must be tackled both at its "causes" (e.g. AGN-driven winds) and its "effects" (alteration of the gas reservoir in AGN hosts). The most informative cosmic time is $z \simeq 1-3$, at the peak of AGN activity and galaxy build up (the so-called cosmic noon), up to the fastest phase of BH growth. The aim of this thesis is to provide new insights regarding some key questions that still remain open in this research field: *i)* What are the properties of AGN-driven sub-pc scale winds at $z > 1$? *ii)* Are AGN-driven winds effective in influencing the life of galaxies? *iii)* Do AGN impact directly on star formation (SF) and gas content of their hosts?

The first part of this thesis regards the assessment of AGN feedback as "caught in the act", that is, the study of AGN-driven winds in the X-rays, while the second part addresses the "effects" of AGN feedback on their host galaxies.

Visible in the X-rays, ultra-fast outflows (UFOs) are AGN-driven winds that are considered the primary engine of kpc-scale outflows. Gravitationally lensed quasars (GLQs) are favorable sources to study UFOs at high-z since the lens magnification provides us with a natural signal-to-noise ratio booster. One of the goals of this thesis is to provide the community with a statistically robust sample of high-z AGN, not preselected based on AGN-driven winds ("feedback-unbiased" sample), to meaningfully assess properties and detection fraction (DF) of UFOs at $z > 1$ in an unbiased way. I also present what I refer to as the "feedback-biased" sample, built collecting all the high-z UFOs reported in the literature as of Summer 2021 and complementing them with our XMM-*Newton* exploratory survey of high-z GLQs showing UV winds (almost all of which are also part of the "feedback-unbiased" sample). Through this second sample, we carried out a comprehensive study of UFOs to determine the efficiency of such outflows in regulating BH growth and galaxy build up, and to assess their main driving mechanism. Lastly, I give a "work-in-progress" estimate of the high-z UFO DF as $\gtrsim$40%, interestingly similar to the measurements in the local ($z < 0.1$) and, more recently, also in the low-z ($0.1 < z < 0.5$) Universe.

The feedback-unbiased sample comprises also Q2237+030 and APM 08279+5255, two peculiar GLQs. Q2237+030 is a well-known lensing system, thanks to its nearby lensing galaxy ($z_{\rm Q} = 1.69$, $z_{\rm L} = 0.04$). The available X-ray data, taken over 18 years, allowed for the investigation of UFO presence and possible recurrence. Here I provide the first wind duty cycle estimation in a single high-z quasar: $\simeq$30% (45%) of the selected observations show UFO features at 95% (90%) confidence level. APM 08279+5255 is a unique high-z GLQ, extremely bright in many bands, and well known for what concerns UFOs: having shown some of the fastest UFOs ever seen, it soon became a key benchmark to test the efficiency of AGN-driven wind propagation. During the latest

XMM-*Newton*+*NuSTAR* exposures, taken in 2019 after almost 10 years of hardly no visibility, the source is found in a fainter state and there is no sign of UFO absorption features. Unfortunately, the data did not allow speculations on whether this is due to the lower flux level or to other causes. This fainter state, coupled with the first hard X-ray sampling of APM 08279+5255, allowed us to measure X-ray reflection and the high-energy cutoff in this source for the first time. From the analysis of previous XMM-*Newton* and *Chandra* observations, X-ray reflection is demonstrated to be a long-lasting feature of this quasar. The estimated high-energy cutoff ($E_{\rm cut} = 99^{+91}_{-35}$ keV) sets a new redshift record for the farthest ever measured and places APM 08279+5255 in the allowed region of the compactness-temperature diagram of X-ray coronae, in agreement with previous results on high-z quasars.

In the second part of the thesis, I address the "effects" of AGN feedback on the life of their host galaxies. If AGN influence galaxy growth, then they will reasonably impact the molecular gas reservoir first, and then SF as a consequence. Literature results concerning comparative studies of the gas content in high-z AGN hosts and non-active galaxies (i.e., that do not host AGN) are still controversial, possibly because they are mainly focused on high-luminosity AGN ($\log(L_{\rm Bol}/{\rm erg\ s^{-1}}) > 46$), i.e. good candidates for driving outflows. To provide reliable results for galaxy evolution models, two surveys of unbiased, high-z, X-ray-selected AGN were conceived: SUPER and KASHz. The SUPER project recently found that significant CO depletion is present only in the most massive host galaxies ($\log(M_*/{\rm M_\odot}) > 11$), demonstrating the importance of using unbiased samples representative of the AGN population at cosmic noon. I present in this thesis our efforts to extend the analysis of the SUPER project and provide an expanded sample of AGN at cosmic noon, by merging SUPER and KASHz AGN. CO luminosities (used as proxy for molecular gas masses) were retrieved from archival ALMA data, other key galaxy properties from dedicated SED fitting. We carried out a comparative study of SUPER+KASHz AGN and non-active galaxies, matched in z M_*, $L_{\rm FIR}$ (our observational proxy for SFR), applying the Bayesian framework developed by the SUPER project. Our results confirm that the host galaxies of more regular AGN are generally very similar to non-active galaxies. However, we report on the possibility of a luminosity effect regulating the efficiency with which AGN might impact on galaxy growth. Lastly, this work provides a new, sizable sample of more regular AGN to compare the predictions of cosmological simulations with real observations.

Chapter 1

Introduction

The Cosmos hosts a variety of fascinating objects, each of them unique on its own. In midst of such a manifold collection, supermassive black holes (SMBHs), astrophysical entities of extremely large masses ($M_{\rm BH} \gtrsim 10^6\,{\rm M}_\odot$) encapsulated in very compact regions ($r < 10$ AU), are probably among the most peculiar ones. The compactness of SMBHs is such that the generated potential well can only be described as a mathematical singularity at the SMBH center. In other words, their potential well is so deep that not even light can escape, hence the name of *black* holes. Astronomers discovered that many galaxies, and most interestingly all of the massive ones, host a (quiescent) SMBH at their center based on the properties of gas and stars in the inner regions of local galaxies. Moreover, to reach such high masses, quiescent SMBHs must have gone through an accreting phase in the past, the so called Active Galactic Nuclei (AGN) phase. AGN are unique objects that can emit a huge amount of energy, allowing us to study some of the most energetic events of the Cosmos and to test our understanding of the processes involving SMBHs.

In the last two decades or so, AGN have also gained great importance in the study of galaxy growth and evolution, especially for what concerns massive systems. In fact, the current cosmological framework predicts that the most massive Dark Matter halos should host galaxies of unrealistically large masses ($M_* > 10^{13}\,{\rm M}_\odot$) and overestimates the expected number of giant galaxies ($M_* \simeq 10^{12}\,{\rm M}_\odot$) (e.g., Somerville & Davé 2015; Wechsler & Tinker 2018). This issue can be addressed by introducing an agent that prevents the over-growth of massive systems: AGN (negative) feedback. In this sense, AGN have become a key ingredient of galaxy evolution models and cosmological simulations. In fact, the energy released by the AGN, either in the form of radiation or winds or jets, is expected to be fundamental in suppressing galaxy growth. On the observational side, however, we are still struggling in pinning down the efficiency of these events and their actual effect on galaxy growth. The aim of the present thesis is to address some of the key questions that still remain open in

field of AGN feedback and in particular of AGN-driven winds: *i)* Are AGN-driven winds effective in influencing the life of galaxies? *ii)* What are the properties of AGN-driven sub-pc scale winds at $z > 1$? Can they generate efficient galaxy-wide feedback? *iii)* Does AGN activity impact directly on star formation and gas content of galaxies?

1.1 Active Galactic Nuclei

The majority of SMBHs at the center of galaxies are quiescent, like Sgr A* in the Milky Way, but approximately $1\% - 10\%$ of them are "active" (i.e., AGN; typical masses of $10^6 - 10^9$ $M_\odot$, Peterson 2004). These objects show an activity that cannot be ascribed to thermonuclear reactions; they are characterized by bolometric luminosities ranging from 10^{42} up to 10^{48} erg s^{-1}, covering several decades of frequency, from radio up to γ-rays (e.g., Padovani et al. 2017), and by a rapid time variability that implies extremely compact emission regions (i.e. high energy densities, Ulrich et al. 1997). According to the AGN paradigm, such an emission can be explained by accretion of matter onto a central SMBH (see Sect. 1.1.1): the BH is surrounded by gas that, orbiting around it, loses angular momentum and spirals towards the center, releasing gravitational energy then transformed into electromagnetic emission. This process, plus the secondary ones it triggers, is powerful enough to account for the overall non-stellar AGN emission, which can also overcome that of the entire host galaxy.

AGN have been cataloged depending on their average properties, usually based on the first objects showing peculiar properties in a given, single band. Such different categories, however, often do not correspond to intrinsically different source types, leading to a bestiary of AGN that over-expresses their real diversity (Padovani et al. 2017). Nonetheless, there are two main properties that allow us to divide AGN into general categories: obscuration and radio emission.

Mainly based on their optical and X-ray properties, AGN are divided in type I (unabsorbed/non-extincted) and type II (absorbed/extincted) sources. However, when the observations allow for the analysis of the polarized emission, type II objects reveal that (almost) every type II AGN "hides" a type I (e.g., Antonucci & Miller 1985). This was interpreted as proof of the AGN paradigm, meaning that all AGN are powered by the same mechanisms, with type II sources showing additional elements that cause a modification of their spectra. All this led to the formulation of the "unified models" (Antonucci 1993), which state that the different properties are determined by the line of sight along which we observe them.

The one and only discriminating factor in this unification resides in the radio loudness* of the AGN, which allows for the distinction in radio-loud and radio-quiet

*One of the possible definitions of the radio loudness parameter corresponds to the ratio of the

objects. Nonetheless, the scientific community is now moving to a "jetted"-"non-jetted" paradigm (Padovani 2017) since the latest radio facilities can detect faint radio emission also in sources that were historically known as "radio-quiet". Such an emission can for instance be ascribed to star formation (SF) processes (Bonzini et al. 2015) or to the activity of the innermost regions of the AGN (see for instance the connection between X-ray and radio emission in low-luminosity AGN Panessa et al. 2007).

1.1.1 The AGN paradigm: accretion onto a massive, compact object

When matter orbits around a compact object, viscosity and turbulent processes induce an outward-transfer of the matter's angular momentum, which then spirals toward the center dissipating its gravitational energy. For a given mass m, the available energy is $E = \eta mc^2$, where η is the efficiency by which the gravitational energy is converted in electromagnetic energy and c the speed of light. Such energy is radiated at a rate

$$L = \frac{dE}{dt} = \eta \dot{m} c^2 \tag{1.1}$$

where $\dot{m} = dm/dt$ is the mass accretion rate. When accreting onto an object of mass M, the falling mass m dissipates its gravitational energy at a rate of

$$L = \frac{dU}{dt} = \frac{GM}{r}\frac{dm}{dt} = \frac{GM\dot{m}}{r} \tag{1.2}$$

which, when compared to Eq. (1.1), allows to find a relation between the conversion efficiency and the mass of the central object: $\eta \propto M/r$. Therefore, the more massive the accreting object (or alternatively, the higher the compactness), the more efficient the conversion is. Regarding the accretion onto SMBHs, the efficiency is assumed to be approximately 10%.

Even though the falling matter is dissipating its energy, the system is stable given that the outward radiation pressure is balanced by the inward gravitational force of the free falling gas. From this equilibrium, one can estimate the minimum mass of the central object and the maximum luminosity the system can irradiate. Assuming a spherical distribution of ionized gas (hydrogen) and being $\hat{r}$ the outward radial versor, the force induced by the pressure radiation provided by the Thompson scattering is

$$\vec{F}_{\rm rad} = \sigma_e \; P_{\rm rad} \; \hat{r} = \sigma_e \frac{L}{4\pi r^2 c} \; \hat{r} \tag{1.3}$$

which acts on the electrons but, thanks to the electrostatic interaction, it is communicated also to the protons. The gravitational attraction produced by the central

radio flux density at 5GHz and the optical one at 4400 Å (Kellermann et al. 1989).

mass is equal to

$$\vec{F}_{\rm grav} = -\frac{GM(m_{\rm p}+m_{\rm e})}{r^2}\,\hat{r} \approx -\frac{GMm_{\rm p}}{r^2}\,\hat{r}, \quad \text{since } m_{\rm p} \gg m_{\rm e}. \tag{1.4}$$

For the system to be in equilibrium, the following condition has to be satisfied: $F_{\rm rad} \leq F_{\rm grav}$. Substituting the modules through Eqs. (1.3) and (1.4), one can derive the maximum rate at which the energy can be irradiated, the so-called Eddington luminosity:

$$L_{\rm Edd} = \frac{4\pi GMm_{\rm p}c}{\sigma_{\rm e}} = 1.26 \times 10^{38}\frac{M}{M_\odot}\ {\rm erg\ s^{-1}} \tag{1.5}$$

The Eddington luminosity also implies a minimum mass that the central object needs to have in order to assure the equilibrium of a system that is irradiating at the Eddington limit:

$$M_{\rm Edd} = 8 \times 10^5\ L_{[44]}\ M_\odot. \tag{1.6}$$

Therefore, assuming a quasar at the Eddington limit with a luminosity $L_{\rm QSO} \approx 10^{46}$ erg s^{-1}, its central compact object should have a minimum mass of $\approx 10^8\ M_\odot$. Moreover, from Eq. (1.5) one can infer that $L_{\rm Edd} \propto M$, i.e. the more luminous the AGN is, the more massive the central object must be. From the variability timescales shown by these sources, one can estimate the size of the emitting regions ($d \leq c\Delta t$). Such timescales can be of the order of days, hours, even minutes, the latter implying sizes as small as the Solar System. Given the lower limit to the mass determined by the Eddington luminosity and such limited size, these systems are likely to host a SMBH (Rees 1984).

Black holes can be characterized by three parameters: mass, charge and angular momentum. They are usually assumed neutral (null charge) and the angular momentum is described by the spin of a BH, which corresponds to the adimensional angular momentum per unit mass: $a = Jc/GM_{\rm BH}^2$, where J is the BH angular momentum. It can take all values between -1 and 1, where positive numbers indicate that the BH rotates in the same direction as the accreting matter, negative values indicate counter-rotation. When describing the properties of a black hole, one fundamental concept is the event horizon, that is the distance at which the escape velocity from the gravitational well equals that of light. Such distance is directly related to the gravitational radius:

$$r_{\rm g} = \frac{GM_{\rm BH}}{c^2} \tag{1.7}$$

which is often used as unit to measure "small" distances from a SMBH. The event horizon directly depends on the spin of the BH; its radius, in units of $r_{\rm g}$, is equal to $r_{EH} = 1 \pm (1-a^2)^{1/2}$. For a non-rotating BH ($a = 0$) it is equal to the Schwarzschild radius ($R_{\rm S} = 2r_{\rm g}$). For a maximally rotating BH ($a^2 = 1$), it corresponds to the

gravitational radius.

SMBHs can accrete matter at very different rates, which are closely intertwined to the properties of the accretion flow (Giustini & Proga 2019, for a review): from standard geometrically thin, optically thick Shakura–Sunyaev disk to advective dominated accretion flows. Based on the geometry and rate of the accretion flow, AGN can develop different kinds of outflows: from high-velocity bipolar jets (low accretion rates) to powerful radiation-driven accretion disk winds (accretion rates as high as super-Eddington). Moderate to high accretion rates are those expected to launch accretion disk winds in a radiation-driven manner. Depending on the launching radius and ionization state, such winds imprint characteristic absorption lines in the UV and X-ray spectra of AGN. The discovery of such characteristic absorption lines generated additional categories to classify AGN in the UV band: broad- and narrow-absorption line sources (BAL: $FWHM \geq 2000$ km s^{-1}, and NAL: $FWHM \leq 500$ km s^{-1}), with intermediate cases taking the names of mini-BAL and mini-NAL AGN. The winds generated in the innermost parts of the accretion disk produce features visible in the X-ray band and will be described in a following section (see 1.2 and in particular 1.2.2).

1.1.2 The basic ingredients of AGN

The detailed structure of AGN has not been completely determined yet, but all proposed models and geometries converge on the presence of, at least, the following components, listed below and schematically drawn in Figure 1.1.

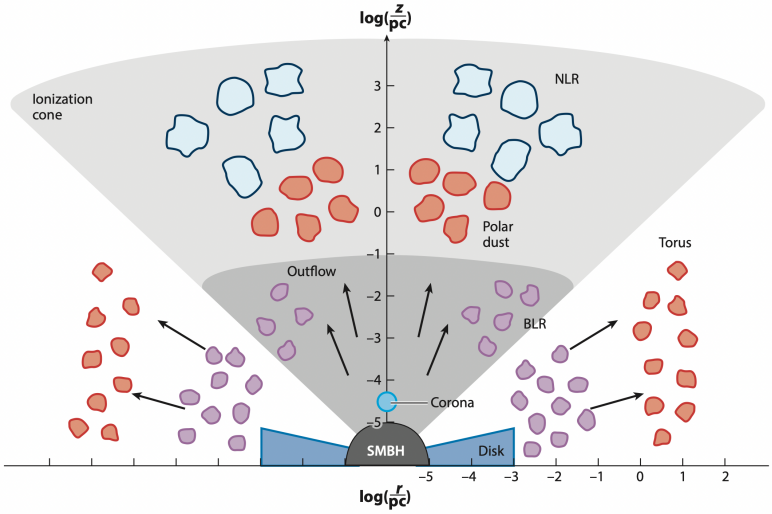

Figure 1.1: Cartoon showing the predicted structure of a radio-quiet AGN. Credit: Hickox & Alexander (2018).

Accretion disk (see also §1.1.1). The properties of the accretion flow are still under debate. The commonly assumed theory is that of an optically thick, geometrically thin accretion disk (Shakura & Sunyaev 1973). The emission of such an accretion flow can be approximated as the superposition of many black body (multi-color black body), induced by the local dissipation of the gravitational energy of the gas. In this scenario, the disk can be considered as an ensemble of annuli, each emitting as a black body peaking at a different temperature; the total disk emission is given by the superposition of each annuli black body. Assuming that half of the dissipated gravitational energy is converted into radiation and that the other half heats up the disk, one can compute the radial profile of the disk temperature. Being $dU/dt = GM\dot{m}/r$ the rate at which the energy is dissipated (following the virial theorem), the corresponding luminosity is $L = GM\dot{m}/2r$. Applying the Stefan-Boltzmann law to both the sides of the disk, the following equality can be found

$$L = \frac{GM\dot{m}}{2r} = 2\pi r^2 \sigma_{\rm SB} T^4 \tag{1.8}$$

from which, isolating the temperature, one can derive the relation $T(r)$, valid under the before mentioned assumptions:

$$T(r) = \left(\frac{GM\dot{m}}{4\pi\sigma_{\rm SB} r^3} \right)^{1/4} \tag{1.9}$$

Following a proper physical treatment (e.g., King 2008), the surface temperature of the disk $T(r)$ becomes:

$$T(r) = \left[\frac{3GM\dot{m}}{8\pi\sigma_{\rm SB} r^3} \left(1 - \left(\frac{R_{\rm in}}{r} \right)^{1/2} \right) \right]^{1/4} \tag{1.10}$$

where $R_{\rm in}$ is the inner radius of the accretion disk. As Eqs. (1.9)-(1.10) predict, the temperature of the disk grows toward the center, therefore so does the peak frequency of the annuli black body spectra. Typical temperatures are in the $10^5 - 10^6$ K range and produce a multicolor black body spectrum that covers the optical/UV band (i.e. the big-blue bump; see Fig. 1.2), sometimes reaching also the soft X-ray frequencies, based on the SMBH mass.

Hot corona (see also §1.2.1). The disk is predicted to be surrounded by the so-called hot corona, whose actual properties and location are still debated. The simplest modeling provides this component as the main X-ray source (two-phase model, Haardt & Maraschi 1991), considering it as made of hot ($\mathrm{T} \sim 10^8 - 10^9$ K), rarefied ($\mathrm{n} \sim 10^8$ cm^{-3}), optically thin gas, probably placed above or within the inner part of the accretion disk at a distance of $\sim 3 - 10$ $\mathrm{r_g}$ (Fabian et al. 2015).

Broad line region (BLR) At sub-pc distances from the central source, we find the so-called Broad Line Region (BLR), which is thought to be made up of gas clouds orbiting around and partially covering the central source. The bulk motions are dominated by the central SMBH, thus the dynamical properties of this region are used to infer those of the central engine. The BLR gas reprocesses the optical/UV emission through permitted lines, while the forbidden lines are all collisionally suppressed due to the high density of the clouds ($\sim 10^{9-10}$ cm^{-3}). The temperature of the gas, given the intensity and characteristics of the emission lines, is approximately equal to 10^4 K, while the Doppler-induced broadening of the lines spans from 500 km s^{-1} to more than 10^4 km s^{-1}, producing a mean FWHM of $\Delta v \sim 5000$ km s^{-1}.

Narrow line region (NLR) At larger distances from the center (up to hundreds of parsecs), we find the Narrow line region (NLR), whose gas, similarly to BLR, seems to be arranged in clouds but at a lower temperature ($T \sim 10^{3-4}$ K). The presence of forbidden lines indicates that the typical densities are also lower than those of the BLR ($\sim 10^4$ cm^{-3}) and so is the broadening of the lines ($200 \lesssim \Delta v \lesssim 900$ km s^{-1}), as the name suggests. Part of the NLR is placed far enough from the central source to also contain dust. It is the only AGN region to be spatially resolved in the optical band (with the unique exception of results by Gravity, instrument that allowed to spatially resolve the BLR; Gravity Collaboration et al. 2018), where ionization cones rather than a spherical distribution can be appreciated, suggesting an axisymmetric structure rather than a spherical one.

Molecular torus The region between ~ 0.1 and ~ 10 pc from the SMBH is referred to as the molecular torus. Its properties ($n \sim 10^{4-7}$ cm^{-3}, $\Delta v \sim 1000$ km s^{-1}; e.g., Jaffe et al. 2004) are inferred from the interpolation of those of BLR and NLR; given its distance from the ionizing source, it contains dust and molecular gas. Its actual geometry is still strongly debated (i.e. either smooth or clumpy, even if the second option is now the one collecting more consensus; e.g., Stalevski et al. 2012, 2016) and so is its spatial extent (see Hickox & Alexander 2018, for a review). Most models do however agree on the fact that this gas shall absorb the optical/UV emission and thermally reprocess it in the Mid-IR (MIR) band, producing a black body that peaks around tens of microns, as observed (see Fig. 1.2).

Relativistic jets Relativistic jets are the peculiar characteristic of radio-loud AGN, which correspond to $\lesssim 10\%$ of the AGN population. They are thought to be aligned with the simmetry axis of the system and seem to be originated in the same regions where the optical/UV and X-ray continuum are produced, even though the responsible mechanism is still under debate. Their emission is mainly attributed to synchrotron and inverse Compton which, based on the Synchrotron-Self-Compton model, can cover from radio to γ-ray frequencies.

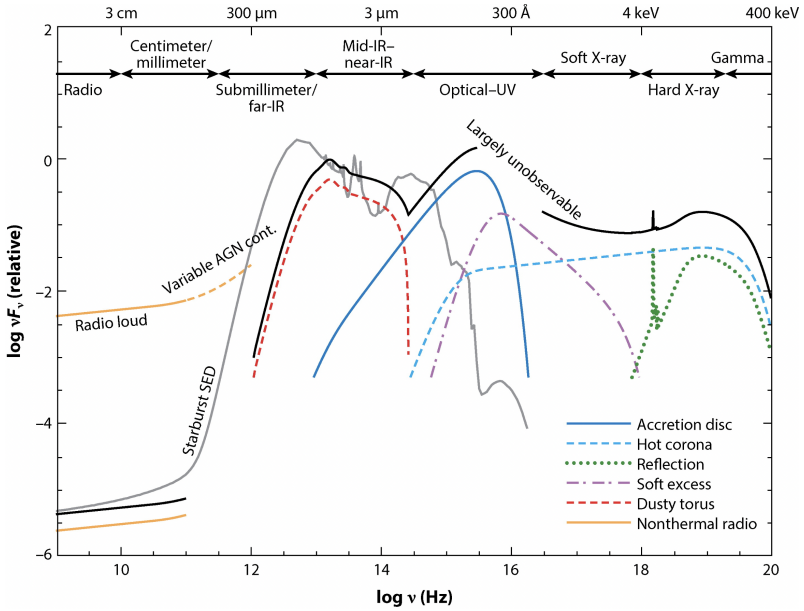

Figure 1.2: Schematic view of the Spectral Energy Distribution (SED) of an AGN. Credit: Hickox & Alexander (2018).

Table 1.1: Typical size ranges of the various AGN components, as discussed in the main text. [a] Radius of the event horizon.

Component	Approximate size
SMBH	$R_{\rm s} \sim 0.01 - 10$ AU[a]
Accretion disk	$R_{\rm in} \sim 0.01 - 60$ AU
	$R_{\rm out} \sim 1 - 1000$ AU
BLR	$R_{\rm BLR} \sim 0.01 - 1$ pc
Torus	$R_{\rm torus} \sim 1 - 10$ pc
NLR	$R_{\rm NLR} \sim 10^2 - 10^4$ pc
Jet	$R_{\rm jet} \sim 10^2 - 10^3$pc

1.2 X-ray emission of AGN

AGN emission in the X-ray band ($\sim 0.1 - 100$ keV; see Fig. 1.3) allows us to investigate the innermost regions of these systems. At such wavelengths, we can study the physics of accretion, mainly through the direct emission from the corona, and also how matter is distributed around the central source, by investigating how the direct emission gets reprocessed by the surrounding medium.

1.2.1 Direct emission: X-ray corona and high-energy cutoff

Observational efforts in the past three decades have demonstrated the validity of the two-phase model (Haardt & Maraschi 1991; Haardt et al. 1994) in describing AGN

emission at high-energies. Optical/UV disc photons are predicted to be Compton up-scattered by the electrons of the hot corona ($T_{\rm e} \sim 10^{8-9}$K), which surrounds the central SMBH. The "Comptonization" process generates the cutoff-power-law-like spectrum measured in the X-rays, in which the cutoff energy is set by the temperature of the hot corona. Models predict $\Gamma = 1.5 - 2.5$ for the photon index of radio-quiet AGN (Haardt et al. 1997): however, the observed range seems to be narrower ($\Gamma = 1.8 - 2.0$, e.g. Perola et al. 2002; Piconcelli et al. 2005), holding up to $z \gtrsim 6$, even if with a slightly steeper range at $z > 6$ (e.g., Vito et al. 2019; see also the recent results on the HYPERION sample, Zappacosta et al. 2023). The Inverse-Compton process is efficient until photons are up-scattered to energies comparable to those of the relativistic electrons. At very hard energies, photon-photon collisions decay into electron-positron pairs which can, in turn, annihilate and produce energetic photons. Pair production can then become a runaway process acting as a natural thermostat for the corona. The conditions in which this takes place depend on a combination of corona temperature and radiative compactness (Cavaliere & Morrison 1980), as well as on the plasma optical depth (τ). In fact, Comptonization models of hot coronae with slab geometry predict a cutoff in the X-ray power law at $E_{\rm cut}/k_{\rm B}T_{\rm e} \simeq 2(3)$ for optically thin(thick) plasma (e.g., Petrucci et al. 2001). The typically employed quantities (Cavaliere & Morrison 1980; Guilbert et al. 1983) include the dimensionless temperature parameter θ:

$$\theta = \frac{k_{\rm B}T_{\rm e}}{m_{\rm e}c^2} = \frac{E_{\rm cut}}{K m_{\rm e}c^2}, \tag{1.11}$$

with $K = 2(3)$ for an optically thin(thick) plasma, along with the dimensionless compactness parameter ℓ:

$$\ell = \frac{L_{\rm X}}{R_{\rm X}} \frac{\sigma_T}{m_{\rm e}c^3}, \tag{1.12}$$

where $m_{\rm e}$ and $T_{\rm e}$ are electron mass and temperature, respectively, $L_{\rm X}$ and $R_{\rm X}$ are the luminosity and size of the X-ray source, respectively, $\sigma_{\rm T}$ is the Thomson scattering cross-section, and $k_{\rm B}$ is the Boltzmann constant.

In principle, by populating the $\ell - \theta$ diagram, it is possible to probe the mechanisms regulating the corona temperature and test the pair-production thermostat predictions. To this aim, broadband X-ray spectra of compact sources are needed to properly model the primary emission and, in particular, its high-energy cutoff. This was extensively done with hard X-ray observatories, such as *BeppoSAX* (e.g., Petrucci et al. 2001; Dadina 2007, 2008), *INTEGRAL* (e.g., Malizia et al. 2014), and *Swift* (e.g., Vasudevan et al. 2013; Koss et al. 2017). A real breakthrough in the study of X-ray coronae has arrived thanks to *NuSTAR* (Harrison et al. 2013), the first focusing hard X-ray telescope, which allowed for an improved estimation of the coronal temperature in nearby sources. By gathering literature results from both

non-focusing instruments and *NuSTAR*, Fabian et al. (2015) built a compilation of $E_{\rm cut}$ measurements in both local AGN and black-hole binaries, finding many of their coronae to lie at the edge of the runaway pair-production region in the $\ell - \theta$ plane. Similar results were later obtained by Ricci et al. (2018) based on sources of the *Swift*/BAT AGN Spectroscopic Survey (BASS, Ricci et al. 2017). Interestingly, Ricci et al. (2018) also discovered a negative correlation between the average high-energy cutoff and Eddington ratio[†] in BASS AGN, regardless of either luminosity or SMBH-mass selection.

With its wide hard X-ray bandpass, *INTEGRAL* allowed for detailed studies of the coronal high-energy cutoff in local AGN (e.g., Molina et al. 2009, 2013; De Rosa et al. 2012), many of which were later updated and confirmed by *NuSTAR* measurements. Nonetheless, *NuSTAR* can properly constrain the high-energy cutoff only if this falls in its bandpass or, otherwise, only in high count-rate sources. The outstanding results obtained by *NuSTAR* have thus been restricted to nearby AGN ($z \lesssim 0.1$) with $E_{\rm cut} \lesssim 200$ keV and $L_{\rm X} \lesssim 10^{45}$ erg s^{-1} (see, e.g., the recent work by Akylas & Georgantopoulos 2021), until recently, when Lanzuisi et al. (2019, hereafter, L19) were able to probe the high-luminosity regime ($L_{\rm X} > 2\times10^{45}$ erg s^{-1}) through *NuSTAR* observations of high-z AGN. L19 were the first to well constrain the high-energy cutoff of two AGN at $z \gtrsim 2$ (2MASSJ1614346+470420 at $z = 1.86$ – hereafter, 2MASSJ16; B1422+231 at $z = 3.62$ – hereafter B1422) using *NuSTAR* data, confirming the measurement for B1422 by Dadina et al. (2016) from XMM-*Newton* data. Both sources show rather low $E_{\rm cut}$ values ($\lesssim 100$ keV) and fall in the limited allowed region for high-luminosity AGN of the $\ell - \theta$ plane. Interestingly, the measured $E_{\rm cut}$ values are much lower than those of BASS AGN showing similar $\lambda_{\rm Edd}$ ($E_{\rm cut} \sim 150 - 170$ keV, Ricci et al. 2018). Recently, Tortosa et al. (2022) presented the first systematic broadband X-ray study of super-Eddington-accreting AGN with simultaneous *NuSTAR* and XMM-*Newton* or *Swift*/XRT data, discovering that also these very peculiar sources comply to the hot-corona-thermostat model.

1.2.2 Reprocessed emission: absorption and X-ray reflection

X-ray emission of AGN can be reprocessed by absorption and subsequent re-emission. Based on how, and if, the reprocessed photons reach the observer, astronomers refer to the phenomenon as reflection (photons are re-emitted on the same side of the absorber – can reach the observer) and absorption (the gas is blocking part of our line of sight to the source – re-emitted photons might not reach the observer).

[†]Eddington ratio: $\lambda_{\rm Edd} = L_{\rm bol}/L_{\rm Edd}$. This parameter expresses the AGN accretion power in fraction of Eddington accretion power (see Eq. 1.5), i.e. the maximum above which the system should lose equilibrium.

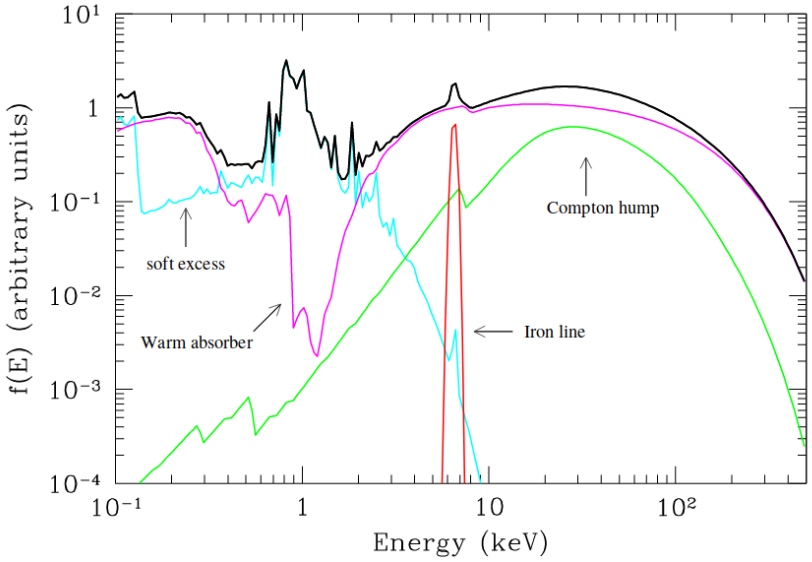

Figure 1.3: Average total spectrum (black line) of a type I AGN in the $0.1 - 150$ keV energy range. The primary emission (power-law) is absorbed by a warm absorber (pink line); soft excess (cyan line), cold reflection component (green line) and iron line emission (red line) are also shown. Credit: Risaliti & Elvis (2004).

X-ray reflection The reflection component was first predicted based on pure geometrical arguments; part of the coronal emission come to us directly, while another part illuminates the accretion disk, where its optically thick, relatively cold medium absorbs and re-emits the X-ray photons (see Figure 1.1). The surfacing emission is altered both by photoelectric absorption at soft energies and by Compton scattering with the cold electrons of the disk at hard energies. The reflection continuum is thus bump-shaped, showing a peak at $20 - 30$ keV, and is often referred to as the reflection (or Compton) hump. The interaction with the disk imprints fluorescence emission lines on the X-ray spectrum, produced by the most abundant elements (i.e. Fe, O, C, Mg, Ni) in the $0.1 - 8$ keV band. Only those elements whose intensity overcomes the primary emission can be seen in the total spectrum. The most prominent features are usually produced by iron: Fe Kα line at 6.4 keV, iron absorption edge at ~ 7.1 keV and, if intense enough, Fe Kβ line at 7.05 keV (the reported energies are valid in the case of neutral iron; e.g., Makishima 1986). The equivalent width (EW[‡]) of a line measures its strength with respect to the continuum emission. Radio-quiet type I objects present Fe Kα EWs that span in the range $50 - 350$ eV, with a typical value of ~ 150 eV. The described physical origin applies to a Shakura-Sunyaev standard disk, but it is still debated whether the molecular

[‡]The equivalent width corresponds to the width of a rectangle having one side equal to the continuum baseline and area equal to that delimited by the line profile and the spectral continuum level: EW$=\int \frac{F_c - F_s}{F_c} d\lambda$, where F_c and F_s are the intensity of the underlying continuum and of the observed spectrum (line+continuum), respectively.

torus or even the BLR might be responsible for part, if not all, of this component.

Soft excess Many sources show a strong emission at low energies ($0.1 - 2.0$ keV), the so-called soft excess, that cannot be accounted for by the only primary emission (i.e. the power-law). Its origin is still strongly debated. One scenario, now considered obsolete, indicates that this component is the high-energy tail of the disk black body emission. However, when modeled with a thermal component, the returned temperature of the disk is rather constant even for sources showing considerably different SMBH masses and luminosities. This result led to the formulation of other possible origins for the soft excess: relativistically blurred, ionized reflection from the accretion disk itself, if ionized (Ross & Fabian 2005; García et al. 2019, e.g.,) or thermal Comptonization of disk photons by a warm and optically thick corona ("warm Comptonization"; e.g., Petrucci et al. 2018; Ursini et al. 2020).

X-ray absorbers and winds Intervening matter along the line of sight can produce an energy-dependent reduction of the source flux due to photoelectric absorption. The quantities used to parameterize the absorbing matter are thickness (in terms of column density $N_{\rm H}$ [cm^{-2}]), ionization state[§], covering fraction (CF, percentage of absorbed flux with respect to the total produced by the source) and, if not at rest with the source, velocity of motion with respect to it ($v_{\rm out}$). In particular, the thickness determines the threshold energy below which X-ray photons are absorbed: $N_{\rm H} \propto E^{-3.5}$. If the material is neutral/low-ionized and blocks all the emission produced by the source (CF = 1), all the photons below such threshold energy are absorbed. If the absorber is ionized or partially covering the source (for instance, organized in small clouds) or both of the previous cases, then some of the photons at energies below the threshold are not blocked by the absorber and thus part of the flux is seen directly.

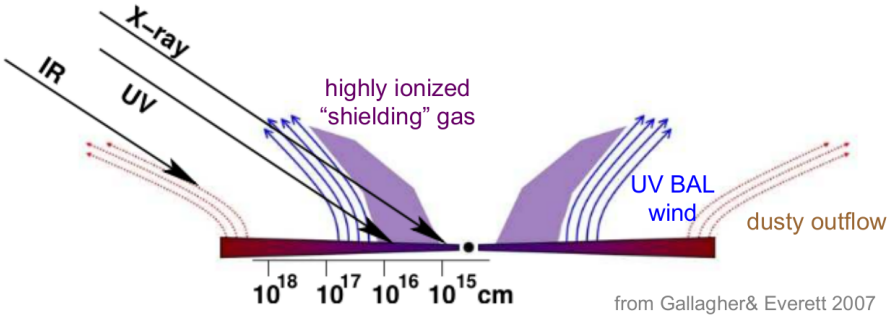

Figure 1.4: Sketch of winds arising at different radii of the accretion disk. Credit: Gallagher & Everett (2007).

[§]The state of the gas is parameterized through the ionization parameter ξ, which depends on the X-ray luminosity $L_{\rm X}$ of the incident radiation, the gas density n and the distance from the source: $\xi = L_{\rm X}/nr^2$.

Observationally, type II Seyferts show absorption due to neutral matter that is significantly higher than that of the Milky Way, which is thought to be produced by the molecular torus (e.g., Bassani et al. 1999). Such absorption affects the soft energy band, while the hard band is well reproduced by the same models as of type I sources, a fact that has been interpreted as a confirmation of the unified models. About 50% of AGN type I (e.g., Nandra & Pounds 1994; Piconcelli et al. 2005) show absorption features in the soft X-rays that cannot be ascribed to the cold matter that obscures type II objects. This led to the idea of a partially ionized, optically thin material, the so-called warm absorbers (WAs), placed at a distance similar to that of the BLR. With low resolution spectroscopy, the features produced by WAs are essentially seen as prominent ionized O absorption edges. The advent of high-resolution gratings spectroscopy (i.e. XMM-*Newton* and *Chandra*) allowed for the spectral resolution of more line profiles, revealing the complexity of these absorbers. By means of such grating observations, we now know that WAs show multiple ionization and kinetic components, outflowing at $v_{\rm out} \approx 100 - 1000$ km s^{-1} (Kaspi et al. 2002). Their origin can be possibly interpreted as a radiatively driven wind arising from the accretion disk (e.g., Giustini & Proga 2019). Winds in the X-ray band have also been detected in the form of Ultra Fast Outflows (UFOs, Tombesi et al. 2010a), which manifest themselves through blueshifted highly-ionized iron resonant lines above 7 keV. These components are even more extreme than WAs, showing column densities up to $\log(N_{\rm H}/{\rm cm}^{-2}) \simeq 24$, ionization parameters up to $\log[\xi/({\rm erg\ s}^{-1}{\rm cm})] \simeq 5$ and outflow velocities as high as half the speed of light ($v_{\rm out} > 0.1c$). Moreover, the properties of these two gas phases (WAs and UFOs) seem to correlate when compared to their typical distances from the central SMBH (i.e. UFOs are located nearer the centre than WAs; Tombesi et al. 2013; Serafinelli et al. 2019), and also for what concerns the correlation between $N_{\rm H}$, $\log \xi$ and $v_{\rm out}$, with UFOs populating the higher-end of the parameters distribution in each parameter space (e.g., Tombesi et al. 2013). These results led to the idea that WAs and UFOs are two related wind phases, with UFOs being the trigger of WAs. Winds have been observed also at lower frequencies, located at larger distances from the central BH, for instance in bright Ultra Luminous IR Galaxies (ULIRGs) and in BAL-QSOs. This fact lead to the idea that, based on the distance from the AGN, the intervening material changes its properties and that there might be a correlation among the various components (Figure 1.4 displays a sketch of how such winds are thought to arise from the inner parts of the accretion disk; Gallagher & Everett 2007, but see also Giustini & Proga 2019). Such AGN-driven winds may well be at the origin of AGN feedback, as will be discussed in Section 1.3.

1.3 AGN feedback

The sphere of influence of the central SMBH[¶] is spatially limited and involves only the innermost regions of galaxies. Yet, in the past ≃25 years, astronomers found multiple observational (e.g., Strateva et al. 2001; McConnell et al. 2011) and theoretical (e.g., Silk & Rees 1998; Somerville et al. 2008; Lapi et al. 2014) evidence for a connection between the buildup of the central SMBH and the host galaxy, leading to the formulation of the so-called "AGN/galaxy co-evolution". Accretion onto the central SMBH can release a huge amount of energy that, if efficiently coupled to the surrounding material, easily allows the AGN to shape galaxy growth by heating/exciting/removing the gas of the interstellar medium (ISM; e.g., Silk & Rees 1998). AGN could thus influence SF up to its suppression, for instance by preventing the cooling of the hot halo on the macro scales (Gaspari & Sądowski 2017). Despite its importance, we still lack a full understanding of AGN feedback (e.g., Kormendy & Ho 2013; Harrison 2017; Harrison et al. 2018; Ward et al. 2022).

To be relevant for AGN/galaxy co-evolution, AGN feedback must have been most effective when both SMBH growth and SF rate (SFR) cosmic densities were at their peaks (the "cosmic noon", $z \simeq 1-3$, Madau & Dickinson 2014; Aird et al. 2015) and when galaxies, being smaller, were most easily affected by it. Hence, sources at cosmic noon are the most promising and most informative targets to investigate AGN feedback, both in terms of "causes" (e.g., AGN-driven winds) and "effects" (e.g., reduced gas fraction and disturbed gas kinematics in AGN hosts).

One way models and simulations relate AGN activity to galaxy evolution is through AGN-driven winds (e.g., King 2005), that would propagate from the innermost regions of the accretion disk to kpc-scales. To understand if AGN are effective in shaping the build up of galaxies, investigating the average properties and duty cycle that characterize sub-pc-scales winds (that is, UFOs) is needed as much as assessing the long term impact of AGN activity on the SF and gas reservoir on kpc-scales.

1.3.1 AGN-driven outflows
‖

One of the most promising (and most targeted) mechanisms to establish AGN feedback is an inside-out chain of AGN-driven winds that links highly-ionized accretion-disk winds to galaxy-wide ionized/molecular outflows (e.g., Zubovas & King 2012; Wagner et al. 2013; Gaspari et al. 2020). AGN-driven outflows have

[¶]The sphere of influence of a SMBHs is defined as the region where its gravitational potential overcomes that of the galaxy: $r < r_{\rm h} = \frac{GM_{\rm BH}}{\sigma^2} \sim 11.2(M_{\rm BH}/10^8\,{\rm M}_\odot)/(\sigma/200\ {\rm km\,s^{-1}})^2$ pc, (Peebles 1972; Ferrarese & Ford 2005).

[‖]This section is mainly based on Faucher-Giguère & Quataert (2012); King & Pounds (2015); Costa et al. (2020).

indeed been observed in many sources and various gas phases, in AGN at all redshifts (e.g., Cicone et al. 2014; Carniani et al. 2017; Vietri et al. 2018; Fluetsch et al. 2019; Kakkad et al. 2020; Chartas et al. 2021; Molina et al. 2022b; Mehdipour et al. 2022), up to $z > 6$ (Bischetti et al. 2022, 2023), and were found to naturally explain the diminishing/removal of gas from galaxies (e.g. Cicone et al. 2014; Brusa et al. 2018; Veilleux et al. 2020). However, whether they can actually produce a long-term effect on the SF of galaxies is still matter of debate (e.g., Carniani et al. 2016; Cresci & Maiolino 2018; Scholtz et al. 2020; Lamperti et al. 2021). For instance, the gas carried away by the kpc-scale outflows might get trapped in the host halo or in the galaxy itself and then fall back again onto the system at later times (e.g., Arribas et al. 2014; King & Pounds 2015)

Part of the detected outflows match or exceed the kinetic power threshold whereby winds can efficiently act on galaxy growth ($\dot{E}_{\rm out}/L_{\rm bol} \simeq 0.5 - 5\%$; e.g., Di Matteo et al. 2005; Hopkins & Elvis 2010, but see also Harrison et al. 2018). In this scenario, UFOs, the fastest AGN-driven winds ($v_{\rm out} > 0.1\,{\rm c}$) observed so far, are the possible first link in the wind chain, based on both observational results (e.g., Marasco et al. 2020; Tozzi et al. 2021) and simulations (e.g., Faucher-Giguère & Quataert 2012; King & Pounds 2015; Costa et al. 2020). By propagating in the galaxy, such accretion-disk winds could shock other gas phases of the ISM, generating a cascade of outflows that are then expected to influence the SF of galaxies.

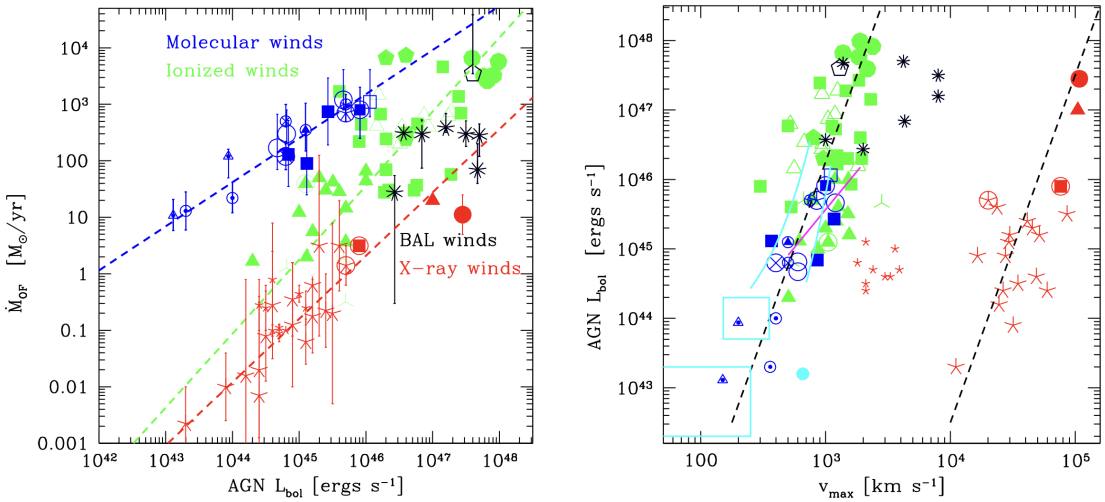

Figure 1.5: Mass outflow rate vs. AGN bolometric luminosity (*Left* panel) and outflow kinetic luminosity (*Right* panel) plots from Fiore et al. (2017) for molecular winds (blue markers), ionized winds (green markers), BAL winds (black markers) and X-ray winds (red markers). The dashed lines in the left panel represent the best fit correlations of molecular, ionized and X-ray winds, color-coded as the respective markers. The dashed lines in the right panel represent the correlations for kpc-scale winds (left) and X-ray outflows (right), indicating the link between the two outflow phases.

UFOs are predicted to be expelled in shells of thick and very ionized gas, accelerated at semi-relativistic velocities. The outward surface of the shell forward-shocks the ISM, while the inner surface of the UFO produces a reverse shock, which releases energy in the wind itself. If such energy is radiated away (i.e., cooling of the shocked wind is efficient), then only the ram pressure of the UFO is conserved, the acceleration of the ISM is limited (momentum-conserving wind) and thus the gas will eventually fall back on the SMBH and feed the accretion mechanism. If the energy produced by the reverse shock is thermalized in the inner-disc wind (i.e., cooling is inefficient), the shocked gas propagates via adiabatic expansion through the ISM, conserving its kinetic energy and reaching much larger radii (energy-conserving wind). Such kinetic energy is thus transmitted to the galactic ISM which can be accelerated up to velocities of $\simeq 10^3$ km s^{-1}. To probe which scenario the observed outflows answer to, one can measure and compare kinetic power ($\dot{E}_{\rm out}$) and momentum boost ($\dot{p}_{\rm out}$)

$$\dot{E}_{\rm out} = \frac{1}{2}\dot{M}_{\rm out} v_{\rm out}^2 \tag{1.13}$$

$$\dot{p}_{\rm out} = \dot{M}_{\rm out} v_{\rm out} \tag{1.14}$$

of each wind phase and see which is conserved between sub-pc- and kpc-scale outflows. The mass outflow rate $\dot{M}_{\rm out}$ can be estimated assuming a spherical expansion, that following Crenshaw et al. (2003) translates to:

$$\dot{M}_{\rm out} = 4\pi r_{\rm out} \mu m_{\rm p} C_{\rm g} N_{\rm H} v_{\rm out} \tag{1.15}$$

where $r_{\rm out}$ is the wind launching radius, μ is the mean atomic mass per proton (1.3 for solar abundances), $m_{\rm p}$ is the proton mass, and $C_{\rm g}$ is the covering factor of the wind. The covering factor can be measured from the p-Cygni line profile (e.g., Nardini et al. 2015, for PDS 456); since many sources do not show this kind of feature, astronomers generally use the global UFO detection fraction as wind covering factor ($C_{\rm g} \simeq 0.3 - 0.4$; Tombesi et al. 2010a; Igo et al. 2020; Matzeu et al. 2022a). The launching radius is a very difficult parameter to constrain and in principle can assume any value between the distance at which the outflow velocity equals the escape velocity of the BH potential well ($r_{\rm min}$) and the maximum distance defined by the ionization state ξ of the outflow medium ($r_{\rm max}$):

$$r_{\rm min} = \frac{2{\rm G}M_{\rm BH}}{v_{\rm out}^2}, \quad r_{\rm max} = \frac{L_{\rm X}}{N_{\rm H}\xi} \tag{1.16}$$

Given the unknown actual location of the launching site, astronomer usually conservatively assume the wind launching radius as equal to $r_{\rm min}$, thus deriving the lower limit of the wind energetics.

From Eqs. 1.13–1.15, one can infer that $\dot{E}_{\rm out} \propto v_{\rm out}^3 N_{\rm H}$ and $\dot{p}_{\rm out} \propto v_{\rm out}^2 N_{\rm H}$.

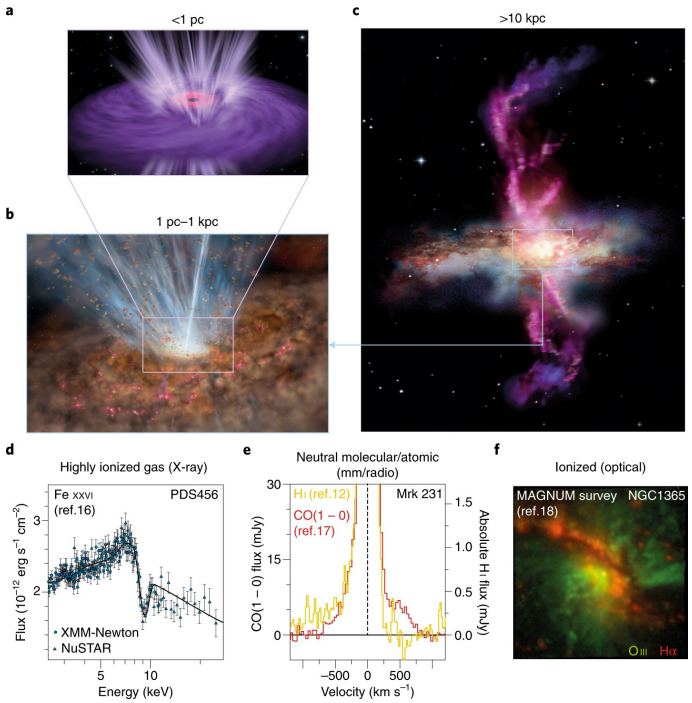

Figure 1.6: Schematic viewing of the different outflow scales, from accretion-disc, to galaxy- and halo-scales (Panels a-c). Panels d, e, f show the UFO of PDS 456 (Nardini et al. 2015), the molecular outflow of Mrk 231 (Cicone et al. 2012; Morganti et al. 2016) and the kpc-scales outflow in NGC 1365 (Venturi et al. 2018). Credits: (Cicone et al. 2018).

Measuring the column density and the speed of outflows with accuracy is a very hard task, especially at high redshift. Due to the need of multiwavelength observations, AGN that were found to host UFOs and kpc-scale outflows are less than a dozen at all redshifts (Cicone et al. 2018; Smith et al. 2019; Marasco et al. 2020; Bonanomi et al. 2023) and, due to the additional complexity of challenging exposures, less than a handful at $z > 1$ (Chartas et al. 2021; Tozzi et al. 2021). Moreover, many of such sources did not allow to discern between the two propagation scenarios due to the large uncertainties involved, especially on the UFO side. A possible workaround comes from a typical approach of astronomers: build big samples to study the overall behavior of a certain phenomenon. In this case, Fiore et al. (2017) collected all the measurements of AGN-driven winds available in the literature at the time and studied the possibility of scaling relations between the properties of a given wind phase (UFOs, WAs, ionized, molecular), given that only few AGN present multi-phase winds. Two of their main results are that *i)* the most powerful AGN generate the most massive outflows (see Fig. 1.5, Left) and *ii)* ionized and molecular outflows populate the same relation in the $L_{\rm bol}$–$v_{\rm max}$ plane (see Fig. 1.5, Right), which is statistically consistent with that found for UFOs. Fiore et al. (2017) thus conclude that the ratio of the maximum velocities of UFOs and molecular-ionized winds is

conserved for a given bolometric luminosity. This is consistent with the scenario of a unique wind accelerated by the same engine that expands across the galaxy and affects its evolution both by enhancing (positive feedback) and quenching (negative feedback) its star formation, by compressing or sweeping out the gas, respectively (Cresci & Maiolino 2018; King & Pounds 2015, see also Fig. 1.6 for a summary of the different outflow phases and scales).

More recently, Fluetsch et al. (2019) quantified the energetics and the origin (AGN vs. SF activity) of uniformly-analyzed molecular outflows in a sample of 45 local ($z < 0.2$) targets collected from the literature, for which they recalculated outflow and host galaxy properties in a homogeneous way. The sample includes both AGN host galaxies and star-forming/starburst galaxies, spanning a range in AGN bolometric luminosity from $\log(L_{\rm Bol}) \simeq 41$ up to $\simeq 46$ erg s^{-1} and in SFR from $\simeq$0.1 up to several 100 M$_\odot$ yr^{-1}. The molecular-mass loading factor ($\eta = \log(\dot{M}_{\rm out}(H_2)/{\rm SFR})$) is higher in AGN host galaxies compared to star-forming galaxies, although a significant boost is only seen in galaxies in which the AGN luminosity is high relative to the bolometric luminosity of the total galaxy+AGN system ($L^{\rm AGN}_{\rm Bol}/L^{\rm tot}_{\rm Bol} > 0.7$; see Fig. 1.7). Moreover, Fluetsch et al. find that the mass outflow rate correlates with the AGN luminosity and with the Eddington ratio, although with large scatter, further indicating that the AGN plays a key role in driving such outflows.

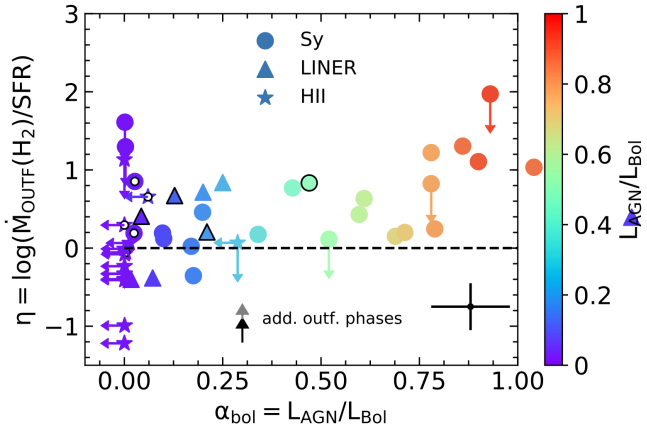

Figure 1.7: Mass loading factor as a function of AGN fractional contribution to the bolometric luminosity, $L^{\rm AGN}_{\rm Bol}/L^{\rm tot}_{\rm Bol}$ from Fluetsch et al. (2019). Circles indicate Seyfert host galaxies, LINERs are plotted as triangles and purely star-forming galaxies as stars. The data points are colour-coded according to their AGN contribution (LAGN/Lbol), as given in the colour bar on the right. The black dashed line shows the relation for an outflow mass-loading factor $\eta = 1$.

Besides probing how the inner-disk winds can trigger galaxy-scale outflows (e.g., Fiore et al. 2017; Smith et al. 2019; Mizumoto et al. 2019), we are also still struggling to constrain the occurrence rate of UFOs themselves. They have been mostly studied in bright and nearby Seyfert galaxies (detection fraction of $\simeq$30–40%, Tombesi et al.

2010a; Igo et al. 2020) and recent results from the SUBWAYS group confirmed a similar detection rate also in the low-z ($0.1 < z < 0.5$) Universe (Matzeu et al. 2022a). Moreover, these winds show clear variability from one observation to the other (Cappi et al. 2009) and also within single observations (e.g., Dadina et al. 2005; Giustini et al. 2011; Gofford et al. 2014), with variations happening on timescales as short as a few kiloseconds. The current idea is thus that UFOs might well be common and widespread, but episodic events. However, we are still lacking robust statistical studies of their average properties in the distant Universe. In particular, it is of extreme relevance to fill the gap at cosmic noon, a key cosmic time for feedback processes. So far, only less than 20 sources at $z \geq 1.4$ have been analyzed with this goal in the X-ray band (for instance, APM 08279+5255, PG1115+080, H1413+117, HS 0810+2554, and MG J0414+0534, Hasinger et al. 2002; Chartas et al. 2003, 2007b, 2016a; Dadina et al. 2018, but see also Chartas et al. 2021). Interestingly, almost all UFOs seen at $z > 1$ were observed in gravitationally lensed quasars (GLQs), and, to our knowledge, thus far the only bright, non-lensed sources at $z \geq 1.5$ are HS 1700+6416 and PID 352 (Lanzuisi et al. 2012; Vignali et al. 2015). That high-z UFOs are associated with GLQs is not surprising given the need of good signal-to-noise ratio (S/N) spectra to determine the presence of these winds. In this sense, the magnification provided by the gravitational lens[**] is a unique tool to obtain good quality data in a sustainable amount of observational time.

The physical quantities $\dot{E}_{\rm out}$ and $\dot{p}_{\rm out}$ also allow us to probe the acceleration mechanisms of accretion-disk winds. In particular, the energy loading factor ($\dot{E}_{\rm out}/L_{\rm Bol}$) of a wind accelerated by radiation pressure must be lower or equal to the wind covering factor, i.e., $\dot{E}_{\rm out}/L_{\rm Bol} \leq C_{\rm g} \simeq 0.4$[††]. Additionally, the momentum boost $\dot{p}_{\rm out}$ in the case of radiative driving cannot be higher than the radiation pressure produced by the AGN emission ($\dot{p}_{\rm rad} = L_{\rm bol}/c$). As mentioned, such quantities usually carry with them large uncertainties; however, many UFOs detected at high-z require acceleration mechanisms either than radiation pressure, such as magnetic driving (e.g., Fukumura et al. 2010), to explain the large kinetic powers and momentum boosts (e.g., Dadina et al. 2018), as will be discussed in §2.2. Moreover, Luminari et al. (2020, 2021) recently presented revised limits for the radiative acceleration mechanism. By the inclusion of relativistic effects, they found a reduced efficiency for radiation-driving mechanisms, resulting in lower attainable velocities ($v_{\rm out} < 0.15c$). This provides additional proof that the acceleration mechanism of UFOs, especially for the fastest ones, is likely more complex than a pure radiation-driven flow.

[**]See Appendix A for the theoretical background on gravitational lensing.

[††]Assuming a spherically symmetric emission from the source, the wind can only absorb that part of AGN flux that illuminates it, which corresponds to the covering factor of the wind.

1.3.2 Effects of AGN on the molecular gas reservoir of galaxies

The Schimdt-Kennicutt law (Schmidt 1959; Kennicutt 1989) is a fundamental relation that links the molecular gas content and the level of SF of galaxies. This relation was first presented in terms of surface densities, since it was discovered in the local Universe, where spatially resolved studies are accessible. Subsequently, especially for high-z studies, astronomers started using an integrated form of this relation, linking the global SFR of galaxies to their total molecular mass (e.g., Carilli & Walter 2013; Sargent et al. 2014). Moreover, Lada et al. (2012) demonstrated that such a link between the available molecular gas mass and the SF efficiency extends at all scales, relating extragalactic sources to giant-molecular clouds and, at the same time, local SF processes to the global SF efficiency of galaxies. If AGN play a key role in shaping the growth and evolution of galaxies (e.g., Fabian 2012; Harrison 2017), then we can reasonably expect them to have an impact on the molecular gas phase of their host's ISM. In particular, AGN are expected to heat/dissociate/eject the molecular gas reservoir, with the consequence of reducing the material that otherwise would have been turned into stars. Thus, besides addressing AGN feedback as "caught in the act" (i.e., AGN-driven outflows), comparative studies of the molecular gas properties in AGN host galaxies and non-active galaxies (i.e., galaxies not hosting an AGN), matched in SFR, redshift, stellar mass, can shed light on whether AGN have indeed affected the evolution of galaxies, regardless of whether outflows are concurrently detected in the source.

Molecular hydrogen (H_2) is a self-shielding molecule with widely spaced excitation levels due to its lack of a permanent dipole (least energetic transition: $J = 2 \rightarrow 0$, $T \simeq 510$ K), thus it is extremely hard to observe. For this reason, astronomers had to come up with a proxy, as we usually do, and found one in the carbon monoxyde (CO), the second most abundant molecule after H_2. The CO molecule has a strong binding energy, that can preserve it from destructive reactions, and has a permanent electric dipole, that allows for strong rotational transitions that can be observed in the *mm*/radio band. Its rotational levels are closely spaced and the equivalent temperature for the first rotational transitions ($J = 1 \rightarrow 0$, $J = 2 \rightarrow 1$; hereafter, $1-0$ and $2-1$, respectively) is easily reached in a cold and quiescent cloud ($T_{\rm eq}^{1-0} \simeq 5.5$ K, $T_{\rm eq}^{2-1} \simeq 16$ K). CO is thus the primary tracer of molecular gas (e.g., Carilli & Walter 2013; Hodge & da Cunha 2020), even though other molecules are needed to trace the densest molecular regions due to the low critical density of CO ($n_{\rm cr} \simeq 10^3 - 10^4\,{\rm cm}^{-3}$ for $J_{\rm up} < 7$). Astronomers use the luminosity of the ground state transition $L'_{\rm CO(1-0)}$ as tracer of molecular gas mass ($M_{\rm H_2} = \alpha_{\rm CO} L'_{\rm CO(1-0)}$), even if there is a strong debate of which value of $\alpha_{\rm CO}$ best represents the galaxy in question. The value calibrated on the Milky Way ($\alpha_{\rm CO} = 4\,{\rm M}_\odot\,({\rm K\ km\ s^{-1}\ pc^2})^{-1}$, Bolatto et al. 2013) is a good approximation for regular star-forming galaxies (Carilli & Walter 2013), while the much lower value

of $\alpha_{CO} = 0.8\,M_{\odot}\,(K\ km\ s^{-1}\ pc^2)^{-1}$ (Solomon & Vanden Bout 2005) is more representative for high-z sub-mm galaxies, which usually show an extremely dense ISM and a much higher SF activity (e.g., Birkin et al. 2021). The general assumption for star forming galaxies at cosmic noon is usually $\alpha_{CO} = 3.6\,M_{\odot}\,(K\ km\ s^{-1}\ pc^2)^{-1}$ (e.g., Daddi et al. 2010; Kakkad et al. 2017; Kirkpatrick et al. 2019; Circosta et al. 2021, hereafter C21). Measuring the ground transition of CO is not always possible, especially at high-z. However, we can recover the CO(1-0) flux from the CO Spectral Line Energy Distribution (CO SLED), which expresses the relative strength of the CO rotational lines as a function of the quantum number J. The CO SLED is a powerful tool that allows to assess the excitation mechanism(s) of the molecular gas, for instance SF processes and AGN activity (e.g., Pozzi et al. 2017; Mingozzi et al. 2018; Boogaard et al. 2020; Valentino et al. 2021; Esposito et al. 2022). In terms of proxy for molecular masses, the CO transitions that guarantee reasonable results correspond to rotational levels $J < 5$, since the relative strength of such transitions and CO(1-0) is typically less uncertain (see Carilli & Walter 2013, for a review). The higher-J transitions are usually explained as arising from high-density ($n_H \sim 10^5\,cm^{-3}$), high-temperature ($T \sim 100\,K$) molecular gas and thus as produced by the AGN radiation field and/or shocks by AGN-driven outflows (e.g., Gallerani et al. 2014; Mingozzi et al. 2018; Vallini et al. 2019; Li et al. 2020; Pensabene et al. 2021).

Results regarding if and how AGN affect this particular gas phase are however controversial and seem to hint at a dichotomy between low-z and high-z scenarios. AGN hosts in the local Universe are usually seen as indistinguishable from non-active galaxies (e.g., Rosario et al. 2018; Koss et al. 2021; Salvestrini et al. 2022) or even gas richer, in the sense that the more powerful the AGN, the more gas rich is the host galaxy (e.g., Vito et al. 2014; Husemann et al. 2017). Moreover, some results hint at enhanced SF efficiencies in AGN hosts thanks to this large molecular gas reservoir (e.g., Shangguan et al. 2020; Jarvis et al. 2020). This fact is not surprising if one considers that the gas powering AGN activity is the same that can then be converted into stars. Such results, however, are linked to the *total* molecular gas mass of local and low-z galaxies. Spatially resolved ($< 0.5''$) studies of local and low-z hosts showed that AGN efficiently deplete the central regions of galaxies (e.g., Rosario et al. 2019; Fluetsch et al. 2019), with indications that the central (within few 100 pc) SF activity is indeed reduced due to the presence of AGN, while the galaxy-wide SFR is left "untouched" (e.g., García-Burillo et al. 2021; Lammers et al. 2022, but see also Molina et al. 2022a, in which SF activity is enhanced in the proximity of the AGN).

The scenario at high-z is instead much different, but still controversial. High-z AGN hosts are usually CO-depleted when compared to control samples of non-active

galaxies, either in terms of gas fraction[‡‡] or of depletion timescales (e.g., Brusa et al. 2016, 2018; Kakkad et al. 2017; Perna et al. 2018; Bischetti et al. 2021). However, some works have also found no difference in the gas fraction of regular galaxies and AGN hosts (e.g., Kirkpatrick et al. 2019). Such a dichotomy between results on local and high-z targets could arise from selection effects. High-z studies usually rely on few, high-luminosity ($\log(L_{\rm Bol}/{\rm erg\ s^{-1}}) > 46$) and heterogeneous targets, both because high-power AGN are the best candidates to produce efficient feedback (e.g., Fiore et al. 2017; Costa et al. 2018; Fluetsch et al. 2019, and see also Figs. 1.5 and 1.7) and also because of the challenging observations required for distant objects.

To obtain reliable estimates of the occurrence and impact of galactic-scale winds, multi-wavelength studies of unbiased high-z AGN samples are indeed required. Two surveys of high-z, X-ray selected AGN were recently conceived to fill this observational need (see Fig. 1.8): KASHz (KMOS AGN Survey at High redshift; Harrison et al. 2016, Scholtz et al. in prep) and SUPER (SINFONI Survey for Unveiling the Physics and Effect of Radiative feedback, PI: V. Mainieri; Circosta et al. 2018, hereafter, C18). Both surveys share the aim of studying the interplay between AGN-driven ionized winds, traced through [OIII] emission lines, and host galaxy SF activity in a sample of AGN built without priors regarding AGN feedback. On the one hand, SUPER targets are resolved down to small scales (<2 kpc) by means of AO-assisted VLT/SINFONI observations but the sample is limited to ∼40 objects at $z \sim 2-2.5$. KASHz, on the other hand, has a much larger sample (≃235 objects, $z \sim 0.6-2.6$) but resolves only much larger scales (>5 kpc), since VLT/KMOS is seeing-limited. In this context, the different observational capabilities and selection criteria make KASHz what can be considered a parent sample for SUPER, thus using them jointly allows us to capitalize their strengths.

C21 carried out the first systematic comparative study of the molecular gas content in AGN hosts at $z \simeq 2-2.5$, drawing targets from the SUPER survey. To avoid the additional uncertainty inherent to the choice of a CO-to-molecular mass conversion factor, C21 analyzed the CO(3-2) emission and far-IR (FIR) luminosity of all SUPER Type 1 AGN, as proxy for the molecular gas content and SFR, respectively. The authors discovered that gas depletion is marginal in SUPER hosts, and becomes significant only narrowing the sample down to those targets at the higher-end of CO and FIR distributions (see Fig. 1.8, right). Such a result demonstrates the importance and the need of including also 'regular' AGN ($\log(L_{\rm Bol}/{\rm erg\ s^{-1}}) > 44.2$) in our high-$z$ samples.

Lastly, predictions from cosmological simulations seems to be likewise contro-

[‡‡]The definition of gas fraction varies within different studies, with some using $f_{\rm gas} = M_{\rm gas}/M_{\rm tot}$ ($M_{\rm tot} = M_{\rm gas} + M_*$) and some others using $f_{\rm gas} = M_{\rm gas}/M_*$. Throughout this work, we assume the latter definition, thus $f_{\rm gas} = M_{\rm gas}/M_*$.

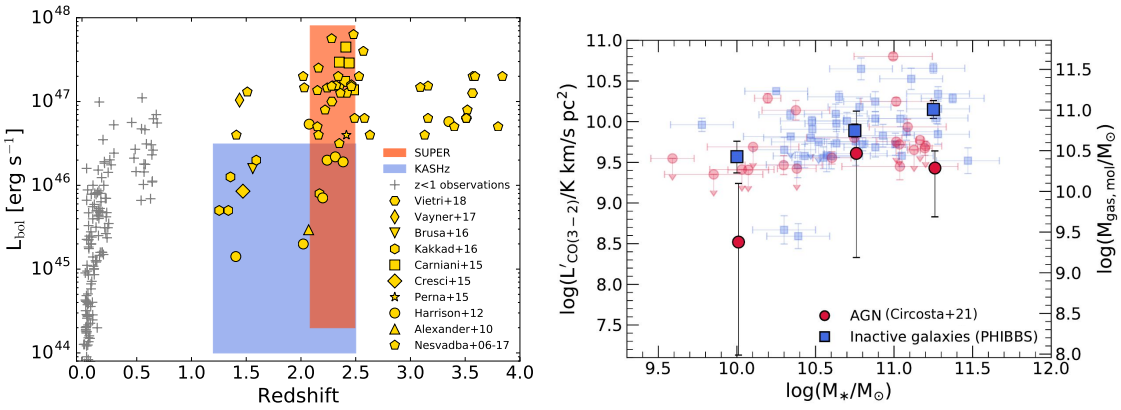

Figure 1.8: *Left panel:* $L_{\rm bol}$ vs. z distribution of all the integral-field spectroscopy observations available in literature characterizing AGN feedback through [OIII]-traced ionized outflows (adapted from C18). Blue and red shaded areas indicate the parameter space probed by KASHz and SUPER surveys, respectively. *Right panel:* CO(3-2) luminosity and molecular gas masses vs. stellar masses (adapted from C21). Red points refer to SUPER AGN and blue points to the control sample of non-active galaxies. The mean values per stellar-mass bin are shown in darker colors.

versial. Ward et al. (2022) recently analyzed the output of three key cosmological simulations (Illustris-TNG, EAGLE and Simba) with the same methods observational astronomers employ to analyze data of real galaxies and AGN hosts, considering a sample of local targets and a sample of cosmic noon ($z = 2$) objects. The authors conclude that none of the selected simulations predict strong negative correlations between AGN power and molecular gas fraction or specific SFR (sSFR = SFR/M_*). Moreover, powerful AGN seem to preferentially reside in gas rich, highly-star-forming galaxies, and gas-depleted and quenched fractions in the control samples of regular galaxies are higher than those of AGN hosts. Ward et al. (2022), however, argue that there is a quantifiable difference among the predictions of the selected simulations. For instance, this is true for the distribution of galaxies in the $L_{\rm bol} - f_{\rm H_2}$ plane. Selecting the best implementation in the simulations is hard because the range covered by model predictions and observational efforts hardly overlap at both the considered redshifts. This is mainly due to the difficulty in reproducing sizable samples of high-luminosity AGN ($L_{\rm bol} \gtrsim 10^{43.5}$ erg s^{-1} at $z = 0$, $L_{\rm bol} \gtrsim 10^{45}$ erg s^{-1} at $z = 2$) in cosmological simulations, since they are rare and short lived to be captured in current simulations, which are too limited in box-size and time-sampling. Until the development of next-generation cosmological simulations, the best approach is to provide observational reference points in a luminosity range that is covered by present-day simulations and thus hope to discriminate between the different predicted relations.

1.4 Thesis outline

Given the described state-of-the-art in the characterization of high-z AGN feedback, the purpose of this thesis is to investigate the impact of AGN on galaxy growth around the cosmic noon via a two-track, multiwavelength approach.

The first track focuses on the characterization of AGN feedback in terms of its "cause": AGN-driven winds as visible in the X-rays at sub-pc-scales, that is, UFOs. In Chapter 2, I will present our efforts in producing statistical studies of high-z UFOs, both in a sample of GLQs built without priors regarding AGN feedback and in a sample of AGN selected because showing AGN-driven winds in other gas phases. Chapter 3 is dedicated to one notable high-z GLQ of both samples, Q2237+030, which allowed us to measure the duty cycle of UFOs in a single, high-z source for the first time. Next, I will describe in Chapter 4 the analysis of the latest X-ray observations of APM 08279+5255, another well known high-z GLQ, especially remarkable for its wind duty cycle of virtually one. The X-ray observations, however, were tailored at testing the predictions of the hot-corona-thermostat model at the highest redshift reached so far, allowing to investigate the inner geometry of the accreting system.

The second track of this thesis focuses on the "effects" of AGN feedback at kpc-scales, as traced by the molecular gas reservoir of galaxies. In Chapter 5, we performed a comparative study of non-active galaxies and AGN hosts at cosmic noon. We built a sizable sample of AGN hosts drawn from the X-ray selected AGN of SUPER and KASHz surveys, with the aim of expanding the work presented in C21. To match our goal, we employ ALMA data to measure the molecular masses and we retrieve the properties of our galaxies from SED fitting.

Chapter 6 presents the conclusions of this thesis and the possible future expansion of the presented work of research.

Throughout this thesis, we assume a flat ΛCDM cosmology (Planck Collaboration et al. 2020), with $H_0 = 70.0$ km s^{-1} Mpc^{-1} and $\Lambda_0 = 0.73$.

Chapter 2

Statistical studies of high-redshift UFOs

To meaningfully investigate whether UFOs are present or absent in a certain target, high S/N spectra are required to be sure that non-detections are not due to the low quality of the data. Exquisite spectra of local Seyferts can generally be obtained with exposure times of few tens of kiloseconds. As a consequence, UFOs were extensively studied in local AGN, allowing for statistical studies of their properties (e.g., Tombesi et al. 2010a,b; Gofford et al. 2013, 2015; Matzeu et al. 2016; Igo et al. 2020) and for the assessment of a possible link with WAs (e.g., Tombesi et al. 2013).

Regarding the high-z Universe, the picture is not as ideal. Obtaining good spectra of high-z ($z > 1$) AGN is not a trivial exercise, especially in the X-ray band. On the bright side, the redshifting of the photon energy ends up helping us, moving the band of interest for UFOs towards the peak of the effective area of observatories like *Chandra* and XMM-*Newton* (that is, close to $\simeq$ 1–2 keV). Nonetheless, only few high-z AGN allowed for a meaningful assessment of UFOs in their X-ray data. As mentioned in Chapt. 1, Sect. 1.3, a powerful tool for in-depth spectral studies of high-z AGN, especially in the X-ray band, resides in gravitational lensing. In fact, almost all of the targets that allowed for the investigation of X-ray winds in the high-z Universe are GLQs (Chartas et al. 2021, and see also Sect. 2.2).

In this Chapter, I will present our efforts in providing statistical studies of UFOs at high-z, with the aim of aligning our knowledge of local and distant-Universe events. Firstly, we addressed the topic in a sample built by selecting sources at $z > 1$ with good-enough X-ray data for our purposes (Sect. 2.1 in order to assess the detection fraction of UFOs at high-z in a sample built without prior knowledge regarding AGN feedback. Secondly, we investigate the properties and driving mechanism(s) of high-z UFO by collecting all the available measurements in the literature, complemented with new detections obtained through our XMM-*Newton* exploratory survey of high-z NAL GLQs (Sect. 2.2).

2.1 "Feedback-unbiased" sample of high-redshift GLQs

Aim of this Section is providing the community with a statistically robust sample of high-z AGN to yield solid results regarding the average properties of UFOs at $z > 1$. To be representative of the whole high-z AGN population, we built such a sample by selecting targets only based on the availability of good archival X-ray spectra, without assuming any kind of prior regarding AGN feedback. As such, we refer to this sample as the "feedback-unbiased" sample. As already mentioned, GLQs are by far the most promising targets for this kind of studies at high-z. Nonetheless, our ultimate aim is to include both lensed and non-lensed AGN to maximize the quality of our data and to obtain a sample the least biased as possible.

2.1.1 Surveys of GLQs and target selection

We started to build the "feedback-unbiased" sample by searching for X-ray data of lensed AGN. We first built a catalog of lensed, high-z AGN by drawing confirmed GLQs with background source at $z_{\rm q} > 1$ from from the CASTLES (CfA-Arizona-Space-Telescope-LEns-Survey, Muñoz et al. 1998) and the SQLS (Sloan Digital Sky Survey Quasar Lens Search, Inada et al. 2012) catalogs. We obtained a sample of 99 GLQs, 52 of which with background source at $1 < z_{\rm Q} < 2$ and 47 with background source at $z_{\rm Q} > 2$ (see Table B.1 in Appendix B). By this selection, we included also GLQs with undetermined lens redshift (22 targets). Even though a not-well-constrained lensing system would impede the determination of intrinsic source (and, possibly, wind energetics) properties, we deemed not necessary to exclude these GLQs a priori since gravitational lensing is an achromatic phenomenon and is not expected to fake UFO features in the source spectra, the secure detection (or non-detection) of which is our primary goal. Moreover, since UFOs were detected both in radio-quiet and radio-loud targets (e.g., Tombesi et al. 2010b; Dadina et al. 2018), we only exclude lensed blazars (that is, PKS 1830-211), since the jet would blind us toward any other properties visible in the X-rays.

The resulting GLQ catalog was then cross-matched with all available X-ray data archives (*Chandra*, XMM-*Newton*, *NuSTAR*, *Swift*, *Suzaku*) through the dedicated tool on the HEASarc website. We also queried the latest versions (as of Spring 2020) of the source catalogs by *Chandra* and XMM-*Newton*: the *Chandra* Source Catalog v.2.0, which includes *Chandra* observations up to 2014, (Evans et al. 2019, 2020) and 4XMM-DR9 (Webb et al. 2020a,b), that includes XMM-*Newton* observations up to February 2019. The query returned a total of 850 exposures taken by the five observatories that grant X-ray exposure of 72 GLQs of our initial catalog, that corresponds to a mean of almost 12 exposures per GLQ. The total number of observations is divided up between the five X-ray facilities as follows: 45% by *Chandra*, 15% by XMM-*Newton*, 37% by *Swift*, 2% by *NuSTAR* and 1% by *Suzaku*. The tool

in HEASarc returns a match when the queried coordinates fall inside the field of view of an observation. As a consequence, a positive match might also mean that the target of interest is observed as a serendipitous source, possibly at very high off-axis angles, i.e. where the effective area drops significantly due to vignetting.

Thanks to their large effective area in the soft band, the best observatories for UFO analysis at $z > 1$ are *Chandra* and XMM-*Newton*, which have indeed proven their capabilities many times (e.g., Chartas et al. 2009; Lanzuisi et al. 2012; Dadina et al. 2018, but see also the compilation in Chartas et al. 2021 and Sect. 2.2). *Swift* exposures are generally very short (from tens of ks to as short as few 100s) and more aimed at monitoring the source flux than at extracting precise spectral properties, while *NuSTAR*'s effective area usually does not grant the high-quality spectra we are looking for for high-z sources. Moreover, the *Suzaku* archive totalled 7 observations: three are short exposures (less than 30 ks) of HE0512-3329, one is a longer exposure of Q0142-100 ($\simeq$60 ks), three are long exposures ($\simeq$100 ks) of APM 08279+5255. Regarding the first two sources, we inspected the archive data products, finding that the data quality did not match our standards (less than 300 source net counts in the full observed-energy band). Regarding the third source, the *Suzaku* observations of APM 08279+5255 are already presented and analyzed for UFOs in Saez et al. (2009). For these reasons, we narrowed down the GLQ sample to those sources for which *Chandra* and/or XMM-*Newton* data, i.e., the most promising data, were available. The final "feedback-unbiased" catalog comprises 58 non-blazar, confirmed GLQs at $z > 1$ with available *Chandra* and/or XMM-*Newton* archival data, either observed on-axis or as serendipitous sources, for a total of 508 different exposures. One of the 58 GLQs is Q2237+030, a very interesting lensing system due to its very nearby lens, which is the target of 37 *Chandra* and 3 XMM-*Newton* archival observations, taken from 2002 and 2018 (as of September 2019). With such a rich dataset for a single source, we decided to carry out a systematic search for UFOs and investigate the possible recurrence of their features in this GLQ, analysis that we present in Chapter 3.

Having set aside the exposures of Q2237+030, we investigated how many of the archival observations of the final "feedback-unbiased" catalog could yield useful data to our purposes. We employed a different approach for *Chandra* and XMM-*Newton* data samples for a very simple reason: when dealing with XMM-*Newton* data, the way one selects the good-time intervals (GTIs) of an observation has a strong impact on the final spectrum due to the background (often strong) variability produced by soft-p$^+$ flares, while *Chandra* final data products are much less dependent on the first steps of the data reduction thanks to the significantly lower background provided by the higher spatial resolution. The adopted criteria and procedures are described in the following Sections.

2.1.2 Analysis of *Chandra* data

First, we skimmed our *Chandra* observation list relying on the CSC v.2.0 information to retrieve the exposures that would yield useful data to our purposes. We selected our best data sample based on the number of source net counts in the 2–10 keV rest-frame band, that is the region of interest for UFO spectral features and the Fe Kα complex. The corresponding observed-frame band for the redshift range of our sample ($1 < z < 4$) varies from 1–5 keV ($z = 1$) to 0.4–2 keV ($z = 4$). The CSC v.2.0 lists the source properties in the 0.5–1.2, 1.2–2 keV and 2–7 keV observed-frame energy range. We thus imposed a threshold in the full band (0.5–7 keV observed-frame) and in the soft band (0.5–2.0 keV observed frame) so to meaningfully cover the 2–10 keV rest-frame range over the full redshift range of our sample ($1 \lesssim z \lesssim 4$). Given the large available dataset, we could test different thresholds in terms of data quality, and we summarize here the ones yielding the most promising *Chandra* data: we narrowed down the data sample to those observations that the CSC v.2.0 lists as providing source spectra *i)* with more than 500 counts in the 0.5–7 keV observed-frame energy range for $1 \lesssim z \lesssim 2$ and *ii)* with more than 350 counts in the 0.5–2 keV observed-frame energy range for $2 \lesssim z \lesssim 4$. Threshold *i)* would guarantee at least 20–25 spectral bins over the 0.5–7 keV observed-energy range in a grouping regime apt to the use of χ^2 statistics, that is, of at least 20 cts/bin. We obtained threshold *ii)* as a consequence of threshold *i)*, by converting the expected counts in the 2–10 keV rest-frame energy band of a lower-z source ($z \simeq 1.5$) that passed criterium *i)* to the corresponding observed range of a higher-z GLQ ($z \simeq 2 - 4$). Such a procedure was widely tested on Q2237+030, as presented in Chapter 3. We performed the crossmatch with a 6″-radius cone centered on the target coordinates in the NASA/IPAC Extragalactic Database (i.e., those that we report in this thesis) which, based on the image separation listed in Table B.1, should allow to cover almost all the lensing images of each target with a small contamination of other field sources.

Based on this S/N double cut, the "feedback-unbiased" sample includes a total of 35 *Chandra* observations of 20 GLQs, for a total of 39 spectra that passed our criteria. This means that in some observations more than one lensing image has a spectrum above threshold. We consistently reduced and analyzed all the selected data using the latest software (as of June 2020): ciao v.4.12 and CALDB v.4.9.1 (Fruscione et al. 2006). Given that gravitational lensing might introduce spectral differences among the lensing images, we investigated the single-image X-ray properties of each GLQ, whenever their images were spatially resolved. In the case of B1422+231 and HS0810+2554 (two "quads", i.e. GLQs with four lensed images), images A and B are blended in the *Chandra* data, so we extracted the spectra of image A+B. For all targets, source regions were selected with variable radii (from 0.8″ to 1.5″, depending on the target images) and, when necessary, by imposing a certain

Table 2.1: Summary of the *Chandra* that passed our selection criteria (see main text for details).

NAME	RA	DEC	z_Q	z_L	Nim	sep (″)	obsID	exp. (ks)	cts[0.5-7]	cts[0.5-2]
HE 0047-1756	00:50:27.835	-17:40:09.27	1.6756	0.41	2	1.44	9515	34.1	1185	932
Q 0142-100	01:45:16.610	-09:45:17.31	2.73779	0.49	2	2.24	5192	13.6	613	511
Q J0158-4325	01:58:41.44	-43:25:04.20	1.29	0.317	2	1.22	14483	19	524	397
Q J0158-4325	01:58:41.44	-43:25:04.20	1.29	0.317	2	1.22	14485	19	605	464
Q J0158-4325	01:58:41.44	-43:25:04.20	1.29	0.317	2	1.22	14486	19	587	414
HE 0230-2130	02:32:33.1	-21:17:26	2.162	0.52	4	2.05	12799	30	690	506
SDSS J0246-0825	02:46:34.11	-08:25:36.2	1.686	0.723	2	1.09	9516	50.2	1721	1402
MG J0414+0534	04:14:37.73	+05:34:44.3	2.64	0.96	4E	2.4	1628	9.1	512	344
MG J0414+0534	04:14:37.73	+05:34:44.3	2.64	0.96	4E	2.4	3395	28.8	1287	857
MG J0414+0534	04:14:37.73	+05:34:44.3	2.64	0.96	4E	2.4	3419	97.9	569	397
MG J0414+0534	04:14:37.73	+05:34:44.3	2.64	0.96	4E	2.4	3419	97.9	1318	945
MG J0414+0534	04:14:37.73	+05:34:44.3	2.64	0.96	4E	2.4	3419	97.9	4665	3099
MG J0414+0534	04:14:37.73	+05:34:44.3	2.64	0.96	4E	2.4	12800	30	907	583
B 0712+472	07:16:03.58	+47:08:50.0	1.34	0.41	4	1.46	4199	99	833	584
HS 0810+2554	08:13:31.3	+25:45:03.2	1.5	-	4	0.96	3023	4.9	591	441
HS 0810+2554	08:13:31.3	+25:45:03.2	1.5	-	4	0.96	16110	101	5535	4034
APM 08279+5255	08:31:41.59	+52:45:17.0	3.87	-	3	0.38	1643	9.2	882	667
APM 08279+5255	08:31:41.59	+52:45:17.0	3.87	-	3	0.38	2979	90.3	5397	3849
APM 08279+5255	08:31:41.59	+52:45:17.0	3.87	-	3	0.38	7684	90.2	6608	4875
SBS 0909+532	09:13:01.05	+52:59:28.83	1.38	0.83	2	1.17	8176	20.1	2845	2052
Q 0957+561	10:01:20.83	+55:53:49.6	1.413	0.36	2	-	2038	3237	26.9	2521
SDSS J1004+4112	10:04:34.91	+41:12:42.8	1.74	0.68	5	14.72	5794	81.2	1521	1202
SDSS J1004+4112	10:04:34.91	+41:12:42.8	1.74	0.68	5	14.72	5794	81.2	1184	916
SDSS J1029+2623	10:29:13.945	+26:23:17.98	2.199	0.58	3	22.54	11755	56.5	760	551
HE 1104-1805	11:06:33.45	-18:21:24.2	2.32	0.73	2	3.19	375	49.2	841	639
PG 1115+080	11:18:17.00	+07:45:57.7	1.72	0.31	4	2.32	363	26.8	1193	934
PG 1115+080	11:18:17.00	+07:45:57.7	1.72	0.31	4	2.32	1630	9.9	525	401
PG 1115+080	11:18:17.00	+07:45:57.7	1.72	0.31	4	2.32	7757	29.1	1964	1472
PG 1115+080	11:18:17.00	+07:45:57.7	1.72	0.31	4	2.32	10796	15.2	638	445
Q 1120+0195	11:23:20.730	+01:37:47.52	1.472	-	-	-	3013	111.6	4682	3327
B 1152+200	11:55:18.297	+19:39:42.24	1.0188	0.439	2	1.59	5909	9.1	1130	924
B 1152+200	11:55:18.297	+19:39:42.24	1.0188	0.439	2	1.59	6249	18.1	632	466
B 1152+200	11:55:18.297	+19:39:42.24	1.0188	0.439	2	1.59	6249	18.1	2113	1708
Q 1355-2257	13:55:43.434	-22:57:23.17	1.37	0.48)	2	1.23	9514	31.6	1888	1462
B 1422+231	14:24:38.09	+22:56:00.6	3.62	0.34	4E	1.68	367	28.8	1259	898
B 1422+231	14:24:38.09	+22:56:00.6	3.62	0.34	4E	1.68	4939	50.2	5575	4058
B 1422+231	14:24:38.09	+22:56:00.6	3.62	0.34	4E	1.68	12801	30	1176	774
WFI 2026-4536	20:26:10.43	-45:36:27.1	2.23	-	4	1.34	7758	10.2	762	605
WFI 2026-4536	20:26:10.43	-45:36:27.1	2.23	-	4	1.34	14963	36	1116	835

Notes. Columns cts[0.5-7] and cts[0.5-2] are derived from CSC v.2.0: Column cts[0.5-7] corresponds to the cnts_aper_b variable (broad band: 0.5–7 keV observed-frame), Column cts[0.5-2] is the sum of cnts_aper_s (soft band: 0.5–1.2 keV observed-frame) and cnts_aper_m (medium band: 1.2–2 keV observed-frame).

offset between the image centroid and the center of the extraction region so to reduce the contamination of the neighboring images. Background regions were selected as annuli (inner radius: $\simeq 10''$, outer radius: $50''$) centered on the GLQ whenever possible, excluding X-ray field sources by adjusting the inner and/or outer radius alongside making sure to select a large enough background region. When excluding field sources by adjusting the size of an annulus region was not a trivial task, we used two separate $30''$-radius circles on two opposite sides with respect to the target, so to still sample the possible non-uniformity of the background. We then checked for pileup and none of our data present pileup levels that would significantly change the source spectral shape.

We applied the described regions to extract the single-image lightcurves. No significant variability (i.e., variable above the 99% confidence threshold) is detected in any lightcurve (binned at 100s), thus we employed the same regions to extract the single-image spectra. Each single-image spectrum was then fitted with a `zpowerlaw` model, i.e., the continuum emission produced by the primary X-ray source. All models are modified by Galactic absorption, according to the results by HI4PI Collaboration et al. 2016. We then inspected statistical parameters and residuals of each spectrum to assess the quality of the fit and weigh whether other spectral components would be needed to explain the data: extra absorption at the redshift of the GLQ, emission and/or absorption lines, X-ray reflection.

Many of our spectra are well reproduced by a single power law model. Only HS 0810+2554 and MG J0414+0534 require extra absorption at the quasar redshift, with moderate column densities ($\log(N_{\rm H}/{\rm cm}^{-2}) \simeq 21.5$ and $\log(N_{\rm H}/{\rm cm}^{-2}) \simeq 22.6$, respectively) consistent with previous results on image-integrated spectra collected by *Chandra* or XMM-*Newton* (Chartas et al. 2016a; Dadina et al. 2018, respectively). The selected observations of SDSS 1004+4112 and Q J0158-4325 were part of the data sample of Chen et al. (2012), who studied the Fe Kα emission lines in multi-epoch, single-image stacked spectra of six GLQs. We find hints of Fe Kα emission lines in the single-image, single-epoch spectra of these two GLQs that are consistent with the results of Chen et al. (2012). Regarding the study of UFOs, literature results are all based on XMM-*Newton* data (i.e., unresolved lensing images) or on spatially-integrated, multi-image (and often multi-epoch) spectra from *Chandra* (except for Q2237+030, as discussed in Chapter 3). However, by stacking multiple images and/or observational epochs, one might end up diluting or destroying the signal of the most variable UFO features (see Chapter 3, Sect. 3.5). In this work, we thus decided to first approach the *Chandra* data through single-image, single-epoch spectra of each selected *Chandra* exposure to investigate the presence of UFOs, including the possibly highly variable ones. In this way, we can take into account the possible spectral differences among images due to time delays and microlensing events which might turn out as penalizing effects when stacking the different images

in a single spectrum.

Part of our *Chandra* data sample are also observations of GLQs already known to host UFOs: APM 08279+5255 (Chartas et al. 2002, 2009), PG 1115+080 (Chartas et al. 2007a), MG J0414+0534 (Dadina et al. 2018), HS 0810+2554 (Chartas et al. 2016a). We confirm the presence of the two UFO components, as found for the two longest *Chandra* exposures by Chartas et al. (2002, 2009), in APM 08279+5255 also from the analysis of its single-image, single-epoch spectra. However, we do not detect the UFO lines presented in literature in the single-image, single-epoch spectra of the other three GLQs. This behavior could be explained by the fact that the other three GLQs are lensed in four images and APM 08279+5255 in three images* (Ibata et al. 1999). The literature spectra and the ones analyzed in this work are more similar for what concerns APM 08279+5255 with respect to the other three GLQs, which are lensed in four images and present a much lower S/N in their single-image spectra than in the *Chandra* stacked or XMM-*Newton* spectra.

The analysis of the *Chandra* first batch of data yielded also results that we were not expecting. Interestingly, two spectra show absorption lines at energies lower than 6 keV, image A of Q 1355-2257 and image A+B of B 1422+231 (during obsID 12801), at $E = 5.5 \pm 0.2$ keV and $E = 5.3 \pm 0.2$ keV rest frame, respectively, possibly associated with gas inflows. Following Protassov et al. (2002), we ran Monte Carlo simulations to assess the actual significance of both lines. We do so by simulating 1000 fake spectra for each of the two mentioned GLQ images using their best fit model, deprived of the absorption line component. We then fit the fake data with the baseline model and add a line component to measure the statistical improvement yielded by the addition of such a spurious line. We then build the spurious detection probability distribution, from which we read the significance of the detection in the real data as the probability of having a higher statistical improvement with the spurious line than that obtained using the real data. We perform the Monte Carlo simulations twice, firstly by allowing the energy of the `zgauss` component to vary throughout the energy range (case 1) and secondly by limiting it to the range expected for inflows (case 2), i.e. the 2.4–6.4 keV rest-frame energy range. We find that the line in B 1422+231 is detected at a confidence level of 95.2% and 98.4% for case 1 and 2, respectively, and the one in Q 1355-2257 at a confidence level of 98.2% and 98.9% for case 1 and 2, respectively. Lastly, we find a UFO line at 16.7 ± 0.2 keV in the A+B spectrum of B 1422+231 collected in obsID 4939. We ran Monte Carlo simulations also for this line (1000 steps), firstly letting the `zgauss` component vary in the full spectral range (case 1) and secondly letting it vary in the 6.4–20 keV rest-frame energy range (case 2), i.e. covering the UFO features region of interest. We find the line of B 1422+231 during obsID 4939 to be detected at the 89% and

*More precisely, APM 08279+5255 is lensed in two very bright images (A and B) and a dimmer image in the middle (C), which is blended to image A in *Chandra* data.

92.5% confidence level for case 1 and 2, respectively. We measured the EW limit of an absorption line placed at the same energy ($E \simeq 16.7$ keV) in the other *Chandra* spectra of B 1422+231 and found all such limits to be well consistent with the EW measured in the A+B spectrum of obsID 4939. Thus, we cannot firmly rule out the presence of such a UFO in the other *Chandra* spectra, even though no sign of such a UFO is seen in the XMM-*Newton* data analyzed by Dadina et al. (2016); Lanzuisi et al. (2019).

2.1.3 Analysis of XMM-*Newton* data

As mentioned in Sect. 2.1, XMM-*Newton* final data products are much more influenced by the first steps of the reduction, in particular of the GTI filtering threshold. For this reason, we decided not to rely on the values listed in the 4XMM-DR9 catalog and to reduce all the observations from scratch. We also decided to privilege targeted observations and exclude the exposures associated to deep fields, namely CDFS, AXAF ultra deep field, Groth-Westphal Strip, to maximize the possibilities of retrieving good-quality spectra for our sources (even though data from deep fields have proven themselves useful in some exceptional cases, e.g., PID 352, Vignali et al. 2015). The resulting XMM-*Newton* data sample totaled 60 observations of 24 GLQs (see Table B.2 in Appendix B). Given the large number of datasets, we selected a starting batch of exposures. We excluded those observations already published as showing (or not showing) UFOs (namely, the one published in Dadina et al. 2016, those included in the compilation by Chartas et al. 2021, which we describe in Sect. 2.2, and those analyzed in Bertola et al. 2020, 2022, which we present in Chaps. 3 and 4). Many GLQs are serendipitous sources in fields centered on other targets and fall at off-axis angles larger than 6′. In particular, two GLQs (SDSS J1313+5151 and Q 0957+561) were observed at $\theta \simeq 12.7'$ and $\theta \simeq 14'$ in repeated observations of a same target, each pointing with a similar exposure. We keep all the serendipitous GLQs in our first batch, regardless of the off-axis angle. However, for SDSS J1313+5151 and Q 0957+561, we preliminary selected the first observation of the sequence to have a first idea of the number of spectral counts and the spectral properties of our targets. Thus, the first batch of XMM-*Newton* data totalled 19 observations of 14 GLQs (see Table 2.2). Six of these GLQs are also part of the first batch of *Chandra* data. However, the main goal of our study is not to address the spectral variability of our sources throughout the epochs, but to find the best "local best-fit" (that is, the best fit of each spectrum) and thus assess whether we detect absorption features that can be associated to UFOs in that specific spectrum. For this reason, we do not discuss here the spectral variability through the epochs of our sources and defer such an analysis to a future work.

We reduced the observations of the XMM-*Newton* first batch using the latest software available in July 2020, that is HEASoft 6.27.2 and SAS 18. Some of these

Table 2.2: Observation log of the selected XMM-*Newton* exposures (first XMM-*Newton* batch).

GLQ	obsid	XMM_target	Date	Exp. (ks)	Off-axis $\theta(')$	PI
HE 1104-1805	0112630101	HE1104-1805	2001-06-14	36.4	0.104	Turner
RX J0911.4+0551	0083240201	RXJ0911.4+0551	2001-11-02	20.7	0.0	Hjorth
HE 2149-2745	0062940401	HE2149-2745	2001-11-08	39.4	1.495	Chartas
HST 15433+5352	0060370101	SBS1542+541	2002-02-03	11.4	9.16	Mathur
HST 15433+5352	0060370901	SBS1542+541	2002-02-06	34.1	9.16	Mathur
SDSS 1138+0314	0111970701	TLeo	2002-06-01	12.9	9.214	Mason
SDSS 1138+0314	0111971501	TLeo	2002-06-01	7.8	9.214	Mason
H 1413+117	0112251301	H1413+117	2002-08-02	29.6	0.105	Turner
H 1413+117	0112250301	H1413+117	2001-07-29	26.6	0.105	Turner
SBS 0909+532	0143150301	SBS0909+532	2003-04-17	33.1	0.083	Reeves
SBS 0909+532	0143150601	SBS0909+532	2003-05-18	21.7	0.083	Reeves
Q 1120+0195	0145750101	Q1120+0195	2003-06-23	42.2	0.014	Chartas
Q 0957+561	0147760101	SN2001ci	2003-10-14	44.4	13.04	Pietsch
Q 0957+561	0802710101	NGC3079	2017-11-01	22.8	14.04	Hodges-kluck
PSS J2322+1944	0202140301	PSSJ2322+1944	2003-12-16	35.9	0.007	Priddey
SDSS 1004+4112	0207130201	RBS825	2004-04-20	60.7	0.047	Lamer
SDSS J1313+5151	0653530101	Abell1703	2010-05-27	17.3	12.678	Gastaldello
HST 14176+5526	0723860101	SDSSJ141711+522540	2014-01-05	30.3	4.001	Lin
B 1152+199	0804680101	B1152+199	2017-12-27	119.9	0.004	Nardini

observations were significantly affected by soft-p$^+$ flares (see Table 2.3: Soft-p$^+$=1 for flared, Soft-p$^+$=2 for significantly flared). For these observations, we carefully searched for the best GTI filtering threshold to maximize the source S/N. Operationally, we filtered the data against different count rate thresholds (CRTs), then we extracted the source and background EPIC spectra and assessed the S/N for each CRT. The best GTI filtering thresholds were then selected as those yielding background-subtracted source spectra brighter than background spectra by at least a factor of 2 in the 2–10 keV rest-frame energy range. We list in Table 2.3 the chosen CRTs for each XMM-*Newton* camera and each target, alongside the yielded number of total counts and the source fraction[†] in the 0.3-10 keV band for each camera. Source regions were selected as circles of radii enclosing only the PSF core ($r_{\rm src} \lesssim 30''$, corresponding to an average EEF of $\simeq 85\%$). Different source regions were also tested but did not return better results than those encircling the PSF core. Background regions were selected as source-free circles with radii of at least $50''$ in the same chip as our GLQ. We checked for pileup and none of our data present pileup levels that would significantly change the source spectral shape. We used the described extraction regions to produce the background-subtracted lightcurves of each GLQ (grouped with 100s time bins) as observed by each camera of XMM-*Newton*. We checked for source variability through a user-developed python code that allowed us to exclude time bins with null counts (i.e., background-dominated bins). None of our targets were found to be highly variable (i.e., variable above the 99% confidence threshold). We list the total counts and the source fraction of each definitive spectrum in Table 2.3. As Table 2.3 shows, half of the observations from this first batch provided spectra with very few source counts (< 500 cts in EPIC-pn and even less in EPIC-MOS). We thus discard these spectra from our sample. Moreover, HST 15433+5352 and HST 14176+5526 are not detected in the XMM-*Newton* fields, thus we did not extract their spectra. SDSS1313+5151 instead is a slightly more peculiar case. The detector lightcurve of the selected observation (i.e., the first one of the monitoring) is completely flared, as if a soft-p$^+$ flaring event lasted for the full exposure. We reduced and inspected all the other eight exposures of the same field, only to discover that all of them are similarly significantly flared. Since our target falls at the very outskirts (off-axis angle $\theta \simeq 12.7'$) of the fields centered on the ABELL 1704 cluster, such highly-flared observations are of no use for our purposes, thus we discard them and as a consequence, we discard our target, SDSS 1313+5151.

We thus proceeded to analyze the surviving XMM-*Newton* sample, that is, 7 observations of 5 GLQs, jointly fitting EPIC-pn, -MOS1 and -MOS2 data apply the

[†]The source fraction corresponds to the fraction of source net counts vs. total counts (source plus background) as measured in the source extraction region. The background contribution in the source region is obtained by scaling the counts in the background region based on the ratio of the extraction areas.

Table 2.3: XMM data reduction parameters

GLQ	obsID	CRT_{pn}	CRT_{m1}	CRT_{m2}	Soft-p^{+}	$N_{H,Gal}$	z_Q	pn_{cts}	pn_{src}	$m1_{cts}$	$m1_{src}$	$m2_{cts}$	$m2_{src}$
HST 15433+5352•	0060370101	1.5	0.6	0.6	2	-	-	-	-	-	-	-	-
HST 15433+5352•	0060370901	2	0.6	0.6	1	-	-	-	-	-	-	-	-
HE 2149-2745**	0062940401	1.5	0.7	0.7	0	0.0201	2.033	263	53.2%	60	57.2%	40	38.5%
RX J0911.4+0551**	0083240201	0.9	0.4	0.4	2	0.0299	2.8	221	61.9%	328	67.9%	348	70.9%
SDSS 1138+0314**	0111970701	0.7	0.3	0.3	0	0.0186	2.44	223	87.0%	80	88.6%	144	84.0%
SDSS 1138+0314**	0111971501	0.8	0.4	0.4	0								
H 1413+117**	0112250301	1	0.4	0.4	0	0.0168	2.55	242	73.2%	41	85.4%	80	82.6%
H 1413+117**	0112251301	1	0.4	0.4	0	0.0168	2.55	260	68.2%	60	88.1%	61	69.4%
HE 1104-1805**	0112630101	0.9	0.3	0.3	2	0.0457	2.32	601	92.1%	246	92.0%	226	89.7%
SBS 0909+532	0143150301	1	0.5	0.5	1	0.015	1.3764	2469	96.0%	1008	96.8%	996	96.9%
SBS 0909+532	0143150601	1	0.4	0.4	0	0.015	1.3764	6431	95.6%	2083	96.8%	2162	97.3%
Q 1120+0195	0145750101	0.7	0.3	0.3	1	0.036	1.472	1916	90.8%	829	91.1%	885	90.4%
Q 0957+561	0147760101	0.9	0.4	0.4	2	0.00878	1.413	3966	96.0%	2013	95.8%	1836	97.5%
Q 0957+561	0802710101	0.9	0.3	0.3	1	0.00878	1.413	3349	92.8%	1052	97.6%	1047	97.6%
PSS J2322+1944**	0202140301	1	0.6	0.5	1	0.0355	4.1179	477	62.6%	181	67.1%	167	65.3%
SDSS J1004+4112	0207130201	1	0.6	0.6	1	0.00955	1.74	7126	96.9%	2622	97.1%	2681	96.9%
SDSS J1313+5151•	0653530101	10	2.0	2.0	1	-	-	-	-	-	-	-	-
HST 14176+5526•	0723860101	-	0.5	0.5	1	-	-	-	-	-	-	-	-
B 1152+199	0804680101	1	0.5	0.5	1	0.0247	1.0188	41242	95.9%	13283	95.0%	12813	95.5%

Notes. ** Observation discarded because the yielded spectra have a too low S/N for our purposes. • Undetected. Columns 3-5, labeled as CRT, list the selected GTI filtering threshold for each EPIC camera. Column 6 flags the observations based on the level of flaring (0=no flaring, 1=evident flaring, 2=significantly flared). Columns 9, 11, 13 list the total spectral counts in the 0.3–10 keV observed-energy band for EPIC-pn, MOS1, MOS2, respectively. Columns 10, 12, 14 list the source fraction in the 0.3–10 keV observed-energy band for EPIC-pn, MOS1, MOS2.

χ^2 statistics. Given the high count statistics of these spectra (see Table 2.3), we grouped them with `specgroup`, an `ftool` that allows to set the desired grouping scheme (20 cts/bin in this case) and impose a maximum oversampling ratio of the instrumental energy resolution (which we set to 1/3). In high count statistics spectra, fixing the oversampling ratio is fundamental to obtain spectral bins that still resemble the energy resolution of the instrument.

As done for the *Chandra* batch, we fitted the data of each source with a power law model, modified by Galactic absorption according to the measurements by HI4PI Collaboration et al. (2016). Then, we inspected residuals and parameters to assess whether other model components were required to properly reproduce the data. The XMM-*Newton* spectra are, in general, quite well fit by this simple model, like for instance those of Q 0957+561, a RL AGN, very bright in X-rays. We find indication of extra absorption at the source redshift in Q 1120+0195 (partial coverer, $N_{\rm H} = (6.4\pm1.5)\times10^{22}$ cm^{-2}, covering factor CF> 0.4), while SBS 0909+532 presents positive residuals in the soft band that can be phenomenologically accounted for with a thermal component, whose temperature is consistent between the two observations. B 1152+119 is the most promising source of the XMM-*Newton* first batch since its exposure was tailored at observing emission and/or absorption narrow features. The EPIC spectra of B 1152+199 are well reproduced by a single power law and show an absorption line at $E_{\rm rest} = 12.7 \pm 0.1$ keV. Following Protassov et al. (2002), we ran Monte Carlo simulations to build the probability distribution of a spurious line detection and thus assess the actual significance of the measure line at 12.7 keV. We do so by simulating 1000 fake spectra for each EPIC camera, using the joint best fit model of the EPIC spectra of B1152+119, deprived of the absorption line component, following the procedure outlined in Sect. 2.1.2. We find that the 12.7 keV line in B1152+119, image A is detected at the 98.8% confidence level. As a consequence, such line cannot be considered a strong detection (the threshold is usually set at the 99% confidence level) but represents a strong hint of the presence of a UFO, to be tested with physical wind models, like `warmabs` (as done in Sect. 2.2 and in Chapter 3) or state-of-the-art models like WINE (Laurenti et al. 2021) or XRADE (Matzeu et al. 2022b).

2.1.4 Summary of results

We have built a sample of high-z GLQs and queried all the available X-ray data archives with the aim of providing a comprehensive analysis of UFO features in their X-ray spectra. We narrowed down our dataset to those observatories and those exposures that could yield useful X-ray spectra for our purposes. We thus selected *Chandra* and XMM-*Newton* observations, and, in first instance, we analyzed a "first batch" of data for both.

Regarding *Chandra* first data batch, we relied on the information available in the

CSC v.2.0 to select those observations passing our data-quality criteria (see Sect. 2.1.2), totalling 35 exposures. We chose to investigate single-image, single-epoch spectra to assess the possible spectral differences among the lensed images. Thus, the *Chandra* first batch totaled 39 spectra, since some GLQs present more than image above the selection threshold. We detect in the single-image, single-epoch spectra of APM 08279+5255 the prominent UFOs discovered by Chartas et al. (2002, 2009) in image-integrated data, while we do not see the prominent lines of the other GLQs known to show UFOs (PG 1115+080, Chartas et al. 2007a; MG J0414+0534, Dadina et al. 2018; HS 0810+2554, Chartas et al. 2016a). We attribute this discrepancy to the fact that APM 08279+5255 is lensed in three images (two very bright, one much dimmer), while the other sources are quads and, as such, the count statistics of their single-image spectra is significantly lower than that of the image-integrated data. We find shallow hints (92.8% confidence level, from Monte Carlo simulations) of a UFO absorption line in images A+B of B1422+231, from obsID 4939, at very high energy ($E \simeq 16.7$ keV) and thus very high outflow velocity ($v_{\rm out} \simeq 0.7c$ assuming Fe XXVI). Since such a GLQ that was never found to show UFOs in its XMM-*Newton* exposures (Dadina et al. 2016; Lanzuisi et al. 2019), we consider such hints are probably spurious. However, in a more recent observation of the same quasar (obsID 12801), we detect at the 98.4% confidence level an absorption line possibly produced by gas inflows in the spectrum of images A+B of B1422+231. We find that also Q 1355-227 shows a similar absorption line, detected at the 98.9% confidence level. Similar inflows have been claimed only in very few sources (Nandra et al. 1999; Dadina et al. 2005; Pounds et al. 2018) and were often not confirmed by subsequent analysis (e.g., Ruszkowski & Fabian 2000; Ponti et al. 2009).

Regarding the XMM-*Newton* first batch of data, we reduced 17 observations of 14 GLQs (XMM-*Newton* first batch), some of which required careful attention due to very high background contamination. Of these 17 exposures, only seven observations (of 5 GLQs) provided good-enough S/N spectra for our purposes (see Table 2.3). We found an absorption line at $E \simeq 12.7$ keV in the EPIC spectra of B 1152+119, detected at the 98.8% confidence level, as indicated by Monte Carlo simulations. We interpret such a line as a strong hint of the presence of a UFO in this source, to be confirmed through physical wind models, like `warmabs` (as done in Sect. 2.2 and in Chapter 3) or state-of-the-art models like WINE (Laurenti et al. 2021) or XRADE (Matzeu et al. 2022b).

2.2 Properties of high-redshift UFOs

Besides providing the community with a "feedback-unbiased" analysis of high-z UFOs, we also addressed the link between two different phases of AGN-driven winds, UV winds and UFOs, and the properties of UFOs themselves in a "feedback-biased"

sample of high-z AGN. We refer to such a sample with the term "feedback-biased" to differentiate its selection from that of the sample in Sect. 2.1, in which we selected GLQs solely based on the redshift of the background quasar and on the availability of good X-ray data in the archives. For the analysis of UFO properties at $z > 1$, we collected all the high-z UFO detections available in the literature as of Summer 2021 and complemented them with our XMM-*Newton* exploratory survey of high-z GLQs showing UV winds, that is, we know already that the AGN in this second sample show AGN feedback signatures as traced by an AGN-driven wind phase.

By the "feedback-biased" sample, we aim at carrying out a comprehensive study of UFOs detected in a heterogeneous sample of 14 QSOs in a redshift range of 1.41–3.91. Our goals are to *i)* derive the outflow properties in a sample of QSOs close to the peak of cosmic AGN activity, *ii)* determine the efficiency of such outflows in regulating BH growth and galaxy build up and *iii)* assess the relation between the properties of these winds and those of the AGN, like the bolometric luminosity, and compare our findings with those in the local Universe.

To that aim, we built a sample of NAL QSOs, selecting GLQs showing blueshifted C IV troughs having widths smaller than 500 $\mathrm{km\,s^{-1}}$ from the lens searches in recent SDSS surveys (Inada et al. 2012, 2014; More et al. 2016). We chose NAL GLQs instead of BAL AGN since NAL GLQs are less X-ray absorbed/weak than BAL quasars and, as such, should grant better S/N data when observed by present day facilities with similar exposure times. We thus initiated an XMM-*Newton* campaign to observe our sample of 6 NAL GLQs at $z > 1.4$. We note that, since the NAL sample was built without prior knowledge of the co-existence of a UFO in the selected GLQs, it is unbiased toward UFO detection and can be used to infer the fraction of $z > 1$ NAL quasars that contain UFOs.

As mentioned, we also included the seven AGN at $z > 1$ already known for showing UFOs: APM 08279+5255 (Chartas et al. 2009), PG 1115+080 (Chartas et al. 2007a), HS 1700+6416 (Lanzuisi et al. 2012), PID 352 (Vignali et al. 2015), HS 0810+2554 (Chartas et al. 2016a), MG J0414+0534 (Dadina et al. 2018), and Q 2237+030 (Bertola et al. 2020, see also Chapter 3). We complemented our sample with archival *Chandra* data of another NAL GLQ (SDSS 1029+2623), since its X-ray spectra were never searched for UFOs before (Ota et al. 2012). All the sources of the "feedback-biased" sample presented in this Section are also part of the "feedback-unbiased" sample of Sect. 2.1, but SDSS J0921+2854 and SDSS J1442+4055, because part of a more recent SDSS lens search (More et al. 2016) that was not included in the sample presented in Section 2.1.

We present in this thesis only the main results obtained from this study and refer the interested reader to Chartas et al. (2021) for what concerns the data analysis. We summarize the physical properties of the UFOs of the "feedback-biased" sample in Table 2.4.

Table 2.4: Properties of the UFOs detected in the high-z sample from Chartas et al. (2021).

GLQ	Obs. Date	$N_{\rm H}$	$C_{\rm SR}$	$r_{\rm min}$	$r_{\rm max}/r_{\rm min}$	$\log \xi$	$v_{\rm out}$	$\dot{M}_{\rm out}$	$\dot{E}_{\rm out}/L_{\rm bol}$	$\dot{p}_{\rm out}/(L_{\rm bol}/c)$
APM 08279+5255	2002 Feb 24	$10^{+6.0}_{-6.0}$	1.44	121^{+43}_{-38}	24	$4.0^{+0.8}_{-0.1}$	$0.16^{+0.02}_{-0.02}$	101^{+59}_{-53}	$0.11^{+0.07}_{-0.06}$	$1.35^{+0.84}_{-0.72}$
APM 08279+5255	2002 Feb 24	$1.0^{+0.8}_{-0.5}$	2.21	25^{+7}_{-7}	7,756	$3.2^{+0.2}_{-0.3}$	$0.35^{+0.03}_{-0.03}$	$5.0^{+3.2}_{-2.6}$	$0.026^{+0.018}_{-0.014}$	$0.15^{+0.10}_{-0.08}$
APM 08279+5255	2002 April 28	$1.7^{+0.2}_{-0.2}$	1.59	76^{+24}_{-22}	2,926	$3.1^{+0.1}_{-0.7}$	$0.20^{+0.02}_{-0.02}$	$12.7^{+3.9}_{-3.6}$	$0.022^{+0.009}_{-0.007}$	$0.22^{+0.08}_{-0.07}$
APM 08279+5255	2002 April 28	$1.4^{+0.4}_{-0.8}$	2.77	14^{+4}_{-4}	7,208	$3.5^{+0.8}_{-0.4}$	$0.46^{+0.03}_{-0.03}$	$4.6^{+2.3}_{-2.1}$	$0.04^{+0.02}_{-0.02}$	$0.19^{+0.10}_{-0.09}$
APM 08279+5255	2007 Oct 6	$3.9^{+1.1}_{-0.9}$	1.51	94^{+32}_{-28}	557	$3.6^{+0.9}_{-0.3}$	$0.18^{+0.02}_{-0.02}$	33^{+13}_{-11}	$0.043^{+0.017}_{-0.016}$	$0.61^{+0.42}_{-0.30}$
APM 08279+5255	2007 Oct 6	$8.3^{+1.0}_{-1.0}$	3.39	10^{+3}_{-3}	1,190	$3.9^{+0.2}_{-0.3}$	$0.54^{+0.03}_{-0.03}$	23^{+7}_{-6}	$0.28^{+0.08}_{-0.08}$	$1.3^{+0.9}_{-0.6}$
APM 08279+5255	2007 Oct 22	$1.2^{+0.2}_{-0.3}$	1.33	178^{+51}_{-47}	5,477	$3.1^{+0.1}_{-0.2}$	$0.13^{+0.02}_{-0.02}$	14^{+4}_{-4}	$0.013^{+0.011}_{-0.007}$	$0.20^{+0.17}_{-0.11}$
APM 08279+5255	2007 Oct 22	$1.0^{+0.2}_{-0.2}$	2.34	21^{+6}_{-6}	53,891	$3.1^{+0.1}_{-0.1}$	$0.38^{+0.03}_{-0.03}$	4^{+1}_{-1}	$0.031^{+0.029}_{-0.017}$	$0.16^{+0.15}_{-0.09}$
APM 08279+5255	2008 Jan 14	$0.9^{+0.4}_{-0.4}$	1.67	63^{+2}_{-2}	5,815	$3.3^{+0.7}_{-0.6}$	$0.22^{+0.02}_{-0.02}$	6^{+3}_{-3}	$0.016^{+0.012}_{-0.009}$	$0.14^{+0.11}_{-0.08}$
APM 08279+5255	2008 Jan 14	$4.0^{+4.0}_{-3.2}$	3.95	$8.5^{+2.1}_{-2.1}$	2,317	$3.9^{+0.5}_{-0.5}$	$0.59^{+0.03}_{-0.03}$	13^{+8}_{-7}	$0.23^{+0.20}_{-0.14}$	$0.77^{+0.62}_{-0.46}$
HS 1700+6416	2000 Oct 31	$5.6^{+4.4}_{-0}$	2.34	$3.1^{+1.7}_{-1.5}$	55	$3.9^{+1.0}_{-0.4}$	$0.38^{+0.05}_{-0.05}$	33^{+21}_{-18}	$0.10^{+0.09}_{-0.07}$	$0.54^{+0.41}_{-0.36}$
MG J0414+0534	2017 Mar 11	$9.8^{+5.7}_{-3.6}$	1.91	$4.7^{+2.9}_{-2.4}$	206	$3.0^{+0.1}_{-0.1}$	$0.28^{+0.05}_{-0.05}$	$6.2^{+4.2}_{-3.6}$	$0.49^{+0.40}_{-0.32}$	$3.5^{+2.3}_{-2.3}$
SDSS J1442+4055	2019 Jan 18	$3.5^{+1.5}_{-1.7}$	2.83	$6.6^{+3.1}_{-2.9}$	1,155	$6.6^{+3.1}_{-2.9}$	$0.47^{+0.03}_{-0.05}$	$5.5^{+3.7}_{-3.2}$	$1.2^{+0.9}_{-0.8}$	$5.1^{+4.0}_{-3.2}$
SDSS J1029+2623	2010 Mar 11	$7.4^{+2.6}_{-2.4}$	3.82	$0.6^{+0.2}_{-0.2}$	880	$2.8^{+0.1}_{-0.1}$	$0.58^{+0.01}_{-0.02}$	$0.9^{+0.6}_{-0.5}$	$4.3^{+2.9}_{-2.5}$	15^{+10}_{-8}
SDSS J1529+1038	2015 July 19	$3.2^{+4.9}_{-1.9}$	1.79	$5.6^{+4.5}_{-3.4}$	62	$3.6^{+0.4}_{-0.4}$	$0.25^{+0.06}_{-0.08}$	$2.0^{+1.6}_{-1.2}$	$0.37^{+0.26}_{-0.26}$	$3.0^{+2.3}_{-2.0}$
SDSS J0904+1512	2015 Nov 8	$4.0^{+2.3}_{-2.4}$	1.83	$9.1^{+5.5}_{-4.5}$	59	$3.84^{+0.16}_{-0.19}$	$0.26^{+0.05}_{-0.04}$	$4.8^{+2.6}_{-2.9}$	$0.9^{+0.7}_{-0.6}$	$6.9^{+5.8}_{-4.7}$
PG 1115+080	2001 Nov 25	$1.9^{+0.5}_{-0.5}$	1.17	23^{+12}_{-11}	63	$3.23^{+0.07}_{-0.03}$	$0.08^{+0.02}_{-0.02}$	$1.7^{+1.0}_{-0.9}$	$0.045^{+0.039}_{-0.028}$	$1.1^{+0.8}_{-0.6}$
PG 1115+080	2001 Nov 25	$1.6^{+0.4}_{-0.3}$	2.30	$1.4^{+0.5}_{-0.5}$	1913	$3.14^{+1.2}_{-0.03}$	$0.37^{+0.01}_{-0.01}$	$0.31^{+0.16}_{-0.14}$	$0.17^{+0.12}_{-0.11}$	$0.9^{+0.2}_{-0.1}$
Q 2237+0305	2017 Jan 4	10^{+4}_{-4}	1.51	30^{+25}_{-24}	18	$3.1^{+0.2}_{-0.3}$	$0.18^{+0.06}_{-0.09}$	16^{+13}_{-10}	$1.58^{+1.24}_{-1.10}$	17.5^{+10}_{-11}
SDSS J1353+1138	2016 Jan 1	$3.9^{+2.4}_{-2.3}$	2.16	$7.3^{+4.1}_{-3.4}$	213	$3.6^{+0.2}_{-0.1}$	$0.34^{+0.02}_{-0.09}$	$11.2^{+3.7}_{-3.0}$	$0.18^{+0.24}_{-0.23}$	$2.0^{+1.8}_{-1.4}$
SDSS J1128+2402	2018 May 28	$2.3^{+1.7}_{-1.3}$	3.60	$0.5^{+0.2}_{-0.2}$	1,949	$3.15^{+0.15}_{-0.15}$	$0.56^{+0.01}_{-0.02}$	$0.35^{+0.25}_{-0.21}$	$0.41^{+0.34}_{-0.27}$	$1.5^{+1.3}_{-1.0}$
PID352	–	$2.2^{+3.1}_{-1.6}$	1.36	12^{+9}_{-7}		$2.9^{+1.47}_{-0.38}$	$0.14^{+0.02}_{-0.06}$	$1.9^{+1.7}_{-1.2}$	$0.14^{+0.11}_{-0.09}$	$1.95^{+1.65}_{-1.23}$
HS 0810+2554	2014 Oct 04	$2.1^{+1.0}_{-1.1}$	1.26	11^{+7}_{-5}	1.5	$5.0^{+1.0}_{-0.4}$	$0.11^{+0.05}_{-0.03}$	$1.2^{+0.9}_{-0.7}$	$0.15^{+0.14}_{-0.10}$	$2.6^{+2.2}_{-1.9}$
HS 0810+2554	2014 Oct 04	$1.4^{+0.3}_{-0.5}$	2.59	$0.7^{+0.3}_{-0.3}$	317	$4.1^{+0.4}_{-0.2}$	$0.43^{+0.04}_{-0.05}$	$0.21^{+0.12}_{-0.11}$	$0.35^{+0.23}_{-0.22}$	$1.7^{+1.1}_{-1.1}$
SDSS J0921+2854	2018 May 15	$3.7^{+2.4}_{-1.5}$	2.49	$1.3^{+0.6}_{-0.6}$	6,381	$3.1^{+0.2}_{-0.3}$	$0.41^{+0.02}_{-0.01}$	$1.1^{+0.8}_{-0.6}$	$2.6^{+2.4}_{-1.9}$	13^{+12}_{-9}
SDSS J0921+2854	2018 Oct 24	$6.0^{+2.7}_{-2.4}$	3.30	$0.8^{+0.3}_{-0.3}$	62	$3.14^{+0.1}_{-0.04}$	$0.53^{+0.01}_{-0.01}$	$1.3^{+0.9}_{-0.7}$	$5.2^{+3.9}_{-3.7}$	20^{+13}_{-14}

Notes. The hydrogen column density $N_{\rm H}$ has units of $\times 10^{23}{\rm cm}^{-2}$, the minimum radius of the absorber has units of $\times 10^{13}$m, and the ionization parameter ξ has units of erg cm s^{-1}. The properties of the outflowing X-ray absorbing gas are obtained from the photoionization model XSTAR. $\dot{M}$, $\dot{E}_{\rm K}$, and $\dot{p}$ are derived from equations 1, 2, and 3, respectively. To correct for relativistic effects proposed in Luminari et al. (2020), the values of $N_{\rm H}$, $\dot{M}$, $\dot{E}_{\rm K}$, and $\dot{p}$ need to be multiplied by the factor $C_{\rm SR}$. $N_{\rm H}$, $\dot{M}$, $\dot{E}_{\rm K}$, and $\dot{p}$ have been calculated assuming that the distance between the outflowing absorber and the center of the black hole is $r_{\rm min}$ given by Eq. 1.16. For APM 08279+5255, PG 1115+080, and HS 0810+2554 we list the properties of the two detected outflowing absorbers per observation. For SDSS J0921+2854 we list the outflow properties of one detected component in two observations.

From the analysis of our XMM-*Newton* exploratory survey of high-z NAL QSOs, we find that all of them present UFOs, but SDSS 0904+1512. As a result, we can infer that the coexistence of UFOs and UV NAL is significant in $> 83\%$ of our NAL sample. Such sample is however small and at least doubling the source number would be required to confirm such a result. For comparison, samples that are unbiased regarding the presence of UV winds show a detection fraction of UFOs of $\simeq 40\%$ (Tombesi et al. 2010a; Gofford et al. 2013; Igo et al. 2020; Matzeu et al. 2022a). Moreover, we report the detection of a UFO also in the multi-image, stacked *Chandra* spectra of SDSS 1029+2623, but we do not consider it in the computation of the UFO detection fraction in NAL QSOs given the different datasets available for this source (*Chandra* data instead of XMM-*Newton* spectra). However, would we consider it, the detection fraction would become $> 85\%$, thus our conclusions would not significantly change.

We computed the physical parameters of UFOs for the full "feedback-biased" sample (literature results plus the "new" NAL QSOs), uniformly applying the same formulas for $\dot{E}_{\rm out}$, $\dot{p}_{\rm out}$, $\dot{M}_{\rm out}$ (Eq. 1.13-1.15) and conservatively assuming the wind as launched from the minimum distance possible (see Sect. 1.3, Eq. 1.16). Luminari et al. (2020) incorporated relativistic effects in radiative transfer codes and investigated their impact on the estimated wind parameters. The authors find that the column densities measured including Special Relativity are generally higher that those measured with "standard" wind models, like `warmabs`, and provide a prescription to compute a multiplicative special-relativity correction factor for the wind column density ($C_{\rm SR}$). We summarize all values in Table 2.4, not corrected for the special relativistic effects, to allow for a more-straightforward comparison with results in the literature. We list in Table 2.4 the special-relativity correction factors to be applied to the column density and thus to the derived wind parameters.

We first investigated the relation between outflow velocity $v_{\rm out}$ and bolometric luminosity for our high-z sample and for two literature samples of local AGN: the Gofford sample ($0.00234 < z < 0.18$), extracted from Gofford et al. (2013), and the Tombesi sample ($0.00233 < z < 0.1040$), taken from Tombesi et al. (2012). From the Gofford sample, we excluded *i)* APM 08279+5255, because it is a high-z source and is already part of our high-z sample, *ii)* NGC 3783 and NGC 4395 because of their unconstrained outflow velocites and *iii)* MCG-6-30-15 and NGC 3516 because their X-ray outflow properties are more typical of WAs than UFOs. We include in these samples those outflowing absorbers with $\log(N_{\rm H}/{\rm cm}^{-2}) > 22$, $\log(\xi/{\rm erg\ cm\ s}^{-1}) > 3$ and $v_{\rm out} > 3000$ km s^{-1}.

For a radiation-driven flow, we would expect $v_{\rm out} \propto L^b$ with $b = 1/2$ (see, for instance, Eq. 1 of Chartas et al. 2002). The high-z sample does not show any correlation ($b = 0.03 \pm 0.06$, Kendall's rank correlation coefficient of $\tau = 0.1$ with a null probability of $P_{null} = 0.55$) between the two quantities (see Fig. 2.1,

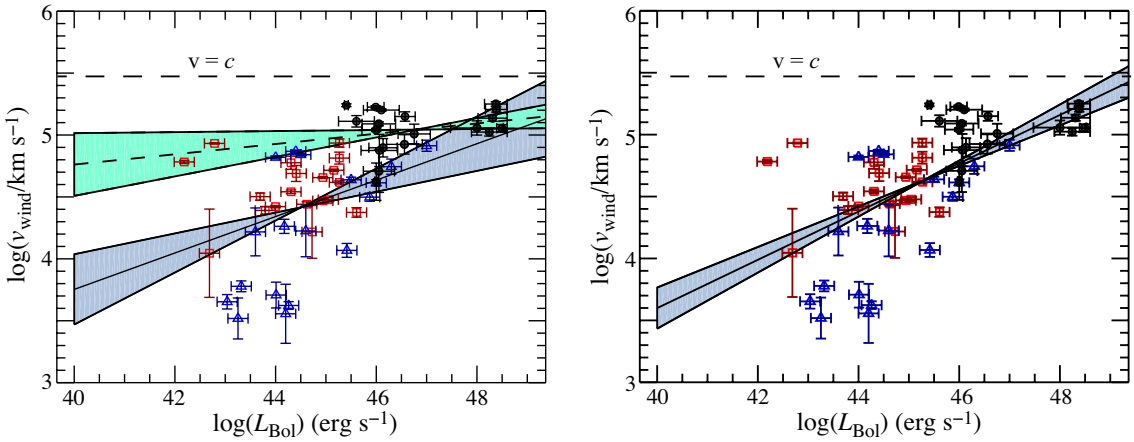

Figure 2.1: Outflow velocity of X-ray ionized outflows vs. bolometric velocity of the AGN for the Tombesi sample (blue triangles), Gofford sample (red squares) and our high-z sample (black filled circles). *Left panel:* Power-law least-squares fit of the high-z sample (dashed black line and cyan filling) and of the combined Gofford and Tombesi samples (solid black line and blue filling). *Right panel:* Power-law least-squares fit of the combined Gofford, Tombesi and high-z sample. The filling between solid lines shows the uncertainty on the best-fit relation. Figure is from Chartas et al. (2021).

Left). Regarding the two local samples, we find that $v_{\rm out}$ and $L_{\rm bol}$ are strongly correlated only in the Gofford sample, even if with a smaller power law exponent than what expected for pure radiation driving ($b = 0.29 \pm 0.09$, Kendall's rank correlation coefficient of $\tau = 0.45$ with a null probability of $P_{null} = 8.9 \times 10^{-3}$). The absence of correlation in the Tombesi sample ($b = 0.02 \pm 0.06$, Kendall's rank correlation coefficient of $\tau = 0.11$ with a null probability of $P_{null} = 0.52$) could be ascribed to its lack of UFOs with velocities lower than 10000 km s^{-1}. The combined fit of the two local samples returns $b = 0.15 \pm 0.06$ (see Fig. 2.1, *Left*) but the correlation has a lower significance than that of the Gofford sample alone. However, the combined fit of Gofford and Tombesi local AGN and our high-z QSOs presents a strong $v_{\rm out}$–$L_{\rm bol}$ correlation, (see Fig. 2.1, *Right*), with $b = 0.20 \pm 0.03$ (Kendall's rank correlation coefficient of $\tau = 0.51$ with a null probability of $P_{null} = 6 \times 10^{-8}$), that is again a power-law index lower that the expectation for a pure radiation-driven flow. In general, none of the three samples (and none of their combinations) are consistent with pure radiation driving. The high-z sample, however, is by far the one showing the most extreme outflow velocities that, coupled with the lack of correlation between outflow velocity and AGN luminosity, strongly suggests the need of an additional mechanism in the acceleration of the outflows (e.g., Fukumura et al. 2010, 2014; Sądowski & Gaspari 2017; Luminari et al. 2021). Such a lack of dependence between $v_{\rm out}$ and $L_{\rm bol}$ is also in agreement with the saturation effect inherent to radiative acceleration, which does not allow to reach velocities larger than $v_{\rm out} = 0.1c$ (e.g., Saez & Chartas 2011; Luminari et al. 2020); in fact, all the

high-z UFOs presented in Chartas et al. (2021) (and see Table 2.4) show velocities above such threshold, further supporting the need of acceleration mechanisms other than radiative driving.

We also investigated the relation between the various outflow parameters (UFO velocity, column density, ionization parameter) and the properties of our AGN (bolometric luminosity, X-ray luminosity, and Eddington ratio). We find no significant correlation between them, while relations between $v_{\rm out}$ and $L_{\rm X}$ were reported for APM 08279+5255 (Chartas et al. 2002, 2009; Saez & Chartas 2011), PDS 456 (Nardini et al. 2015; Matzeu et al. 2017; Reeves et al. 2018) and HS 1700+6416 (Lanzuisi et al. 2012). This apparent discrepancy could be explained by the dilution of such relation in our sample, since UFOs in high-z AGN may depend on acceleration mechanisms other than radiation driving, which these might vary between AGN. This hypothesis is also supported by the fact that 10 out of the 14 QSOs in our high-z sample show kinetic-luminosity-to-bolometric-luminosity ratios higher than 0.4 (see Table 2.4).

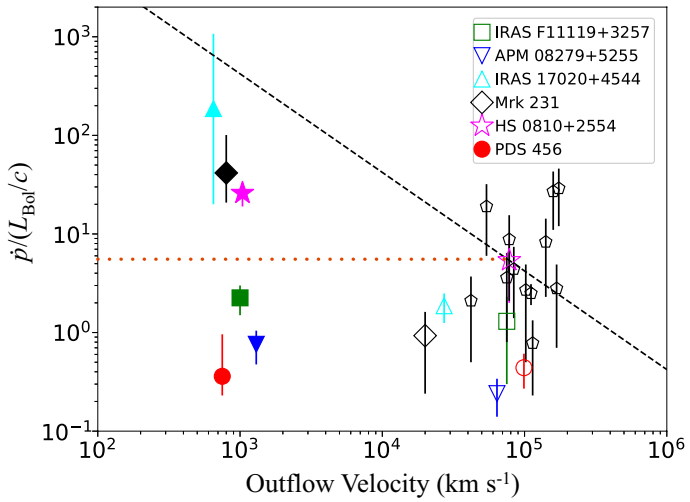

Figure 2.2: Momentum boost $\dot{p}_{\rm out}/(L_{\rm bol}/c)$ vs. outflow velocity $v_{\rm out}$. Filled (unfilled) symbols correspond to molecular (X-ray fast) outflows. Black pentagons mark the UFOs presented in Chartas et al. (2021), other symbols mark literature measurements of multi-scale AGN-driven outflows (Tombesi et al. 2015; Veilleux et al. 2017; Feruglio et al. 2015, 2017; Bischetti et al. 2019; Chartas et al. 2020). Dashed and dotted lines mark the expected momentum-boost in the energy- and momentum-conserving scenario, respectively, for HS 0810+2554. Figure is from Chartas et al. (2021).

By comparing the energetics of UFOs and kpc-scale outflows one can shed light on whether the two wind phases are linked and in which driving scenario (i.e., momentum vs. energy conserving). Figure 2.2 shows the distribution of momentum boost vs. outflow velocity of the UFOs in our high-z sample, complemented with the momentum boost of kpc-scale outflows in the molecular component (as measured in Chartas et al. 2020, and references therein). Our AGN present UFOs with

larger momentum boost than those showing UFOs and kpc-scale outflows from the literature. By this, we can expect our high-z AGN to be extremely good candidates for hosting kpc-scales, to be tested through tailored sub-mm observations. Smith et al. (2019) presented a compilation of AGN hosting both a UFO and a kpc-scale outflow (molecular and/or ionized), which span a large range of efficiency factors in the momentum boost vs. outflow velocity plane. The authors concluded that the coupling of the energetics of the nuclear and galaxy-scale outflows likely depends on specific physical conditions in each object. Bonanomi et al. (2023) recently updated such a compilation with other literature results (Longinotti et al. 2018; Sirressi et al. 2019; Marasco et al. 2020; Chartas et al. 2020; Tozzi et al. 2021). Such an increase in statistics appears to have even complicated the interpretation of the link between wind phases, possibly highlighting the limitations of such a comparison. In fact, one of the often-not-mentioned issues in trying to connect nuclear and galaxy-scale outflows is the different timescales at play between the two wind phases, which could in part explain those cases that fall in between the momentum- and energy-driven scenarios (even though other interpretations are possibile; e.g., the molecular gas phase is tracing only a fraction of the total outflowing mass as proposed in Bischetti et al. 2019).

2.3 Discussion and results

In general, our investigation in the archives of XMM-*Newton* and *Chandra* confirms an idea that the X-ray community has not yet explicitly put into words: present-day facilities struggle to match the required data quality to study this kind of events with "short" exposures of (possibly serendipitous) high-z targets. This does not mean that the current facilities are not competitive in the field (see Chartas et al. 2021 and Sect. 2.4 of this thesis), but long exposures are often needed to collect good-enough-S/N spectra. This kind of studies would have had a chance with the XIFU (X-ray Integral Field Unit) on board of *Athena*, that by means of its large effective area and an unprecedented energy resolution would have granted X-ray spectra of high-z AGN that are impossible to obtain for high-z AGN as of today[‡]. At present, all of our hopes reside in the decisions of the New-*Athena* redefinition team.

Nevertheless, we can combine the results obtained with the "feedback-unbiased" sample and the compilation of high-z AGN showing UFOs of Chartas et al. (2021) that we present in Sect. 2.2, to obtain an estimate of the UFO detection fraction at $z > 1$. This, however, has to be treated with caution and as a work-in-progress number, due to all the discussed issues of our search for data and the different treatment of the *Chandra* data between the analysis of the *Chandra* first data batch

[‡]Since they would require integration times that no TAC would grant on a since source.

and results in the literature. UFOs were detected in 11 GLQs[§] (or 12, if we believe to the strong hints in B 1152+199) out of a sample of 26 (considering only those GLQs with good-enough XMM-*Newton* data from Sect. 2.1, which are shared with the *Chandra* batch). By this, we obtain a work-in-progress detection fraction of $\gtrsim$40% (or $\gtrsim$45% considering also B 1152+199), very similar but slightly higher than that measured in the local (Tombesi et al. 2010a; Igo et al. 2020) and low-z Universe (Matzeu et al. 2022a).

There are many possible ways to obtain a more reliable estimate of the high-z UFO detection fraction, for instance:

- Crossmatch the "feedback-unbiased" sample with the soon-to-be-released CSC 2.1, which will include observations taken up to 2021 – by selecting only data that the CSC 2.0 indicated as matching our criteria, we automatically discarded all *Chandra* exposures taken after 2014;
- Investigate the multi-image stacked *Chandra* spectra to increase the S/N of the data and the possibility to detect weak, but persistent, features (see Sect. 3.5);
- Search for high-z GLQs in newer lens catalogs from GAIA, SDSS, DES (Ducourant et al. 2018; Lemon et al. 2018, 2019, 2020) and mine the X-ray archives as done for the GLQ sample and possibly propose deep observations to obtain new data of remarkable candidates;
- Increase the sample size by including also non-lensed, bright AGN at $z > 1$. This can be achieved by mining the X-ray archives as done for the GLQ sample and by proposing deep observations to obtain new data of remarkable candidates. In this sense, I was recently awarded 150ks with *Chandra* to observe the X-ray brightest, non-lensed AGN at $z > 3$, part of the WISSH sample Lastly, just as a reference, the Milliquas v7.2 Catalog (Flesch 2021, latest update: April, 2023), a compilation of quasars from the literature including those from SDSS-DR18 and LAMOST QSO DR6-DR9, totals more than 79k quasars at $z > 1$ with an X-ray counterpart, of which just less than 45k from 4XMM-DR12 (Webb et al. 2020a), $\simeq$18k with a *Chandra* counterpart and the remaining with a *ROSAT* or *Swift* counterpart.

The presented summary shows that even before the launch of *Athena* there are plenty of good candidates to study UFOs at high-z and that the archives of present X-ray telescopes can be goldmines for this, with the downside that many observations might not provide data with enough S/N for this kind of investigation.

[§]We only consider GLQs in this computation, thus we exclude HS 1700+6416 and PID 352.

Chapter 3

X-raying winds in distant quasars: The first high-redshift wind duty cycle

Part of the "feedback-unbiased" sample described in Chapter 2 are also sources that present peculiar characteristics to study UFOs. One of them, the Einstein Cross, stood out as a remarkable case in terms of available number of observations, time spanned by such observations and data quality. The quality of the available data allowed us to carry out the first systematic and comprehensive temporally and spatially resolved X-ray spectral analysis of this source, granting the opportunity to study UFOs in such a rich dataset for the first time at high-z. The present chapter is broadly based on the work in Bertola et al. (2020).

3.1 Introduction

The Einstein Cross (Q2237+030, hereafter Q2237) is a quasar at $z_{\rm Q} = 1.695$ that is quadruply imaged by a lensing galaxy at $z_{\rm L} = 0.039$. It is the first GLQ with a nearby lensed to have ever been discovered (Huchra et al. 1985) and, as such, it was soon recognized as a unique case to study both macro- and microlensing properties. Q2237 was first detected in the X-rays by the high resolution camera on board of ROSAT (Wambsganss et al. 1999) but only after the advent of *Chandra* astronomers were able to resolve its four images and study microlensing effects also in the X-ray band (Dai et al. 2003). It has thus been the target of many microlensing monitoring campaigns, enabling an investigation of the size of the quasar's emitting regions both in optical and X-rays (e.g., Mosquera et al. 2013; Guerras et al. 2017). Gravitational lensing theoretical models agree on predicting time delays between the four source images (A, B, C, D, as named in Yee 1988, see Fig. 3.1) of shorter than a day ($\Delta t_{\rm AB} \approx 2$ hrs, $\Delta t_{\rm AC} \approx -16$ hrs, $\Delta t_{\rm AD} \approx -5$ hrs) and a global magni-

fication factor* of $\mu \approx 16$ (Schmidt et al. 1998; Wertz & Surdej 2014). Dai et al. (2003) succeeded in confirming the shortest time delay ($\Delta t_{\rm AB} = 2.7^{+0.5}_{-0.9}$ hrs) through the first *Chandra* observation of this GLQ. Q2237 was also studied to assess its X-ray spectral properties, either over single observations, from *Chandra* (Chen et al. 2012) and XMM-*Newton* (Fedorova et al. 2008), or from *Chandra* spectra stacked over multiple observations, both keeping the images separate (Dai et al. 2003; Chen et al. 2012) and summing all the images (Chen et al. 2012; Reynolds et al. 2014). In this chapter, we will present the first systematic and comprehensive temporally and spatially resolved X-ray spectral analysis of this source, taking advantage of the rather complementary strengths that characterize *Chandra* and XMM-*Newton*. In Sect. 3.2 we list the analyzed data and present the reduction procedures. *Chandra* and XMM-*Newton* spectra are first analyzed separately in Sects. 3.3 and 3.4, respectively, then all the results are combined and discussed in Sect. 3.6. Additional results obtained from the *Chandra* stacked spectra are presented in Sect. 3.5.

3.2 Data reduction

We collected, reduced, and analyzed all available X-ray data of Q2237 as of September 2019: 40 archival observations in total, 37 from *Chandra* and 3 from XMM-*Newton* (hereafter, XMM 2002, XMM 2016, and XMM 2018), spanning over 18 years (∼6.7 yr in the quasar rest frame), for a total of ∼0.9 Ms exposure. The Einstein Cross was the target of each pointing, therefore it is always observed on-axis. Tables 3.1 and 3.2 summarize the main information of all the observations. The *Chandra* exposures range from 7.3 ks to 34.2 ks, while those of XMM-*Newton* are much longer (42.9 ks, 24.9 ks, and 141.6 ks, in chronological order). None of the observations provide simultaneous *Chandra* and XMM-*Newton* data; the time elapsed between each XMM-*Newton* pointing and the closest *Chandra* observation ranges from one to six months. Since one of the main goals of the present work is to search for and robustly assess (through appropriate statistical tests and simulations) the presence of feedback and the significance of wind-related features in the X-ray spectra of the Einstein Cross, the lack of simultaneity between the *Chandra* and XMM-*Newton* data does not influence the results of this study. Conversely, this lack turns out to be quite convenient in assessing the recurrence of these features at different epochs and will allow us to investigate their presence on a more extended time baseline.

The use of data from both facilities is fundamental to our goal. On the one hand, given the superb angular resolution of Chandra, we can carry out a spectral analysis that is spatially resolved over the single images of the quasar (see Fig. 3.1). On

*Macro-magnification of the individual images: $\mu_{\rm A} \simeq 4.6$, $\mu_{\rm B} \simeq 4.5$, $\mu_{\rm C} \simeq 3.8$, and $\mu_{\rm D} \simeq 3.6$ (Schneider et al. 1988).

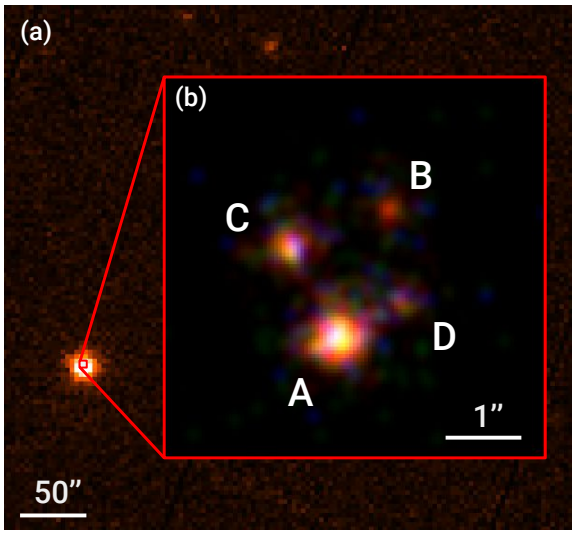

Figure 3.1: (a) EPIC-pn cleaned image of XMM 2002 in the 0.3–10 keV observed-energy band. The red square marks the 5″region of the *Chandra* image centered on the quasar and shown in inset (b). (b) Raw *Chandra* image of Q2237+030 (ObsID 431) binned with a bin size of 0.1″, color-coded based on the observed-energy bands: 0.4–2 keV in red, 2–4.5 keV in green, and 4.5–7 keV in blue. The images are named A, B, C, and D as in Yee (1988). Given the quasar redshift ($z_{\rm Q} = 1.695$), 1″separation corresponds to a distance of 8.68 kpc.

the other hand, XMM-*Newton* provides high count-statistics spectra, by means of its larger effective area, which allow us to investigate the spatially integrated source emission through more complex and physical spectral models. All the data were reduced through the respective standard pipelines, using CIAO 4.9 and SAS 16.1, so as to uniformly apply the latest calibrations to all observations. To extract individual image spectra from the *Chandra* data, we selected four circular regions ($r_{\rm A,B,C} = 0.8''$and $r_{\rm D} = 0.6''$, with encircled energy fraction – EEF – at 1.5 keV of 90% and 80%, respectively) imposing a certain offset with regard to the image centroids so as to limit the contamination from neighboring images. The background extraction region was selected as a source-free circle of 50″radius in the same chip as the target. Furthermore, to consistently analyze the data, we adopted the same regions for all the *Chandra* observations, after checking that they actually corresponded to the emission peak of the individual components in each pointing.

Regarding XMM-*Newton* data, we used as extraction regions a 25″-radius circle for the source ($EEF_{\rm Epn} \simeq 85\%$ at 1.5 keV) and an 80″-radius circle for the background in all the XMM-*Newton* observations. While the background in *Chandra* is extremely low (below 0.2% of the total counts), the first two XMM-*Newton* observations were significantly affected by soft-p$^+$ flares. We thus made use of the method described in Sect. 2.1 to select the best GTI filtering threshold, applied to the 2–8 keV observed-energy range ($\sim$ 5.4–22 keV rest frame).

Table 3.1: Information of each *Chandra* observation and details of the individual-image spectra. Those with more than 500 counts are marked with an asterisk (high-statistics sample - HSS). The observations are listed from earliest to latest date.

ObsID	Date	Exposure	A_{cts}	B_{cts}	C_{cts}	D_{cts}	A_{CR}	B_{CR}	C_{CR}	D_{CR}
431	2000-09-06	30.29	*1272±36	233±15	*523±23	177±13	41.99±1.18	7.69±0.50	17.26±0.26	5.84±0.44
1632	2001-12-12	9.54	309±18	51±7	99±10	52±7	32.39±1.84	5.34±0.75	10.38±1.04	5.45±0.76
6831	2006-01-09	7.27	97±10	86±9	26±5	35±6	13.35±1.36	11.83±1.28	3.57±0.70	4.82±0.81
6832	2006-05-01	7.94	211±15	111±11	90±10	58±8	26.58±1.83	13.98±1.33	11.34±1.19	7.31±0.96
6833	2006-05-27	7.95	118±11	56±7	54±7	21±5	14.83±1.37	7.04±0.94	6.79±0.92	2.64 ±0.58
6834	2006-06-25	7.94	272±16	111±11	74±9	54±7	34.26±2.07	13.98±1.33	9.32±1.08	6.80±0.93
6835	2006-07-21	7.87	319±18	79±9	64±8	49±7	40.52±2.27	10.03±1.13	8.13±1.02	6.22±0.89
6836	2006-08-17	7.93	170±13	62±8	60±8	40±6	21.43±1.64	7.82±0.99	7.56±0.98	5.04±0.80
6837	2006-09-16	7.95	166±13	62±8	39±6	35±6	20.89±1.62	7.80±0.99	4.91±0.79	4.40±0.74
6838	2006-10-09	7.99	157±13	53±7	51±7	34±6	19.65±1.57	6.63±0.91	6.38±0.89	4.26±0.73
6839	2006-11-29	7.87	*538±23	189±14	108±10	113±11	68.32±2.95	24.00±1.75	13.71±1.32	14.35±1.35
6840	2007-01-14	7.98	441±21	132±11	118±11	84±9	55.29±2.63	16.55±1.44	14.79±1.36	10.53±1.15
11534	2009-12-31	28.46	*1756±42	454±21	164±13	*802±28	61.70±1.47	15.95±0.75	5.76±0.45	28.18±1.00
11535	2010-04-25	29.43	377±19	101±10	52±7	150±12	12.81±0.66	3.43±0.34	1.76±0.25	5.10±0.42
11536	2010-06-27	27.89	342±19	105±10	44±7	163±13	12.26±0.66	3.76±0.37	1.57±0.24	5.84±0.46
11537	2010-08-07	29.36	228±15	68±8	44±7	116±11	7.76±0.51	2.31±0.28	1.50±0.23	3.95±0.37
11538	2010-10-02	29.36	*501±22	154±12	49±7	423±21	17.06±0.76	5.22±0.42	1.67±0.24	14.41±0.70
11539	2010-11-23	9.83	93±10	31±6	13±4	40±6	9.46±0.98	3.15±0.57	1.32±0.37	4.09±0.64
13195	2010-11-26	9.83	91±10	23±5	10±3	27±5	9.25±0.97	2.34±0.49	1.01±0.32	2.74±0.53
13191	2010-11-27	9.83	82±9	19±4	9±3	29±5	8.34±0.92	1.93±0.44	0.91±0.31	2.95±0.55
12831	2011-05-14	29.36	*2677±52	*575±24	215±15	429±21	91.19±1.76	19.58±0.82	7.32±0.50	14.61±0.71
12382	2011-12-27	29.79	343±19	128±11	59±8	100±10	11.51±0.62	4.29±0.38	1.98±0.26	3.36±0.34
13960	2012-01-09	29.36	308±18	122±11	52±7	117±11	10.49±0.60	4.15±0.38	1.77±0.25	3.98±0.37
13961	2012-08-02	29.24	*906±30	244±16	213±15	202±14	30.98±0.10	8.34±0.53	7.28±0.50	6.91±0.49
14513	2012-12-26	28.62	*684±26	247±16	339±18	260±16	23.89±0.91	8.26±0.55	11.84±0.64	9.08±0.56
14514	2013-01-05	29.36	*622±26	215±15	298±17	268±16	21.18±0.85	7.32±0.50	10.15±0.59	9.13±0.56
14515	2013-08-31	9.73	164±22	57±8	62±8	30±5	16.85±1.32	5.86±0.78	6.37±0.81	3.08±0.56
16316	2013-08-26	9.83	120±11	44±7	47±7	30±5	12.21±1.11	4.48±0.68	4.78±0.70	3.05±0.56
16317	2013-08-28	9.83	105±10	43±7	45±7	24±5	10.68±1.04	4.37±0.67	4.58±0.68	2.44±0.50
14516	2013-10-01	29.35	230±15	122±11	70±8	96±10	7.83±0.52	4.15±0.38	2.38±0.29	3.27±0.33
14517	2014-05-14	29.36	*1071±33	384±20	322±18	156±12	36.48±1.11	13.08±0.67	10.97±0.61	5.31±0.43
14518	2014-06-08	29.28	*628±25	263±16	206±14	117±11	21.45±0.86	8.98±0.55	7.03±0.49	3.99±0.37
18804	2016-04-24	28.60	*1009±32	269±16	132±11	126±11	35.28±1.11	9.40±0.57	4.61±0.40	4.41±0.39
19638	2016-12-22	33.34	302±17	120±11	51±7	77±9	9.05±0.52	3.60±0.33	1.53±0.21	2.31±0.26
19639	2017-01-04	32.92	249±16	113±11	46±7	68±8	7.56±0.48	3.43±0.32	1.40±0.21	2.06±0.25
19640	2017-12-20	34.23	402±20	210±14	76±9	94±10	11.74±0.59	6.13±0.42	2.22±0.26	2.74±0.28
19641	2018-01-14	34.23	368±19	170±13	92±10	77±9	10.75±0.56	4.96±0.38	2.10±0.25	2.25±0.26

Notes. The exposure time is given in units of kiloseconds. The observations are listed from earliest to latest date. The image net (i.e., background-subtracted) counts and CRs are referred to the 0.4–7 keV observed-energy range. The count rates are given in units of 10^{-3} cts s^{-1}. A, B, C and D are referred to the four lensed images of Q2237.

Table 3.2: Information of each XMM-*Newton* observation of Q2237+030.

	ObsID	Date	Total exposure	Cleaned exposure	Net counts	Net CR
XMM 2002	0110960101	2002-05-28	42.87	23.53	3837±62	16.3±0.3
XMM 2016	0781210201	2016-11-26	24.90	6.58	683±26	10.4±0.4
XMM 2018	0823730101	2018-05-19	141.60	108.00	6569±81	6.0±0.1

Notes. The exposure time and the cleaned exposure are given in units of kiloseconds. The source net (i.e., background-subtracted) counts and CRs are referred to the EPIC-pn spectra in the 0.3–10 keV observed-energy band. The net CR is given in units of 10^{-2} cts s^{-1}. EPIC-pn does not resolve the images thus the values in this table are the total values of the four images.

We managed to match our criteria and obtain good quality data for XMM 2002 EPIC-pn (CRT = 5.0 cts s^{-1}, $S_{\rm cts} = 918 \pm 30$ cts in the 2–8 keV observed-energy band). Regarding XMM 2016 EPIC-pn, mainly due to the combination of high flares and its shorter exposure, the GTI filtering threshold that satisfies our condition (CRT = 2.0 cts s^{-1}, $S_{\rm cts} = 200 \pm 14$ cts in the 2–8 keV observed-energy band) drastically reduces the source net counts in the energy band of interest. We left the XMM 2016 observation out of our analysis because the yielded count statistics (of spectra integrated over the four images of the quasar) undoes the advantages provided by XMM-*Newton*. We applied on EPIC-MOS data the same GTI threshold search as for the EPIC-pn, using the same extraction regions ($EEF_{\rm EMOS} \simeq 80\%$ at 1.5 keV). We obtained good quality data for both cameras in XMM 2002 (CRT = 1.0 cts s^{-1}, $S_{\rm cts} = 440 \pm 21$ cts and $S_{\rm cts} = 412 \pm 20$ cts, for MOS1 and MOS2 respectively, in the 2–8 keV observed-energy band). For completeness, we applied such GTI threshold search also on XMM 2016 EPIC-MOS 1 and 2 but, as expected given the results for the EPIC-pn spectrum and the lower effective area that EPIC-MOS 1 and 2 provide, we only managed to confirm the exclusion of this observation.

XMM 2018, instead, shows a more stable background that allowed us to select the GTI threshold directly from the detector light curves (CRT = 0.9 cts s^{-1} and CRT = 0.2 cts s^{-1} for EPIC-pn and EPIC-MOS, respectively). The properties of XMM-*Newton* cleaned data are listed in Table 3.2.

3.2.1 Single-image multi-epoch Chandra light curves

We produced the *Chandra* single-image multi-epoch light curves as the image mean count rate (CR), shown in Fig. 3.2, versus the respective observation date. Each image presents flux variations up to a factor of ∼4 among epochs. At first glance, the mean count rates seem to vary with similar trends for all the four images. However, when taking a closer look, discrepancies between the four light curves can be seen. In fact, as expected due to the proximity of the lensing galaxy ($z_{\rm l} = 0.039$) and as found by Chen et al. (2011, 2012) and Dai et al. (2003) through flux-ratio analysis, Q2237 presents microlensing events in the X-ray band that are expected to last a

few months (Mosquera & Kochanek 2011). Moreover, Dai et al. (2003) also found that more than one image of the Einstein Cross can undergo a microlensing event during a single observation. The intrinsic variability timescale of the quasar, having an Hβ-based BH mass of $M_{\rm BH} \simeq 1.2 \times 10^9\,{\rm M}_\odot$ (Assef et al. 2011), is much longer than all the image time delays induced by the lens (Dai et al. 2003; Schmidt et al. 1998).

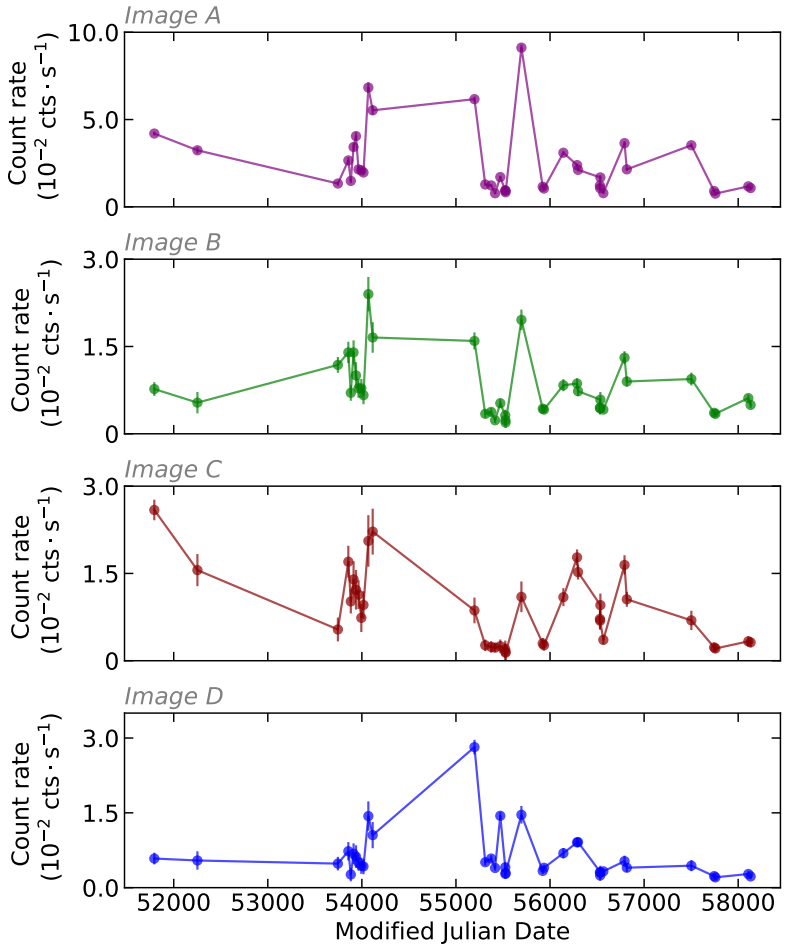

Figure 3.2: *Chandra* individual-image multi-epoch light curves. We show the mean count rate between 0.4–7.0 keV observed frame of each observation vs. time. From top to bottom: Image A, image B, image C, image D. The error bars are derived from the error on the Poisson-distributed counts.

Therefore, the dissimilarities between the light curves in Fig. 3.2 at a given epoch are likely due to microlensing (Chen et al. 2011). The effect of a microlensing event is to selectively magnify the emission arising from that particular portion of the background source that is behind the caustic. This results in a perturbation of the macrolensing-magnified image flux and is most relevant for the images with lower macro-magnification. An outflowing absorber moving along our line of sight (LOS) may produce detectable blueshifted absorption lines of highly ionized iron. We then

expect microlensing events, when present, to result in a dilution of these absorption lines since they would magnify the unabsorbed emission regions that do not lie along our LOS. Microlensing events can then be considered as a competing effect to the detection of the UFO signatures in which we are mainly interested. In this regard, microlensing events are unlikely to produce fake UFO absorption lines in our spectra or to shift their energy. Although a thorough analysis of the microlensing events is beyond the scope of our work, their effect on highly blueshifted absorption lines would be an interesting numerical simulation topic for a future project.

3.2.2 XMM-Newton light curves

Since the BH mass of Q2237 is estimated to be on the order of $10^9\,M_\odot$ (Assef et al. 2011), we do not expect much short timescale variability ($< 1\%$, Ponti et al. 2012). As a sanity check, we produced the background-subtracted source light curves for the two longest observations available, XMM 2002 and XMM 2018. We grouped the light curves into 200s time bins, and split them into soft-energy (0.3–2 keV) and hard-energy (2–10 keV) bands, excluding all the background-dominated time bins (those at the beginning and at the end of the observation). The soft-band light curves are variable at the 95% confidence level both for XMM 2002 and XMM 2018. The hard-band light curves are more stable, being variable at the 28% confidence level in XMM 2002 and at 34% in XMM 2018. We did not deem it necessary to split the observations based on the source variability, so we extracted the time-averaged spectra integrated over the whole net exposures.

3.3 Chandra spectral analysis

We first fitted each spectrum with a single power law modified by Galactic absorption ($N_{\rm H} = 5.1 \times 10^{20}$ cm^{-2}; Kalberla et al. 2005) model (Model `pl`=`phabs*zpo`), restricting the spectral fitting to the 0.4–7 keV observed-energy range (1–19 keV rest-frame energy range). The *Chandra* data sample was then narrowed down to those spectra with the highest count statistics, that is to those allowing a better constrain the presence of absorption or narrow emission and absorption features. For what concerns the lower S/N data, we analyzed their stacked spectra including all the *Chandra* observations, as reported in Sect. 3.5.

3.3.1 X-ray continuum spectral variability

The full *Chandra* dataset allowed us to probe the source spectral variability on timescales of weeks to years. Figure 3.3 shows the best-fit photon index Γ_i (i= A, B, C, D) obtained with Model `pl` as a function of time. The maximum photon-index variation, in terms of difference between the highest and the lowest Γ_i values

over a single image, changes from image to image, with image A showing the smallest ($\Delta\Gamma_A \approx 0.94$) and image B the largest ($\Delta\Gamma_B \approx 1.63$) variations. By fitting with

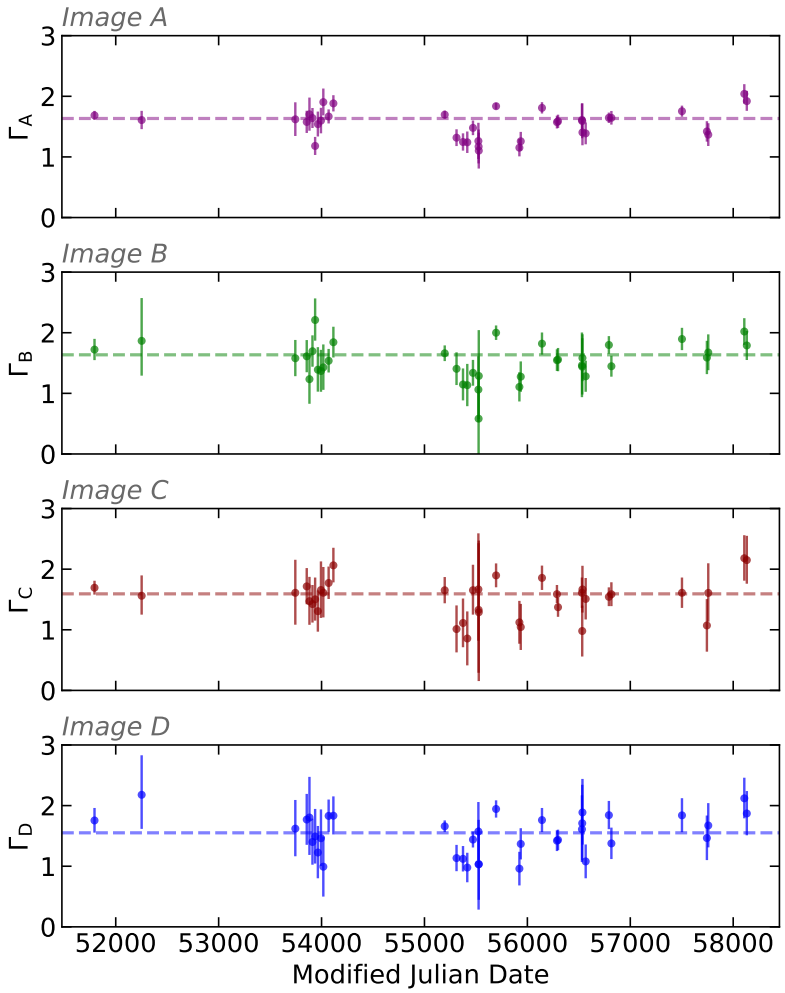

Figure 3.3: Variation of the photon index (1σ errors) for each image in the *Chandra* data as a function of time. The dashed line represents the best fit obtained using a constant function.

a constant (dashed lines in Fig. 3.3), the spectral slope was found to be significantly variable ($> 99.9\%$ confidence) in each image. Considering the ratios of the Γ_i, we can check whether the photon-index variations are intrinsic (if common to all images) or induced by microlensing. We find the ratios consistent with being constant overall and approximately equal to one. This agrees with the approximation applied by Chen et al. (2012), who analyzed the first 20 *Chandra* observations of our list assuming the same photon index for the four images at any given epoch. Moreover, the maximum Γ variations of all the images are consistent with each other when propagating their 1σ errors, thus no image shows a significantly higher maximum photon-index variation with regard to the others. Therefore, we can assume the vari-

ations of the continuum to be overall consistent between the four images, meaning they are not induced by microlensing but are inherent to the quasar.

To investigate the presence of any intrinsic spectral variability, we restricted our analysis to the high-statistics sample (HSS) to better constrain the best-fit spectral parameters. This sub-sample is made up of the fourteen spectra that show more than 500 source net counts in the 0.4–7 keV observed-energy range (those marked by a star in Table 3.1). The count threshold was selected to allow us to apply χ^2 statistics after binning the source spectra to at least 20 cts/bin. Fourteen spectra were extracted from eleven observations, since in three epochs (ObsIDs 431, 11534, 12831) two images exceed our threshold. In Fig. 3.4 we show three representative HSS spectra: that with the most counts (ObsID 12831 A), one of those with the least (ObsID 431 C), and one with an intermediate number of counts (ObsID 14517). Spectra with lower count statistics were used to produce stacked spectra, both keeping the images separate and combining the four images, the results of which are presented in Sects. 3.5.1 and 3.5.2, respectively. We anticipate that the results obtained with the stacked spectra are overall consistent with the ones presented here.

Table 3.3: Summary of the best-fit parameters for Model `pl_a` (`phabs*zphabs*zpowerlw`) when applied to the high-statistics sample. Significance levels above 99% confidence according to the F-test are in boldface, corresponding to the spectra actually requiring extra absorption (i.e., besides the Galactic one).

ObsID	Γ	$N_{\rm H}$	$\Delta\chi^2$	Confidence
431 A	$1.86^{+0.12}_{-0.12}$	$0.34^{+0.20}_{-0.20}$	8.4	98.8%
431 C	$1.90^{+0.42}_{-0.36}$	$0.53^{+0.23}_{-0.20}$	5.9	97.7%
6839 A	$1.80^{+0.20}_{-0.20}$	$0.46^{+0.52}_{-0.42}$	3.2	84.6%
11534 A	$1.91^{+0.11}_{-0.10}$	$0.62^{+0.29}_{-0.25}$	19.3	$>$ **99.99%**
11534 D	$2.01^{+0.20}_{-0.18}$	$1.28^{+0.57}_{-0.48}$	24.3	$>$ **99.99%**
11538 A	$2.06^{+0.28}_{-0.26}$	$2.88^{+1.40}_{-1.17}$	22.0	**99.9%**
12831 A	$1.98^{+0.09}_{-0.09}$	$0.27^{+0.22}_{-0.21}$	4.7	96.7%
12831 B	$2.10^{+0.27}_{-0.24}$	$0.50^{+0.60}_{-0.49}$	2.9	95.6%
13961 A	$2.02^{+0.18}_{-0.16}$	$0.67^{+0.53}_{-0.44}$	7.0	97.7%
14513 A	$1.80^{+0.20}_{-0.18}$	$0.88^{+0.67}_{-0.56}$	7.1	98.4%
14514 A	$1.79^{+0.22}_{-0.20}$	$0.77^{+0.80}_{-0.66}$	3.7	85.6%
14517 A	$1.79^{+0.14}_{-0.13}$	$0.59^{+0.49}_{-0.40}$	6.5	97.2%
14518 A	$1.84^{+0.24}_{-0.22}$	$1.01^{+1.03}_{-0.84}$	4.1	96.5%
18804 A	$2.10^{+0.19}_{-0.18}$	$1.45^{+0.85}_{-0.71}$	13.8	**99.9%**

Notes. Column 1: ObsID and image; Col. 2: Photon index; Col. 3: Column density in excess of the Galactic value (in units of 10^{22} cm^{-2} and placed at $z = 1.695$); Col. 4: $\Delta\chi^2$ compared to Model `pl` ($\Delta dof = 1$); Col. 5: F-test confidence level. All the errors are computed at a 90% confidence level for one parameter of interest.

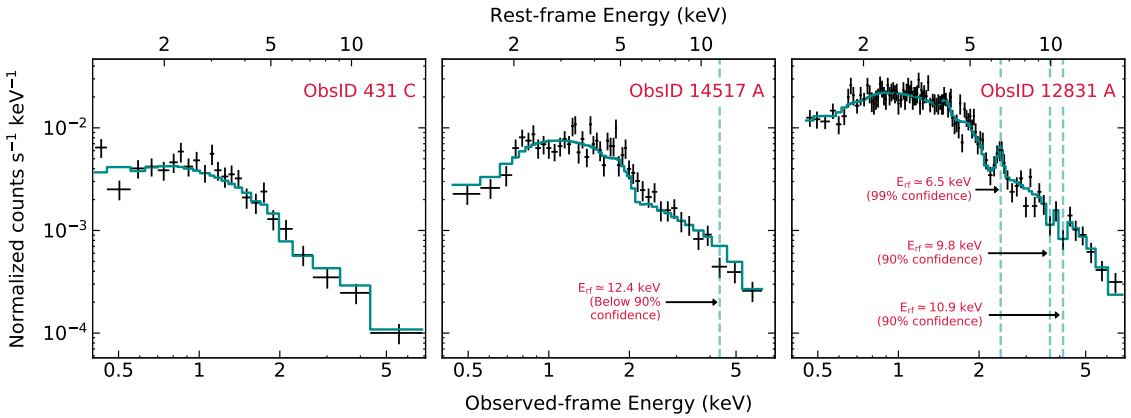

Figure 3.4: Data (black) and best-fit model (blue) for three of the *Chandra* HSS spectra, representative of three statistics regimes. From left to right: ObsID 431 C (least counts), 14517 A (intermediate counts), and 12831 A (highest counts). The dashed vertical lines indicate the energies of the emission and absorption lines found by adopting the blind-search method of Tombesi et al. (2010a). Only those above 90% were included in the best-fit models (i.e., those in Tables 3.4 and 3.4).

To search for additional spectral continuum complexities in the HSS, we first modified Model `pl` by adding a `zphabs` component, accounting for photo-electric absorption of the primary emission in a cold medium (Model `pl_a=phabs*zphabs*zpo`), which we placed at the quasar's redshift. Only four spectra[†] of the HSS require extra absorption at more than 99% confidence level (evaluated through the F-test), while for the other ten we could only derive an upper limit to such additional column density. All the best-fit values and the respective F-test significance are listed in Table 3.3, with those at more than 99% confidence level shown in boldface. Among the four spectra that significantly require some extra absorption, two are referred to two images from the same epoch (ObsID 11534 image A and D) and show consistent column densities within 1σ errors. Considering only the cases where extra absorption is required by the data, we find the column density to be variable at more than 99% confidence throughout the three epochs. To test our assumption regarding the absorber location, we compared the two spectra (ObsID 11534 A and 11538 A) showing the largest variation in column-density values by plotting their 90% confidence contours of $N_{\rm H}$ vs. photon index. As shown in Fig. 3.5, their column densities are not consistent, while their photon indices are. Furthermore, the time interval between the two observations (see Table 3.1) is ~ 275 d in the observer frame, that is ~ 102 d $\simeq 0.3$ yrs in the quasar rest frame. Considering that the two spectra refer to the same image, we interpret the $N_{\rm H}$ discrepancy and the short time elapsed as indications of the extra absorption being dominated by a component at the redshift of the quasar.

[†]ObsIDs 11534 A and D, 11538 A, 18804 A.

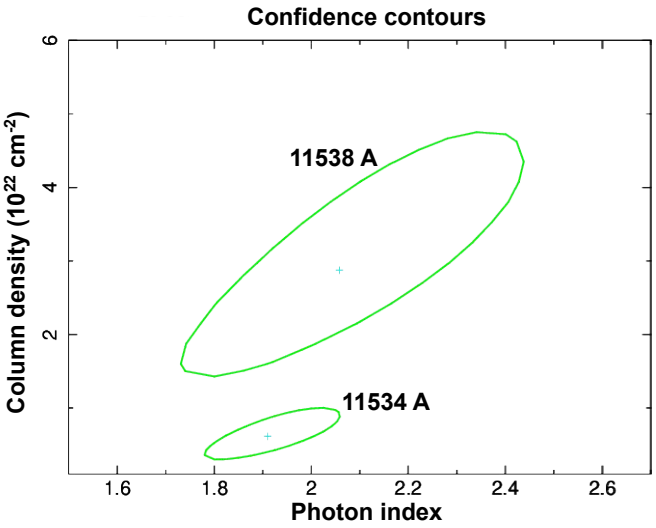

Figure 3.5: The 90% confidence contours of $N_{\rm H}$ vs. Γ for ObsIDs 11534 A and 11538 A. These correspond to the spectra that show the largest difference in column density, among the four that require a cold absorber at more than a 99% confidence level.

3.3.2 Narrow emission and absorption features

We searched for emission and absorption features, again only in the HSS spectra to obtain better constraints. A first blind search was carried out by applying the method of Miniutti & Fabian (2006), as implemented in Cappi et al. (2009) and Tombesi et al. (2010a). Stepping both the energy and the normalization of a Gaussian component over the entire spectral range, such method allowed us to visualize the statistical improvement ($\Delta\chi^2$ for two parameters) produced by the addition of a narrow feature ($\sigma = 0.01$ keV) in terms of energy versus normalization confidence contours over the whole energy range. We then built the best-fit models of all the HSS spectra by adding a Gaussian component for each emission and absorption line indicated at more than 90% confidence level by the blind search. Even though it is known to be unreliable when assessing the significance of narrow features (Protassov et al. 2002), we computed the F-test significance for each line to have a slightly better constraint than that of the blind search and only kept those features that are still above the 90% confidence level. Finally, we evaluated the actual significance of each absorption line at $E_{\rm rf} > 7$ keV by building a Bayesian posterior predictive probability distribution through Monte Carlo simulations, as argued for by Protassov et al. (2002).

We applied the Tombesi et al. (2010a) tool over the 0.4–5.0 keV observed-energy range (∼1–13 keV rest-frame energy band), which corresponds to the range of interest for both soft X-ray features and iron resonant lines. The upper energy limit was set to exclude bins with the lowest S/N. We selected as baseline models either Model pl or Model pl_a based on the requirement of extra absorption (see Table 3.3). We

obtained the best-fit models by adding a narrow `zgauss` component for each line indicated at a confidence above 90% from the blind search. We only kept those lines with a significance above 90% confidence both from the blind search and the F-test; these are summarized in Table 3.4. This procedure indicated the presence (at a 90% confidence level) of blueshifted iron resonant absorption lines in 5 spectra out of 14.

Table 3.4: Rest-frame energies and equivalent widths of (a) the emission and (b) the absorption lines detected at more than 90% confidence in the high-statistics sample, based on the F-test. Significance levels above 99% confidence, according to the F-test in (a) and according to Monte Carlo simulations in (b), are reported in boldface.

Emission lines

ObsID	$E_{\rm line}$	EW	Cont.	F-test
431 A	$5.90^{+0.31}_{-0.36}$	368^{+277}_{-278}	90%	90.4%
11534 A	$3.65^{+0.13}_{-0.10}$	101^{+69}_{-68}	90%	93%
	$5.35^{+0.13}_{-0.12}$	179^{+111}_{-111}	90%	93%
11534 D	$2.25^{+0.10}_{-0.10}$	163^{+137}_{-107}	90%	98.5%
12831 A	$4.04^{+0.14}_{-0.15}$	75^{+57}_{-57}	90%	93%
	$6.47^{+0.11}_{-0.12}$	284^{+148}_{-148}	99%	**99.7%**
13961 A	$3.78^{+0.16}_{-0.12}$	173^{+105}_{-105}	90%	96%

Absorption lines

ObsID	$E_{\rm line}$	EW	Cont.	F-test	MC
431 A	$11.92^{+0.23}_{-1.69}$	1181^{+778}_{-575}	99%	99.5%	**99.5%**
11534 A	$8.01^{+0.42}_{-0.14}$	287^{+212}_{-185}	90%	97%	90.3%
12831 A	$9.78^{+0.43}_{-0.18}$	255^{+211}_{-169}	90%	95%	84.2%
	$10.90^{+0.53}_{-0.20}$	368^{+258}_{-196}	99%	99.1%	94.9%
13961 A	$9.39^{+1.90}_{-0.08}$	1025^{+542}_{-532}	99%	98.3%	**99.1%**
14514 A	$12.51^{+0.10}_{-2.28}$	1861^{+1354}_{-1273}	90%	92%	98.4%

Notes. Column 1: ObsID and image; Col. 2: Line energy (in units of keV); Col. 3: Line rest-frame equivalent width (in units of eV); Col. 4: Blind-search confidence level; Col. 5: F-test confidence level; Col. 6: Monte-Carlo-simulation confidence level. All the errors are computed at a 90% confidence level for one parameter of interest. The energy width of the lines is set to 0.01 keV.

Finally, we evaluated the actual significance of the absorption lines in Table 3.4 through Monte Carlo simulations. Following Protassov et al. (2002), each of these 5 spectra was simulated 1000 times via the `XSPEC fakeit` function from the respective null model (Model `pl` or Model `pl_a` if extra absorption was required – see Table 3.3). Monte Carlo simulations confirmed that all the absorption lines at $E_{\rm rf} > 7$ keV are detected above 90% confidence except the one at 9.8 keV in ObsID 12831 A (see Table 3.4). Thus, we find blueshifted iron resonant absorption lines in 5 epochs out of the 11 included in the HSS. We then evaluated the global probability of detecting

these absorption lines in 5 out of 14 spectra by chance via the binomial distribution. We conservatively considered all the lines as detected at 90% confidence, even though more than half show higher significance. The probability of a by-chance detection is $P = 7.76 \times 10^{-3}$, yielding an overall significance of 99.2% (i.e., slightly below 3σ) for the detection of these absorption lines at $E_{\rm rf} > 7$ keV throughout the HSS. To inspect the persistence of such features through the different epochs, we overlapped the 1.6σ confidence contours of narrow emission and absorption lines separately (Figs. 3.6 and 3.7, respectively).

The emission lines (Fig. 3.6) span over the 2.2–6.5 keV rest-frame energy band. The microlensed Fe Kα line found by Dai et al. (2003) in the combined spectra of ObsIDs 431 A and 1632 A ($E = 5.7^{+0.2}_{-0.3}$ keV, $\sigma = 0.87^{-0.30}_{-0.15}$ keV) is only marginally detected (90% confidence) in the spectrum of ObsID 431 A as a narrow line, probably due to the fact that we are analyzing single-epoch spectra while Dai et al. (2003) stacked the first two observations. The energy of the highly significant emission line in ObsID 12831 A ($E_{\rm rf} = 6.47^{+0.11}_{-0.12}$ keV) is consistent, within 1.6 σ errors, with the centroid energy of the skewed line found by Reynolds et al. (2014) ($E = 6.58 \pm 0.03$ keV) in the combined spectra of all the images, stacking the first 26 observations (ObsIDs 431 – 14514). Following Dai et al. (2003) and Chartas et al. (2016a, 2017), the remaining emission lines can be associated with microlensed Fe Kα lines.

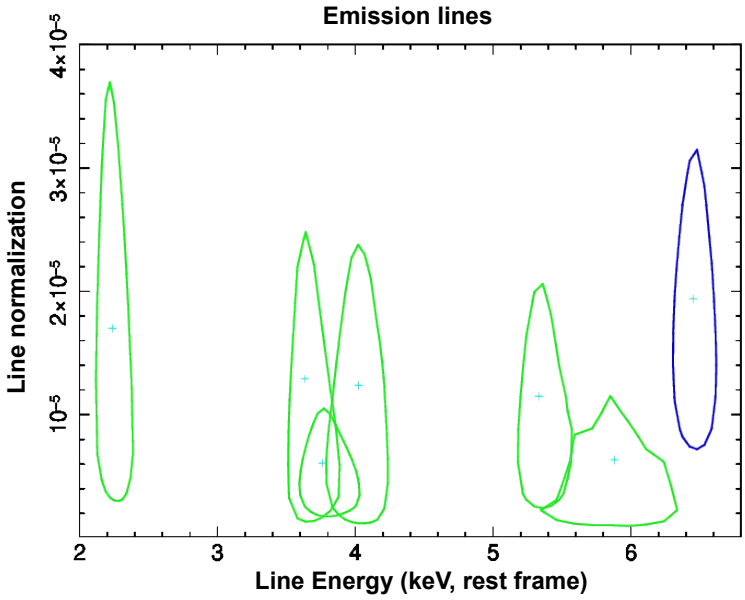

Figure 3.6: The 90% energy-normalization confidence contours (1.6σ) for the emission lines reported in Table 3.4 (ObsIDs 431 A, 11534 A, 11534 D, 12831 A, 13961 A). The blue contour corresponds to the line detected at more than a 99% confidence level in ObsID 12831 A (based on the F-test significance).

The absorption features (Fig. 3.7) show a group of lines around 11 keV and one

line at about 8 keV. Each of the confidence contours of the lines clustered around 11 keV cover a wide range of energy. This could be interpreted as due to the blend of two or more lines given the lower S/N at the higher energies, thus larger energy bins, or ascribed to intrinsic very broad lines as seen in other high-z lensed and unlensed quasars, for instance APM 08279+5255 (Chartas et al. 2009) and HS 1700+6416 (Lanzuisi et al. 2012). By letting the width of the absorption lines in Table 3.4 free to vary, we found them to be consistent with zero, with upper limits ranging from 0.8 keV (ObsID 12831 A) up to 3.2 keV (ObsID 13961). The feature in ObsID 13961 A is the most peculiar; an intrinsically broad ($\sigma = 2.2^{+1.0}_{-0.5}$ keV) line would yield a better fit but the low statistics prevent us from simultaneously constraining the three line parameters (energy, width, normalization). As a result, we consider all the lines in Table 3.4 as consistent with being narrow.

The two highly significant absorption lines (blue contours in Fig. 3.7) are both found at energies above 9 keV (rest frame) and are consistent with each other at the 1.6σ level. These features are detected in observations 431 and 13961, which are separated by twelve years (~ 4.5 yrs proper time), and are also consistent in energy with the slightly less significant features of ObsIDs 12831 and 14514. Thus, the lines at $E_{\rm rf} > 9$ keV are presumably produced by the same highly ionized outflow which is most likely variable, based on the time elapsed between the observations. Interestingly, there seems to be no clear correlation between the additional absorption found in Sect. 3.3.1 and the detection of these absorption lines above 7 keV. In fact, only one spectrum (ObsIDs 11534 A) out of the four requiring an additional cold absorber presents such lines above 90% confidence.

Finally, we analyzed the combined spectra of images B+C+D from ObsIDs 431, 12831, and 13961, which are those observations in which image A shows highly significant absorption and/or emission lines (see Tables 3.4 and 3.4). Since the time delays between the images are short when compared to the intrinsic variability timescale, in the absence of microlensing events one would expect the B+C+D combined spectra to show the same kind of features as image A at a confidence at least higher than 90%, since the number of counts in such stacked spectra is similar to that of the respective image A. We find that the B+C+D spectra do not present any of the lines of Tables 3.4 and 3.4 at more than 90% confidence. However, the upper limits we derive on their EWs are consistent with those of the respective image A lines. Our interpretation is that one, or more than one, of images B, C, and D is microlensed, thus the absorption lines are smeared out in the individual image spectra. Moreover, the Fe Kα emission lines are likely blueshifted or redshifted, becoming even more diluted when we stack the images together.

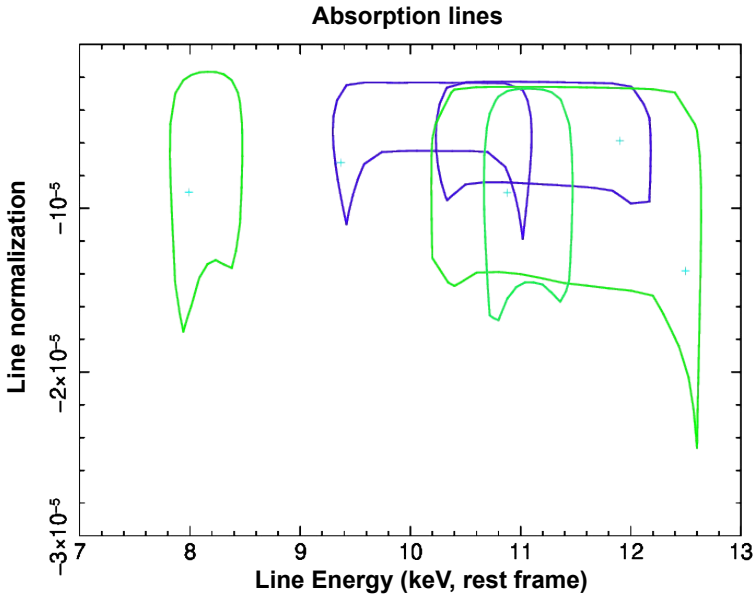

Figure 3.7: The 90% energy-normalization confidence contours (1.6σ) for the absorption lines reported in Table 3.4 (ObsIDs 431 A, 11534 A, 12831 A, 13961 A, 14514 A). Those in blue correspond to the lines detected at more than a 99% confidence level (based on the Monte-Carlo-simulation significance).

3.3.3 Summary of the Chandra spectral results

We find clear spectral index variability at a significance larger than 99% as inferred from the analysis of the whole *Chandra* dataset (Fig. 3.3). From the photon-index ratios, such variations seem to be intrinsic and not induced by microlensing. Photon-index variability might also be induced by variable absorption in some observations, as the HSS analysis pointed out (Table 3.3). Having a variability timescale of ~ 0.3 yrs (rest frame), such an absorber is most likely dominated by an in situ component.

Five spectra of the HSS also show narrow emission lines below 3.5 keV in the observed frame (significance above 90% confidence - Table 3.4). In one spectrum (ObsID 12831 A) we detect a highly significant narrow emission line at $E_{\rm rf} = 6.47^{+0.11}_{-0.12}$ keV; its energy centroid is consistent with that detected by Reynolds et al. (2014). The line found by Dai et al. (2003) is only marginally detected in the spectrum of ObsID 431 A.

Finally, five spectra show narrow absorption features in the 3–5 keV observed-frame energy band ($\sim$ 8–13.5 keV rest frame) at more than 90% confidence (assessed through Monte Carlo simulations - Table 3.4). A certain recurrence and/or persistence of those features in this energy range is indicated by the consistency of their confidence contours (Fig. 3.7), although we note that the error associated with the energy of the lines is typically large. The overall significance of detecting such

features in the HSS is proved to be almost 3σ.

3.4 XMM-Newton spectral analysis

Having assessed the source spectral variability and the presence of spectral complexities in the *Chandra* observations, we analyzed the XMM-*Newton* spectra, and attempted to model such complexities with physically-motivated reflection and complex absorption models. Both XMM 2002 and XMM 2018 spectra were grouped in order to obtain at least 20 counts per bin. Given the large number of counts (Table 3.2), we set the minimum energy width of each bin at one third of the CCD resolution using the task `specgroup` within SAS 16.1, so as not to oversample the energy resolution of the instrument. Due to background-dominated bins at the higher energies, the spectral fitting of XMM 2002 and XMM 2018 data was performed in the 0.3–8 keV observed-energy range (0.8–22 keV rest-frame energy range) and in the 0.3–7 keV observed-energy range (1–19 keV rest-frame energy range), respectively, to obtain more reliable results. For both observations, we analyze and report here only the EPIC-pn spectra, which deliver the best S/N, but our results were also compared and confirmed by checking their consistency with the EPIC-MOS data.

3.4.1 XMM 2002

The observed-frame best-fit residuals to Model pl (Fig. 3.8, panel b and Table 3.5) show clear spectral complexities throughout the whole energy band. Those that stand out are a deficit of counts at ~ 2.7 keV ($E_{\rm rf} \sim 7.4$ keV) and at ~ 4.4 keV ($E_{\rm rf} \sim 11.8$ keV), the latter being consistent with the bulk of those in the *Chandra* spectra. Moreover, an excess of counts at ~ 2.1 keV ($\rm E_{rf} \sim 5.7$ keV) and signatures of absorption in the soft band below ~ 0.6 keV ($E_{\rm rf} \sim 1.6$ keV) are also present.

Based on the results obtained from the *Chandra* observations, we investigated the need for an extra cold absorber at the quasar's redshift, either uniformly or partially covering the source (Model pl_a=`phabs*zphabs*zpo`; and Model pl_pca=`phabs*zpcf*zpo`, respectively; best-fit parameters in Table 3.5). The data indeed require extra absorption at the quasar redshift and are slightly better ($\Delta\chi^2 \sim 6$ for one additional parameter) reproduced by a partial covering medium. By adding a narrow Gaussian component to Model pl_pca for each of the narrow features hinted at by the residuals in Fig. 3.8 (panel b), the two in absorption are required by the data ($\Delta\chi^2 > 10$ for the addition of two parameters, each), while the emission line is only marginally detected (90% confidence). Following Protassov et al. (2002), we evaluated the actual significance of the two narrow absorption features through Monte Carlo simulations, as follows. To obtain the null models, we started from Model pl_pca plus the three narrow Gaussian components; the absorption line

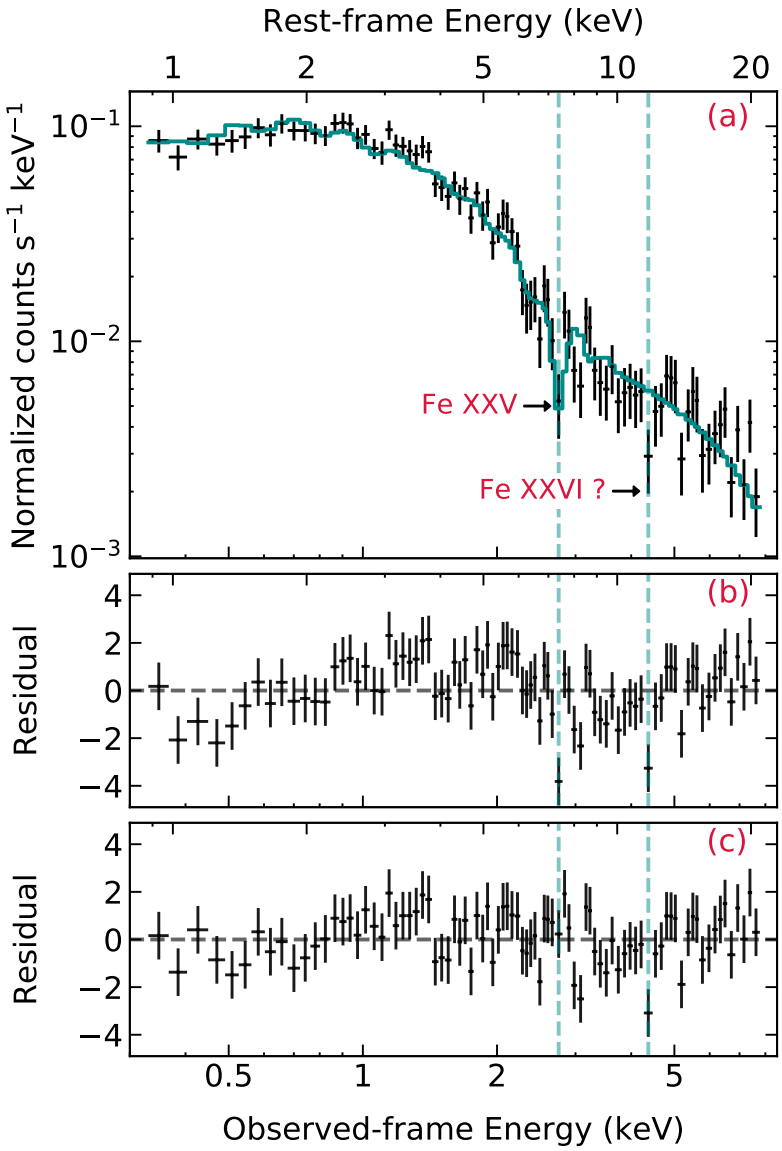

Figure 3.8: XMM 2002 EPIC-pn spectrum of Q2237. Panel (a): XMM 2002 data (black) and best-fit model (solid blue line) with Model pl_wa. The dashed blue lines indicate the UFO signatures. Panel (b): XMM 2002 best-fit residuals for Model pl. Panel (c): XMM 2002 best-fit residuals for Model pl_wa. The latter model self-consistently accounts for the absorption line at $E_{\rm rf} \simeq 7.4$ keV. The data are grouped to obtain at least 20 cts/bin, with the minimum energy width set to one third of the CCD energy resolution. The best-fit parameters are summarized in Table 3.5. Due to background-dominated bins above 8.0 keV, we restricted the fitting to the 0.3–8 keV observed-energy range (0.8–22 keV rest-frame energy range).

whose actual significance was to be measured was then deleted before performing the simulations. For each of the two null models, we simulated 1000 spectra through the `fakeit` function in `Xspec`. The two absorption lines turn out to be detected at

$E_{\rm rf} = 7.4$ keV and $E_{\rm rf} = 11.8$ keV at confidence levels of 97.9% and 87%, respectively.

Given their energies, they are likely blueshifted iron resonant lines, thus produced by a (highly) ionized and outflowing material. To test this scenario through physically-motivated models, we used `warmabs` (Kallman & Bautista 2001), an analytic XSTAR model for self-consistent ionized absorption (Model pl_wa= `phabs*warmabs*zpo`), which also takes into account the production of absorption lines. Based on the results for other high-z GLQs (Chartas et al. 2021, for review), we assumed solar abundances and a gas turbulent velocity of 5000 km s^{-1}, letting the column density ($N_{\rm H}$), the ionization parameter (logξ), and the redshift of the absorber ($z_{\rm o}$) vary. The `warmabs` model assumes that the AGN emission modeled in `Xspec` is the same radiation that illuminates and ionizes the absorber. The initial conditions (abundances and density) of the medium are loaded through a population file, which depends on the power-law slope of the illuminating radiation. To find the best-fit Γ, we created different population files (with fixed n= 4×10^4 cm^{-3}, $v_{\rm turb} = 5000$ km s^{-1} and varying the photon index) until the incident-radiation and the best-fit power-law photon indexes converged (within the errors). Model pl_wa yielded the best description of the XMM 2002 data ($\chi^2_{\rm r} = 1.20$), with best-fit parameters for the ionized absorber of $N_{\rm H} = 2.8 \pm 0.2 \times 10^{23}$ cm^{-2}, log (ξ/erg s^{-1}cm) = $2.5^{+0.1}_{-0.3}$, and $z_{\rm o} \simeq 1.445$ (see Table 3.5 and Fig. 3.8, panel a and c). The observed value $z_{\rm o}$ of the absorber redshift is related to the intrinsic redshift $z_{\rm a}$ of the medium (i.e., in the source rest frame) as $(1 + z_{\rm o}) = (1 + z_{\rm a})\,(1 + z_{\rm q})$. Thus, the outflow velocity $v_{\rm out}$ can be determined from the relativistic Doppler effect formula $1 + z_{\rm a} = \sqrt{(1-\beta)/(1+\beta)}$, where $\beta = v_{\rm out}/c$. Given $z_{\rm q} = 1.695$, the outflow velocity corresponding to $z_{\rm o} \simeq 1.444$ is $v_{\rm out} = 0.10 \pm 0.01c$. This ionized wind model naturally explains both the structure in the soft band and the absorption feature at $E_{\rm rf} \simeq 7.4$ keV (Fig. 3.8), as opposed to the absorber of Model pl_pca, which, being cold, cannot be the origin of such a line. Given the wind ionization state and the outflow velocity, this line is consistent with being dominated by Fe XXV, which has a rest-frame energy at rest ($v_{\rm out} = 0$) of 6.7 keV. This same model fails to account for the second absorption line at $E_{\rm rf} \simeq 11.8$ keV (4.4 keV, see Fig. 3.8, panel a and c) as expected based on the outflow parameters: in fact, the Fe XXVI line produced by an absorber outflowing at $v_{\rm out} = 0.1c$ as that obtained with Model pl_wa would fall at $E = 7.7$ keV.

Moreover, the narrow emission line at $E_{\rm rf} = 5.7 \pm 0.2$ keV is only marginally detected (90% confidence) when adding a Gaussian component to Model pl_wa. Its energy is consistent with that of the emission line in *Chandra* ObsID 431 A (see Sect. 3.3.2) and with that of the microlensed Fe Kα found by Dai et al. (2003). Its width ($\sigma < 0.01$ keV), however, is not consistent with the broad one found by Dai et al. (2003) ($\sigma = 0.87^{+0.30}_{-0.15}$ keV). The results of Fedorova et al. (2008), who analyzed the

Table 3.5: Summary of the best-fit parameters for each model tested for XMM 2002 data.

Model	Γ	$N_{\rm H}$	CF	logξ	$z_{\rm abs}$	R	$E_{\rm e.l.}$	$\Delta\chi^2$	$\Delta\nu$	$\chi^2_{\rm r}$ (ν)
pl	1.66 ± 0.04	–	–	–	–	–	–	–	–	1.56 (85)
pl_a	1.82 ± 0.07	0.32 ± 0.12	–	–	1.695	–	–	22.6	1	1.31 (84)
pl_pca	1.91 ± 0.11	$2.1^{+1.4}_{-1.2}$	$0.50^{+0.10}_{-0.12}$	–	1.695	–	–	28.9	2	1.25 (83)
pl_wa	1.74 ± 0.04	$28.2^{+1.4}_{-1.8}$	–	$2.5^{+0.1}_{-0.3}$	$\simeq 1.445$	–	–	34.1	3	1.20 (82)
pl_pca_pex_el	2.57 ± 0.32	$2.3^{+0.7}_{-0.7}$	$0.74^{+0.07}_{-0.11}$	–	1.695	$0.58^{+0.40}_{-0.27}$	$5.7^{+0.2}_{-0.2}$	54.2	5	0.98 (80)
pl19_pca_pex_el	1.90	$1.1^{+1.0}_{-0.8}$	$0.51^{+0.44}_{-0.12}$	–	1.695	< 0.18	$5.7^{+0.2}_{-0.2}$	41.1	4	1.13 (81)

Notes. Column 1: Model name; Col. 2: Photon index; Col. 3: Column density in excess of the Galactic value (units of 10^{22} cm^{-2}); Col. 4: Covering fraction of the extra absorption; Col. 5: Logarithm of the extra-absorption ionization parameter (erg s^{-1} cm); Col. 6: Observed redshift of the extra absorption; Col. 7: Reflection scaling factor; Col. 8: Energy of the emission line (units of keV); Cols. 9 and 10: $\Delta\chi^2$, $\Delta\nu$ compared to Model pl ($\chi^2 = 132.6, \nu = 85$); Col. 11: $\chi^2_{\rm r}$. The energy width of the emission line is set to 0.01 keV. All the errors are computed at a 90% confidence level for one parameter of interest. *Model list*: Model pl = `phabs*zpo`; Model pl_a = `phabs*zphabs*zpo`; Model pl_pca = `phabs*zpcf*zpo`; Model pl_wa = `phabs*warmabs*zpo`; Model pl_pca_pex_el = `phabs*zpcf*(zpo+pexrav+zgauss)`; Model pl19_pca_pex_el = `phabs*zpcf*(zpo+pexrav+zgauss)` with $\Gamma = 1.9$. All the models include Galactic absorption ($N_{\rm H} = 5.1 \times 10^{20}$ cm^{-2}).

XMM 2002 observation, tentatively detecting an emission line at $E_{\rm rf} = 6.0^{+0.7}_{-1.0}$ keV with an energy-width upper limit of $\sigma < 0.9$ keV, are consistent with ours.

Finally, we stress that the significance obtained for the 7.4 keV absorption line through the Monte Carlo simulations does not correspond to that of the UFO. In fact, assessing the F-test significance of the `warmabs` component leads to a detection of the outflow that is well above the 99.99% confidence level. This is linked to the fact that the UFO not only explains the absorption line by itself but also acts on the shape of the soft-band continuum, as the two lower panels of Fig. 3.8 show.

For the sake of completeness, we also tested a reflection scenario. Instead of self-consistent reflection models that bind the Fe Kα line to the 6.4–6.7 keV range, we built a phenomenological model to let the emission line be placed at lower energies (Model `pl_pca_pex_el`= `phabs*zpcf*(zpo+pexrav+zgauss)`). The reflected-power-law photon index was set to that of the intrinsic emission, the abundances equal to solar, the inclination angle to 60°, the cutoff energy to 300 keV, and the reflection fraction[‡] to be negative, so as to only model the reflected emission through the `pexrav` component. The best-fit reflection fraction and photon index (Table 3.5) are $\mathrm{R} = 0.58^{+0.40}_{-0.27}$ and $\Gamma = 2.57 \pm 0.32$ ($\chi^2_{\rm r} = 0.98$), which corresponds to a considerably steeper power law, at the limits of the expected values for an AGN (e.g., Perola et al. 2002; Piconcelli et al. 2005). In this case, the emission line is detected at $E_{\rm rf} = 5.7 \pm 0.2$ keV above 99% confidence as a narrow line, with an EW of $\mathrm{EW} = 154^{+99}_{-103}$ eV. The steep power law may be caused by the known degeneracy between photon index and column density. Therefore, we tried setting the photon index (Model `pl19_pca_pex_el`) to $\Gamma = 1.9$, the standard value for high-z quasars (e.g., Vignali et al. 2005; Just et al. 2007), which is also consistent with the average Γ of the *Chandra* HSS and that of the absorption models for this spectrum (see Table 3.5). When doing so, we find a worse fit and the reflection fraction becomes consistent with zero (90% confidence upper limit: $\mathrm{R} < 0.18$). Therefore, the reflection component turns out not to be required by the 2002 data, confirming earlier results by Fedorova et al. (2008).

3.4.2 XMM 2018

As for the other spectra, we began our analysis of the XMM 2018 EPIC-pn spectrum by inspecting the best-fit residuals to Model `pl` (Fig. 3.9, panel b, Table 3.6). Due to background-dominated bins above 7 keV, we restricted the fitting to the 0.3–7 keV observed-energy range (1–19 keV rest-frame energy range). The residuals (Fig. 3.9, panel b) show complexities in the soft-energy band that are likely due to an absorber and indicate a prominent emission line just below 3 keV in the observed frame. At higher energies, however, the distribution is quite flat, although noisy,

[‡]The reflection fraction R is defined as the fraction relative to the reflected emission expected from a slab subtending a 2π solid angle.

suggesting the absence of a significant reflection component. No hints of absorption lines in the hard-energy band are seen either.

Using the same logical steps as for XMM 2002, we started by adding more complex absorption models to fit the low energy continuum. All the best-fit parameters of the tested models are summarized in Table 3.6. Given the shape of the residuals, the absorber during this observation could either be cold and partially covering the emitting source, or ionized (Model pl_pca and Model pl_wa[§], respectively). For completeness, we also investigated the case of a cold medium blocking all the intrinsic emission (Model pl_a) which, as expected, turned out not to be required by the data. In all three cases, we set the absorber's redshift to the systemic of the quasar, based on the results obtained with the *Chandra* data (Sect. 3.3.1) and because no absorption lines above 7 keV rest-frame were found (i.e., there are no hints of outflowing material). Limiting the analysis to one feasible absorption component, the XMM 2018 spectrum is best reproduced by a power-law emission modified by a partial covering medium (Model pl_pca, see Table 3.6). The prominent emission line indicated by the residuals (Fig. 3.9, panel b) is found to be narrow (Model pl_pca_el, Table 3.6 and Fig. 3.9, panel a and c) with a 90% energy-width upper limit of $\sigma < 0.53$ keV. Thus, XMM 2018 data are well reproduced by a rather thick absorber that blocks part of the intrinsic emission ($N_{\rm H} \simeq 1.0 \times 10^{23}$ cm^{-2}, CF $\simeq 0.53$) and a significant emission line with rest-frame energy and EW of $E_{\rm rf} = 6.84 \pm 0.11$ keV and EW $= 267 \pm 111$ eV. The energy is inconsistent with both that of the marginal detection in the 2002 data (see Sect. 3.4.1) and that of the skewed emission line found by Reynolds et al. (2014). To see whether the line could be ascribed to the absorber, we evaluated the upper limit of the medium ionization state through the `warmabs` model. To mimic the partial absorption of the intrinsic emission, we included two power-law plus emission-line components, the first seen directly and the other as scattered by the absorber (Model pl_pcwa=`phabs*[(zpo+zga)+warmabs*(zpo+zga)]`), both modified by Galactic absorption. The slopes and the line parameters of the two terms were linked to each other, since the primary emission is the same for both components. We inferred a 90% upper limit to the ionization parameter of $\log(\xi/\mathrm{erg\ s^{-1}cm}) = 2.2$ and a covering fraction CF $= 0.58 \pm 0.33$, which is consistent with that obtained with Model pl_pca (Table 3.6). The inferred ionized state is not consistent with that of the UFO detected in XMM 2002, and nor are the column densities. Since the absorber parameters are strongly dependent on the photon index, we compared the confidence contours of $\log\xi$ vs. Γ, from which we infer that the absorber in XMM 2018 is consistent at 3σ with that in XMM 2002. Thus, even though it is unlikely that the two absorbers are the same gas that changed in covering fraction, we can-

[§]Chemical abundances and the gas turbulent velocity were set as for XMM 2002 (see Sect. 3.4.1). The best-fit Γ was found using the same method as for XMM 2002.

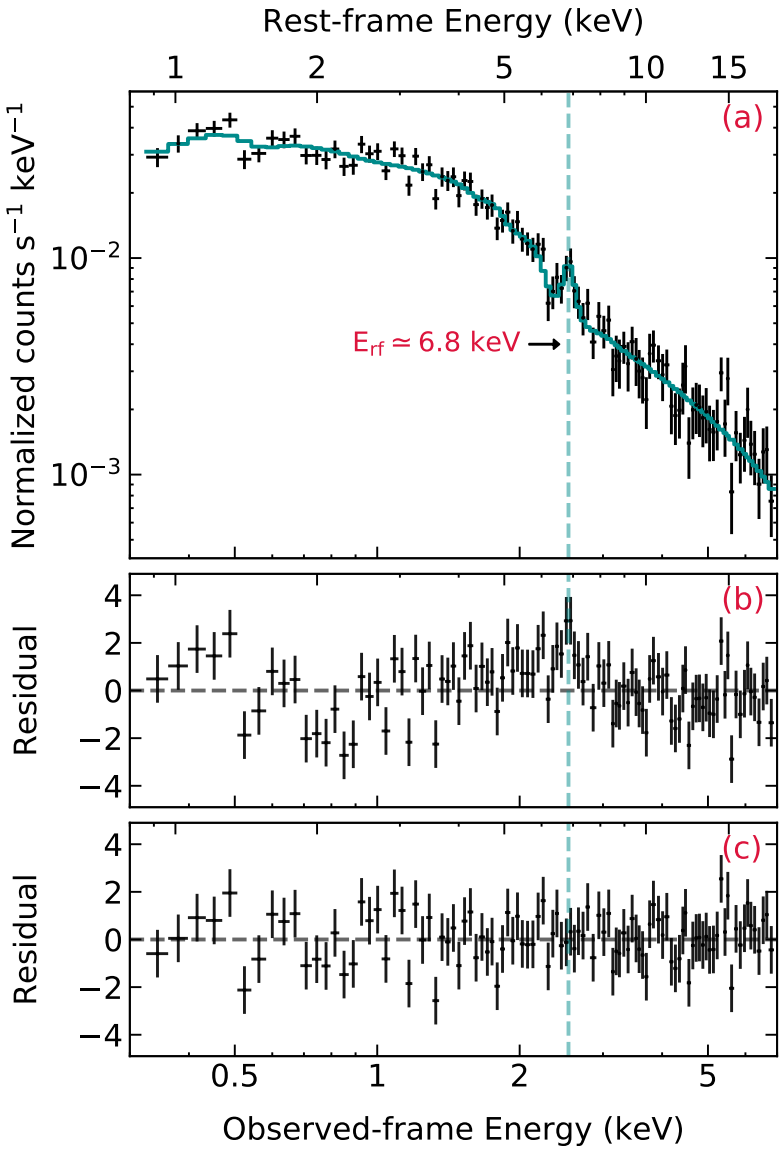

Figure 3.9: XMM 2018 EPIC-pn spectrum of Q2237. Panel (a): XMM 2018 data (black) and best-fit model (solid blue line) with Model pl_pca_el. The dashed blue line indicates the emission line at $E_{\rm rf} = 6.84 \pm 0.11$ keV. Panel (b): XMM 2018 best-fit residuals for Model pl. Panel (c): XMM 2018 best-fit residuals for Model pl_pca_el. The data are grouped to obtain at least 20 cts/bin, with the minimum energy width set to one third of the CCD energy resolution. The best-fit parameters are summarized in Table 3.6. Due to background-dominated bins above 7.0 keV, we restricted the fitting to the 0.3–7.0 keV observed-energy range (1–19 keV rest-frame energy range).

not rule this possibility out. Following Makishima (1986), the absorber ionization state ($\log(\xi/\mathrm{erg\ s^{-1}cm}) \leq 2.2$) translates into a medium that is dominated by iron from Fe I to Fe XX, while, from its energy, the line we detect is consistent with being dominated by Fe XXV–XXVI. Thus, this feature cannot be produced by the absorber

itself since it would require a much more ionized gas ($\log(\xi/\mathrm{erg\ s^{-1}cm}) \geq 3.0$). Unfortunately, we are not able to verify whether an additional highly ionized medium could be required by the data because the S/N of XMM 2018 does not allow us to constrain such a complex model. Another possible explanation for the 6.8 keV line could be the microlensing differential magnification of a relativistic blurred Fe Kα produced by the Compton reflection in the accretion disk, as proposed in other sources by Chartas et al. (2016b, 2017). Based on this argument, we tested whether a reflection scenario would give a better representation of the XMM 2018 data, using the same phenomenological model discussed in Sect. 3.4.1 (Model `pl_pca_pex_el`). This model returns a best fit that on a statistical basis is as good as that of Model `pl_pca`, but its reflection fraction R is consistent with zero at the 90% confidence level ($R \leq 0.16$, see Table 3.6). On the one hand, this result confirms that the Compton reflection is not a dominant component in the Einstein Cross emission but, on the other hand, it does not completely rule out the interpretation of the 6.8 keV emission line as a microlensed Fe Kα line. Standard reflection models, like `pexrav`, assume the reflection continuum as produced by the whole disk. In the case of a microlensing event magnifying the inner regions of the approaching side of the accretion disk, Popović et al. (2006) demonstrate that only the emission associated to the blueshifted part of the Fe Kα line is enhanced, while the reflection continuum is not, unless the microlensing event is monitored for its whole duration. Since the source crossing time in the Einstein Cross is estimated to be a few months (Mosquera & Kochanek 2011), we cannot rule out the possibility of this emission line being a microlensed Fe Kα.

3.4.3 Summary of the XMM-Newton results

The XMM 2002 spectra are best physically and statistically reproduced by a complex absorber with $N_{\mathrm{H}} \simeq 2.8 \times 10^{23}\mathrm{cm}^{-2}$, $\log(\xi/\mathrm{erg\ s^{-1}cm}) \simeq 2.5$, and outflow velocity of $v_{\mathrm{out}} \sim 0.1\mathrm{c}$, typical of UFOs. This also explains the prominent absorption iron resonant line measured at $E_{\mathrm{rf}} \simeq 7.4$ keV and interpreted as Fe XXV.

The 2018 data do not show any similar blueshifted absorption features and are best fitted by a partially covering, mildly ionized material, with $N_{\mathrm{H}} \simeq 1.0 \times 10^{23}$ cm^{-2}, CF $\simeq 0.53$ and with a 90% ionization-state upper limit of $\log(\xi/\mathrm{erg\ s^{-1}cm}) < 2.2$. We detect a significant narrow emission line at $E_{\mathrm{rf}} = 6.84 \pm 0.11$ keV, with an EW of EW $= 267 \pm 111$ eV. This line is inconsistent with being produced by the absorber itself because, given its energy, a much more ionized medium would be required.

Constraining the reflection component is challenging for both the XMM spectra, also due to the limited energy range provided at high energies. We find that for the 2002 data, a reflection component is statistically significant only when a very steep power law ($\Gamma \simeq 2.65$) is assumed, while it is negligible when a typical AGN slope ($\Gamma \simeq 1.9$) is adopted. Regarding the 2018 data, despite the presence of a prominent

Table 3.6: Summary of the best-fit parameters for each tested model for XMM 2018 EPIC-pn spectrum. The fitting was carried out over the 0.3–7.0 keV observed-energy range because the data are background dominated above 7 keV.

Model	Γ	$N_{\rm H}$	CF	logξ	$z_{\rm abs}$	R	$E_{\rm e.l.}$	$\Delta\chi^2$	$\Delta\nu$	$\chi^2_{\rm r}$ (ν)
pl	1.56 ± 0.03	–	–	–	–	–	–	–	–	1.64 (102)
pl_a	1.56 ± 0.03	< 0.04	–	–	1.695	–	–	-0.4	1	1.72 (101)
pl_pca	1.99 ± 0.10	$11.1^{+2.5}_{-2.2}$	0.56 ± 0.08	–	1.695	–	–	47.3	2	1.20 (100)
pl_pca_el	1.96 ± 0.10	$10.3^{+2.5}_{-2.2}$	0.53 ± 0.09	–	1.695	–	6.84 ± 0.11	62.4	4	1.07 (98)
pl_wa	1.62 ± 0.03	< 0.19	–	$2.4^{+0.4}_{-0.6}$	1.695	–	–	2.1	2	1.65 (100)
pl_pca_pex_el	$2.03^{+0.20}_{-0.15}$	$9.4^{+3.0}_{-2.3}$	0.56 ± 0.09	–	1.695	< 0.16	6.84 ± 0.10	63.7	5	1.07 (97)

Notes. Column 1: Model name; Col. 2: Photon index; Col. 3: Column density in excess of the Galactic value (units of 10^{22} cm^{-2}); Col. 4: Covering fraction of the extra absorption; Col. 5: Logarithm of the extra-absorption ionization parameter (erg s^{-1} cm); Col. 6: Observed redshift of the extra absorption; Col. 7: Reflection scaling factor; Col. 8: Energy of the narrow emission line (units of keV); Cols. 9 and 10: $\Delta\chi^2$, $\Delta\nu$ compared to Model pl ($\chi^2 = 167.4, \nu = 102$); Col. 11: $\chi^2_{\rm r}$. The energy width of the emission line is set to 0.01 keV. All the errors are computed at a 90% confidence level for one parameter of interest. *Model list*: Model pl = `phabs*zpo`; Model pl_a = `phabs*zphabs*zpo`; Model pl_pca = `phabs*zpcf*zpo`; Model pl_wa = `phabs*warmabs*zpo` with $z \equiv z_{\rm q}$; Model pl_pca_el = `phabs*zpcf*(zpo+zgauss)`; Model pl_pca_pex_el = `phabs*zpcf*(zpo+pexrav+zgauss)` with $\Gamma = 1.9$. All the models include the Galactic absorption ($N_{\rm H} = 5.1 \times 10^{20}$ cm^{-2}).

emission line at $E_{\rm rf} = 6.84 \pm 0.11$ keV, a reflection component is found not to be statistically required.

3.5 Chandra stacked spectra

We inspected the *Chandra* stacked spectra to investigate the persistence of the features found in the *Chandra* single-image, single epoch data and how these compare to those in the XMM-*Newton* data. First, we produced the individual-image stacked spectra combining all the epochs (Sect. 3.5.1), then we combined all the images from all the epochs to obtain the final stacked spectrum (Sect. 3.5.2). All the spectra were combined through the CIAO tool `combine_spectra`, then grouped to obtain at least 20 cts/bin, and analyzed applying the χ^2 statistics. All the best-fit values for each tested model are summarized in Table 3.7.

3.5.1 Stacked spectra of the individual images

The single-image stacked spectra (total source time of 749 ks per image) of images B, C, and D show a similar number of counts in the 0.4–7 keV observed-energy band (5500 cts, 3975 cts, and 4766 cts, respectively), comparable to that of XMM 2002 and 2018, while for image A we obtain much better statistics (17700 cts). The analysis applied to these spectra follows the same logic used for the XMM-*Newton* data. In Fig. 3.10 we show the best-fit residuals to Model pl of the four stacked spectra. The best-fit values of the photon index are consistent across the four images (see Table 3.7). All images show hints of absorption in the soft-energy band but these appear to be more prominent in image A. Moreover, they all present signatures of strong emission lines between 5 and 7 keV. Interestingly, images A, B, and D show hints of a line around 6.4 keV, while for image C such a line seems to be placed at slightly lower energies ($\simeq 5.5$ keV). Hints of an absorption line at $\simeq 7.4$ keV seem to be present in images A and D but not in images B and C. Regarding the hard-energy end of the spectra, none show hints of reflection since residuals above 8 keV rest frame appear to be quite flat (although noisy).

We searched for an additional absorption component in each stacked spectrum through the same models used in Sect. 3.4 (Model pl_a and Model pl_pca). All four images require extra absorption and are best reproduced by a partial covering medium placed at the quasar's redshift (best-fit values in Table 3.7). By superposing the $\Gamma - N_{\rm H}$ contours, we find that the column density is consistent within 1σ errors for all the stacked images. In terms of photon index, $\Gamma_{\rm B}$, $\Gamma_{\rm C}$, and $\Gamma_{\rm D}$ are consistent within 1σ, while $\Gamma_{\rm A}$, being the steepest, is consistent with the others only within 2.6σ. Regarding the superposed $N_{\rm H} - {\rm CF}$ contours, the best-fit values to both the parameters are consistent within 1.6σ for all the four images. The best-fit residuals

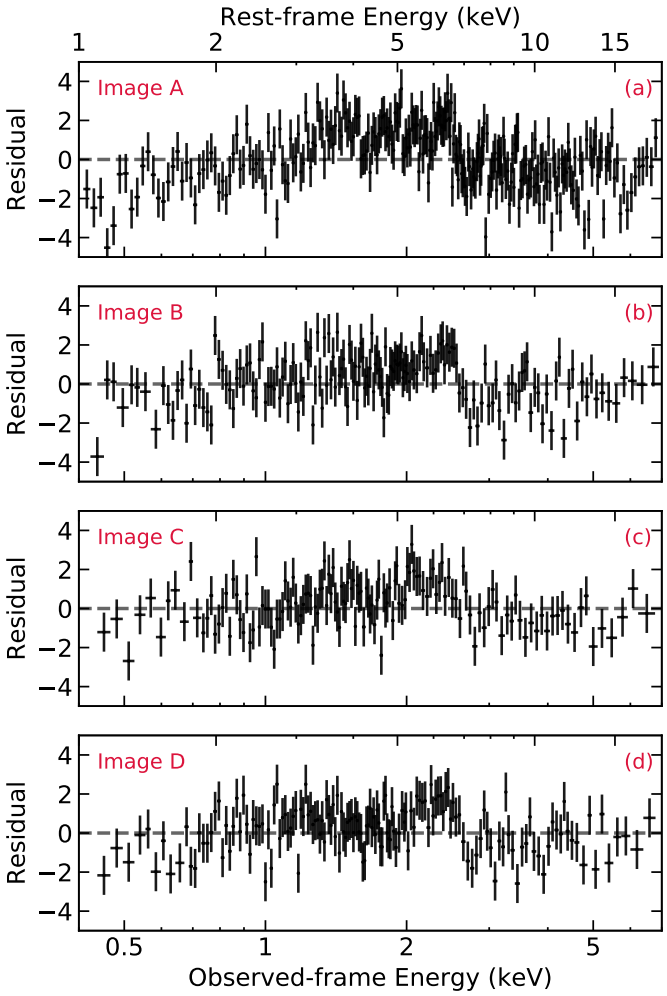

Figure 3.10: Rest-frame best-fit residuals of the individual-image stacked spectra to Model pl. From top to bottom: Residuals of image A, B, C, and D.

of each spectrum to Model pl_pca still show hints of the lines discussed above.

Images A, B, and D show a highly significant Fe Kα emission line between $\simeq$ 6.4–6.6 keV, which we first constrained as a narrow Gaussian component (Model pl_pca_el, Table 3.7). Regarding image C, we find a highly significant narrow line placed at lower energies ($\simeq$ 5.6 keV), while we only marginally detect the Fe Kα at 6.4 keV (see Table 3.7). Given the results obtained by Reynolds et al. (2014) over the combined spectra of all images from all epochs, we searched for broad emission lines in the single-image stacked spectra. When letting the width of these lines vary, the improvement in the goodness of the fit is highly significant only for image D ($\Delta\chi^2 = 11.0$ for $\Delta\nu = 1$), with new best-fit parameters $E_{\rm rf} = 6.28 \pm 0.20$ keV and $\sigma = 0.41^{+0.14}_{-0.18}$ keV. We marginally detect a broad emission line in image A (E $= 6.45 \pm 0.08$ keV, $\sigma = 0.16 \pm 0.09$ keV) and image B ($E_{\rm rf} = 6.18^{+0.43}_{-0.30}$ keV, $\sigma = 0.47^{+0.23}_{-0.35}$ keV), while for image C the data are best reproduced by a narrow

Table 3.7: Summary of the best-fit parameters of each model tested for the *Chandra* stacked spectra.

Model	Image	Γ	$N_{\rm H}$	CF	$E_{\rm el}$	$\sigma_{\rm el}$	$E_{\rm al}$	$\sigma_{\rm al}$	$\chi^2_{\rm r}$ (ν)
pl	A	1.67 ± 0.03	–	–	–	–	–	–	2.20 (260)
pl	B	1.64 ± 0.03	–	–	–	–	–	–	1.58 (166)
pl	C	1.64 ± 0.03	–	–	–	–	–	–	1.40 (138)
pl	D	1.62 ± 0.03	–	–	–	–	–	–	1.39 (153)
pl_pca	A	2.07 ± 0.06	$4.53^{+0.88}_{-0.85}$	0.59 ± 0.04	–	–	–	–	1.42 (258)
pl_pca	B	1.96 ± 0.10	$3.44^{+1.68}_{-1.49}$	0.55 ± 0.08	–	–	–	–	1.29 (164)
pl_pca	C	1.98 ± 0.14	$5.85^{+2.87}_{-2.73}$	0.51 ± 0.11	–	–	–	–	1.22 (136)
pl_pca	D	1.89 ± 0.10	$2.73^{+1.70}_{-1.48}$	0.53 ± 0.12	–	–	–	–	1.16 (151)
pl_pca_el	A	2.05 ± 0.06	$4.09^{+0.86}_{-0.82}$	0.58 ± 0.04	6.49 ± 0.08	< 0.01	–	–	1.28 (256)
pl_pca_el	B	1.95 ± 0.10	$3.04^{+1.58}_{-1.42}$	0.55 ± 0.08	$6.60^{+0.13}_{-0.22}$	< 0.01	–	–	1.20 (162)
pl_pca_el (1)	C	1.91 ± 0.14	$4.45^{+3.11}_{-2.97}$	$0.46^{+0.11}_{-0.14}$	5.56 ± 0.08	< 0.01	–	–	1.12 (134)
pl_pca_el (2)	C	1.95 ± 0.14	$5.08^{+2.90}_{-2.77}$	$0.49^{+0.10}_{-0.13}$	$6.37^{+0.20}_{-0.34}$	< 0.01	–	–	1.19 (134)
pl_pca_el	D	1.89 ± 0.10	$2.40^{+1.59}_{-1.41}$	$0.53^{+0.18}_{-0.11}$	$6.50^{+0.13}_{-0.23}$	< 0.01	–	–	1.07 (149)
pl_pca_bel	A	2.05 ± 0.06	3.93 ± 0.84	0.58 ± 0.04	6.45 ± 0.08	0.16 ± 0.08	–	–	1.27 (255)
pl_pca_bel	B	1.92 ± 0.10	$2.32^{+1.58}_{-1.45}$	$0.54^{+0.19}_{-0.11}$	$6.18^{+0.43}_{-0.30}$	$0.47^{+0.23}_{-0.35}$	–	–	1.17 (161)
pl_pca_bel	C	1.85 ± 0.13	$2.52^{+3.28}_{-2.20}$	$0.42_{-0.16}$	5.94 ± 0.23	$0.52^{0.24}_{-0.17}$	–	–	1.09 (133)
pl_pca_bel	D	1.88 ± 0.10	$1.90^{+1.50}_{-1.38}$	$0.54_{-0.13}$	6.28 ± 0.20	$0.41^{+0.14}_{-0.18}$	–	–	1.00 (148)
pl_pca_el_al	A	2.05 ± 0.06	4.18 ± 0.85	0.58 ± 0.04	6.49 ± 0.08	< 0.01	$7.26^{+0.19}_{-0.15}$	< 0.01	1.27 (254)
pl_pca_el_al	B	1.94 ± 0.10	$3.11^{+1.63}_{-1.46}$	0.54 ± 0.09	$6.60^{+0.14}_{-0.22}$	< 0.01	$7.49^{+0.19}_{-0.21}$	< 0.01	1.17 (160)
pl_pca_el_al	C	1.91 ± 0.14	$4.60^{3.20}_{-2.99}$	$0.45^{+0.11}_{-0.14}$	5.57 ± 0.08	< 0.01	$7.57^{+0.40}_{-0.22}$	< 0.01	1.12 (132)
pl_pca_el_al	D	1.87 ± 0.10	$2.43^{+1.63}_{-1.44}$	$0.53^{+0.17}_{-0.11}$	$6.50^{+0.13}_{-0.23}$	< 0.01	7.41 ± 0.17	< 0.01	1.04 (147)
pl_pca_el	A+B+D	1.99 ± 0.05	3.65 ± 0.69	0.54 ± 0.04	6.50 ± 0.06	> 0.01	–	–	1.27 (305)
pl_pca_bel	A+B+D	1.98 ± 0.05	3.36 ± 0.70	0.54 ± 0.04	$6.43^{+0.07}_{-0.26}$	$0.23^{+0.23}_{-0.08}$	–	–	1.21 (304)
pl	A+B+C+D	1.66 ± 0.02	–	–	–	–	–	–	2.48 (319)
pl_pca	A+B+C+D	2.00 ± 0.04	$4.43^{+0.71}_{-0.69}$	0.55 ± 0.03	–	–	–	–	1.53 (317)
pl_pca_el	A+B+C+D	1.99 ± 0.04	3.48 ± 0.68	0.52 ± 0.04	6.49 ± 0.07	< 0.01	–	–	1.32 (315)
pl_pca_el_al	A+B+C+D	1.98 ± 0.04	3.92 ± 0.69	0.53 ± 0.04	6.49 ± 0.07	< 0.01	7.43 ± 0.09	< 0.01	1.27 (313)
pl_pca_bel	A+B+C+D	1.95 ± 0.04	2.92 ± 0.70	0.51 ± 0.04	6.09 ± 0.14	0.52 ± 0.11	–	–	1.23 (314)
pl_pca_bel_al	A+B+C+D	1.94 ± 0.05	2.86 ± 0.73	0.50 ± 0.04	6.13 ± 0.14	$0.61^{+0.16}_{-0.13}$	7.36 ± 0.11	< 0.01	1.17 (312)
pl_pca_bel_bal	A+B+C+D	1.93 ± 0.05	2.84 ± 0.75	0.50 ± 0.04	$6.30^{+0.24}_{-0.20}$	0.73 ± 0.16	7.28 ± 0.10	$0.26^{+0.16}_{-0.11}$	1.15 (311)
pl_pca_bel_el_al	A+B+C+D	1.96 ± 0.04	3.26 ± 0.68	0.52 ± 0.04	6.44 ± 0.07	0.22 ± 0.07	7.42 ± 0.10	< 0.01	1.14 (310)
					5.62 ± 0.09	< 0.01			

Notes. Column 1: Model name; Col. 2: Combined images; Col. 3: Column density in excess of the Galactic value (units of 10^{22} cm^{-2}); Col. 4: Covering fraction of the extra absorption; Col. 5: Energy of the emission line (in units of keV); Col. 6: Width of the emission line (in units of keV); Col. 7: Energy of the absorption line (in units of keV); Col. 6: Width of the absorption line (in units of keV); Col. 7: Reduced χ^2 (degrees of freedom). All the errors are evaluated at 90% confidence. *Model list*: Model `pl`=`phabs*zpo`; Model `pl_pca`=`phabs*zpcf*zpo`; Model `pl_pca_el`=`phabs*zpcf*(zpo+zgauss)`; Model `pl_pca_el_al`=`phabs*zpcf*(zpo+zgauss+zgauss)`. When the width of the emission and absorption line is a free parameter of the model, it is reported as a bel/bal component in its name.

line. The resolved width found for the emission lines can be explained as follows. From the HSS (see Sect. 3.3.2), we know that the Fe Kα is probably microlensed, thus its energy likely varies from epoch to epoch at a fixed image. Detecting a broad, neutral Fe Kα line in the single-image stacked spectra can be interpreted as indicating that the most frequent effect is the microlensing of the Fe Kα line at energies near 6.4 keV, while those events producing more extreme energy shifts are more rare or less effective, as also shown in Chartas et al. (2016b) for RX J1131-1231.

The narrow absorption line is marginally detected (at 90%-99% confidence) at $E_{\rm rf} \simeq 7.3$–7.5 keV in the stacked spectra of image A, B, and D (best-fit parameters in Table 3.7). However, as the residuals in Fig. 3.10 suggest, it is not required for image C.

3.5.2 Stacked spectra of all images

The final stacked spectrum has a total exposure time of almost 3Ms and 32030 source net counts in the 0.4–7 keV observed-energy range. Its best-fit residuals to Model pl are shown in Fig. 3.11, panel a. As expected from the results in the previous section, we find evidence for absorption in the soft-energy band, a prominent emission line at $\simeq$6.5 keV that seems skewed at lower energies, and hints of an absorption line at $\simeq$7.4 keV. Adding a partial covering cold absorber significantly improves the quality

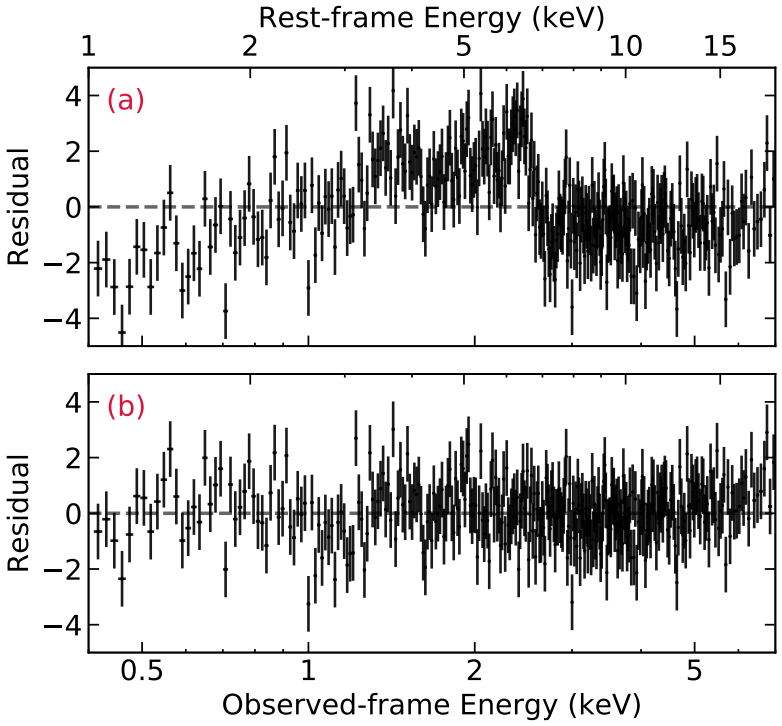

Figure 3.11: Best-fit residuals of the final *Chandra* spectrum to Model pl (*panel a*) and Model pl_pca_bel_el_al (*panel b*).

of the fit (see Table 3.7). The obtained best-fit parameters agree with those of the single images (see Sect. 3.5.1) and the residuals still show an excess at ≃6.5 keV and a deficit of counts at ≃7.4 keV. By adding two narrow Gaussian components to the model, we find a highly significant emission line at $E_{\rm rf} = 6.49 \pm 0.07$ keV ($\Delta\chi^2/\Delta\nu = 70/2$) and an absorption line at $E_{\rm rf} = 7.43 \pm 0.09$ keV ($\Delta\chi^2/\Delta\nu = 18/2$). However, the residuals still indicate the emission line to be skewed at lower energies, so we let its width vary (Model pl_pca_bel_al). We find a much better best fit ($\Delta\chi^2 = 32.3$, $\Delta\nu = 1$), with a broad emission line at $E_{\rm rf} = 6.13 \pm 0.14$ keV and $\sigma = 0.61^{+0.16}_{-0.13}$ keV. When also allowing the absorption-line width to vary (Model pl_pca_bel_bal), we find it significantly ($\Delta\chi^2 = 10.1$, $\Delta\nu = 1$) consistent with being broad ($\sigma = 0.26^{+0.16}_{-0.11}$ keV) and placed at $E_{\rm rf} = 7.28 \pm 0.10$ keV. This also changes the centroid and the width of the emission line, which become $E_{\rm rf} = 6.29^{+0.24}_{-0.20}$ keV and $\sigma = 0.72 \pm 0.16$ keV. However, the best-fit residuals of Model pl_pca_bel_bal indicate that the model is overestimating (underestimating) the data at energies lower (higher) than the best-fit centroid of the Fe Kα emission line. This could be the indication of a relativistically blurred Fe Kα line. In fact, the energy and width we find using Model pl_pca_bel_al are consistent with those found by Reynolds et al. (2014), which they interpret as a relativistically broadened line. If we exclude the absorption line from the model, we find the same skewed centroid energy and width as in the preliminary analysis done by Reynolds et al. (2014). However, based on the single-image stacked-spectra results, the width of the emission line could be artificially produced by the stacking, since the line in image C is placed at lower energies with regard to the other three (see Fig. 3.10). Thus, we produced a new stacked spectrum, combining all the epochs of only images A, B, and D. Considering the absorber and the emission feature (Model pl_pca_bel), we find that the line is less broad ($\sigma = 0.23^{+0.23}_{-0.08}$ keV) and, more importantly, its centroid is placed at higher energies ($E_{\rm rf} = 6.43^{+0.07}_{-0.26}$ keV). Moreover, constraining the width of the line to be lower than the CCD resolution or letting it vary freely make almost no difference on a statistical basis (see Table 3.7). Finally, if we compute the F-test significance for the addition of the width as a free parameter, we find that it is not required by the data. Thus, the skewed emission line at $\simeq$ 6.13 keV is most probably generated by the blending of two distinct lines.

Given the results obtained with the combined spectrum of images A+B+D and those from the individual-image stacked spectra, we tried to model the skewed emission line as a narrow component plus a broad component, the first at $\simeq$ 5.6 keV and the second at $\simeq$ 6.5 keV (Model pl_pca_bel_el). This produced a $\Delta\chi^2 = 17.1$ for two parameters of interest (compared to Model pl_pca_bel), which according to the F-test translates into a detection above 99.99% confidence of the narrow line placed at $E_{\rm rf} = 5.62 \pm 0.08$ keV. The broad Fe Kα is now detected at $E_{\rm rf} = 6.44 \pm 0.07$ keV with $\sigma = 0.22 \pm 0.07$ keV, which is inconsistent with

the centroid energy of the relativistically skewed line found by Reynolds et al. (2014) ($E_{\rm rf} = 6.58 \pm 0.03$ keV). We also detect the narrow absorption line at $E_{\rm rf} = 7.42 \pm 0.10$ keV (Model pl_pca_bel_el_al) at 99.8% confidence (from the F-test). This model also corresponds to the one that returns the best representation of the data, both on the basis of the distribution of the residuals (see Fig. 3.11, panel b) and in terms of statistical improvement. This result corroborates our statement of the skewed line being the blending of the two distinct lines seen in the individual-image staked spectra. Thus, when stacking the spectra of a gravitationally lensed quasar, checking the properties of each image is fundamental.

3.6 Discussion and results

We have presented the results obtained from the analysis of all the available X-ray data of the Einstein Cross (Q 2237+030), a quasar at $z = 1.695$ that is gravitationally lensed in four images by a foreground spiral galaxy. We analyzed 40 archival observations, 37 taken by *Chandra* and 3 by XMM-*Newton*, covering a period of 18 years, for a total of ~ 0.9 Ms.

From the *Chandra* data, we probed the source spectral variability, using the photon-index variations through the epochs as proxy. These are qualitatively consistent across the four images (i.e., intrinsic), which supports the assumption made by Chen et al. (2012), who linked the photon index across the images when fitting spectra extracted from the same observation. To assess the origin of such variability, we limited the analysis to the HSS, which is made up of the 14 spectra extracted from 11 observations that show the highest number of counts (above 500 cts in the 0.4–7 keV observed-frame energy range); this allowed us to better constrain the model parameters. We find that an additional cold absorber is definitely required (above 99% confidence) in four of the HSS spectra, corresponding to three different epochs. Moreover, the column density is consistent with being variable at more than 99% confidence between the epochs. Thus, the spectral variability is likely ascribed to a variable absorber placed at the quasar's redshift, but we cannot exclude the possibility that part of it could be produced by the variation of the source intrinsic power-law emission as well.

The XMM-*Newton* data are fundamental in investigating the need for extra absorption and the nature of the medium, given the much higher count statistics they provide. We find that the XMM 2002 data are consistent with a UFO scenario with $N_{\rm H} = 2.8^{+0.1}_{-0.1} \times 10^{23}$ cm^{-2}, $\log(\xi/{\rm erg\ s^{-1}cm}) = 2.5^{+0.1}_{-0.3}$ and $v_{\rm out} = 0.1 \pm 0.01c$, which explains the prominent absorption line at $E_{\rm rf} = 7.4 \pm 0.1$ keV. However, the same UFO cannot explain the second absorption line detected at ~ 11.8 keV, unless we assume it to be the indicator of a blueshifted Fe XXVI Lyα ($E_{\rm rf} = 6.97$ keV at rest) produced by an even faster component outflowing at $\sim 0.5c$. This would not

be the first UFO showing more than one outflow component and at such extremely high velocities (see, for instance, the case of APM 08279+5255, Chartas et al. 2009, and of HS1700+6416, Lanzuisi et al. 2012).

The rest-frame absorption-corrected 2–10 keV luminosity of Q2237 during the 2002 observation is $L_{2-10} \simeq 6.6 \times 10^{45}$ erg s^{-1}. Given a magnification factor of $\mu \approx 16$ (Schmidt et al. 1998), the intrinsic absorption-corrected luminosity is $L^{\rm int}_{2-10} \simeq 4.1 \times 10^{44}$ erg s^{-1}. From the UV luminosity $\log(\lambda L_\lambda/{\rm erg/s})_{1450} \simeq 45.53$ reported in Assef et al. (2011) and assuming a conversion factor of $\simeq 4$ (Richards et al. 2006), we find a bolometric luminosity of $L_{\rm bol} \simeq 1.4 \times 10^{46}$ erg s^{-1}. Based on Duras et al. (2020), the predicted 2–10 keV intrinsic luminosity would be $L^{\rm int}_{2-10} \simeq 4 \times 10^{44}$ erg s^{-1}, which is in good agreement with the one we measure. Assef et al. (2011) estimate the black hole mass $M_{\rm BH}$ from the Hβ broadening to be $\log(M_{\rm BH}/{\rm M}_\odot) = 9.08 \pm 0.39$, which leads to an Eddington luminosity of $L_{\rm Edd} \simeq 1.5 \times 10^{47}$ erg s^{-1} ($\lambda_{\rm Edd} \approx 0.1$).

Assuming the high significance of the outflow observed in XMM 2002 at $v_{\rm out} \simeq 0.1c$, we can derive the physical properties of the wind, by adopting standard 'prescriptions' (e.g., Tombesi et al. 2012; Crenshaw & Kraemer 2012) and including the uncertainties on the best-fit parameters, so to place this detection in a broader context and compare it with the measurements in other QSOs at $z \geq 1.5$ and in the local Universe. Following Crenshaw & Kraemer (2012), the mass-outflow rate can be obtained using the formula in Eq. 1.15. We conservatively assume the outflow to be detected at the minimum distance from the BH, where the observed velocity $v_{\rm out}$ equals the escape velocity from the BH potential well, thus $r_{\rm min}$ (see Eq. 1.16). We obtain $r_{\rm min} \approx 3.6 \times 10^{16}$ cm, which corresponds to $\simeq 100$ gravitational radii ($r_{\rm g} = {\rm G}M_{\rm BH}/c^2$); considering the uncertainties on $M_{\rm BH}$, we find for $r_{\rm min}$ the range $r_{\rm min} \approx (0.9 - 7) \times 10^{16}$ cm. Using $r = r_{\rm min}$ as the radial location of the outflow, we estimate the lower limit to the following quantities. The mass outflow rate, given all the assumptions above, turns out to be $\dot{M}_{\rm out} \approx 5$ M$_\odot$ yr^{-1}. Taking into account the 1σ uncertainties of the parameters, we find quite a wide range for the mass-outflow rate: $\dot{\rm M}_{\rm out} \sim (0.6 - 10.3)$ M$_\odot$ yr^{-1}. As a result, all the following quantities derived using $\dot{M}_{\rm out}$ will have likewise wide uncertainties. The outflow mechanical output (Eq. 1.13) is $\dot{E}_{\rm kin} = 1.5 \times 10^{45}$ erg s^{-1}, which corresponds to an outflow efficiency of $\dot{E}_{\rm kin}/L_{\rm bol} \approx 0.1$. We obtain an outflow momentum rate of $\dot{p}_{\rm out} = \dot{M}_{\rm out} v_{\rm out} \approx 9.9 \times 10^{35}$cm g s^{-2}, which is approximately twice the radiation pressure $\dot{p}_{\rm rad} = L_{\rm bol}/c$. Therefore, this UFO is consistent with generating efficient wind-driven AGN feedback that might indeed act on the evolution of the quasar host galaxy, given the $\dot{E}_{\rm kin}/L_{\rm bol} > 0.5\%$–$5\%$ threshold predicted by the models (e.g., Di Matteo et al. 2005; Hopkins & Elvis 2010). Moreover, since the outflow momentum rate is higher than $L_{\rm bol}/c$, magnetic forces might be playing a non-secondary role in accelerating this UFO. The derived wind parameters (column density, ion-

ization state, and outflow velocity) are consistent with those of UFOs in local AGN (Tombesi et al. 2010a) but the kinematic properties, albeit with wide uncertainties, seem to be higher than the average values for local objects (Tombesi et al. 2012). They are instead consistent with those of high-z AGN, for instance PID352 (Vignali et al. 2015, but see also the recent compilation by Chartas et al. 2021), a bright, unlensed source at $z \approx 1.6$ that shows a similar $L_{\rm bol}$ ($\sim 10^{46}$ erg s^{-1}). Furthermore, the properties of this UFO agree with the $v_{\rm out} - L_{\rm bol}$ and $L_{\rm bol} - \dot{E}_{\rm kin}$ relations in Fiore et al. (2017), computed for a compilation of local and (a small number of) high-redshift X-ray winds (see Figs. 1.5).

Interestingly, the XMM 2018 spectra do not show any absorption line in the hard band and seem to be best reproduced by a partially covering, mildly ionized absorber, with an ionization parameter of $\log(\xi/\mathrm{erg\ s^{-1}cm}) \leq 2.2$ (90% confidence limit). The intrinsic, absorption-corrected 2–10 keV luminosity for the 2018 observation is $L^{\rm int}_{2-10} \simeq 2.0 \times 10^{44}$ erg s^{-1}, approximately 49% of that found for the 2002 data. From the upper limit to the ionization state, we evaluated the lower limit to the absorber maximum distance from the central BH (being $\xi = L_{\rm X}/N_{\rm H} r_{\rm max}$): $r_{\rm max} \geq 4.7$ pc. Thus, it seems to be placed at a distance consistent with the typical range of the broad line region or the molecular torus (e.g., Jaffe et al. 2004; Burtscher et al. 2013; Hickox & Alexander 2018). Since accretion-disk winds are thought to have a global covering fraction less than unity, we propose a scenario where the wind has changed its direction with regard to the LOS and the disk between the two XMM observations, and part of the clouds contained within the molecular torus or the broad line region intercept the LOS during the second pointing. Given the short time elapsed, we think it is unlikely that the outflow has been totally suppressed between the two observations. Given that the *Chandra* observations were taken in between XMM 2002 and XMM 2018, we find that our statement is supported by the UFO signatures in the *Chandra* data. Moreover, the lowest timescale of the absorber variability obtained from *Chandra* HSS ($\simeq 0.3$ yrs rest frame) is linked to its distance from the central BH as $d \approx c\Delta t \approx 0.09$ pc, consistent with the innermost regions of the torus and of the broad line region, thus in agreement with the proposed scenario (e.g., Perola et al. 2002; Risaliti et al. 2009; Burtscher et al. 2013). However, the lower statistics of the *Chandra* spectra prevent us from modeling the detected absorption lines with a physically accurate wind model, that is, we are unable to investigate and constrain the presence of more complex absorbers than a neutral medium with the *Chandra* data.

In the *Chandra* HSS we find emission lines that span from ~ 2.2 to ~ 6.5 keV rest frame; following Dai et al. (2003) and Chartas et al. (2016b, 2017), this might be interpreted as microlensed and relativistic Fe Kα lines. Moreover, the energy range they cover is consistent with the energies of the redshifted Fe Kα emission lines found by Chartas et al. (2016b) in RX J1131-1231. Interestingly, the only highly

significant emission line is consistent with a regular Fe Kα line ($E_{\rm rf} = 6.47^{+0.11}_{-0.12}$ keV). Despite this fact, also this line seems to be microlensed since we do not detect it in the stacked spectrum of images B+C+D from the same observation. From a preliminary search for microlensing events in the *Chandra* multi-epoch light-curve ratios, there is no clear link among the observations in which we detect these emission lines and microlensing effects. In XMM 2018 we find a significant emission line at $\simeq 6.8$ keV that is inconsistent with being produced by the absorber, due to its ionization state. Even though a reflection component is not required by the data, such a line could be produced by a microlensing caustic that is crossing the inner regions of the accretion disk's approaching side. Such a microlensing event will lead to the magnification of blueshifted Fe Kα emission from a narrow inner region of the disk without magnifying the distant reflected continuum (Popović et al. 2006; Krawczynski & Chartas 2017; Krawczynski et al. 2019). The present data, however, do not allow us to verify either the presence of another highly ionized absorption component, since the data S/N is too low to constrain such a complex model, or the case of a microlensing event magnifying the inner regions of the accretion disk, since longer and less sparse *Chandra* monitoring would be required.

In the *Chandra* spectra, we detect, for the first time in this source, several blueshifted iron resonant absorption lines, with an overall significance slightly below 3σ. Interestingly, all the most significant lines ($> 99\%$ confidence level) of the HSS (Table 3.4) are grouped around the value of 11 keV and have energies consistent with the least significant (87% confidence level) feature of XMM 2002. If confirmed, they would imply a second and more extreme wind component with $v_{\rm out} \approx 0.3$–$0.5c$. Thus, the Einstein Cross could have experienced a multi-velocity UFO event, as found for other quasars, either nearby (e.g., PDS 456, Boissay-Malaquin et al. 2019; IRAS 00521–7054, Walton et al. 2019) or more distant (e.g., APM 08279+5255, Chartas et al. 2009).

To have a more complete picture of the X-ray features of Q2237, we also analyzed *i)* the *Chandra* single-image spectra, stacked over the 37 observations (749ks per image), and *ii)* the spatially integrated spectrum, stacking all the available *Chandra* data ($\simeq$3Ms total exposure). We find that a cold and partial covering absorber and primary X-ray emission are common to all the individual-image stacked spectra, although image A shows a slightly steeper photon index. This supports our previous result in which the absorber's column density was dominated by the in situ component (see Sect. 3.3). Regarding the narrow features, however, it is harder to provide a uniform description of the four spectra. On the one hand, image C is surely the most peculiar: while images A, B and D show a a highly significant Fe Kα emission line at energies $\simeq$ 6.4–6.6 keV with $\sigma \simeq 0.4$ keV, image C presents an emission line at $\simeq$5.6 keV (consistent with being narrow) and a marginally detected Fe Kα. On the other hand, the energies of the narrow Fe Kα from all the stacked images (also

that of the marginal detection in image C) are consistent within 1σ, and so they remain if we consider the energy of the broad lines. Regarding the absorption lines, we find hints of an absorption line at $\simeq 7.4$ keV in images A and D but not in images B and C. This further points to image C being the one showing the most different spectral features, superposed to a similar continuum.

The total spectrum of the source, obtained by integrating over the four images and stacking all the 37 analyzed *Chandra* exposures, gives us information about the persistence of the features seen in the single-image, single-epoch data and in the single-image, stacked spectra. First, we detect a broad Fe Kα line, with energy centroid and width consistent to those measured by Reynolds et al. (2014), who interpret such values as due to relativistic blurring. However, bearing in mind the peculiarity of the spectrum of image C, we also analyzed the combined spectrum of images A+B+D, which shows an emission line that is well consistent with a narrow (or not-so-broad, $\sigma < 0.4$ keV) Fe Kα emission line.

We conclude that the skewness of the Fe Kα emission line in the total *Chandra* spectrum is an artifact produced by the blending of two distinct lines, as seen in the individual-image stacked spectra. Moreover, even the broadening of the Fe Kα emission lines seen in the single-image, stacked spectra should be considered carefully. In fact, since we stacked a sizable number (37) of epochs, we should bear in mind that these broad emission lines could likely be produced by the combination of single-epoch microlensed Fe Kα, which we actually see in the single-image spectra (Sect. 3.3.2). In this sense, the differences in significance found between the four images are to be interpreted as the result of different microlensing events occurring in the respective image during the epochs. In conclusion, when stacking the single-image, single-epoch spectra of a GLQ, checking the spectral properties of each image through the epochs is fundamental to assess whether the observed phenomenon is actually intrinsic to the quasar or due to the lensing system.

Regarding the absorption lines, the spectral features of the stacked *Chandra* spectra confirm the presence of two distinct outflow components based on the following arguments. The absorption lines at higher energies ($\simeq$11.8 keV) of the single-epoch *Chandra* spectra are absent in the stacked spectra, whereas we detect (marginally or significantly) the absorption line at $\simeq$7.4 keV. The 11.8 keV features are probably associated with an outflow whose ionization state (i.e., as traced by the absorption line energy) varies more rapidly than that of the wind producing the 7.4 keV line. Thus, it indicates that the two winds are consistent with being launched at different radii with regard to the central engine, meaning the one associated with the 11.8 keV is produced closer to the BH. Moreover, this scenario would also agree with that proposed in Sect. 3.6 based on the significance of the two lines in XMM 2002. This would imply that the absence of lines in XMM 2018 is the indication that either both outflows are weak (in terms of velocity component along the line

of sight) or that the outermost is weak and the other is so extremely ionized that it becomes undetectable during the 2018 observation.

Given the large number of X-ray observations of Q2237, for the first time ever we can roughly evaluate the wind duty cycle for a single high-z source. However, almost two thirds of the dataset did not provide a S/N high enough to constrain the presence or absence of the narrow features. For this reason, we checked for any statistical systematic effect induced by the S/N of the selected data. First, we computed the upper-limit EW of the undetected absorption lines (i.e. detected below the 90% confidence level, those not listed in Table 3.4) in the HSS data and compared it with those of the lines in Table 3.4. We find that, at given S/N, the upper-limit EWs of the undetected lines are always lower than the 90% confidence lower limit of the EWs in Table 3.4. Second, we checked for any correlation between the significance of the lines and the S/N of the continuum emission close to the line (see Fig. 3.12). The confidence level of the detected lines decreases for increasing S/N and the most significant lines show the largest EWs and lie in spectra with lower S/N. We can thus rule out any statistical systematic effect in our results.

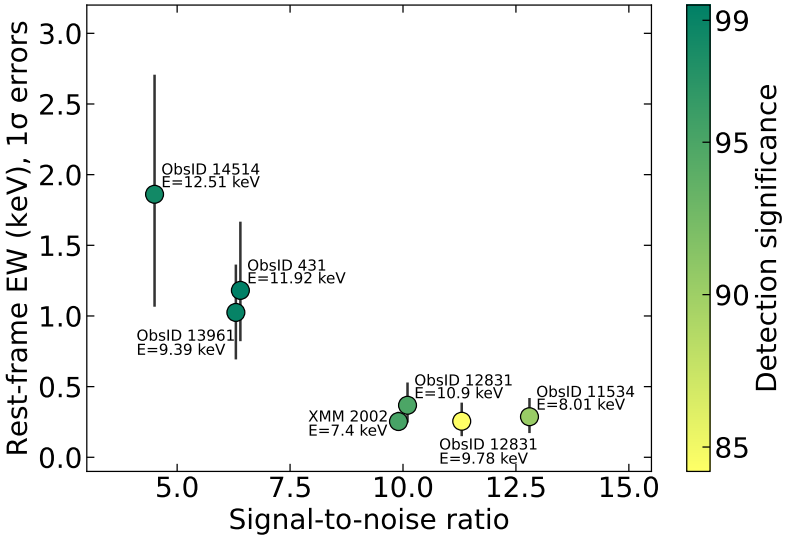

Figure 3.12: Rest-frame EW of detected absorption lines vs. S/N of data in the neighborhood of each line. Data are color-coded based on the significance of the line detection. Errors on the EW are given at the 1σ level.

In total, we detect UFO signatures at more than 90% confidence in 6 observations (5 from *Chandra*, 1 from XMM-*Newton*) out of the 13 analyzed to this purpose (11 from *Chandra*, 2 from XMM-*Newton*). Thus, we find the wind duty cycle to be $DC_{\rm w} \approx 0.46$ at 90% confidence. If we only consider those observations that show absorption lines at more than 95% confidence (3 from *Chandra*, 1 from XMM-*Newton*), the duty cycle turns out to be $DC_{\rm w} \approx 0.31$. Nonetheless, we cannot exclude the presence of UFO signatures that are too weak to be detected due to

the too low S/N of the HSS spectra showing the least number of counts. For this reason, our estimates of $DC_{\rm w}$ represent the wind-duty-cycle lower limit over the 13 observations that provide data with high-enough statistics. Although strictly related to the S/N of the spectra, our estimation of this parameter represents the best we are able to achieve with present-day data.

Chapter 4

The properties of the X-ray corona in the distant ($z = 3.91$) quasar APM 08279+5255

Part of the "feedback-unbiased" sample presented in Chapter 2 is also a very remarkable high-z AGN, APM 08279+5255 (hereafter, APM 08279). Its *Chandra* and XMM-*Newton* observations prior to 2008 are presented in Chartas et al. (2009) and, as such, were excluded from the data sample we present in Sect. 2.1 but are part of our analysis of the properties of high-z UFOs outlined in Sect. 2.2. However, new XMM-*Newton* and *NuSTAR* data were taken in 2019 that we did not include in the mentioned studies, since they deserved a dedicated analysis presented in Bertola et al. (2022), on which the present Chapter is broadly based.

4.1 Introduction

One of the most studied high-z quasars is APM 08279 ($z = 3.91$; Irwin et al. 1989) is a BAL quasar lensed in three images by an as-yet-undetected foreground galaxy, possibly set at $z = 1.06$ (Ellison et al. 2004). Due to the lensing-system uncertainty, different models predict very different magnification values, ranging from $\mu_{\rm L} = 4$ (Riechers et al. 2009) to $\mu_{\rm L} = 100$ (Egami et al. 2000). Regardless of the actual magnification factor, APM 08279 is among the brightest high-z AGN in many bands, with one of the best sampled high-z spectral energy distributions (SEDs; e.g., Stacey et al. 2018; Leung et al. 2019). In fact, APM 08279 is a very well known quasar in many astrophysical research fields, ranging from one of the best characterized high-z interstellar mediums (in the atomic, ionized and molecular phase; e.g., Weiß et al. 2007; Bradford et al. 2011; van der Werf et al. 2011; Walter et al. 2011; Decarli et al. 2012), to the first high-z SMBH mass estimate from reverberation mapping of the Si IV and C IV emission lines (of Saturni et al. 2016), to AGN feedback, seen in both the highly-ionized (Hasinger et al. 2002, hereafter H02, Chartas et al. 2002,

2009, hereafter C09, Saez et al. 2009; Saez & Chartas 2011; Hagino et al. 2017) and molecular gas phase (Feruglio et al. 2017). APM 08279 is also a very peculiar source for UFOs and, as such, is often used as benchmark to test wind models (e.g., Fukumura et al. 2010; Luminari et al. 2021). In fact, APM 08279 was the first high-z source in which UFOs were detected (Chartas et al. 2002) and it was later found to host some of the fastest X-ray winds ever seen ($v_{\rm out}$ up to $0.76c$, C09). However, the most remarkable feature of APM 08279 is the double-velocity UFO present in all the observations up to early 2008 (C09; Saez et al. 2009), except for its first X-ray exposure (H02).

We present in this Chapter the first X-ray broadband analysis of APM 08279, making use of the latest XMM-*Newton* observations followed up by the first ever *NuSTAR* exposures of this source (2019, PI: G. Lanzuisi). The Chapter is organized as follows: reduction and analysis of the 2019 observations are discussed in Sects. 4.2–4.3. Our results are then compared to previous *Chandra* and XMM-*Newton* observations, which we re-analyzed, in Sect. 4.4. We then place the observed X-ray corona properties in a broader context in Sect. 4.5.

Table 4.1: Log of APM 08279+5255 observations from 2019

Observation	ObsID	Date	Net Exposure (ks)	f_{2-10}
XMM 101	0830480101	2019 *Mar* 24	24.1	$2.9^{+0.1}_{-0.3}$
Nu02	60401017002	2019 *Apr* 19	93.5 | 92.8	$2.8^{+0.2}_{-0.4}$ | $3.2^{+0.3}_{-0.4}$
Nu04	60401017004	2019 *Apr* 22	59.7 | 59.2	$2.6^{+0.4}_{-0.4}$ | $3.4^{+0.3}_{-0.6}$
XMM 301	0830480301	2019 *Apr* 23	24.5 | 28.2 | 25.7	$2.3^{+0.1}_{-0.2}$ | $2.4^{+0.1}_{-0.3}$ | $2.5^{+0.2}_{-0.3}$

Notes. Values of XMM 101 refer to EPIC-pn only; values of XMM 301 refer to EPIC-pn, -M1, -M2 respectively; values of *NuSTAR* refer to FPMA, FPMB, respectively. Observed-band 2–10 keV absorbed flux (10^{-13} erg cm^{-2} s^{-1}, errors at 90% confidence level) is estimated using `acutpl` model. Net exposure: exposure time after cleaning the event file from flare events.

4.2 Data reduction

APM 08279 was observed by XMM-*Newton* on 2019 *March* 24 for 31.4 ks (hereafter, XMM 101). On that date, EPIC-MOS cameras failed, thus it was observed again on 2019 *April* 23 for additional 33.3 ks (hereafter, XMM 301). These exposures were followed up by *NuSTAR* on 2019 *April* 19 for 93.5 ks (hereafter, Nu02) and on 2019 *April* 22 for 59.7 ks (hereafter, Nu04). The observation log is shown in Table 4.1.

XMM-*Newton* data were reduced applying standard procedure and the latest calibration files through SAS v.18.0. The event files of EPIC-pn cameras were filtered at 1.2 and 1.0 counts per second in the 10–12 keV band, for XMM 101 and 301, respectively, while those of XMM 301 EPIC-MOS cameras were filtered at 0.3 counts

per second, in the same band. EPIC-pn source spectra were extracted from circular regions of 25″ radii for both XMM 101 and 301 ($\simeq$ 80% encircled energy fraction); EPIC-MOS source spectra were extracted using 20″-radius circles ($\simeq$ 75% encircled energy fraction). Background spectra were extracted from circular regions of 60″ radii for each XMM-*Newton* camera. Wider source regions, coupled with different GTI filtering thresholds and other background extraction regions, were tested. No significant improvement of the spectral S/N was yielded, therefore, we stuck to the filtering and spectra extraction setup just described (i.e., source regions encircling the PSF core).

NuSTAR observations were processed using the standard pipeline of *NuSTAR* Data Analysis Software package (NuSTARDAS) v.2.0.0 (within Heasoft v.6.28) and calibrated with *NuSTAR* CALDB v.20200813. No significant background flares are present in these observations – a fact that we checked through the IDL script `nustar_filter_lightcurve`*. After testing different extraction regions to find the ones yielding the best S/N, we selected 40″-radius circles for the source ($\simeq$ 60% encircled energy fraction). These were coupled to annular background regions, centered on the target, with inner (outer) radii of 110″(170″) to exclude the wings of the source PSF and sample the non-uniform local background. This extraction setup was used for both FPMA and FPMB in each observation. Unfortunately, APM 08279 turned out to be fainter than expected based on past observations (as described in Sect. 4.4). Thus, during these exposures, source spectra are background dominated above $15 - 20$ keV regardless of the reduction and spectra-extraction setup.

4.3 Spectral analysis of 2019 data

Having checked that no significant intra-observation flux variability is present, we fit the time-averaged spectra with *Xspec* v.12.11.1. EPIC-pn data belong to the high-statistics regime, whereas EPIC-MOS and *NuSTAR* spectra to the mid-to-low-statistics regime ($\simeq$600 and 300 net counts, respectively). We grouped our data to 1 count/bin and applied C-statistics (Cash 1979) because matching the requirements to use the χ^2 statistics (at least 20 cts/bin) would have led to a loss in the energy resolution of *NuSTAR* and EPIC-MOS due to the coarse binning. Nevertheless, we also tested our models on spectra grouped at 20 cts/bin using χ^2 statistics as a sanity check and found results consistent to those presented here.

XMM 301 and the two *NuSTAR* observations are almost simultaneous, while XMM 101 was taken 30 days before XMM 301. No significant spectral variability is present between the two XMM-*Newton* epochs†. Thus, we fit spectra from the

*https://github.com/NuSTAR/nustar-idl

†The ratio of the two EPIC-pn spectra shows no evident trend and is well consistent with being constant.

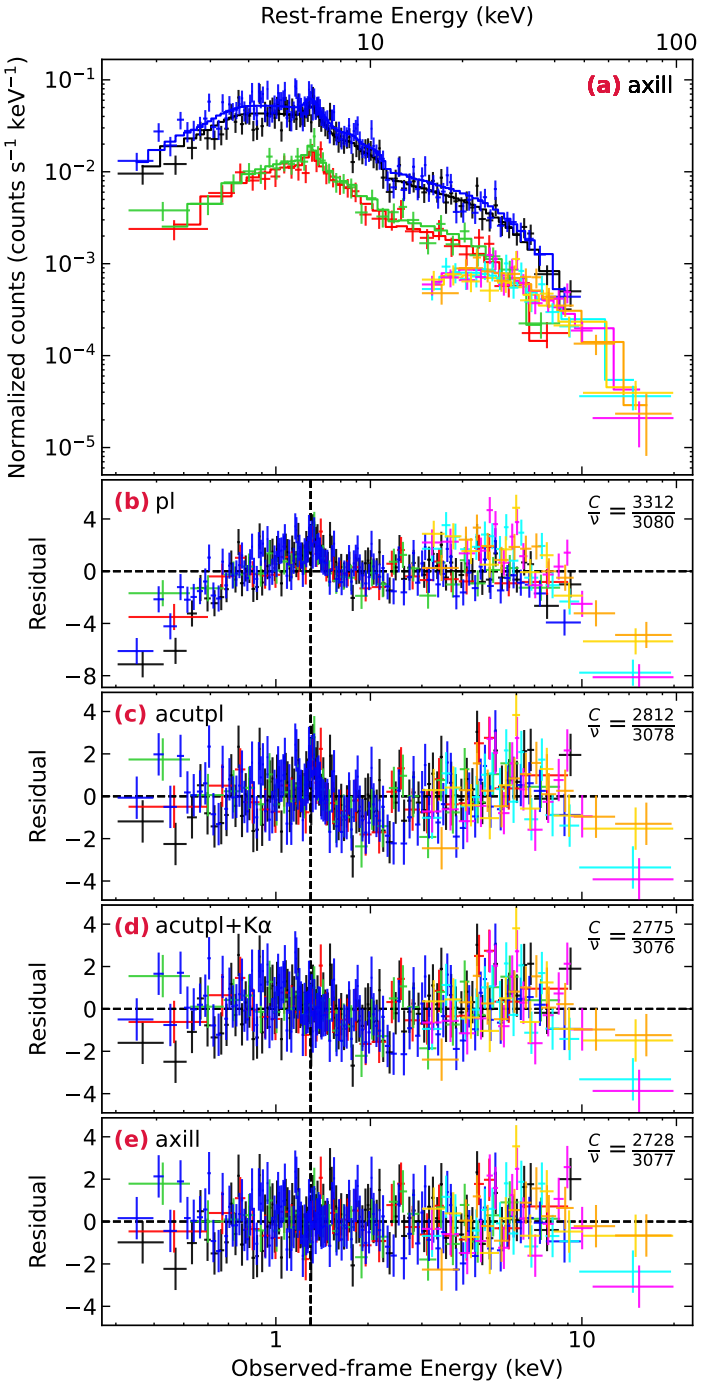

Figure 4.1: Broadband X-ray spectra of APM 08279 collected by XMM-*Newton* and *NuSTAR* in 2019. Panel (a): Observed-frame spectra and best-fit model (axill model). Panels from (b) to (e): Observed-frame residuals. Vertical black dashed lines mark the energy of the Fe Kα emission line. Spectra in each panel were rebinned to 4σ (with setplot rebin 4 100 in Xspec) for showing purposes. Data are color-coded as follows: XMM 301 EPIC-pn is shown in black, XMM 301 EPIC-MOS1 in red, XMM 301 EPIC-MOS2 in green, XMM 101 EPIC-pn in blue, Nu02 FPMA in cyan and FPMB in magenta, Nu04 FMPA in yellow, and FPMB in orange. Models from top to bottom: (a) axill model, (b) pl model, (c) acutpl model, (d) acutpl+Kα model, (e) axill model, all modified by Galactic absorption ($N_{\rm H} = 4.2 \times 10^{20}\,{\rm cm}^{-2}$). Best-fit parameters are summarized in Table 4.2.

four epochs together by linking all parameters, if not said otherwise, letting cross-calibration constants free to vary. Throughout the Chapter, all models are modified by Galactic absorption ($N_{\rm H} = 4.2 \times 10^{20}\,{\rm cm}^{-2}$, HI4PI Collaboration et al. 2016) and errors and upper limits are given at 90% confidence level, unless otherwise stated.

4.3.1 Broadband X-ray spectra

The joint fit of XMM-*Newton* and *NuSTAR* data allows us to model the broadband-band continuum of APM 08279 in the 0.3–20 keV observed-frame energy range (i.e., ∼1.5–98 keV rest-frame energy range). The spectra present a cutoff at hard energies and soft absorption in excess of the Galactic value, which are clearly visible in the residuals against a single power-law model (`pl` Model; see Fig. 4.1, panel (b)). In fact, a `zphabs*zcutoffpl` model[‡] (hereafter, `acutpl` model; Fig. 4.1, panel (c)) well reproduces both features in statistical terms, but yields a power law that is considerably harder ($\Gamma \simeq 1.3$) than expected values for an AGN (e.g., Vignali et al. 1999; Piconcelli et al. 2005; Just et al. 2007) and a very low high-energy cutoff ($E_{\rm cut} \simeq 34\,{\rm keV}$). Absorption in the soft band is due to a "cold" medium placed at the systemic redshift of the source, with a column density consistent with previous observations (H02; C09). For the rest of the analysis, our models include this additional absorption component. The data clearly present a prominent Fe Kα emission line, detected at $E_{\rm rest} = 6.5 \pm 0.1$ keV ($E_{\rm obs} \simeq 1.3$ keV) as a highly-significant ($\Delta Cstat/\Delta\nu = 37/2$) narrow line[§] on top of an `acutpl` continuum in both XMM-*Newton* observations. Therefore, we tie the Fe Kα line component between the two epochs.

An `acutpl`+Kα model fails to fit the high-energy bump (Fig. 4.1, panel (d)) which, combined with the low photon index and high Fe Kα equivalent width (EW; rest-frame EW $= 318^{+94}_{-90}$ eV) can be evidence for X-ray reflection. We tested this scenario through the non-relativistic reflection model `xillver`, part of the `relxill` package (García et al. 2014; Dauser et al. 2014), which accounts for a direct cutoff power law and its reprocessed emission (continuum and self-consistent emission and absorption features) by a distant, (possibly ionized) medium. Reflection is parameterized through photon index, Γ; high-energy cutoff, $E_{\rm cut}$; iron abundance (that we set to Solar); ionization of the disk, $\log \xi$[¶]; inclination angle, i; and reflection fraction, R[‖]. Low inclination angles return a better fit and are naturally preferred

[‡]The `zcutoffpl` component in *Xspec* models a power law with an exponential cutoff at energies higher than $E_{\rm cut}$, which is a parameter of the model.

[§]The line width is visually resolved, but letting this parameter free to vary yields no statistical improvement ($\Delta Cstat/\Delta\nu = 1/1$). Moreover, the best-fit line width is consistent with being narrow both based on its face value ($\sigma = 0.15$ keV) and its 90% confidence range ($\sigma < 0.7$ keV) in the rest frame. We thus set the rest-frame width of the Fe Kα line to $\sigma = 0.1$ keV.

[¶]See definition in Sect. 1.2.2.

[‖]See definition in Sect. 3.4.1.

Table 4.2: Summary of the best-fit parameters of each model tested on 2019 data.

Model	Γ	$N_{\rm H}$	$E_{\rm cut}$	$E_{\rm Fe\,K\alpha}$	$EW_{\rm Fe\,K\alpha}$	R	Cstat (ν)
(1)	(2)	(3)	(4)	(5)	(6)	(7)	(8)
pl	1.35 ± 0.03	–	–	–	–	–	3312 (3080)
acutpl	1.3 ± 0.1	4.7 ± 0.8	36^{+10}_{-7}	–	–	–	2812 (3078)
acutpl+Kα	1.2 ± 0.1	3.9 ± 0.8	33^{+8}_{-6}	6.5 ± 0.1	318^{+94}_{-90}	–	2775 (3076)
axill	$2.1^{+0.1}_{-0.2}$	6.4 ± 0.8	99^{+91}_{-35}	–	–	$2.8^{+1.1}_{-0.9}$	2728 (3077)

Notes. Column 1: Model name; Col. 2: Photon index; Col. 3: Column density in excess of the Galactic value (units of 10^{22} cm^{-2}); Col. 4: High-energy cutoff rest-frame energy (keV); Cols. 5-6: Rest-frame energy (keV) and equivalent width (eV) of Fe Kα emission line; Col. 7: Reflection fraction; Col. 8: *Cstat* (degrees of freedom ν). The line width of the Fe Kα is set to $\sigma = 0.1$ keV rest frame. All errors are computed at the 90% confidence level for one parameter of interest. *Model list*: Model pl = `phabs*zphabs*zpo`; Model acutpl = `phabs*zphabs*zcutoffpl`; Model acutpl+Kα = `phabs*zphabs*(zcutoffpl+zgauss)`; Model arefl+Kα = `phabs*zphabs*(pexrav+zgauss)`; Model axill = `phabs*zphabs*xillver`. All models include Galactic absorption ($N_{\rm H} = 4.2 \times 10^{20}$ cm^{-2}).

by the data when the parameter is set free to vary; however, the photon statistics prevents us from actually constraining it, thus we set $i = 30°$. Similarly, we first leave the ionization of the disk free to vary and then freeze its value to its best fit ($\log(\xi/\mathrm{erg\ s^{-1}\ cm}) = 1.7$). By the inclusion of the reflection continuum (axill model), we find a better representation of our broadband spectra, both statistically ($\Delta Cstat = 47$ for one additional parameter; see confidence contours in Fig. 4.2) and physically (see Table 4.2). The power-law photon index ($\Gamma = 2.1^{+0.1}_{-0.2}$) agrees with typical values of high-z sources (e.g., Vignali et al. 2005; Just et al. 2007) and so does the high-energy cutoff ($E_{\rm cut} = 99^{+91}_{-35}$ keV) with the few other measurements available at $z > 1$ (Lanzuisi et al. 2016; Dadina et al. 2016; L19). The yielded reflection fraction ($R = 2.8^{+1.1}_{-0.9}$) carries the information that the reflecting material is seeing a source primary emission that is much larger than the one reaching the observer. Two of the possible explanations for such a large value of R are *i)* pc-scale reflection in which the primary source activity has dropped (and so has the direct emission seen by the observer), whereas the reflector is still illuminated by the echo of the previous stronger source emission due to the travel-time delay (e.g., Lanzuisi et al. 2016); *ii)* disc reflection in a lamp-post geometry, where the corona height is low and thus light-bending is severe (e.g., Gandhi et al. 2007).

4.3.2 Search for UFO imprints

With its persistent double-velocity component X-ray wind (C09), APM 08279 is a one-of-a-kind object for studying UFOs in high-z AGN. However, 2019 data (see Fig. 4.1) appear not to show the prominent and broad features previously seen in this source. We thus searched our spectra only for narrow ($\sigma = 0.1$ keV, rest-frame)

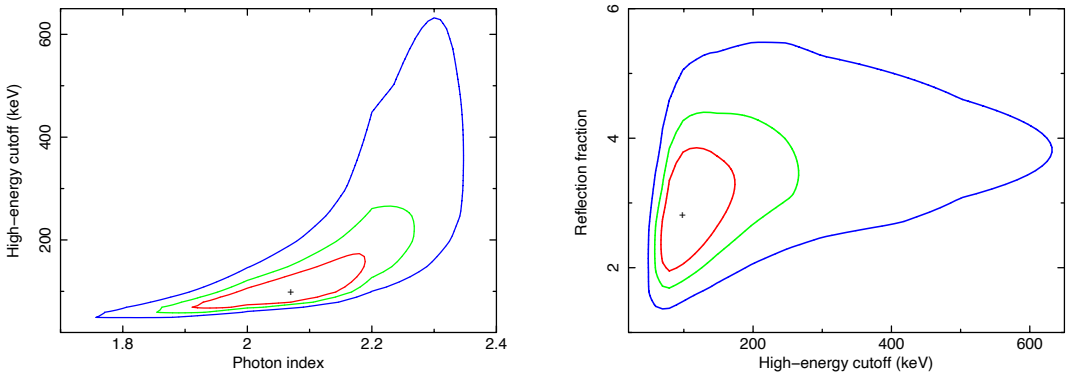

Figure 4.2: Confidence contours of reflection parameters obtained with an `xillver` model (see Sect. 4.3.1 and Table 4.2). *Left* High-energy cutoff vs. photon index. *Right:* Reflection fraction vs. high-energy cutoff. Contours are color-coded as follows: red, green, blue for 68%, 90%, 99% confidence level, respectively.

emission and absorption features. We applied the blind method of Miniutti & Fabian (2006), as implemented in Cappi et al. (2009) and Tombesi et al. (2010a) (but see also Chapter 3, Sect. 3.3.2). We considered the energy range spanned by past UFO events in APM 08279 ($E \simeq 7 - 14$ keV) using the `xillver` best fit as baseline model, also including the *NuSTAR* spectra to correctly model the broadband continuum. We then tested our data including `zgauss` components where the blind search and the residuals to model `xillver` (Fig. 4.1, panel (e)) showed hints of absorption lines.

XMM 301 presents no signs of emission or absorption features additional to those already included in `xillver`, while XMM 101 shows hints of a narrow absorption line at $E_{\rm rest} = 11.7 \pm 0.2$ keV ($\Delta Cstat/\Delta\nu = 9/2$, rest-frame width set to 0.1 keV). We ran Monte Carlo simulations (Protassov et al. 2002) to measure the real significance of the 11 keV line, by simulating 10^4 broadband spectra from our `xillver` best fit model (see Table 4.2) using the `fakeit` function of `Xspec`. By searching the simulated spectra for the detection of spurious emission and absorption lines, we built the posterior probability distribution of finding a real detection. Applying such a distribution to the line at 11.7 keV in XMM 101, we find that its significance is lower than the 90% confidence level. Thus, we find that no UFO features are present in the latest X-ray data of APM 08279.

4.4 X-ray reflection in previous observations

During 2019 exposures, APM 08279 turned out to be fainter than what was previously expected (see Fig. 4.3, upper panel, and Tables 4.1 and 4.3), and clearly showed X-ray reflection signatures for the first time. We thus collected all previous XMM-*Newton* and *Chandra* X-ray observations with the aim of answering the fol-

lowing questions: namely, whether X-ray reflection was already in place before 2019 and, thus, how that would relate to what was observed in 2019.

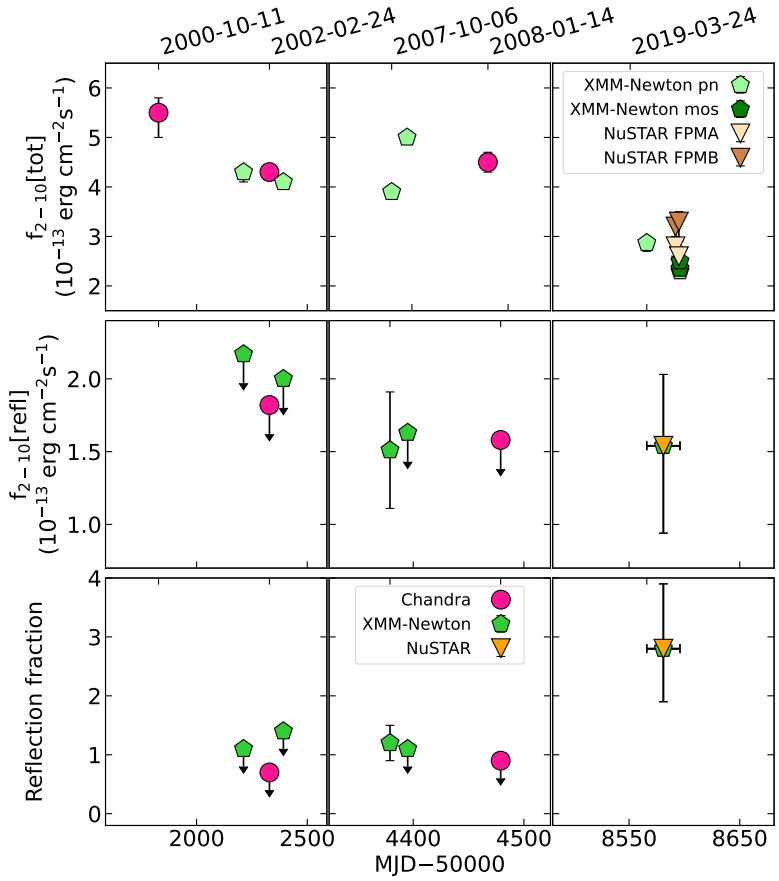

Figure 4.3: Variation of 2–10 keV observed-band total source flux (top panel), 2–10 keV observed-band flux of the reflection component alone (middle panel) and reflection fraction R (bottom panel), of *Chandra* (magenta circles), XMM-*Newton* (light, dark and medium green pentagons for EPIC pn, EPIC MOS, and EPIC pn+MOS, respectively) and *NuSTAR* (ivory, brown, orange triangles for FPMA, FPMB, and FPMA+FPMB, respectively) data from year 2000 to 2019. Top axis shows the dates, bottom axis the modified Julian dates. *Top panel*: Values up to 2009 are taken from C09, the first two points are evaluated from re-analyzed data. Errors are given at 68% confidence, as in C09. When they are not visible, errorbars are smaller than the point size. *Middle panel*: Upper limits are computed using the 90% upper limit of the reflection fraction. *Bottom panel*: Upper limits are computed at 90% confidence level. The first *Chandra* observation (i.e., the shortest one – see main text) is left out due to the low count statistics.

By referring to literature studies (H02; C09), we left out of the data sample the first *Chandra* exposure, the shortest one, because of the low count statistics. Table 4.3 summarizes the relevant information about archival observations, including the acronyms that we use to indicate them. We refer to H02 for the analysis of XMM1

and to C09 for the remaining five (CXO2, XMM2, XMM3, XMM4, CXO3). We reduced the selected *Chandra* (CXO2, CXO3) and XMM-*Newton* (XMM1, XMM2, XMM3, XMM4) archival exposures to uniformly apply the latest calibration files, filtering high-background intervals in XMM-*Newton* data using the same GTI thresholds of C09. The count statistics of these spectra is much higher than that of 2019 data, thanks to the higher flux of APM 08279 and to the longer exposures. Similarly to the approach of C09, spectra with more than 10^4 cts were grouped to 100 cts/bin (EPIC-pn data of XMM2, XMM3, XMM4), while those with few 10^3 cts to 20 cts/bin (XMM1 EPIC-pn, all EPIC-MOS and *Chandra* spectra). We thus applied χ^2 statistics in the spectral analysis of past observations, jointly fitting EPIC-pn and -MOS spectra collected in the same epoch.

Table 4.3: Log of APM 08279+5255 past observations and reflection parameters

Name	ObsID	Date	MJD	Total Exp.	f_{2-10}	Ref.	R
CXO1	1643	2000 Oct 11	51828	9.1	$5.5^{+0.3}_{-0.5}$	a	–
XMM1	0092800101	2001 Oct 30	52212	16.5	$4.3^{+0.1}_{-0.2}$	a	< 1.1
CXO2	2979	2002 Feb 24	52329	88.8	$4.3^{+0.1}_{-0.1}$	b	< 0.7
XMM2	0092800201	2002 Apr 28	52392	102.3	$4.1^{+0.1}_{-0.1}$	a, b	< 1.4
XMM3	0502220201	2007 Oct 06	54379	89.6	$3.9^{+0.1}_{-0.1}$	b	$1.2^{+0.3}_{-0.3}$
XMM4	0502220301	2007 Oct 22	54395	90.5	$5.0^{+0.1}_{-0.1}$	b	< 1.1
CXO3	7684	2008 Jan 14	54479	88.1	$4.5^{+0.2}_{-0.2}$	b	< 0.9

Notes. Absorbed fluxes are estimated in the 2–10 keV observed-band from phenomenological models, and are given in units of 10^{-13} erg cm^{-2}s^{-1}, with errors given at 68% confidence level. The absorbed flux of CXO1 and XMM1 is evaluated from reanalyzed data (see Sect. 4.4), while the other values are taken from the literature (references: a. H02, b. C09). The total exposure is given in units of ks. The reflection fraction is obtained using lit_xill model), i.e. a `zphabs*zedge*xillver` model for XMM1 and a `zphabs*(xillver+zgauss+zgauss)` model for the other data. Values for the absorber, the edge and the absorption lines are set to the best fit of H02 and C09. Errors and upper limits on the reflection fraction are given at the 90% confidence level.

To probe the X-ray reflection, we first drew on the best-fit models from the literature. H02 fit XMM1 data with an absorption edge, whereas C09 fit the spectra firstly using phenomenological models, where the UFOs are modeled only through their main absorption imprint, and secondly using *Xstar* analytical models (`warmabs`). Testing X-ray reflection while already accounting for UFOs through `warmabs` is a non-trivial exercise, so we selected the phenomenological representation of past data (Model 6, C09). We then tested the X-ray reflection by replacing the single power-law emission of literature phenomenological best-fit models with a `xillver` component (lit_xill model). We set the absorption-edge parameters in XMM1 to those reported by H02. Both energy and width of the UFO absorption lines are set to those presented in C09 and we leave their normalization free to vary. The lack of

high-energy coverage in past observations prevents us from constraining the high-energy cutoff. We thus set it to the value measured in 2019 data ($E_{\rm cut} = 100$ keV), safely far from the high-energy end of *Chandra* and XMM-*Newton* spectra. We also set the reflection inclination angle to $i = 30°$, as done in Sect. 4.3.1, and assume a low-ionization reflecting medium as found for 2019 data ($\log(\xi/\mathrm{erg\ s^{-1}\ cm}) = 1.7$).

We investigated the evolution of the source emission through the epochs using three probes: *i)* the 2–10 keV observed-band total source flux, *ii)* the 2–10 keV observed-band flux of the reflection component only, and *iii)* the reflection fraction R. To measure probe *ii)*, we built a pure-reflection model using `xillver` with $R = -1$[**], setting its normalization to the best-fit value of the respective lit_xill model scaled by the measured reflection fraction. When R is only constrained as an upper limit, we derived an upper limit to the 2–10 keV observed-band reflection flux. When R is constrained (as is for XMM3 and 2019 data), we measured the reflection flux by scaling the normalization of the lit_xill model by the best fit value of R. We then assigned as uncertainty the spread in flux obtained by scaling the normalization by the respective upper and lower 90% confidence level values of R. Figure 4.3 shows the evolution of the three probes across the considered observing epochs. The source X-ray flux (upper panel) presents a factor of 1.5 decrease between the period 2000–2008 and 2019 while, despite the many upper limits, the reflection flux (middle panel) is fully consistent with showing no trend across the years. The 2–10 keV observed-energy band corresponds to $\simeq 9.8-49$ keV in the $z = 3.91$ rest-frame, which is where X-ray reflection induces the so-called "reflection hump" and where flux suppression by absorption is strong only in Compton-thick AGN (e.g., Maiolino et al. 1998; Bassani et al. 1999; Matt et al. 2000). Regarding the obscuration hypothesis, we find no evolution in the column density of the low-ionization absorber; the one measured in 2019 data (see Sect. 4.3.1 and Table 4.2) is consistent with results from the literature (H02; C09). As a consequence, the reduction in flux must be ascribed to a decrease of the source primary activity. The trend (or lack of it) in the first two panels of Fig. 4.3 is indeed well matched by the evolution of R (lower panel) which, despite the large uncertainties, shows a discontinuity between 2019 and epochs prior to 2008. Coupling the three probes together suggests that the reflection component seen in 2019 data was likely already in place before 2008, but less evident due to a stronger primary continuum. Lastly, we performed a sanity check through the EW of the Fe Kα measured through a `zgauss` component on top of a `pexrav` continuum, given the impossibility of decoupling Fe Kα line and continuum with `xillver`. The Fe Kα EW follows the same trend as the reflection fraction (relatively steady value before 2008, sharp increase in 2019), thus supporting our interpretation.

In this scenario, the reflection component observed in 2019 can possibly be inter-

[**]Setting $R = -1$ forces the reflection model `xillver` to only model the reflected emission instead of direct and reflected continuum.

preted as the echo of APM 08279 previous activity, due to *i)* the time delay between the X-ray source and the reflector and *ii)* the reduced direct emission observed in the last epoch. This is similar to the case of PG 1247+267: Lanzuisi et al. (2016) explain its very high reflection fraction in terms of X-ray source variability, namely, the primary emission has dropped but the reflection still has not due to the additional light-travel path. Using the same argument, we can place a lower limit on the distance between reflector and X-ray corona, assuming that the variability during the 2008–2019 observational gap is only ascribed to a uniform decrease in the activity of the X-ray corona. We consider the time elapsed between CXO3 and XMM 101 ($\Delta t = 832.4$ d in the quasar rest frame) as that corresponding to the light travel path between X-ray source and reflector ($r_{\rm refl} = c\Delta t$). Under this assumption, we derive the lower limit to the reflector location as $r_{\rm refl} \gtrsim 0.7$ pc (in accordance to the lower limit obtained from the Fe Kα line width: $r_{\rm Fe\ K\alpha} \gtrsim 0.04$ pc), which definitely excludes a disc origin in favor of a distant reflector. By this lower limit, the reflection likely happens in the molecular torus (e.g., Burtscher et al. 2013; Netzer 2015) or, based on the estimate by Saturni et al. (2016) for this quasar, at the boundary of the broad-line region.

4.5 Properties of the X-ray corona

Here we have presented a detailed analysis of the first *NuSTAR* observations of APM 08279, a gravitationally lensed, broad-absorption line quasar at $z = 3.91$, taken jointly to the latest XMM-*Newton* exposures in 2019. By means of primary-emission decrease (see Sect. 4.4) and high-energy sampling, we are able, for the first time, to see and constrain a strong reflection component ($R = 2.8^{+1.1}_{-0.9}$) and the high-energy cutoff ($E_{\rm cut} = 99^{+91}_{-35}$ keV) in this source. Despite the large uncertainties, the high-energy cutoff of APM 08279 is fully consistent with the only other estimates at $z > 1$ (Dadina et al. 2016; L19; see also the tentative measure of Lanzuisi et al. 2016). We thus break the previous redshift record of B1422 (Dadina et al. 2016; L19) and find additional evidence for complex emission mechanisms, very much alike those of local Seyfert galaxies, in high-z AGN (up to $z \approx 4$). It is of interest to notice that we do not find evidence for significant X-ray winds in the 2019 observations of APM 08279, the archetype of high-z UFOs. While these winds are known to be variable and episodic events (e.g., Dadina et al. 2005; Cappi et al. 2006; Giustini et al. 2011; Gofford et al. 2014; Igo et al. 2020; Parker et al. 2021), the present data do not allow us to investigate further on their disappearance. Only a new, dedicated monitoring will be key in probing *i)* whether this new flux state is enduring, *ii)* whether UFOs are no longer a distinctive feature of APM 08279, and *iii)* whether the former might be the cause of the latter. At this regard, we were awarded time with *Swift* (PI: Lanzuisi) to monitor APM 08279 during Summer 2022 and measure its current flux

state and tailor the follow up with XMM-*Newton*+*NuSTAR*. Most interestingly, the source activity rose again from the level of 2019 by a factor of almost 2×. We thus applied for a 140 ks observation with XMM-*Newton* plus a joint 100 ks exposure by *NuSTAR* during XMM-*Newton* AO 22 but unfortunately were not awarded time.

The measured reflection fraction ($R = 2.8^{+1.1}_{-0.9}$) is, even considering the large uncertainties, much higher than what expected based on previous results in the literature for high-luminosity sources: AGN with $L_{\rm X} > 10^{45}$ erg s^{-1} are usually found to show $R < 1$ (Del Moro et al. 2017; Zappacosta et al. 2018). We note that even though lower than our estimate, both the reflection fractions measured in L19 are higher than what expected for high-luminosity sources. However, the case of APM 08279 during 2019 exposures quite differs from those of B1422 and 2MASSJ16, and is more alike that of PG 1247+267, as discussed in Sect. 4.4. Moreover, the Fe Kα EW of APM 08279, measured with the phenomenological model acutpl+Kα (Table 4.2), is larger than the expectation based on the results over samples of high-z and local AGN (e.g., Falocco et al. 2013) and on the Iwasawa-Taniguchi effect[††] (Bianchi et al. 2007) but is consistent, at 90% confidence level, with the highest EWs of the CAIXA sample[‡‡] (corresponding to the 98% percentile of the EW distribution, Bianchi et al. 2009). In fact, such high values of R and of Fe Kα EW in 2019 data, coupled with the non-evolution of the X-ray reflection flux in the 2–10 keV observed band and the lower limit placed on the reflector's distance, likely hint that the reflection component in this last observation could be the echo of APM 08279 previous activity. Moreover, the majority of the reflection fraction values obtained from data prior to 2008 (see Fig. 4.3 and Table 4.3) are in decent agreement with what expected from the literature ($R < 1$). This is additional proof for our interpretation of APM 08279 activity variation (see Sect. 4.4), and for the Seyfert-like mechanisms that give origin to its emission.

L19 adopted the $\ell - \theta$ plane of Fabian et al. (2015) translated into the directly observable quantities $L_{\rm X}$ versus $E_{\rm cut}$, respectively, through Eqs. (1.11) (with $K = 2$, as assumed in Fabian et al. 2015) and (1.12). In the same way, theoretical $\ell(\theta)$ critical lines of Stern et al. (1995) were converted into $L_{\rm X}(E_{\rm cut})$ thresholds, assuming a corona size $R_{\rm X} = 5\,r_{\rm S}$ (Schwarzschild radius: $r_{\rm S} = 2GM_{\rm BH}/c^2$) and SMBH masses $M_{\rm BH} = 10^8\,M_\odot$ and $10^9\,M_\odot$, namely, representative of the sample of Fabian et al. (2015) and of powerful, high-z quasars, respectively. L19 also updated the compilation by Fabian et al. (2015) with more recent $E_{\rm cut}$ measurements, obtained both with and without *NuSTAR* data, and both on individual targets or over samples of

[††]With the Iwasawa-Taniguchi effect (Iwasawa & Taniguchi 1993), or X-ray Baldwin effect (Baldwin 1977), we refer to the observed anti-correlation between the EW of the neutral narrow core of the Fe Kα emission line and the 2-10 keV luminosity.

[‡‡]The Catalog of AGN in the XMM-Newton Archive (CAIXA) sample consists of radio-quiet X-ray unobscured sources, covering a range in X-ray luminosities of $L_{2-10} \simeq 2 \times 10^{41} - 3.9 \times 10^{46}$ erg s^{-1}, and in redshift from z=0.002 to z=4.520.

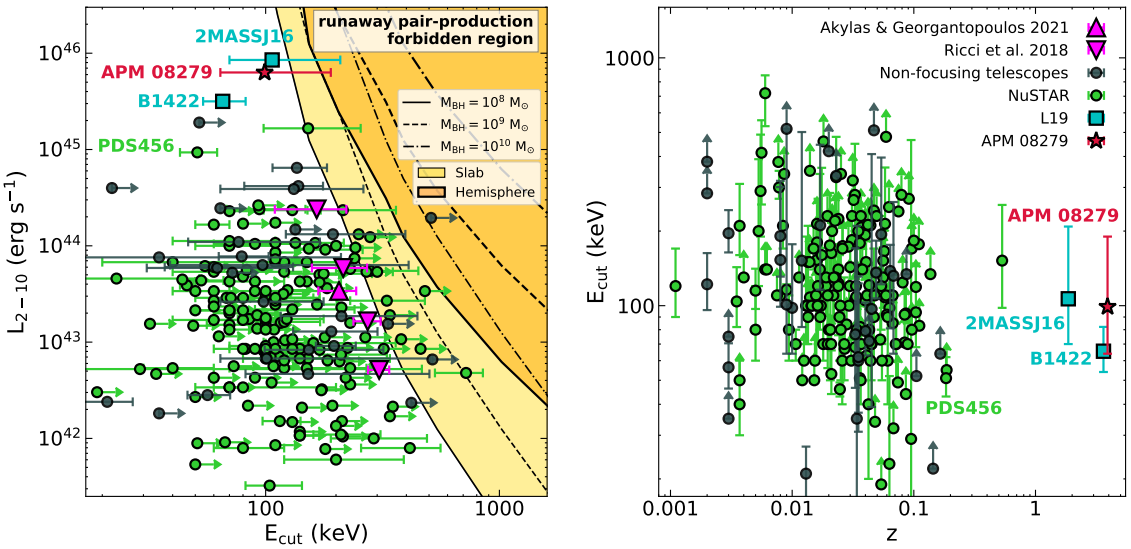

Figure 4.4: Compactness–temperature diagram translated into directly observable quantities and high-energy cutoff distribution as a function of redshift. *Left:* X-ray luminosity vs. high-energy cutoff, updated from L19 (see main text and Tables C.1–C.3 for details). *NuSTAR* measurements are in green, non-focusing telescopes' in grey, high-z AGN from L19 in cyan, and our measurement in red. Magenta downward triangles mark the averaged values for BASS AGN from Ricci et al. (2018), while the magenta upward triangle marks the median point of Seyfert 1 galaxies from Akylas & Georgantopoulos (2021). Yellow (orange) areas delimited by a thin (thick) line show the runaway pair-production region for a 10^8 $M_\odot$ SMBH in the case of slab (hemisphere) geometry. Dashed (dashed-dotted) lines mark the same thresholds for a 10^9 $M_\odot$ (10^{10} $M_\odot$) SMBH. *Right:* High-energy cutoff vs. redshift plane for the same samples as in the left panel.

sources (e.g., Malizia et al. 2014; Tortosa et al. 2017; Buisson et al. 2018; Molina et al. 2019). L19 included also the median values, binned in compactness (i.e., L_X), of the large BASS sample of local AGN as measured by Ricci et al. (2018). Figure 4.4 (left) shows the L_X–E_{cut} plane of L19 further updated with our measurement, the pair-production critical lines for $M_{BH} = 10^{10}\ M_\odot$, and results from other recent works, derived through canonical modeling of the continuum (Kara et al. 2017; Tortosa et al. 2018; Kamraj et al. 2018; Ursini et al. 2020; Baloković et al. 2020; Middei et al. 2020, 2021; Reeves et al. 2021, but see also Ezhikode et al. 2020, where the authors model X-ray reflection accounting for relativistic effects). When multiple estimates for a same source are available, we only kept the latest one. We also added earlier measurements of Dadina (2007) that were not revised in later works, selecting the best constrained value in case of multiple measurements for a single source. All the values populating the graphs in Fig. 4.4 are summarized by Tables C.1–C.3 in Appendix C. Akylas & Georgantopoulos (2021) recently studied the distribution of coronal temperatures in a large sample of Seyfert 1 selected by *Swift* and followed up by *NuSTAR* (118 sources, many also comprised in Ricci et al. 2017, 2018). Figure

4.4 shows the median high-energy cutoff of Seyfert 1 galaxies measured by Akylas & Georgantopoulos (2021). Recent works by Saturni et al. (2016, 2018) have agreed on APM 08279 data being best reproduced by low magnification factors ($\mu_{\rm L} \lesssim 9$). To add our target to the $L_{\rm X}$–$E_{\rm cut}$ plane, we estimated the de-absorbed and de-lensed 2–10 keV luminosity of APM 08279 ($L_{\rm X} = 6.5 \times 10^{45}\,{\rm erg\,s^{-1}}$) assuming a magnification factor of $\mu_{\rm L} = 4$ (Riechers et al. 2009). Like the other high-z AGN, APM 08279 falls in the allowed region for high-mass SMBHs with X-ray luminosity higher than 2×10^{45} erg s^{-1}. Being located in the proximity of the central SMBH, hot coronae are subject to the laws of general relativity (e.g., Wilkins et al. 2021). Tamborra et al. (2018) provide correction factors to be applied to results obtained through canonical reflection models. The authors demonstrate that, without accounting for general relativity, the observed high-energy cutoff ($E^{o}_{\rm cut}$) underestimates the intrinsic value $E^{i}_{\rm cut}$ by a factor $g = E^{i}_{\rm cut}/E^{o}_{\rm cut}$. Tamborra et al. (2018) compute g-factors for a variety of combinations of corona properties and reflection inclination angles. Assuming a $5\,r_{\rm S}$ corona and an inclination angle $i = 30°$ (see Sect. 4.3.1), the corresponding g-factor spans between 1.2 and 1.5. Even assuming the maximum value, the 90% confidence level upper bound of the high-energy cutoff of APM 08279 falls below the critical line for a slab corona and $M_{\rm BH} = 10^{10}\ M_{\odot}$. Thus, APM 08279 would still lie in the allowed region of the $L_{\rm X} - E_{\rm cut}$ plane for a SMBH mass of $\simeq 10^{10}\ M_{\odot}$ even when general relativity effects are accounted for.

L19 found that the median cutoff energy expected for local BASS AGN (Ricci et al. 2018) in the same accretion regime as their high-z sources was much higher than the measured values of B1422 and 2MASSJ16. For what concerns APM 08279, local AGN in the same Eddington regime as our target ($\lambda_{\rm Edd} \simeq 0.4$, Saturni et al. 2018) show a median high-energy cutoff of $E_{\rm cut} \simeq 170$ keV, which is well above the best-fit measurement ($E_{\rm cut} \approx 99$ keV) but consistent with its 90% confidence range (68 keV $< E_{\rm cut} <$ 190 keV). However, the existence of a relation between high-energy cutoff and Eddington ratio was recently debated in the literature: Hinkle & Mushotzky (2021) and Kamraj et al. (2022) find no correlation between accretion parameters and the high-energy cutoff in their new analyses of BASS AGN, as opposed to what seen by Ricci et al. (2018). According to their spectral analysis of *NuSTAR* data alone of *Swift*/BAT selected AGN, Kang & Wang (2022) confirmed the absence of a $E_{\rm cut}$–$\lambda_{\rm Edd}$ relation and, interestingly, they find that some sources fall in the runaway pair-production region of Fig. 4.4. Only a better sampling of both the high-luminosity end and the high-accretion regime will allow us to better understand the physics regulating hot coronae in powerful AGN. Lastly, we addressed the possibility of APM 08279 having a magnification factor more similar to $\mu_{\rm L} = 100$ (Egami et al. 2000), which would make our target a more "regular" AGN ($L_{\rm X}(\mu_{\rm L} = 100) = 2.6 \times 10^{44}\,{\rm erg\,s^{-1}}$, $\lambda_{\rm Edd}(\mu_{\rm L} = 100) \simeq 0.08$). Nevertheless, APM 08279 would still fall in the allowed region of the $L_{\rm X} - E_{\rm cut}$ plane and its high-energy

cutoff would not be consistent with the median value of BASS AGN in a similar accretion regime.

Chapter 5

The molecular view of KASHz AGN

Another important aspect of assessing the role of AGN feedback in shaping galaxy growth is the study of if and how AGN hosts differ from regular (i.e., non-active) galaxies. In this sense, great effort has been put by the community in designing comparative studies of AGN hosts and non-active galaxies, matching the samples based on key properties such as redshift, stellar mass, SFR, to probe whether the two populate different parameter spaces. The idea is that, if AGN feedback has an impact on the gas reservoir, we may expect that if we compare AGN and non-active galaxies with matched properties, they could feature different gas properties because of AGN feedback. In particular, one key aspect investigated by these studies is whether AGN hosts present a reduced amount of molecular gas mass with respect to their non-active siblings, producing a potpourri of results as summarized in Chapter 1, Sect. 1.3. Aim of the present Chapter is to deepen our understanding of the impact of cosmic-noon AGN on the molecular gas reservoir of their hosts, that is at a key cosmic time for AGN feedback processes.

5.1 Introduction

C21 provided the first systematic analysis of the gas content of AGN host galaxies at $z \sim 2$, free of the uncertainties related to the conversion factors between physically relevant quantities (SFR, $M_{\rm gas}$) and their observational proxies ($L_{\rm FIR}$, $L'_{\rm CO}$). Such AGN were drawn from the SUPER survey (C18; see also Sect. 1.3). The authors observed a sizable sample of cosmic noon AGN in the CO(3-2) emission line, thus probing the molecular gas content of the host galaxies as traced by such CO transition instead of converting it into molecular gas mass, that is, without having to assume a CO ladder and a value for $\alpha_{\rm CO}$. Moreover, the authors retrieved the host-galaxy key properties through SED fitting, carried out with the CIGALE code (Noll et al. 2009), thus deriving the galaxy FIR luminosity, decoupled of the AGN

emission, to be used as proxy for the SF. C21 carried out a comparative study of the CO and FIR properties of SUPER AGN and PHIBSS non-active galaxies (Tacconi et al. 2018). The control sample was built by selecting non-active galaxies matched in redshift, stellar mass and FIR luminosity, plus the constraint of being observed in the same CO transition as the AGN sample. C21 find that SUPER host galaxies only show hints of CO depletion when compared to PHIBSS galaxies, as matched in stellar mass or in FIR luminosity. Moreover, such discrepancy becomes significant (at the 2-3σ level) only when narrowing down the AGN sample to those targets with the best constrained galaxy parameter (M_*, $L_{\rm FIR}$), corresponding to $M_* > 10^{11}\,{\rm M}_\odot$, $L_{\rm FIR} \simeq 10^{12.2}\,{\rm L}_\odot$, or when considering the mean of the $L_{\rm CO(3-2)}/M_*$ distributions.

Aim of this Chapter is to capitalize on the methods of C21 and extend their work to a larger sample of AGN at cosmic noon. We expand the C21 sample by including other targets selected solely based on their X-ray properties, without priors on either AGN-driven winds or AGN feedback in general, drawn from the KASHz survey (see Sect. 5.2). The ALMA data selection and reduction is presented in Sect. 5.3. The control sample of non-active galaxies is presented in Sect. 5.4. The procedure used to retrieve the properties of KASHz AGN from SED fitting, using the latest photometry available, is described in Sect. 5.3.1. We then apply a quantitative analysis in the Bayesian framework developed by C21 to compare the new, expanded AGN sample with the non-active galaxies of the control sample (see Sect. 5.4). Results are summarized and discussed in Sect. 5.5.

5.2 KASHz survey

The KASHz project (Harrison et al. 2016, Scholtz et al., 2023 in prep.) is a VLT/KMOS survey of X-ray selected AGN, built with the aim of investigating the impact of AGN feedback over gas kinematics as traced by the Hα, [OIII], Hβ, [N II] and [S II] emission lines. Targets were drawn from five different X-ray deep fields, for which we updated the X-ray information to the latest survey catalogs with respect to what reported in Harrison et al. (2016): *i)* C-COSMOS (*Chandra*-Cosmic evolution survey field, Civano et al. 2016; Marchesi et al. 2016); *ii)* CDFS (*Chandra* Deep Field South, Luo et al. 2017); *iii)* SXDS (*Subaru*/XMM-*Newton* Deep Survey, Ueda et al. 2008; Akiyama et al. 2015); *iv)* XUDS (*Chandra* Legacy Survey of the Subaru-XMM-*Newton* Deep/UKIDSS Ultra Deep Survey (SXDS/UDS) field, Kocevski et al. 2018); *v)* SSA22 protocluster field (Lehmer et al. 2009). The survey includes all the AGN placed at $z \simeq 0.6 - 2.6$ with intrinsic (that is, absorption corrected) 2–10 keV rest-frame luminosity $\log(L_{\rm X}/{\rm erg\ s^{-1}}) \gtrsim 42$ for which Near-IR (NIR) integral-field spectroscopy (IFS) is available, either from our KMOS program or as archival SINFONI data. The survey catalog is complemented by targets from CDFS with X-ray luminosity lower than our threshold, but flagged as AGN in the

Luo et al. (2017) catalog*, for which NIR IFS data are available. Based on our spectral fits performed in the NIR IFS, we confirm and provide a more precise estimate for the redshift of ≃80% of the sample, compared to the values present in the parent X-ray survey catalogs. For ≃ 10% of the sources, we measure spectroscopic redshifts that differ more than $|\Delta z| = 0.1$ with respect to the ones in the parent catalogs. For the remaining ≃ 10%, we either keep the redshift as listed in the X-ray catalogs or update it with spectroscopic estimates as collected from the literature. We retrieve the X-ray properties of our sources from the parent X-ray catalogs and spectral fits performed by the survey collaborations for the XUDS (Kocevski et al. 2018), SXDS (Akiyama et al. 2015), COSMOS (Lanzuisi et al. 2013, 2015; Marchesi et al. 2016) and CDFS fields (Luo et al. 2017; Liu et al. 2017), updating them to the new spectroscopic redshift in case this differs by more than $|\Delta z| = 0.1$. For SSA22 AGN, we collect the sources' spectra from the *Chandra* Source Catalog v.2.0 and fit them ourselves to retrieve intrinsic photon index, column density and absorption corrected X-ray luminosity, since the survey catalog only reports the X-ray flux. The COSMOS collaboration did not estimate the intrinsic parameters of AGN lacking a robust redshift estimate. Thus, for those COSMOS AGN with an unreliable redshift for which we could provide a spectroscopic redshift, we collect the X-ray spectra directly from the COSMOS-legacy collaboration and retrieve the intrinsic X-ray properties through spectral fitting. Regarding the X-ray properties of those AGN in common with the SUPER sample, we refer to the results as obtained from X-ray spectral fitting by C18; C21. The KASHz survey totals 235 AGN, spanning the redshift range $z = 0.6 - 2.6$ and the $L_{\rm X}$ range $\log(L_{\rm X}/\mathrm{erg\ s^{-1}}) = 41 - 45.4$ (obtained with the updated spectroscopic z), which, assuming the bolometric corrections of Duras et al. (2020), corresponds to a bolometric luminosity range of $\log(L_{\rm Bol}/\mathrm{erg\ s^{-1}}) = 42.2 - 47$. Figure 5.1 shows the distribution of X-ray luminosity and bolometric luminosity against redshift of the full KASHz sample. The final catalog of the survey will be presented in Scholtz et al. (2023, in prep), alongside the results from the spectral analysis of [OIII], Hα and Hβ emission lines.

Given the survey selection criteria and observational scheme, KASHz can be considered a sibling survey of SUPER, as mentioned in Sect. 1.3. In fact, the KASHz sample covers a wider range in redshift and AGN bolometric luminosity at the expenses of a lower spatial resolution in the NIR data. Narrowing the KASHz sample to the sources at cosmic noon ($z \simeq 1 - 3$), such subsample covers the $z \simeq 1 - 2.5$

*Sources of the CDFS catalog are classified as AGN if they pass at least one of the following criteria: *i)* $L_{\rm X,int} \geq 3 \times 10^{42}$ erg s^{-1} (luminous X-ray sources); *ii)* $\Gamma_{\rm eff} \leq 1.0$ (hard X-ray sources), where $\Gamma_{\rm eff}$ is the effective photon index, i.e. the one obtained by fitting the data using only a single power law model (e.g., see model pl in Chapter 4); *iii)* $\log(f_{\rm X}/f_{\rm R}) > -1$, X-ray-to-optical (band R) flux ratio; *iv)* spectroscopic classification as AGN; *v)* $\log(L_{\rm X,int}/L_{1.4\ \rm GHz}) > 2.4 \times 10^{18}$, X-ray-to-radio luminosity ratio; *vi)* $\log(f_{\rm X}/f_{K_{\rm S}}) > -1.2$, X-ray-to-NIR (band $K_{\rm S}$) flux ratio. For each criterium using $\log(f_{\rm X})$, this is, in order of priority, the full-band, soft-band, or hard-band detected X-ray flux.

redshift range and the $\log(L_{\rm Bol}/{\rm erg\ s^{-1}}) \simeq 43-47$ bolometric luminosity range, totalling 202 sources, compared to the narrower intervals and smaller sample size of the SUPER survey ($z \simeq 2-2.5$, $\log(L_{\rm Bol}/{\rm erg\ s^{-1}}) \simeq 44.7-46.9$, 48 targets; C18; C21). Moreover, there are 14 AGN[†] that are shared by both samples, since both survey drew their targets from the same X-ray deep fields. For what concerns cosmic noon AGN, KASHz spans a wider range in redshift and includes also less powerful, more "regular" AGN with respect to SUPER. Combined to the SUPER catalog, KASHz AGN can thus help us in building a sample of cosmic noon AGN that is more representative of the overall population at those redshifts.

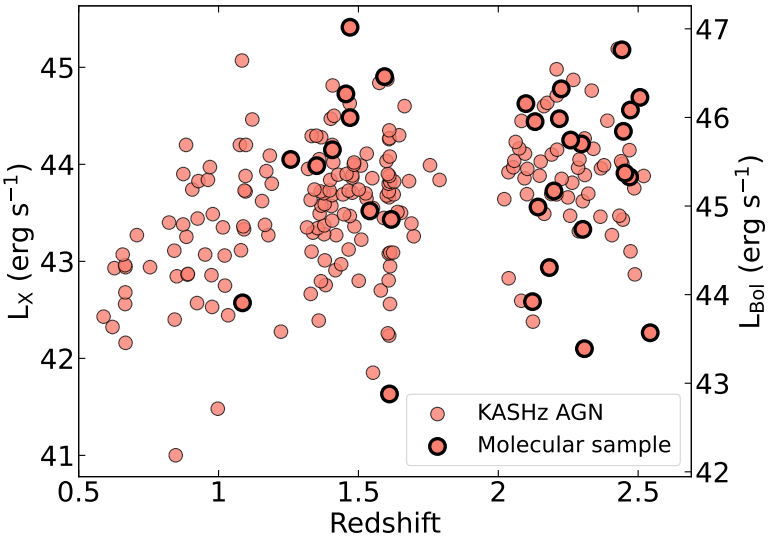

Figure 5.1: Intrinsic 2-10 keV rest-frame X-ray luminosity $L_{\rm X}$ vs. redshift z distribution of the KASHz full sample. The KASHz molecular sample is highlighted by thicker circle edges. The vertical axis on the right shows the bolometric luminosity $L_{\rm bol}$, derived following Duras et al. 2020.

5.3 KASHz molecular sample: ALMA data selection and analysis

We mined the ALMA archive for observations of KASHz AGN placed at $1 < z < 3$ (202 sources). We narrowed our query to ALMA Band 3, 4 or 5, since these are the ones that cover low-J CO transitions ($J_{\rm up} = 2, 3, 4$), best suitable to derive total molecular gas masses, in the redshift range of interest. Moreover, while ALMA bands stretch over tens of GHz, the spectral windows in a single observation can be as narrow as a few GHz. Some KASHz AGN are serendipitous in the fields of targets

[†]Targets shared by KASHz and SUPER surveys: cdfs_36, cdfs_419, cdfs_427, cdfs_522, cdfs_614, cid_1205, cid_1215, cid_346, cid_357, cid_451, cid_970, cid_971, cid_1057, cid_1143.

Table 5.1: KASHz ALMA targets

name	Xfield	RA	DEC	Type	z	Γ	$N_{\rm H}$	L_{2-10}	flag_Lx
cdfs_258	cdfs	53.060	-27.852	2	1.542	1.8	24.20	43.52	5
cdfs_313	cdfs	53.072	-27.834	0	1.612[a]	3.0	0.0	41.63	1
cdfs_419	cdfs	53.097	-27.715	2	2.142	1.8	24.03	43.56	5
cdfs_427	cdfs	53.100	-27.715	2	2.302	1.8	22.46	43.33	5
cdfs_458	cdfs	53.107	-27.718	2	2.297	1.77	23.12	44.21	5
cdfs_522	cdfs	53.118	-27.782	2	2.308	1.92	0.0	42.10	1
cdfs_587	cdfs	53.131	-27.773	2	2.225	1.8	23.24	44.77	1
cdfs_614	cdfs	53.137	-27.700	2	2.453	1.8	24.12	43.91	5
cdfs_718	cdfs	53.160	-27.776	2	2.543	2.43	0.0	42.26	1
cdfs_794	cdfs	53.179	-27.920	2	2.122	2.32	0.0	42.58	1
cid_108	cosmos-l	150.05	2.47742	1	1.258	1.8	22.49	44.05	1
cid_1205[c]	cosmos-l	150.01	2.33296	2	2.258	1.8	23.5	44.25	4
cid_1215[c]	cosmos-l	150.06	2.32905	1	2.447	1.8	22.86	44.34	4
cid_1286	cosmos-l	150.14	2.26507	2	2.199	1.8	22.97	43.72	1
cid_178	cosmos-l	149.58	2.05112	1	1.351	1.8	22.72	43.98	1
cid_346[c]	cosmos-l	149.93	2.11873	1	2.218	1.74	23.05	44.47	4
cid_357[c]	cosmos-l	149.99	2.13197	1	2.132	1.88	0.0	44.44	4
cid_451[c]	cosmos-l	150.00	2.25862	2	2.442	1.8	23.87	45.18	4
cid_499	cosmos-l	149.91	2.32746	1	1.455	1.8	0.0	44.72	1
cid_72	cosmos-l	150.09	2.39907	1	2.472	1.8	0.0	44.56	1
cid_86	cosmos-l	150.11	2.29590	2	2.099	1.8	0.0	44.62	2
cid_864	cosmos-l	149.88	2.31819	2	1.617	1.8	0.0	43.43	1
cid_970[c]	cosmos-l	150.23	2.36176	1	2.506	1.74	0.0	44.69	4
cid_971[c]	cosmos-l	150.24	2.33262	2	2.469	1.8	0.0	43.87	4
lid_1565	cosmos-l	150.54	1.61846	1	1.594	1.8	0.0	44.90	1
lid_1639	cosmos-l	150.74	2.17052	1	1.472[b]	1.8	23.05	44.48	1
lid_1646	cosmos-l	150.78	2.15095	1	1.470[b]	1.8	22.51	45.41	1
xuds_358	xuds	34.322	-5.2300	2	2.182	1.7	20.14	42.93	2
xuds_477	xuds	34.510	-5.0091	0	1.086	1.7	19.86	42.57	2
xuds_481	xuds	34.657	-4.9806	1	1.407	1.7	22.24	44.15	1

Notes. [a] Redshift from Luo et al. (2017). [b] Redshift from Marchesi et al. (2016). [c] Target shared with the SUPER survey. The Type column reports the AGN classification based on the KASHz spectral fits: Type 1, Narrow Line AGN; Type 2, Broad Line AGN; Type 0: undetected in NIR spectra. The flag_Lx column expresses how we derived the X-ray properties of the targets: flag_Lx=1, values as in the parent survey catalogs; flag_Lx=2, redshift of the source is updated based on KASHz NIR spectral fitting, $N_{\rm H}$ and photon index of parent survey catalogs are corrected according to the new spectroscopic redshift estimate; flag_Lx=3, values are retrieved from spectral fit, this work; flag_Lx=4, values are retrieved from spectral fit, C21; flag_Lx=5, values are retrieved from spectral fit, Liu et al. (2017); flag_Lx=6, values are retrieved from spectral fit Liu et al. (2017) and corrected according to the new spectroscopic redshift estimated from KASHz NIR spectra; flag_Lx=7, values are retrieved from spectral fit, Lanzuisi et al. (2013, 2015) and corrected according to the new spectroscopic redshift estimated from KASHz NIR spectra.

at a different redshift, resulting in data that do not serve our purposes because the spectral windows do not cover the CO line frequency of our source. The final sample (to which we will refer to as the KASHz molecular sample) is thus made of 30 AGN (13% of the KASHz sample) and 18 ALMA projects (excluding big mosaics as the ASPECS survey, Aravena et al. 2019; Decarli et al. 2019), for a total of 37 ALMA

fields in Bands 3 and 4 (see Table D.1, in which we report all observations analyzed in this thesis, but those presented in C21). Twelve observations target the CO(2-1) line, eighteen the CO(3-2) and seven the CO(4-3), with three AGN observed in two CO transitions (cdfs_427, cdfs_587, cdfs_614) and two AGN (cdfs_794, cdfs_587) observed twice in the same CO transition but with different spatial resolutions. The KASHz molecular sample includes also:

- Eleven of the 14 AGN that are shared with the SUPER sample: cdfs_419, cdfs_427, cdfs_522, cdfs_614, cid_1205, cid_1215, cid_346, cid_357, cid_451, cid_970, cid_971, of which only the COSMOS targets are part of the ALMA sample presented in C21;
- cdfs_718, the brightest CO emitter in the ALMA Spectroscopic Survey in the *Hubble* Ultra Deep Field (ASPECS ID 1mm.1; Decarli et al. 2019; González-López et al. 2019; Aravena et al. 2019; Boogaard et al. 2020), for which we include the follow up observation targeting CO(4-3) (2019.1.01528.S, PI: L. Boogaard);
- lid_1639 (XID5395, Brusa et al. 2016) and lid_1646 (XID5321, Perna et al. 2015), targeted by the ALMA program 2018.1.00251.S (PI: M. Brusa) covering CO(2-1) and CO(5-4), the analysis of which will be presented in Ricci et al. (2023, in prep.);
- a few AGN that are already well known for their gas kinematics and AGN feedback properties: lid_1565 (XID2028; Cresci et al. 2015; Brusa et al. 2018; Scholtz et al. 2020), cdfs_587 (GMASS0953; Popping et al. 2017; Talia et al. 2018), cdfs_794; (ALESS067.1 Chen et al. 2017; Calistro Rivera et al. 2018).

We also include in our data analysis the sub-*mm* observation of J1333+1649, a SUPER AGN not in C21 because subsequently observed by NOEMA, targeting CO(3-2). We present here the data reduction and analysis of all the ALMA archival observations but those of SUPER targets from COSMOS, for which we refer to the results of C21. We list the KASHz ALMA targets, including those shared with SUPER, in Table 5.1, along with the parent X-ray deep field, AGN type, redshift, X-ray intrinsic photon index, X-ray absorption column density and absorption-corrected X-ray luminosity in the 2–10 keV rest-frame band with a flag corresponding to how we computed it.

We retrieved the calibrated measurement sets using the dedicated service provided by the ALMA Regional Center. We produced continuum maps and (continuum-subtracted) spectral cubes using the task `tclean` in CASA 6.4. We imaged all fields using natural weights with the aim of recovering the total CO flux, thus the total molecular gas mass, of our host galaxies. Would the natural-weighted angular resolution be lower than 2″, we imaged our targets again, applying a taper of 2″ or equal

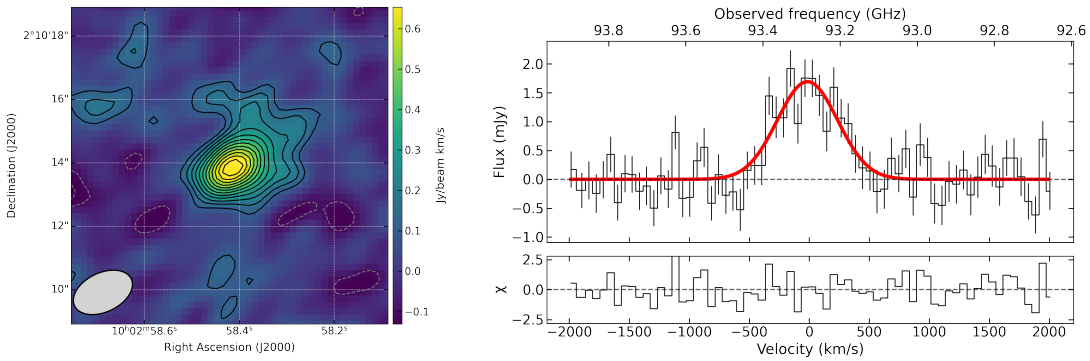

Figure 5.2: CO(2-1) velocity-integrated emission map (*Left*) and spectrum (*Right*), extracted from the region above 3σ significance, of lid_1639. Solid contour levels in the left panels start at 2σ. Dashed contour levels indicate the -2σ level. The beam is shown by the grey ellipse at the bottom-left corner of the map. The CO maps and spectra of the rest of the sample are presented in Appendix D.

to the double of the natural-weighted spatial resolution, in case this was lower than 1″. Each cube was then analyzed with user-developed Python 3.10 notebooks that automatically search for the source emission, perform the spectral extraction and analysis, provide the fit of 1D spectrum and produce the line velocity-integrated (0th order), intensity-weighted velocity (1st order) and velocity dispersion (2nd order) moment maps. Our code makes use of the `spectral-cube`[‡], `numpy` (Harris et al. 2020) and `scipy` (Virtanen et al. 2020) Python packages.

The code flow is the following: *i)* it finds the source emission, both spatially and in frequency range; *ii)* it extracts the source spectrum from the peak pixel or, in case of (semi)resolved emission, it selects the extraction region maximizing the signal-to-noise ratio on the line velocity-integrated map obtained collapsing the cube over ±1000km/s around the expected line frequency (or a narrower velocity range for fainter targets or noisier fields); *iii)* it bins the spectrum to the desired spectral resolution, fits the line and finds the line centroid, FWHM, flux; *iv)* it re-centers the cube to the observed frequency and produces the 0th, 1st and 2nd order moment maps on a spectral range corresponding to ±3× the line width; *v)* it extracts the spectrum from the re-centered cube, re-selecting the extraction area (or peak pixel) on the new 0th moment map; *vi)* it fits the line with a single- and a double-Gaussian function, storing the respective parameters and relative errors. Regarding step *v)*, the spectrum is extracted from the 3σ mask of the target in case this is larger than the corresponding beam, otherwise the spectrum is extracted from the peak pixel of the line velocity-integrated map produced in step *iv)*. We assume as uncertainty of the measured CO flux the root-mean square noise (rms) of the line-free range of the spectrum. We run the whole procedure first on the native-channel-width spectral

[‡] https://github.com/radio-astro-tools/spectral-cube

cubes, for both weighting schemes (natural and tapered). We then produce the final cubes by selecting the weighting scheme that maximizes the source flux and setting a channel width that allows to sample the line FWHM at least 7 times. We consider a source as detected if its emission peak in the velocity-integrated map is at least $3\times$ the rms of the map and if the source emission in the extracted spectrum exceeds the cube rms. We show the velocity-integrated map and spectrum of lid_1646 in Fig. 5.2 as example and present those of the other detected targets in Appendix D (Figs. D.1-D.5). Almost all of our CO lines are well fitted by a single Gaussian component based on the F-test. For those that are significantly better (or slightly better) fitted by a double Gaussian, we produce the cubes and moment maps of the redshifted and blueshifted peaks to check whether the two components are spatially offset from each other. Due to the low resolution of many of the observations in our data sample, the two peaks are usually coincident or offset by only few pixels in the velocity-integrated maps. However, some targets present semi-resolved kinematics (peaks in the 0th moment map separated by approximately one beam), corresponding to the most resolved observations. For the purposes of our study, we are mainly interested in extracting from our data a measure of the CO flux that is as close as possible to the total flux of our host galaxies. Having checked that the single- and double-Gaussian models return consistent values, we refer to the results obtained with the single-Gaussian modeling and defer a detailed analysis of the molecular gas dynamics of our targets to a following work (Bertola et al., in prep.).

As a sanity check of the robustness of our ALMA analysis, we compared the CO flux derived from the spectral fits with the value measured from the target emission in the moment 0 maps (either by reading the peak pixel value or by integrating the flux in the 3σ mask in case this is smaller or larger than the corresponding beam, respectively) and as derived from the 2D fits of the moment 0 maps with the CASA task `imfit`. Figure 5.3 shows that the CO flux measured from the spectral fits is well consistent with both estimates from the moment 0 maps, with the exception of the CO emission of cdfs_794 in the most resolved observation (PI: Hodge). The value measured with `imfit` is consistent with that obtained by Calistro Rivera et al. (2018), where the spectrum was extracted using a circular region of $1''$ radius instead of the 3σ mask. We thus re-extract such spectrum using the same approach as in Calistro Rivera et al. (2018) and find a CO(3-2) flux that is consistent with the value integrated from the $1''$ circle, the 2D fit result of `imfit` and that of Calistro Rivera et al. (see Fig. 5.3).

In case of non-detections (S/N$\lesssim 3$ in the velocity-integrated maps and spectral emission varying within $\pm\mathrm{rms}_{\mathrm{cube}}$ throughout the full frequency range; 11 CO lines of 10 KASHz AGN), we bin the cubes to channels of 40 $\mathrm{km\,s^{-1}}$ width and estimate the flux upper limits from the local rms of the peak channel map as follows. We use a box centered on the AGN coordinates with a $5''$ side so to enclose enough pixels for

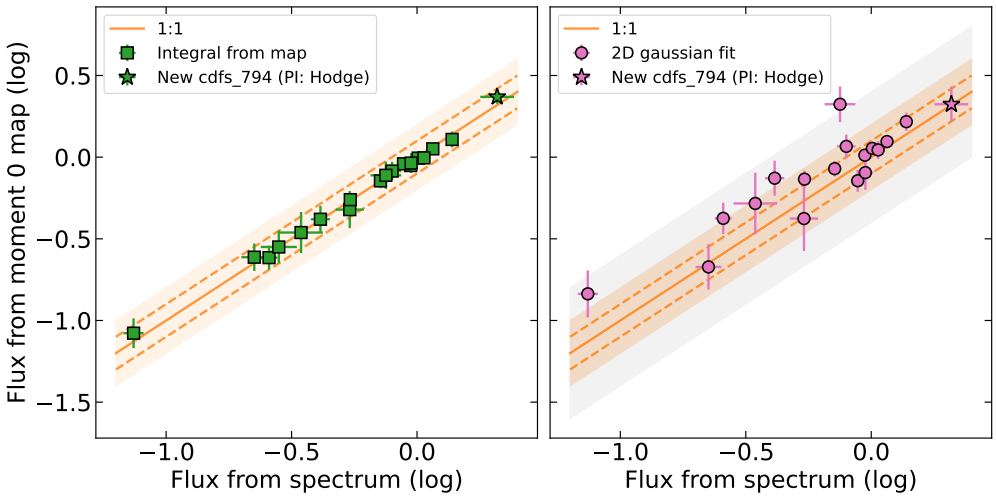

Figure 5.3: CO flux as measured from the moment 0 maps (Left, green squares) and as measured from 2D fits of the moment 0 maps (Right, pink circles) vs. the CO flux as estimated from spectral fits. In both panels, the solid line is 1:1, the dashed lines mark the 0.1dex scatter, the orange shaded area the 0.2dex scatter. The grey shaded area in the right panel marks the 0.4dex scatter. The outlier point in the right panel is the CO(3-2) flux of cdfs_794 as measured from the most resolved observation (beam: 0.579″ x0.499″). The star marks the results obtained with the spectrum extraction procedure of Calistro Rivera et al. (2018).

it to be representative of the local rms. For the less resolved cubes, this corresponds to a box size of at least 5 beams. For the most resolved observations ($\theta \simeq 0.2''$), we reduce the box side to 2.5″, so to obtain a reliable estimate of the local rms around the source. We then compute the upper limit of the line flux as $S^{\rm ul}_{\rm CO} = 3\sigma \times FWHM$, assuming $FWHM = 300$ km/s (e.g., D'Amato et al. 2020; Pensabene et al. 2021). Velocity integrated maps (derived collapsing the cubes in the ±3×FWHM, with FWHM=300 $\rm km\,s^{-1}$) and source spectra are reported in Appendix D (Figs. D.6-D.8). Table 5.2 summarizes all the values of interest derived from the ALMA data analysis.

We assessed the continuum emission of our targets by producing velocity-averaged maps from line-free channels. Six AGN are detected in continuum, two in Band 3 (lid_1646, lid_1639) and four in Band 4 (cdfs_614, cdfs_587, cdfs_718, cdfs_522). We measure the continuum flux from the peak pixel in the continuum map or from the 3σ mask if this is more extended than one beam. Regarding continuum non-detections (24 AGN), we estimate the 3σ upper limit from the local rms measured applying the same method used for the line non-detections. The photometric points obtained from ALMA Band 3 and 4 continuum are included in the SED fitting of the KASHz molecular sample (see Sect. 5.3.1).

Since our sample is heterogeneous in terms of targeted CO transition (CO(2-1), CO(3-2), CO(4-3)), we convert our CO fluxes to the CO(1-0) transition assuming a

CO SLED. We assume the line ratios of Kirkpatrick et al. (2019) ($r_{41} = 0.37 \pm 0.11$, $r_{31} = 0.59 \pm 0.18$, $r_{21} = 0.68 \pm 0.17$) and derive the CO(1-0) line luminosity as (e.g., Carilli & Walter 2013):

$$L'_{\rm CO}[\rm K\ km\ s^{-1}\ pc^2] = 3.25 \times 10^7 S\Delta v \frac{D_{\rm L}^2}{(1+z)^3 \nu_{\rm obs}^2} \tag{5.1}$$

where $S\Delta v$ is the line velocity-integrated flux in Jy km s^{-1}, $D_{\rm L}$ is the luminosity distance in Mpc and $\nu_{\rm obs}$ is the observed centroid frequency of the line in GHz. We summarize in Table 5.2 the CO properties and dust continuum measurements of our sources, alongside the chosen weighting scheme, the beam of the ALMA cubes and continuum maps, the width of the channels in the rebinned cubes, the mean rms of the final cubes and velocity-integrated maps.

Some of our AGN are targeted in more than one ALMA observation (see Table 5.2). We estimate the $L'_{\rm CO}$ from every available CO transition and, having checked for their consistency, we consider the measure retrieved from the less resolved ALMA cube or the lowest-J CO transition so to obtain the CO(1-0) flux that best resembles the total molecular gas mass of the host galaxy. The only exception is cdfs_794: this system was analyzed by Calistro Rivera et al. (2018), finding a near-by companion in the most resolved ALMA observation of our sample, which are blended in the less resolved observation. We thus select the CO(1-0) flux measured from the more-resolved ALMA cube for our analysis. We note that the CO(1-0) transition of cdfs_718, source belonging to the ASPECS sample, was also observed with VLA (Riechers et al. 2020). Our measure, derived by assuming a CO SLED common to our whole sample, is well consistent with the estimate from the ASPECS collaboration.

In total, the number of CO detections is 18 out of 29 targeted CO lines in 24 sources, including also J1333+1649, which corresponds to a detection rate of $\simeq$60% for the ALMA observations analyzed in this thesis. As a comparison, the SUPER sample presented in C21 shows a detection rate of $\simeq$40%.

5.3.1 SED fit of KASHz ALMA targets

We measure the stellar mass M_*, the FIR luminosity $L_{\rm FIR}$ of the host galaxies and the AGN bolometric luminosity $L_{\rm bol}$ of our KASHz ALMA targets from SED fitting performed with CIGALE v.2022.1 (Boquien et al. 2019; Yang et al. 2020), a publicly available, python-based SED-fitting technique. This code adopts a multicomponent fitting approach to disentangle the AGN contribution from the galaxy emission, with model templates that include nebular emission, attenuated stellar emission, dust emission that is heated by SF, AGN emission (from the X-rays to the radio, including the primary accretion disk emission and the dust-heated reprocessed emission). This

Table 5.2: Summary of results from the ALMA data analysis

name	line	z	Weights	$\mathrm{beam_{cube}}$	$\mathrm{z_{CO}}$	Channel	$\mathrm{rms_{cube}}$	$\mathrm{rms_{mom0}}$	FWHM	S_{CO}	r_{j1}	$S_{\mathrm{CO(1-0)}}$	$\mathrm{beam_{cont}}$	S_{cont}
J1333+1649	CO(3-2)	2.089	natural	2.793″ x1.576″	2.102	54	0.267	0.060	281 ± 57	0.281 ± 0.046	0.59	0.053 ± 0.016	–	–
cdfs_258	CO(2-1)	1.540	natural	2.377″ x2.096″	1.540	50	0.214	0.095	300	< 0.213	0.68	< 0.079	2.244″ x1.971″	< 67
cdfs_313	CO(2-1)	1.611	natural	4.218″ x2.727″	1.615	40	0.208	0.053	324 ± 26	0.714 ± 0.027	0.68	0.263 ± 0.066	3.983″ x2.568″	< 36
cdfs_419	CO(3-2)	2.142	natural	2.170″ x1.820″	2.142	40	0.330	0.092	300	< 0.234	0.59	< 0.044	2.111″ x1.797″	< 98
cdfs_427	CO(4-3)	2.302	natural	2.538″ x1.905″	2.302	40	0.230	0.056	300	< 0.182	0.37	< 0.031	2.443″ x1.833″	< 54
cdfs_427	CO(3-2)	2.302	natural	0.813″ x0.601″	2.302	40	0.160	0.047	300	< 0.162	0.59	< 0.031	2.443″ x1.833″	< 54
cdfs_458	CO(3-2)	2.301	natural	0.813″ x0.601″	2.300	70	0.125	0.047	533 ± 99	0.224 ± 0.026	0.59	0.042 ± 0.013	1.522″ x1.324″	< 9
cdfs_522	CO(4-3)	2.308	natural	0.198″ x0.163″	2.309	50	0.125	0.029	397 ± 25	0.943 ± 0.033	0.37	0.159 ± 0.047	0.192″ x0.158″	222 ± 17
cdfs_587	CO(3-2)	2.225	natural	3.382″ x2.136″	2.225	100	0.166	0.081	834 ± 80	0.883 ± 0.050	0.59	0.166 ± 0.052	2.967″ x1.984″	< 39
cdfs_587	CO(3-2)	2.225	natural	1.016″ x0.684″	2.225	100	0.183	0.078	782 ± 120	0.795 ± 0.067	0.59	0.469 ± 0.040	0.817″ x0.561″	< 64
cdfs_587	CO(4-3)	2.225	natural	2.253″ x1.55 ″	2.225	100	0.097	0.049	759 ± 27	1.155 ± 0.033	0.37	0.428 ± 0.012	2.154″ x1.495″	155 ± 14
cdfs_614	CO(3-2)	2.453	natural	2.171″ x1.888″	2.452	60	0.198	0.066	502 ± 88	0.412 ± 0.036	0.59	0.078 ± 0.024	2.305″ x2.014″	< 81
cdfs_614	CO(4-3)	2.453	taper 0.2″	0.282″ x0.246″	2.453	50	0.199	0.033	378 ± 62	0.257 ± 0.020	0.37	0.095 ± 0.007	0.283″ x0.242″	40 ± 12
cdfs_718	CO(4-3)	2.542	natural	3.134″ x2.206″	2.543	60	0.197	0.054	557 ± 54	1.010 ± 0.051	0.37	0.171 ± 0.051	3.000″ x2.111″	91 ± 14
cdfs_794	CO(3-2)	2.122	natural	0.579″ x0.499″	2.121	220	0.188	0.129	695 ± 79	2.086 ± 0.323	0.59	0.392 ± 0.120	0.576″ x0.547″	< 59
cdfs_794	CO(3-2)	2.122	natural	2.503″ x1.585″	2.121	80	0.317	0.109	618 ± 73	1.379 ± 0.063	0.59	0.295 ± 0.079	2.698″ x1.696″	< 55
cid_108	CO(2-1)	1.258	natural	1.779″ x1.431″	1.258	40	0.773	0.129	267 ± 39	0.947 ± 0.070	0.68	0.348 ± 0.087	1.948″ x1.530″	< 155
cid_1286	CO(3-2)	2.199	natural	0.375″ x0.240″	2.199	40	0.530	0.150	300	< 0.567	0.59	< 0.107	0.402″ x0.259″	< 69
cid_178	CO(2-1)	1.356	natural	2.427″ x1.715″	1.356	40	0.400	0.122	300	< 0.283	0.68	< 0.104	2.177″ x1.554″	< 54
cid_499	CO(2-1)	1.457	natural	1.586″ x1.342″	1.457	40	0.860	0.207	300	< 0.675	0.68	< 0.248	1.495″ x1.272″	< 116
cid_72	CO(3-2)	2.471	natural	0.405″ x0.264″	2.471	40	0.595	0.154	300	< 0.54	0.59	< 0.102	0.419″ x0.282″	< 59
cid_86	CO(4-3)	2.096	natural	0.442″ x0.383″	2.097	31.5[a]	0.078	0.017	235 ± 37	0.074 ± 0.006	0.37	0.013 ± 0.004	0.420″ x0.358″	< 23
cid_864	CO(2-1)	1.617	natural	1.603″ x1.399″	1.616	30	0.785	0.125	242 ± 51	0.539 ± 0.069	0.68	0.198 ± 0.050	1.513″ x1.331″	< 123
lid_1565	CO(2-1)	1.593	natural	1.612″ x1.393″	1.594	30	0.840	0.100	154 ± 46	0.344 ± 0.068	0.68	0.127 ± 0.033	1.522″ x1.324″	< 107
lid_1639	CO(2-1)	1.472	natural	1.982″ x1.231″	1.471	60	0.186	0.053	603 ± 49	1.065 ± 0.064	0.68	0.392 ± 0.098	1.871″ x1.155″	52 ± 12
lid_1646	CO(2-1)	1.470	natural	2.522″ x1.718″	1.470	60	0.179	0.031	615 ± 70	0.541 ± 0.026	0.68	0.199 ± 0.050	2.385″ x1.618″	96 ± 10
xuds_358	CO(3-2)	2.183	natural	1.399″ x0.894″	2.183	40	1.200	0.337	300	< 1.08	0.59	< 0.203	1.478″ x0.950″	< 161
xuds_477	CO(2-1)	1.087	natural	1.343″ x0.883″	1.087	40	1.080	0.410	300	< 0.855	0.68	< 0.314	1.461″ x0.955″	< 125
xuds_481	CO(2-1)	1.407	natural	1.502″ x1.009″	1.407	40	1.330	0.500	300	< 1.17	0.68	< 0.430	1.435″ x0.949″	< 147

Notes. Channel width is given in $\mathrm{km\,s^{-1}}$, CO flux in units of mJy, continuum flux in units of μJy, FWHM in units of $\mathrm{km\,s^{-1}}$, $\mathrm{rms_{cube}}$ in units of Jy/beam and $\mathrm{rms_{mom0}}$ in units of Jy/beam $\mathrm{km\,s^{-1}}$. Line ratios were retrieved from of Kirkpatrick et al. (2019), along with their uncertainties: $r_{41} = 0.37 \pm 0.11$, $r_{31} = 0.59 \pm 0.18$, $r_{21} = 0.68 \pm 0.17$. [a] Native channel-width of the ALMA observation.

is an "energy-balance" code, meaning that it takes into account the energy balance between the UV-optical attenuation and the FIR re-emission by dust. The best fit values of the parameters of interest (as selected by the user) are retrieved through Bayesian analysis, that is by building the probability distribution function (PDF), considering all the different models used in the fitting process. Thus, the best fit results correspond to the mean value of each PDF, with uncertainty equal to its standard deviation. One of the major updates in the code was the inclusion of the X-ray module (X-CIGALE is merged in CIGALE from CIGALE v.2022.0), which allows to set a prior on the $\alpha_{\rm OX}$[§] of the AGN by feeding the code with the intrinsic (i.e., absorption corrected) X-ray fluxes. By this, the code can anchor the AGN component in an energy range where the AGN contribution should overcome the galaxy emission and thus should set a reasonable prior to then decouple the two components and compute the energy balance (provided that the AGN in question are not extreme outliers of the $\alpha_{\rm OX}$-L[2500Å] relation; e.g., Lusso & Risaliti 2016; Martocchia et al. 2017). Since our aim is to update the work by C21 in the most consistent way, we use the same setup of models presented in C18: stellar population models with solar metallicity (Bruzual & Charlot 2003), a delayed SF history, the modified Calzetti et al. (2000) attenuation law and a Chabrier (2003) initial mass function, plus the nebular emission following Inoue (2011); Nagao et al. (2011). We model the contribution from the star-forming dust and AGN with the libraries of Dale et al. (2014) and Fritz et al. (2006) (updated following the observational results of Feltre et al. 2012), respectively. The AGN templates of CIGALE were recently updated by the inclusion of the SKIRTOR model, which allows also for a clumpy torus following Stalevski et al. (2012, 2016). Given that the torus emission of our AGN is only sampled by *Spitzer*/IRAC and *Spitzer*/MIPS24μm filters, that is, with poor spectral resolution, we do not foresee significant differences between the Fritz et al. model and SKIRTOR, thus, for consistency with what done by C21, we select the Fritz et al. (2006) templates. Thus, the main difference between our setup and that of C21 resides in the inclusion of the X-ray module.

We collect the Near-UV to FIR photometry referring to the latest results provided by the collaborations of the deep surveys our targets are extracted from:

- COSMOS: We retrieve the Near-UV/optical to MIR photometry from COSMOS2020 (Weaver et al. 2022); we complement the multiwavelength info of our COSMOS targets with the "super-deblended" FIR to (sub-)*mm* photometric catalog of Jin et al. (2018). Three sources of the KASHz molecular sample (lid_1565, lid_1646, cid_72) are not included in the superdeblended catalog, thus, following C18, we collect their 24–500 μm photometry from the previ-

[§]The parameter $\alpha_{\rm OX}$ is defined as $\alpha_{\rm OX} = -\log(L_{\rm 2keV}/L[2500\text{Å}])/\log(\nu_{\rm 2keV}/\nu[2500\text{Å}]) = 0.38\times \log(L_{\rm 2keV}/L[2500\text{Å}])$ and corresponds to the slope of a nominal power-law connecting the rest-frame UV and X-ray emission of AGN (Tananbaum et al. 1979).

ous PACS Evolutionary Probe (PEP) and *Herschel* Multi-tiered Extragalactic Survey (HerMES) DR4 catalogs by Lutz et al. (2011) and Hurley et al. (2017), respectively, using a match radius of 2″. Moreover, cid_72 has only one match in the COSMOS2020 catalog at a distance of 6″ from the coordinates listed in Marchesi et al. (2016), while the best match with the COSMOS2015 source list (Laigle et al. 2016) falls at less than 0.5″. We thus collect the Near-UV/optical to MIR photometry of cid_72 from COSMOS2015;

- CDFS: we collect the Near-UV to MIR photometry from the ASTRODEEP-GS43 catalog of the CANDELS/GOODS-S field (Cosmic Assembly Near-infrared Deep Extragalactic Legacy Survey/Great Observatories Origins Deep Survey-South, Merlin et al. 2021). FIR photometry is retrieved from the *Herschel* Extragalactic Legacy Project (HELP) collaboration (Shirley et al. 2019, 2021), complemented with previous results from PEP and HerMES (Oliver et al. 2012; Hurley et al. 2017) for those CDFS AGN that are not included in the HELP catalog (cdfs_313, cdfs_522, cdfs_718), as done for COSMOS targets. We include in the photometric information of cdfs_718 also the ALMA Band 6 continuum from ASPECS (Aravena et al. 2020; González-López et al. 2020);

- X-UDS: Near-UV to FIR photometry is collected from the "best photometry" catalog provided by the HELP collaboration (N-UV to MIR source catalogs used by the HELP collaboration: Almaini et al. 2007; Furusawa et al. 2008; Tudorica et al. 2017).

We include in the photometry of our sources also the ALMA continuum photometric points (or upper limits), from Band 3 to Band 7, when available, either drawn from this work (see Table 5.2) or from Scholtz et al. (2018); Lamperti et al. (2021) and C21. We flag as upper limits all the HELP FIR fluxes below the 2σ level and feed to X-CIGALE the corresponding 3σ level value as upper limit. We consider those above the 2σ limit as reliable based on the implementation of the flux extraction procedure by HELP collaboration, which uses the optical/NIR position of a target as prior to deblend its flux in the FIR bands. The Superdeblended catalog already flags the upper limits, thus we follow their classification, with the only exception of cid_1205: the source is placed in a crowded field, thus its FIR photometry is well detected but highly contaminated by a nearby source. We thus flag all the Superdeblended filters of cid_1205 as upper limits. An mentioned, the latest versions of CIGALE can take as input also the X-ray flux of an AGN, to set a prior on the 2500Å luminosity based on a user-selected range of $\alpha_{\rm OX}$ values and scatter. For this to work, one has to feed the code with the absorption-corrected (i.e., intrinsic) X-ray fluxes. We compute the X-ray photometric points in the 0.5–2 keV and 2–10 keV observed energy range by k-correcting the intrinsic X-ray luminosity with the intrinsic photon index, either

obtained from the direct fit of the X-ray spectra from the literature (for CDFS and COSMOS targets, Lanzuisi et al. 2013, 2015; Liu et al. 2017, C18; C21) or as derived by the X-ray deep survey collaborations in the survey catalogs (Luo et al. 2017; Akiyama et al. 2015; Kocevski et al. 2018; Marchesi et al. 2016), as flagged in Table 5.1. Since the survey catalogs do not provide an uncertainty for the intrinsic X-ray luminosity, we assigned a uniform and reasonable ±30% uncertainty for each X-ray photometric point in our sample. We divided the runs of CIGALE based on the values of the intrinsic photon index, to speed up the computational time of CIGALE. The detailed list of the photometric bands used for each of the X-ray deep fields is summarized in Appendix E (Table E.1).

We summarize in Table E.2 all the model parameters that we set to a value different than the default of X-CIGALE in our SED fitting runs. We note that the chosen X-CIGALE setup yields ∼ 290M models per redshift.

The results obtained with the described photometric set and the CIGALE setup provide adequate fits of the SEDs of our targets. Mountrichas et al. (2021) and Buat et al. (2021) show that if there is a large discrepancy between the Bayesian estimate and the best fit value of a certain parameter of CIGALE, then the result for that parameter is not reliable. We thus checked for such a consistency for M_*, SFR and $L_{\rm AGN}$ (i.e., $L_{\rm bol}$). All of our results match the acceptance range defined by the authors (that is, the ratio of the Bayesian and the best fit value falls in the 0.5–5 range), thus we consider our results as reliable. Moreover, we compared our results to those of C18; C21 for what concerns the AGN we have in common, since we performed the SED fitting with the updated photometry and including the X-ray module. We compared the main parameters of interest for our analysis, which are M_*, $L_{\rm FIR}$ and $L_{\rm AGN}$. Our results are well consistent with those of C18; C21 within the expected uncertainty of ×0.3-0.4 dex.

We checked the agreement between the best fit SEDs of lid_1646 and lid_1639 and the ALMA photometry in Band 6 (Ricci et al., 2023 in prep). The redward side of the FIR bump is well in agreement with the fluxes in ALMA Band 6, however, given the good sampling of the FIR band for these two sources, we decided to exclude ALMA Band 6 from their filter sets because the observations are very resolved (∼ 0.6″) and might underestimate the target flux, by missing the emission at larger scales. A different case is instead cid_1205: since we have considered all of its FIR data as upper limits, we decided to include the ALMA Band 7 flux of Lamperti et al. (2021) even if the corresponding observation is even more resolved (∼ 0.2″). We consider this as the best choice so to not overestimate the FIR bump of this system, also supported by the fact that Lamperti et al. conclude that their ALMA Band 6 fluxes mostly sample emission due to dust heated by SF.

Lastly, for some of the very Near-UV-bright Broad Line AGN in our sample, we can only constrain an upper limit to the stellar mass. This is however a reasonable

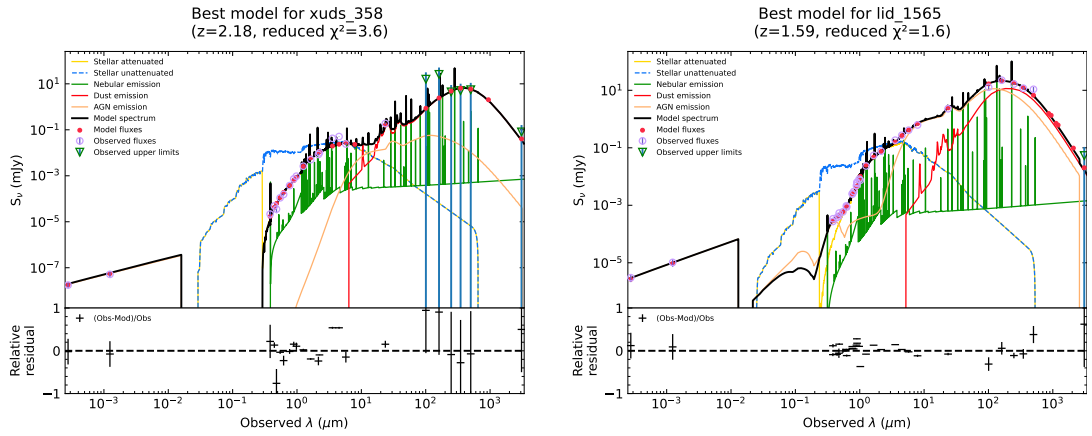

Figure 5.4: Observed-frame, best-fit SED models of a Narrow Line AGN and a Broad Line AGN (xuds_358, *Left*; lid_1565, *Right*). Purple empty circles mark observed flux densities, green triangles the observational upper limits and red filled circles indicate the best-fit model prediction. Yellow (blue dashed) lines are for the stellar (un)attenuated emisson; green lines for the Nebular emission; red lines for dust emission; orange lines for the AGN component and black lines for the total, best-fit model. The top label reports the name of the target, its redshift and the best fit quality (as reduced χ^2). The best-fit SEDs of the rest of the sample are presented in Appendix E.

result, given the degeneracy between the AGN component and the stellar component in the optical/NIR band.

5.4 Control sample of non-active galaxies

To build the comparison sample of non-active galaxies, we start from the Plateau de Bure high-z Blue Sequence Survey catalog (PHIBSS, Tacconi et al. 2018), a project that aims at assessing the gas properties across cosmic time, employing a sample of 1444 targets placed at $z = 0-4.4$. Each target is complemented with estimates of the molecular gas mass as traced by CO emission, FIR luminosity, as measured either from SED fitting or for 1mm dust luminosity. We also include the ALMA/NOEMA survey of sub-*mm* galaxies in the COSMOS, UDS, and ECDFS fields by Birkin et al. (2021) and the non-active galaxies of ASPECS (Boogaard et al. 2020, and references therein), to better sample the higher-end and the lower-end, respectively, of the stellar mass range spanned by our AGN host galaxies. The PHIBSS project includes also the first subsample of ASPECS targets that was presented in Decarli et al. (2016); for such galaxies, we refer to the latest results provided by the ASPECS project, as reported in Boogaard et al. (2020).

As opposed to the study of C21, our AGN sample is not uniform for what concerns the targeted CO transition, thus we collected the CO fluxes of each non-active galaxy in the control sample and converted them to the CO(1-0) transition.

Table 5.3: Summary of the properties of SUPER+KASHz sample

ID	z	$\log \frac{L_{\rm bol}}{\rm erg\ s^{-1}}$	$\log \frac{L_{\rm FIR}}{\rm erg\ s^{-1}}$	$\log M_*$ ($M_\odot$)	$\log L'_{\rm CO}$(K km s^{-1} pc^2)	SFR$_{\rm FIR}$ ($M_\odot$ yr^{-1})	sample
cdfs_258	1.540	44.61 ± 0.81	45.26 ± 0.05	10.79 ± 0.14	< 10.01	55 ± 3	1
cdfs_313	1.611	43.34 ± 0.1	44.58 ± 0.1	11.04 ± 0.05	10.57 ± 0.11	12 ± 1	1
cdfs_419	2.142	45.37 ± 0.16	45.14 ± 0.05	10.99 ± 0.05	< 10.01	41 ± 2	1
cdfs_427	2.302	44.85 ± 0.7	< 44.7	10.91 ± 0.17	< 9.91	< 15	1
cdfs_458	2.297	45.97 ± 0.28	45.48 ± 0.49	11.1 ± 0.25	10.05 ± 0.14	90 ± 44	1
cdfs_522	2.309	43.89 ± 0.05	45.12 ± 0.05	10.97 ± 0.05	10.63 ± 0.13	40 ± 2	1
cdfs_587	2.225	45.86 ± 0.26	45.77 ± 0.05	11.19 ± 0.15	10.62 ± 0.14	178 ± 9	1
cdfs_614	2.453	44.99 ± 0.35	46.02 ± 0.18	10.68 ± 0.67	10.36 ± 0.14	313 ± 57	1
cdfs_718	2.542	44.42 ± 0.05	45.21 ± 0.05	10.52 ± 0.1	10.73 ± 0.13	49 ± 2	1
cdfs_794	2.122	44.83 ± 0.05	46.07 ± 0.05	10.89 ± 0.23	10.96 ± 0.16	355 ± 18	1
cid_108	1.258	45.67 ± 0.05	46.03 ± 0.05	11.54 ± 0.21	10.49 ± 0.11	324 ± 16	1
cid_1205	2.255	45.96 ± 0.09	45.25 ± 0.08	10.88 ± 0.2	< 9.93	53 ± 4	3
cid_1215	2.45	45.67 ± 0.23	46.19 ± 0.18	10.51 ± 0.39	10.52 ± 0.14	462 ± 83	3
cid_1286	2.199	45.5 ± 0.1	44.74 ± 0.54	10.39 ± 0.69	< 10.42	16 ± 9	1
cid_178	1.356	46.01 ± 0.05	45.34 ± 0.39	< 10.93	< 10.02	66 ± 25	1
cid_346	2.219	46.55 ± 0.05	46.17 ± 0.09	< 11.38	10.48 ± 0.14	441 ± 41	3
cid_357	2.136	45.14 ± 0.22	45.73 ± 0.08	10.11 ± 0.36	< 9.58	163 ± 13	3
cid_451	2.450	46.47 ± 0.05	45.16 ± 0.05	11.03 ± 0.07	9.9 ± 0.14	43 ± 2	3
cid_499	1.457	45.93 ± 0.1	45.54 ± 0.05	10.78 ± 0.2	< 10.46	104 ± 5	1
cid_72	2.473	45.52 ± 0.08	46.06 ± 0.07	10.27 ± 0.14	< 10.48	342 ± 25	1
cid_86	2.096	45.64 ± 0.12	45.48 ± 0.09	11.21 ± 0.4	9.45 ± 0.13	91 ± 8	1
cid_864	1.617	44.73 ± 0.33	45.89 ± 0.05	10.62 ± 0.13	10.45 ± 0.11	236 ± 12	1
cid_970	2.501	45.8 ± 0.14	45.93 ± 0.05	10.94 ± 0.12	< 9.65	254 ± 13	3
cid_971	2.473	44.64 ± 0.23	45.24 ± 0.74	10.57 ± 0.45	9.78 ± 0.14	53 ± 39	3
lid_1565	1.593	46.17 ± 0.1	45.79 ± 0.08	11.63 ± 0.11	10.24 ± 0.11	187 ± 14	1
lid_1639	1.472	45.8 ± 0.13	46.44 ± 0.05	10.59 ± 0.05	10.66 ± 0.11	829 ± 41	1
lid_1646	1.470	46.22 ± 0.07	45.66 ± 0.07	11.96 ± 0.12	10.37 ± 0.11	139 ± 9	1
xuds_358	2.182	44.38 ± 0.21	45.6 ± 0.05	11.04 ± 0.12	< 10.69	120 ± 6	1
xuds_477	1.087	44.35 ± 0.05	45.11 ± 0.07	10.38 ± 0.15	< 10.32	39 ± 3	1
xuds_481	1.406	45.54 ± 0.12	45.86 ± 0.06	10.83 ± 0.53	< 10.67	216 ± 14	1
J1333+1649	2.089	47.91 ± 0.02	–	–	10.07 ± 0.14	–	2
X_N_102_35	2.19	46.82 ± 0.02	–	–	< 9.94	–	2
X_N_104_25	2.241	45.97 ± 0.4	–	–	< 9.97	–	2
X_N_128_48	2.323	45.81 ± 0.4	–	–	< 10.01	–	2
X_N_44_64	2.252	45.51 ± 0.07	45.93 ± 0.15	11.09 ± 0.25	10.16 ± 0.14	257 ± 38	2
X_N_53_3	2.434	46.21 ± 0.03	46.41 ± 0.11	–	10.05 ± 0.14	775 ± 85	2
X_N_6_27	2.263	45.85 ± 0.05	< 45.9	–	9.56 ± 0.14	< 239	2
X_N_81_44	2.311	46.8 ± 0.03	45.93 ± 0.2	11.04 ± 0.37	9.68 ± 0.14	257 ± 51	2
cid_1253	2.147	45.08 ± 0.18	46.02 ± 0.3	10.99 ± 0.25	11.03 ± 0.14	316 ± 95	2
cid_1605	2.121	46.03 ± 0.02	< 45.54	–	< 9.61	< 105	2
cid_166	2.448	46.93 ± 0.02	< 45.92	10.38 ± 0.22	10.37 ± 0.14	< 251	2
cid_247	2.412	45.49 ± 0.04	45.73 ± 0.05	10.03 ± 0.2	< 9.64	162 ± 8	2
cid_2682	2.435	45.48 ± 0.1	< 45.54	11.03 ± 0.04	< 9.95	< 105	2
cid_337	2.226	45.34 ± 0.09	45.63 ± 0.03	11.13 ± 0.04	< 9.88	129 ± 4	2
cid_38	2.192	45.78 ± 0.04	< 45.98	11.01 ± 0.12	< 9.98	< 288	2
cid_467	2.288	46.53 ± 0.04	< 45.74	10.1 ± 0.29	< 9.92	< 166	2
cid_852	2.232	45.5 ± 0.11	< 45.57	11.17 ± 0.02	< 10.0	< 112	2
lid_1289	2.408	45.09 ± 0.08	< 44.98	9.59 ± 0.14	< 9.78	< 29	2
lid_1852	2.444	45.25 ± 0.09	< 45.28	10.07 ± 0.13	< 9.63	< 57	2
lid_206	2.33	44.77 ± 0.12	–	10.3 ± 0.25	9.69 ± 0.14	–	2
lid_3456	2.146	45.68 ± 0.07	46.08 ± 0.17	10.75 ± 0.3	< 10.03	362 ± 62	2

Notes. Bolometric luminosity $L_{\rm bol}$, FIR luminosity $L_{\rm FIR}$ (8-1000 μm, star-formation only) and stellar mass M_* are derived from SED fitting (see Sect. 5.3.1). SFRs are obtained from the FIR luminosity applying the Kennicutt (1998) relation corrected for a Chabrier (2003) IMF (i.e., reduced by 0.23 dex). CO luminosity $L'_{\rm CO}$ is derived from Eq. 5.1. Errors are given at 1σ.

We include in the control sample all the non-active galaxies observed in CO(3-2), CO(2-1) and CO(1-0), as obtained by ALMA and NOEMA, and convert them to the CO(1-0) using $r_{21} = 0.6$ and $r_{31} = 0.5$, excitation ratios commonly found for star-forming galaxies in the same range of redshift as our AGN (Daddi et al. 2010; Tacconi et al. 2013; Kakkad et al. 2017). Since Tacconi et al. (2018) only provide the final molecular gas masses, CO fluxes were retrieved from the literature (Boogaard et al. 2020; Birkin et al. 2021, and as listed in Tacconi et al. 2018) or provided by the PHIBSS collaboration (L. Tacconi, private communication). We also checked the nature of the galaxies in the control sample and excluded those that are flagged as AGN. We do not include such targets in our AGN sample because identified as AGN with methods different than ours and because the stellar masses and the SFRs were not corrected accounting for the AGN contribution and could thus be overestimated.

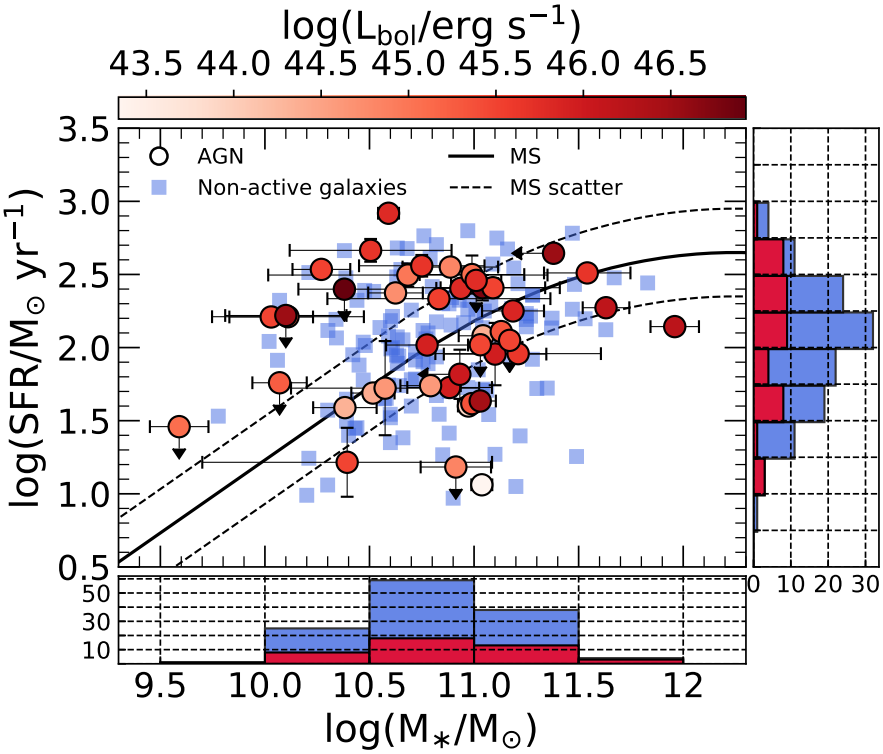

Figure 5.5: Comparison of SFR and stellar mass of the AGN host galaxies (SUPER+KASHz, red circles) and the non-active galaxies of the control sample (blue squares). The red circles are colorcoded based on the AGN bolometric luminosity, as retrieved from SED fitting. The two side panels show the distribution of SFR (right) and M_* (bottom) for AGN (red) and non-active galaxies (blue).

All the targets selected for the comparison sample have available stellar mass estimates and FIR luminosity. However, a small subsample of PHIBSS galaxies has SFR estimates from Hα fluxes. Based on the reasonable agreement between the SFRs derived from Hα and from the FIR for main sequence (MS) galaxies at cosmic

noon (within ≃0.4 dex; Rodighiero et al. 2014; Puglisi et al. 2016; Shivaei et al. 2016), we convert such the SFRs to FIR luminosity applying the Kennicutt (1998) relation corrected for a Chabrier (2003) IMF (i.e., reduced by 0.23 dex).

The final control sample of non-active galaxies consists of those targets satisfying all the selection criteria mentioned above (127 targets). It covers the $1 \leq z \leq 2.5$ redshift range and the same range in stellar mass as our AGN host galaxies, within the uncertainties ($\log M_*/\mathrm{M}_\odot = 9.5 - 12$). We then divide the control sample in bins of stellar mass of 0.5 dex width and proceed with the SFR match with our AGN, selecting all those non-active galaxies that show a SFR equal or lower to that of the AGN in a given mass bin, so to account for SFR upper limits in our sample. We show in Fig. 5.5 the comparison of our AGN sample (SUPER+KASHz) and the comparison sample in terms of SFR vs. M_*, plus the distribution of the two parameters both for AGN hosts and non-active galaxies.

5.5 Results from the merged SUPER+KASHz sample

We present in this Section the quantitative analysis used to compare the properties of the SUPER+KASHz AGN host galaxy sample and those of the control sample of non-active galaxies described in Sect. 5.4, in terms of CO and FIR luminosity, as well as stellar mass and gas fraction.

The full SUPER+KASHz sample is obtained by merging the measurements presented in C21 with those described in this thesis, totalling 43 AGN for which all the quantities of interest (M_*, L_{FIR} and L'_{CO}) are available, either as constrained or as upper (or lower) limits. In other words, we discard those 8 AGN missing at least one of the parameters of interest needed for our analysis, so to have a uniform sample throughout the analysis. In this way, our analysis is also free of the risk of biasing our results due the impossibility of finding a match in the control sample for such systems missing a key parameter.

The final, merged SUPER+KASHz sample presents a CO detection rate of ∼50%, that is, half of the sample has a constrained measure of the CO luminosity. Moreover, the FIR luminosity is well constrained for all targets but 8 of them, while for two AGN (cid_346 and cid_178, which are both bright Broad Line AGN) we could only place an upper limit for the stellar mass from SED fitting. We summarize the properties of the full sample in Table 5.3.

We performed our analysis applying a Bayesian framework as presented in C21, which allows us to take into account the upper (and lower) limits on both the dependent and independent variables when searching for the best fit relation between two quantities. As already mentioned, there is only one main difference in this work with respect to C21: given the heterogeneity of the KASHz sample in terms of CO transition, we carry out our analysis using the CO(1-0) luminosity, thus we assumed

a CO SLED for the AGN that we uniformly applied to all the CO measurements of SUPER+KASHz AGN (see Sect. 5.3) and a second one for the star forming galaxies of the control sample (see Sect. 5.4). Apart from this, our analysis is free of the additional uncertainties inherent to the choice of an $\alpha_{\rm CO}$ conversion factor and the conversion of the FIR luminosity into SFR, just as that of C21.

We address the effects of AGN feedback on the properties of SUPER+KASHz host galaxies by assessing whether they differ from the control sample in terms of: *i)* CO and FIR luminosities, *ii)* CO luminosity and stellar mass, *iii)* distribution of gas fraction, for which we consider the observational proxy $f_{\rm gas} = L'_{\rm CO}/M_*$, and *iv)* gas fraction vs. stellar mass. Moreover, we investigate the possibility of a dependence of the gas fraction of AGN host galaxies on the bolometric luminosity of the AGN.

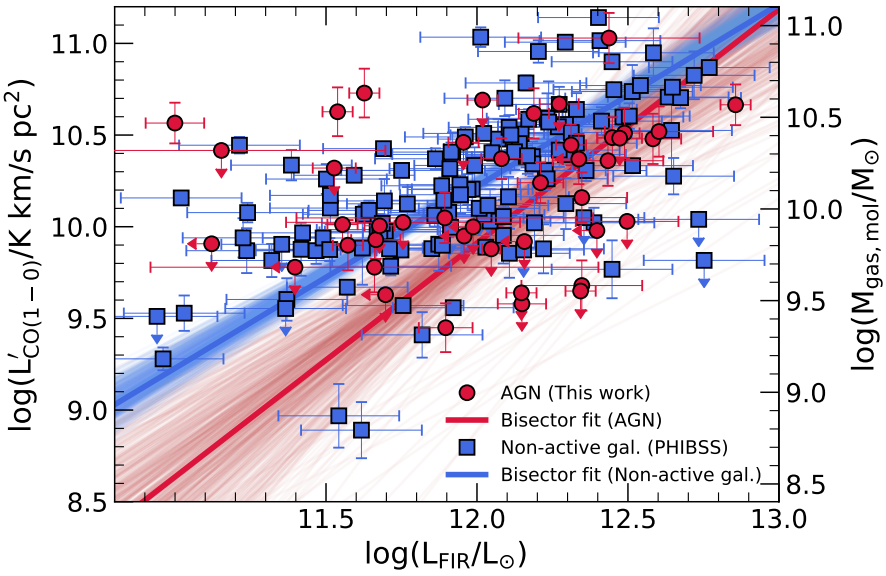

Figure 5.6: CO luminosity vs. FIR luminosity bisector fits of AGN host galaxies (SUPER+KASHz, red circles) and non-active galaxies of the control sample (blue squares). Thick lines mark the bisector fits obtained by adopting a Bayesian framework (see main text). The dispersion of the fits is given by plotting 500 realizations of the bisector fits. The vertical axis on the right is derived by assuming $\alpha_{\rm CO} = 0.8\,{\rm M}_\odot/({\rm K\,km\,s^{-1}pc^2})$ and serves for showing purposes only, since we only consider $L'_{\rm CO}$ in our quantitative analysis (see main text).

5.5.1 CO vs. FIR luminosity

The relation of CO and FIR luminosity can be considered as the integrated form of the Schmidt-Kennicutt law. Our aim is to quantify whether the SUPER+KASHz host galaxies follow a different distribution in this parameter space with respect to the non-active galaxies of the control sample. As mentioned, we follow the procedure of C21 in a Bayesian framework. We fit a linear model to the data applying the

ordinary least-squares (OLS) bisector fit method (Isobe et al. 1990), that is, we take into account the uncertainties on $L'_{\rm CO}$ and $L_{\rm FIR}$ separately and then we consider the bisector of the two lines. We thus derive the two best fits, to then be combined in the bisector fit in a Bayesian framework, so to take into account the upper limits on both quantities. When building the likelihood function of constrained values, we assumed their uncertainties as Gaussian-distributed. We included the upper limits by constructing an error function for each of them, generated as the integration of the Gaussian likelihood from 0 to the value of the upper limit (e.g., see Sawicki 2012), that is, 3σ for both CO and FIR luminosity. We then sample the yielded likelihood function through the `emcee` library (Foreman-Mackey et al. 2013), a python implementation of the invariant MCMC (Monte Carlo Markov Chain) ensemble sampler of Goodman & Weare (2010). We derive the marginalized posterior distribution by sampling the posterior distribution in the parameter space, using as initial guess the best fit obtained through the python module scipy.optimize (Virtanen et al. 2020). We include an additional intrinsic scatter to the relation as a third free parameter (that is, in addition to the slope and intercept) to account for the possibility of underestimated uncertainties, given the wide range of parameters spanned by our sources ($\sim$2.5 dex both in $L'_{\rm CO}$ and in $L_{\rm FIR}$). Best-fit parameters were then derived as the median of the sampled marginalized posterior distribution of the OLS bisector fit parameters, assigning as uncertainties the 18th and 84th percentiles. The final values of slope and intercept for the bisector fit were then derived from the OLS best fit values following Isobe et al. (1990).

Table 5.4: Summary of best fit parameters for SUPER+KASHz AGN and for the control sample of non active galaxies.

	SUPER+KASHz		*Non-active galaxies*	
Bisector fits	a	b	a	b
$\log L'_{\rm CO} = a \log L_{\rm FIR} + b$	$1.28^{+0.29}_{-0.24}$	$-5.41^{+2.95}_{-3.48}$	0.99 ± 0.06	$1.69^{+0.69}_{-0.78}$
$\log f_{\rm gas} = a \log M_* + b$	$-0.83^{+0.2}_{-0.18}$	$8.27^{+2.02}_{-2.17}$	-1.16 ± 0.10	$11.91^{+1.11}_{-1.04}$
$\log f_{\rm gas} = a \log L_{\rm bol} + b$	$-0.82^{+0.16}_{-0.19}$	$36.35^{+8.76}_{-7.22}$	–	–
Distribution	μ		μ	
$f_{\rm gas}$	$-0.96^{+0.15}_{-0.11}$		$-0.57^{+0.05}_{-0.06}$	

Figure 5.6 shows the results of the described procedure for what concerns the integrated Schmidt-Kennicutt planes of AGN sample (red) and non-active galaxies control sample (blue). The dispersion around the bisector fit is obtained by considering values of slope and intercept within one sigma of the sampled marginalized posterior distributions of the two fits (along the x and y axes) and using them to produce 500 realizations of the bisector fit. We report in Table 5.4 the best fit parameters of the best fit relation $\log(L'_{\rm CO}/{\rm K\ km\ s^{-1} pc^2}) = a \log(L_{\rm FIR}/{\rm erg\ s^{-1}}) + b$ in

the $\log L'_{\rm CO} - \log L_{\rm FIR}$ plane for both samples. Our main aim here, however, resides in probing if the two samples are indeed different and in quantifying the shift of the two distributions. Considering the dispersion of the two bisector fits, we derive a discrepancy between the two samples of less than 2σ, consistent with that obtained by C21.

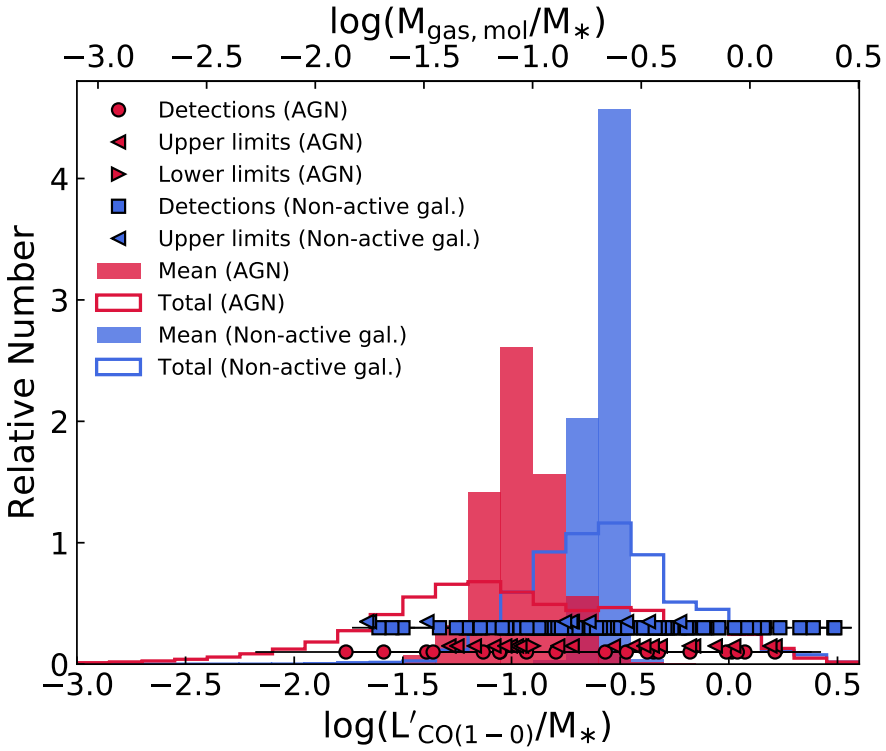

Figure 5.7: Distribution of the gas fraction (in terms of observational proxy $L'_{\rm CO}/M_*$) for AGN host galaxies (SUPER+KASHz, red) and non-active galaxies of the control sample (blue). Unfilled histograms show the total distributions, obtained by joining the sampled posterior distribution of each target for both samples. The filled histograms show the sampled posterior distribution of the mean of the hierarchical Gaussian prior used in our Bayesian analysis. Blue squares indicate the mean of each target in the control sample, red circles that of each AGN in the SUPER+KASHz sample. Blue and red triangles indicate upper limits (or lower limits, if pointing to the right) for the gas fraction of non-active galaxies and AGN, respectively. The top axis is derived by assuming $\alpha_{\rm CO} = 0.8\,{\rm M}_\odot/({\rm K\,km\,s^{-1}pc^2})$ and serves for showing purposes only, since we only consider $L'_{\rm CO}$ in our quantitative analysis (see main text).

5.5.2 Gas fraction distribution

With the aim of gathering a thorough knowledge of the difference among AGN hosts and non-active galaxies, we compared the gas fraction distribution of the two samples, measured through the observational proxy of $f_{\rm gas}$, that is the ratio

between CO luminosity $L'_{\rm CO}$ and M_* ($f_{\rm gas}$ =$L'_{\rm CO}/M_*$). Similarly to C21, we do not address the distribution of the ratio of $L'_{\rm CO}$ and $L_{\rm FIR}$ (observational proxy for the SF depletion time), since around half of our targets present an upper limit in at least one of the two quantities, with a quarter of our sample showing an upper limit for both. Our aim is to derive the mean ($\mu_{f_{\rm gas}}$) of the gas fraction distribution of each sample and quantify how they relate one another. Once more, we carry out our analysis in a Bayesian framework, which allows us to take into account upper limits on both $L'_{\rm CO}$ and M_*. There is only one target (cid_178) that has an upper limit for both quantities, and thus we discard it from this analysis given the impossibility of placing a useful constraint on its gas fraction.

Following C21, we assumed that the gas fractions of both samples follow a Gaussian distribution, supported by the tests performed by C21 to demonstrate the validity of such an assumption both on the xCOLD-GASS reference survey (Saintonge et al. 2017) and in PHIBSS galaxies at cosmic noon. We thus adopt the Bayesian hierarchical method developed by C21: we assumed that the prior distribution, common to both samples, is Gaussian and defined by two hyper-parameters, that is, the mean $\mu_{f_{\rm gas}}$ and the standard deviation $\sigma_{f_{\rm gas}}$, for both of which we set uniform, positive-value priors. Following the approach described in Sect. 5.5.1, we assume that the uncertainties of the constrained gas fractions are Gaussian-distributed and we apply the error function for the upper limits. The total posterior distributions of the gas fractions of AGN hosts and non-active galaxies (red and blue unfilled histograms, respectively; see Fig. 5.7) were built by joining the sampled posterior distribution of each target from both samples and, as such, cover the full range of $f_{\rm gas}$ spanned by each target with the plus of carrying also the information of the upper (lower) limits. The same figure also shows the sampled posterior distribution of the mean of the hierarchical Gaussian prior that we adopted in our Bayesian analysis (red and blue filled histograms). As for the other quantities, we consider the 50th percentile as best value and the 18th and 84th percentiles as uncertainties. We find that the mean $\log(L'_{\rm CO}/M_*)$ of our AGN sample is lower than that of non-active galaxies, as also found by C21 for the sole SUPER sample. However, the mean gas fractions of the SUPER+KASHz sample and the non-active galaxy control sample are different at the 2.5σ level, i.e., similar to the 2.2σ result of C21 when considering only SUPER AGN.

5.5.3 Gas fraction vs. stellar mass

First, we assessed the relations in the CO luminosity vs. stellar mass plane for both samples. We performed bisector fits following the procedure described in Sect. 5.5.1, obtaining very similar results as those of C21. We derive a positive relation between the two quantities both for AGN and non-active galaxies, with a flatter index for the AGN sample and no clear, statistical difference between the two samples (see

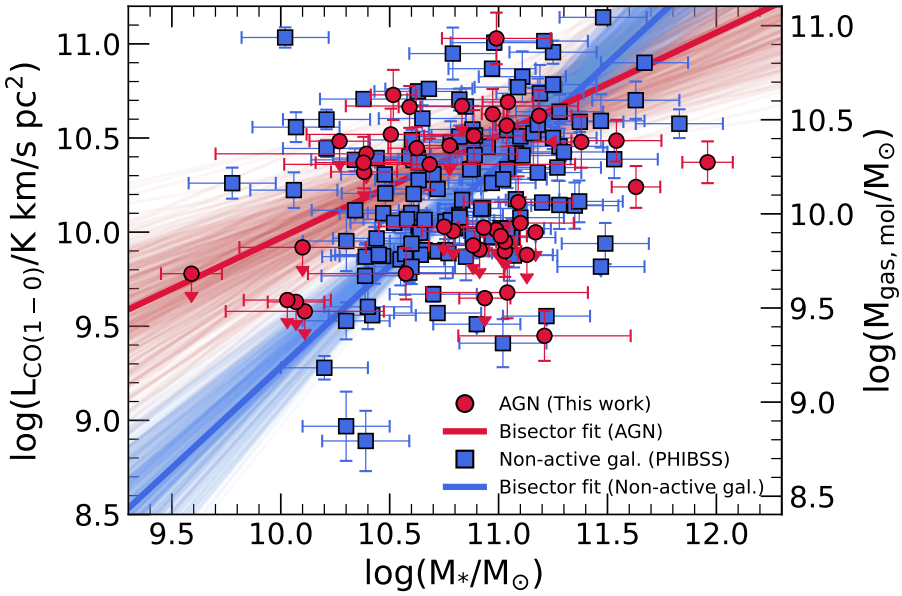

Figure 5.8: CO luminosity vs. stellar mass bisector fits of AGN host galaxies (SUPER+KASHz, red circles) and non-active galaxies of the control sample (blue squares). Thick lines mark the bisector fits obtained by adopting a Bayesian framework (see main text). The dispersion of the fits is given by plotting 500 realizations of the bisector fits. The vertical axis on the right is derived by assuming $\alpha_{\rm CO} = 0.8\,{\rm M}_\odot/({\rm K\,km\,s^{-1}pc^2})$ and serves for showing purposes only, since we only consider $L'_{\rm CO}$ in our quantitative analysis (see main text).

Fig. 5.8), as also found by C21.

We then addressed the relations for $\log(L'_{\rm CO}/M_*)$ vs. $\log M_*$ of SUPER+KASHz AGN and non-active galaxies, adopting the same procedure for the bisector fits as presented in Sect. 5.5.1. The yielded bisector best fits are shown in Fig. 5.9 and best fit parameters are summarised in Table 5.4.

Both samples present a similar trend between gas fraction and stellar mass, with decreasing gas fraction for increasing stellar mass, that corresponds also to the mean general trend of star-forming galaxies as found, for instance, by Tacconi et al. (2018). Regarding the comparison of our SUPER+KASHz AGN and non-active samples, we find that also in this case the two relations are not significantly different (well below 3σ).

5.5.4 Gas fraction vs. bolometric luminosity

Lastly, we investigated the possibility of a correlation between the gas fraction of the host galaxies and the bolometric luminosity of the AGN in the SUPER+KASHz sample. Bolometric luminosities were considered as derived from SED fitting, either from this work (see Sect. 5.3.1) or from C21.

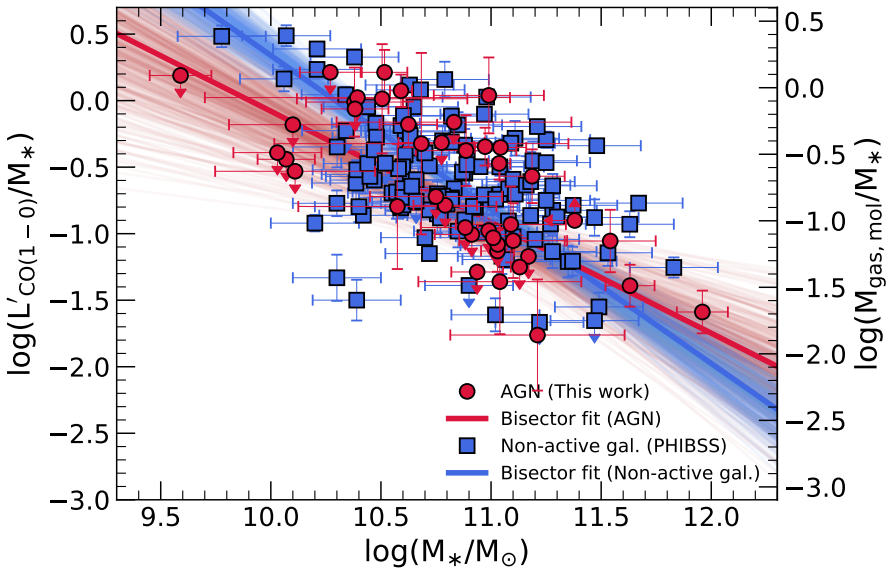

Figure 5.9: Gas fraction vs. stellar mass bisector fits of AGN host galaxies (SUPER+KASHz, red circles) and non-active galaxies of the control sample (blue squares). Thick lines mark the bisector fits obtained by adopting a Bayesian framework (see main text). The dispersion of the fits is given by plotting 500 realizations of the bisector fits. The vertical axis on the right is derived by assuming $\alpha_{\rm CO} = 0.8\,{\rm M}_{\odot}/({\rm K\,km\,s^{-1}pc^2})$ and serves for showing purposes only, since we only consider $L'_{\rm CO}$ in our quantitative analysis (see main text).

We applied again the bisector fit method described in Sct. 5.5.1. The data points show a rather flat distribution, yet the best fit relation hints at a negative trend between the two quantities, with decreasing gas fraction for increasing AGN bolometric luminosity. However, statistical tests, such as the Kendall-τ test, show that the correlation between the two quantities is not significant.

5.6 Do cosmic noon AGN gas-deplete their hosts?

We presented in this Chapter the expansion of the study carried out by C21 on a sample of AGN drawn from the SUPER survey. We enlarged such sample of cosmic noon AGN by drawing sources from a sibling survey of SUPER, that is, the KASHz survey. We collected and analyzed all the available ALMA observations of KASHz AGN in Band 3 and 4, that is, targeting the low-J transitions at the redshifts of our sources ($1 < z < 2.6$). Seven of the KASHz ALMA targets are already part of the SUPER sample analyzed in C21, so for such sources we refer to the ALMA analysis and results as reported in C21. For the other KASHz ALMA targets, we reduced the observations with the aim of recovering the CO flux that best resembles the total CO luminosity of the host galaxies. Thus, we imaged all

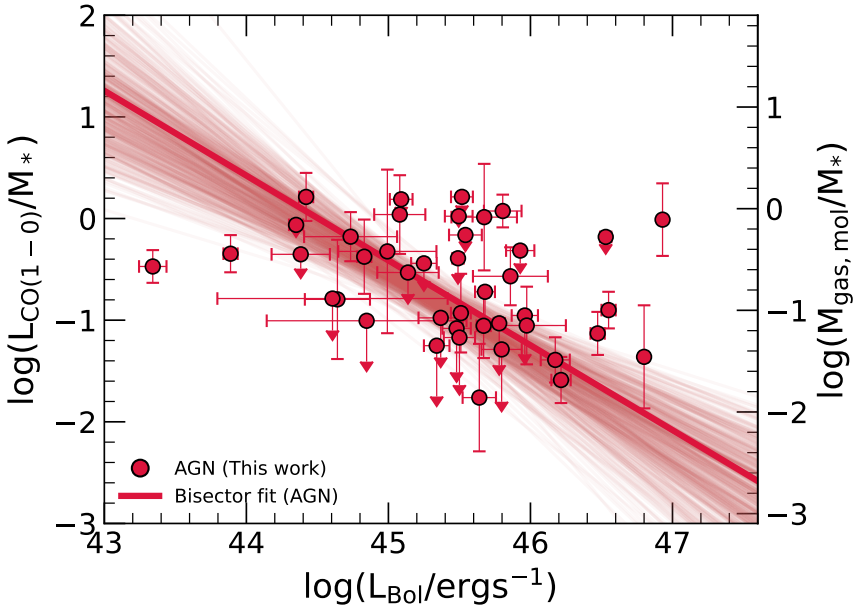

Figure 5.10: Gas fraction vs. bolometric luminosity of AGN host galaxies (SUPER+KASHz, red circles). Thick lines mark the bisector fit obtained by adopting a Bayesian framework (see main text). The dispersion of the fits is given by plotting 500 realizations of the bisector fit. The vertical axis on the right is derived by assuming $\alpha_{\rm CO} = 0.8\,{\rm M}_{\odot}/({\rm K\,km\,s^{-1}pc^2})$ and serves for showing purposes only, since we only consider $L'_{\rm CO}/M_*$ in our quantitative analysis (see main text).

the targets using natural weights and by tapering the beam sizes to 2″ or to twice the natural-weighted spatial resolution in the case of very resolved ALMA cubes. We then applied a uniform analysis of all the continuum-subtracted ALMA cubes, and retrieved the CO fluxes from the fitting of their 1D spectra (see Sect. 5.3).

The one main difference between the analysis presented in this work and that carried out by the SUPER survey group is that our ALMA data is archival and, as such, heterogeneous for what concerns the targeted CO transition of each AGN. For this reason, we uniformly converted the measured CO(2-1), CO(3-2), CO(4-3) emission line fluxes to the CO(1-0) ground transition assuming a CO SLED as derived by Kirkpatrick et al. (2019).

The other key quantities of interest were derived from SED fitting with the CIGALE code v.2022.1 (Boquien et al. 2019; Yang et al. 2020). The photometry of our sources was collected from the most updated catalogs provided by the X-ray deep survey collaborations, the CANDELS/GOODS-S collaboration or the HELP collaboration (see Sect. 5.3.1 and Appendix E for further details). Adopting this procedure, we derived reliable estimates for the stellar mass and the FIR luminosity of our host galaxies (decontaminated from the AGN contribution), which we use as proxy for the SFR, and the bolometric luminosity of the AGN.

The merged SUPER+KASHz AGN sample was then obtained by combining the

sample and results presented in this thesis with those of C21. We removed from this sample those targets for which at least one parameter between $L_{\rm FIR}$ and M_* (if not both) was not available, so to avoid any bias induced by the impossibility of finding a reliable match for such sources in the non-active galaxy sample. The latter was assembled starting from the PHIBSS project (Tacconi et al. 2018), a collection of 1444 star-forming galaxies at $z = 0 - 4.4$ with available CO measurements and key galaxy properties (mainly, SFR, $L_{\rm FIR}$, M_*). We complemented the PHIBSS sample with the sub-*mm* galaxies of Birkin et al. (2021), to better sample the higher end of the MS, and with the non-active galaxies of the ASPECS project (Boogaard et al. 2020, and references therein), to better cover the lower-end of the stellar mass distribution. We then removed from the control sample those targets identified as AGN relying on the literature and on X-ray catalogs. The final shape of the control sample was determined by matching its constituents with those of the SUPER+KASHz AGN sample, first in redshift, then in stellar mass and finally in SFR (see Sect. 5.4), totalling 127 non-active galaxies.

We then performed a comparative study of the properties of our AGN sample and the control sample of non-active galaxies in the Bayesian framework as developed by C21, with the aim of providing a quantitative analysis of the possible differences among the two samples also taking into account the upper (and lower) limits on the measured properties. We assessed the relations in 2D parameter spaces by applying the bisector best fit method in the Bayesian framework described in Sect. 5.5.1, while we investigated the distribution of the gas fraction ($\log(L'_{\rm CO}/M_*)$) in the two samples through the hierarchical Bayesian method as described in Sect. 5.5.2. We carried out our comparative study in the following parameter spaces:

- $L'_{\rm CO(1-0)}$ vs. $L_{\rm FIR}$ (see Sect. 5.5.1);
- $L'_{\rm CO(1-0)}$ vs. M_* (see Sect. 5.5.2);
- $\log(L'_{\rm CO}/M_*)$ distribution (see Sect. 5.5.2);
- $\log(L'_{\rm CO}/M_*)$ vs. M_* (see Sect. 5.5.3).

No significant difference between the two samples was found in all the tested parameter spaces. In general, our study on an enlarged sample of cosmic noon AGN confirms the results of C21, that is, cosmic noon AGN, selected without priors regarding AGN feedback, are statistically indistinguishable from non-active galaxies, matched in z, M_*, SFR.

Then, we addressed the possibility of a correlation between gas fractions and bolometric luminosity in the AGN sample. Even if statistical tests returned that the correlation is not significant, the yielded relation between the two quantities hints at a decreasing trend of $\log(L'_{\rm CO}/M_*)$ for increasing AGN bolometric luminosity. A

similar hint can be derived by comparing the KASHz ALMA sample presented in this work with the SUPER ALMA targets of C21: SUPER ALMA targets are in general more powerful by selection, they qualitatively seem to reside in less massive galaxies and to show lower CO luminosity or stricter upper limits in the case of non-detections. Thus, we might have diluted the tentative CO depletion seen by C21 in SUPER ALMA targets by including in the expanded sample AGN that are more gas-rich (or present loser upper limits) and less-powerful. In fact, all SUPER targets show $\log(L_{\rm bol}/{\rm erg\ s^{-1}}) > 45$, but one with $\log(L_{\rm bol}/{\rm erg\ s^{-1}}) = 44.64$ (that is shared with KASHz), while one-third of KASHz AGN has $\log(L_{\rm bol}/{\rm erg\ s^{-1}}) < 45$.

Moreover, the bolometric range covered by the merged SUPER+KASHz sample mainly includes regular AGN, with 80% of the sample showing $\log(L_{\rm bol}/{\rm erg\ s^{-1}}) < 46$. As Fig. 1.8 (left) shows, the bulk of the high-z AGN host galaxies that were found to be CO depleted or highly influenced by AGN activity contain much more powerful AGN ($46.4 \lesssim \log(L_{\rm bol}/{\rm erg\ s^{-1}}) \lesssim 48$). Thus, if our samples are not biased toward high-luminosity AGN, then their hosts are very much alike their non-active analogs, that is, the effects of AGN feedback on the properties of the hosts, integrated over the full galaxy, are not significant. However, the tentative negative trend seen between the observational proxy for the gas fraction and the luminosity of the AGN hints at the possibility of a luminosity effect regulating the efficiency by which AGN might impact on galaxy growth. Such a possibility will be investigated with the inclusion of high-power AGN, based on the results available in the literature (e.g., selecting cosmic noon AGN from the compilation of Perna et al. 2018 and those of the ASPECS survey, Boogaard et al. 2020), which will grant us an AGN sample spanning five orders of magnitude in bolometric luminosity ($43 \lesssim \log(L_{\rm bol}/{\rm erg\ s^{-1}}) \lesssim 48$).

Bischetti et al. (2021) recently investigated the effects of AGN feedback on the molecular gas reservoir of WISSH (WISE-SDSS selected hyper-luminous) quasars[¶]. Among the various tests, the authors compared the gas fraction of WISSH AGN with that of star-forming galaxies after applying a correction to take into account the evolution of the gas fractions with redshift and distance from the MS ($\Delta{\rm MS} = {\rm sSFR}/{\rm sSFR_{MS}}$). In fact, analyses focused on assessing the molecular gas content of star-forming galaxies throughout cosmic time up to $z \simeq 4$ (e.g., Genzel et al. 2015; Tacconi et al. 2018) pointed out a dependency of the gas fraction on redshift and distance from the MS. Such an effect could impact both on the selection of non-active galaxies for the control sample and on how they then compare to our AGN hosts. Second part of our analysis will be to investigate new methods to select non-active galaxies mitigating such effects, for instance by performing the M_* match after having devided the sample in redshift bins. Moreover, we will test whether the

[¶]The WISSH quasar project is a multi-wavelength campaign designed to probe the most energetic AGN-driven outflows at high-z, in a sample of hyper-luminous objects ($L_{\rm bol} > 10^{47}$ erg s^{-1}, i.e., at the brightest end of the AGN luminosity function) at $z = 1.5 - 5$ (Bischetti et al. 2017).

lack of significant difference among SUPER+KASHz AGN and the control sample could be ascribed to an evolution of the galaxy properties with redshift and distance from the MS that we did not take into account. However, such a correction would be of non-trivial implementation for SUPER+KASHz AGN since for many of our targets ($\simeq$ 21 %) we could only derive upper (or lower) limits for the $L_{\rm FIR}$ and/or M_*, i.e. the key quantities that define the distance of a galaxy from the MS.

As discussed in C21, there are many possible reasons why we do not find significant gas depletion for our AGN sample. The most important ones are:

- we are comparing two phenomena that occur with very different timescales (e.g., Harrison 2017; Harrison et al. 2018): the timescales of visible AGN activity do not necessarily mirror the AGN duty cycle, plus also the timescales of feeding and feedback in general are uncertain. For instance, the AGN might have become less luminous or non-visible by the time the effects of its impact have become observable, or even the galaxy might have accreted more gas from its surroundings reducing the overall effect of AGN activity;

- we are comparing phenomena and effects on too different spatial scales: through high-resolution studies, AGN were seen to create regions of CO depletion in their surroundings (Rosario et al. 2019; Sabatini et al. 2018; Feruglio et al. 2020), where the bulk of the molecular gas is in a warmer phase due to AGN heating (e.g., through accretion radiation in the form of X-ray photons, Fabbiano et al. 2019). However, whether AGN can have a long-term impact and significantly affect the integrated properties of galaxies (total molecular gas mass, total SFR) is still unclear. For instance, if the AGN still has not affected a significant portion of the galaxy, then we are diluting the effects of negative AGN feedback by considering the integrated properties of host galaxies;

- the SUPER and KASHz surveys have selected AGN only based on their X-ray luminosity and redshift, with no priors regarding AGN feedback. Here and in C21, we investigated AGN feedback by studying the overall properties of the AGN sample compared to those of non-active galaxies. Literature results finding AGN hosts to be significantly gas depleted are usually associated with AGN feedback "caught in the act", i.e. with sources showing massive AGN-driven outflows on kpc-scales in at least one gas phase. One might then infer that gas depletion is significant and widespread only in those sources "caught in the act". For example, two AGN of the KASHz sample, lid_1646 and lid_1639 (or XID5321 and XID5395, respectively), reside in significantly depleted host galaxies, which present powerful [OIII] outflows (Perna et al. 2015; Brusa et al. 2016) and also cospatial massive CO(5-4) outflows (Ricci et al. 2023, in prep). Based on the results obtained in this thesis, such AGN are two peculiar cases of our SUPER+KASHz sample. A detailed comparison between [OIII] outflows

and CO properties of SUPER+KASHz targets will be the subject of a future work, possibly revealing other peculiar cases like XID5321 and XID5395.

Lastly, this work provides a new, sizable sample to compare the predictions of cosmological simulations with real observations. In fact, Ward et al. (2022) concluded that none of the analyzed simulations predicts AGN hosts to be more gas depleted than non-active galaxies. However, the AGN luminosity range covered by the simulations and the observations hardly overlapped, especially at $z = 2$, where the authors referred only to WISSH quasars (Bischetti et al. 2021).

Chapter 6

Conclusions and future perspectives

In this thesis I presented my contribution to the collective efforts in pinning down the effects that AGN feedback has on the build up of galaxies. This was done with a dual approach: first, I investigated what I referred to as feedback "caught in the act", that is, AGN-driven winds; second, I addressed the effects of AGN feedback on the host-galaxies properties.

6.1 AGN feedback as "caught in the act"

AGN-driven winds are part of what astronomers have identified as the possible drivers of AGN feedback, and are observed in different gas phases and at all scales. Here, I have focused on the innermost and fastest winds, that is UFOs, visible in the X-rays. This is a particularly important wind phase, since models have identified UFOs as the first link in the generation of galaxy-wide outflows.

6.1.1 Statistical studies of high-z UFOs

One of the aims of this thesis is to provide a statistically meaningful analysis of UFOs in the high-z Universe ($z > 1$), with the ultimate goal of measuring some key quantities that are still unexplored: high-z UFO average properties ($N_{\rm H}$, ξ, $v_{\rm out}$, kinetic power, momentum boost, feedback efficiency), high-z UFO detection fraction, and UFO duty cycle at high-z. In Chapter 2, Sect. 2.1, I presented the analysis of what I referred to as the "feedback-unbiased" sample, that is, the best effort made so far in building a large sample of high-z AGN, selected without prior knowledge regarding AGN feedback signatures, that would allow to study UFOs in a statistically meaningful way. We tackled the problem by first selecting the best candidates for such a scope, that is, GLQs (see Sect. 2.1). By the magnification provided by gravitational lensing, GLQs are the best candidates to obtain good-

S/N data with reasonable exposures and to populate our samples also with more "regular", high-z AGN. However, when searching for data that would have allowed us to constrain the presence/absence of the typical imprints of UFOs, we collided with reality: present-day X-ray facilities like *Chandra* and XMM-*Newton* are effective in probing high-z UFOs, but only through exposures targeted on the selected AGN, that is, planned to obtain spectra of high quality. This is, for instance, the case of the data available for the "feedback-biased" sample of Sect. 2.2, which in fact allowed us to meaningfully assess UFO presence/absence and driving mechanisms, even if the sample is limited in size (14 AGN at $z > 1.4$) and, as such, is not representative of the high-z AGN population.

However, since almost all the GLQs in the "feedback-biased" sample are also included in the "feedback-unbiased" one, we can combine the results of the two analyses and derive a first estimate of the detection fraction of UFOs at high-z: $\gtrsim$40–45%, i.e., very similar (slightly higher) than that measured in the local (Tombesi et al. 2010a; Gofford et al. 2013; Igo et al. 2020) and low-z Universe (Matzeu et al. 2022a).

Future perspectives. The main issue in assessing and studying, on a statistical basis, the presence of UFOs, especially in high-z sources, is to get high-enough count statistics in our X-ray spectra. Our efforts in building a catalog of high-z GLQs for which good S/N X-ray spectra are available showed that the great majority of data in the archives is not deep enough, highlighting the need for new-generation telescopes, such as *Athena* and *Lynx*, to significantly cut down the required exposure times.

While we await for new generation X-ray telescopes, we must deal with the tools at our current disposal to build meaningful samples of distant QSOs: *i)* gravitational lenses that enhance the X-ray flux of the background source and *ii)* search for priors of the X-ray fluxes of promising sources in the available catalogs. The coupling of these two key aspects could help us in building samples suitable for the characterization of UFO properties at high-z by means of the current available facilities.

There are many ways our analysis could be expanded and strengthened so to derive a finally robust assessment of UFO presence and recurrence at high-z (yet, always dependent on the availability of good-enough-S/N data). Many new GLQs have been discovered in recent years, for instance exploiting the great astrometric precision of the Gaia mission (Gaia Gravitational Lenses – GraL; e.g., Ducourant et al. 2018) and by searching for strong lensing systems in the Dark Energy Survey (STRong lensing Insights into the Dark Energy Survey, Lemon et al. 2020). Lemon and collaborators compiled a database of known GLQs and candidates*, totalling more than 200 sources. As a reference, more than 100 GLQs of this database ($\simeq$35%

*link to database, the lasted update in 2019.

of which are in XMM-*Newton* and/or *Chandra* archival fields) are not included in and will be a promising update of the "feedback-unbiased" sample.

Since its launch, *eROSITA* has produced outstanding all-sky images in the X-rays, by means of a much improved sensitivity and angular resolution with respect to its only predecessor, *ROSAT*. The *eROSITA* All-Sky Surveys (eRASS:s) will provide us with the first all-sky survey in the hard X-rays, with the promise of a huge leap forward through the discovery of many new, possibly bright high-z AGN. Even though the angular resolution ($\theta_{\rm res} \simeq 15''$, on-axis) of *eROSITA* does not allow to search for new GLQs, the eRASSs will grant us the unique opportunity to obtain X-ray priors of already-known systems. In fact, the eRASSs catalogs will provide us with fluxes or upper limits and possibly key spectral parameters of all known GLQs in the German *eROSITA* sky, key quantities to design the best observational strategy for their follow-up at X-ray wavelenghts. This will allow us to tackle the second fundamental aspect of the problem: the selection of those AGN whose X-ray flux will grant us, through "affordable" exposure times, to collect good-quality X-ray spectra.

Another key aspect would then be to include in such a sample also non-lensed AGN, so to reduce potential biases as much as possible. This can be done by searching for data in the X-ray archives for bright, non-lensed AGN, as well as by applying for time to observe known bright AGN with present-day facilities. In fact, results that have come about over the last two decades have shown that studies of high-z AGN are observationally challenging but highly rewarding, when carried out by means of long-enough exposures of present-day observatories. I was recently awarded a *Chandra* Cycle 24 proposal (150 ks, PI: Bertola) to point the X-ray brightest, non-lensed QSO at $z > 3$ (SDSS J0745 at z=3.2, part of the WISSH sample). Our aim is to observe the UFO that is expected to be driving, in an energy-conserving regime, the massive ionized [OIII] outflow detected in this source (Bischetti et al. 2017) and provide a redshift record holder for the best-S/N X-ray spectrum at $z > 3$.

6.1.2 Peculiar high-z GLQs

The samples presented in Chapter 2 include also some peculiar AGN, two of which were extensively discussed in this thesis.

The first peculiar AGN is Q 2237+030, a very unique GLQ thanks to its very nearby lens, which led astronomers to monitor such a system through many observational campaigns to probe microlensing events. We capitalized on the large X-ray dataset available for this source (40 exposures from 2000 to 2018; 37 from *Chandra* and 3 by XMM-*Newton*) to investigate presence and possible recurrence of UFOs. We discovered UFO events in this source, one of which in a XMM-*Newton*

dataset, that allowed us to apply physically-motivated wind models to retrieve the UFO properties. With the *Chandra* dataset, instead, we could probe *i)* single-image, single-epoch spectra, *ii)* single-image, multi-epoch stacked spectra and *iii)* image-integrated, multi-epoch stacked spectra. By considering the results obtained from the three different analyses, we could infer that such winds are variable and recurrent in this source as they are often seen to be (e.g., Dadina et al. 2005; Cappi et al. 2009; Giustini et al. 2011). By combining the two data samples, we managed to derive a rough estimate of the wind duty cycle of Einstein Cross, as $DC_{\rm W} \simeq 31\%$ (46%) at a significance of 95% (90%) confidence level, respectively.

The second peculiar AGN addressed in this thesis is APM 08279+5255, a source that we referred to as the archetype for high-z UFOs. We analyzed the latest X-ray exposures of this GLQ, obtained through our joint *NuSTAR*-XMM-*Newton* program aimed at measuring the high-energy cutoff in a few high-z, luminous QSOs. The 2019 data revealed that APM 08279 shows a long-lasting X-ray reflection component and a high-energy cutoff ($E_{\rm cut}= 99^{+91}_{-35}$ keV) consistent with the other two measurements available at high-z and high-$L_{\rm X}$ (Lanzuisi et al. 2019) and in line with $E_{\rm cut}$–$L_{\rm X}$ predictions of the pair-production thermostat model (Fabian et al. 2015), as Fig. 4.4 shows. However, the data yielded also several unexpected results: *i)* the source flux dropped by a factor of ≃2 compared to the level in the period 2000–2008; *ii)* the data do not manifest any UFO feature, with only some hints that can be modeled with a narrow Gaussian absorption line at $E_{\rm obs} \simeq 2.3$ keV (i.e., $E_{\rm rest} \simeq 11.6$ keV, corresponding to $v_{\rm out} \simeq 0.5c$ assuming the line is due to Fe XXVI; see Fig. 4.1); *iii)* in this fainter state, the continuum shape has dramatically changed: a strong reflection component (reflection fraction $R = 2.8^{+1.1}_{-0.9}$) has emerged, associated with a prominent Fe Kα emission line ($EW = 318^{+95}_{-90}$ eV). We concluded that the primary continuum level has dropped since the past decade, resulting in a strong reflection component (seen both in the Compton hump and the neutral Fe Kα line, see Fig. 4.1) from a distant ($r > 0.7$pc), cold reflector, which has not yet responded to the variation in accretion regime. The quality of 2019 data however did not allow for any other speculation on what happened to the nuclear winds of APM 08279.

Future perspectives. We asked and were granted a *Swift* monitoring of APM 08279 during summer 2022 to probe the source's current state. We found that its activity increased, matching again the flux level shown in the early 2000s. We proposed a joint XMM-*Newton*-*NuSTAR* observation, this time tailored at obtaining very good data in the XMM-*Newton* band so to properly assess the presence/absence of UFOs and thus their link with the source state. Unfortunately, very long exposures are needed to achieve our goal (140 ks+100 ks with XMM-*Newton*-*NuSTAR*, respectively) and we were not granted time in the last Announcement of Opportunity. We plan to address the TAC comments and repropose this observing program for next cycle. I have also led the planning and submission of a JWST/NIRSpec

IFU proposal to observe this unique GLQ, in a wavelength range that is only covered by shallow and/or spatially integrated archival data, with the aim of hopefully observing the yet-undetected lensing galaxy, deriving a solid lensing model and ultimately providing a secure measure of the magnification factor. This result will echo in many different astrophysical fields, from *i)* discovering if the FIR lines observed in APM 08279 (e.g., Downes et al. 1999; van der Werf et al. 2011; Walter et al. 2011; Decarli et al. 2012) are powered by a compact starburst core or the full host galaxy, to *ii)* offering a firm reference point for the evolution of the $M_{\rm BH} - \sigma$ relation with redshift, to *iii)* providing a true benchmark to test model predictions regarding the efficiency of AGN-driven winds.

Regarding the assessment of the processes regulating the properties of X-ray coronae, next-generation X-ray telescopes will be crucial in substantially expanding the samples used to test these phenomena. In particular, enlarging the sample with *a)* high-luminosity, lower-z AGN and *b)* with other high-z AGN, especially at the fainter luminosity end, will shed light on whether low- and high-z AGN comply with the same relations. Would they differ, only future studies over a large-enough sample of high-z AGN will disclose whether it is owed to the different luminosity regimes or whether it is a byproduct of a potential evolution with cosmic time. To this aim, the *eROSITA* All-Sky Survey will be key in discovering new high-z AGN, to then be followed up by present facilities such as *NuSTAR* and, hopefully, future hard X-ray instruments.

In the meantime, we have been working toward the expansion of the sample of high-luminosity, high-z AGN through *NuSTAR* observations. Regarding topic *a)*, we searched for the X-ray brightest quasars in the merged catalogs of the XMM-Newton spectroscopic survey of 40 quasars from the Palomar-Green (PG) Bright Quasar Survey (Piconcelli et al. 2005) and the most X-ray luminous ($L_{\rm X} \geq 10^{45}$ erg s^{-1} in the 0.5-2 keV band) radio-quiet QSOs found in the ROSAT Bright Survey (Krumpe et al. 2010). We then proposed in *NuSTAR* Cycle 9 a *NuSTAR*+XMM-*Newton* Large Program to observe the three X-ray brightest AGN ($f_{(2-10)} > 3\times10^{-13}$ erg s^{-1} cm^{-2}, $L_{(2-10)} > 8 \times 10^{44}$ erg s^{-1}) at $0.3 < z < 1.3$ from such merged catalog to further shed light on the processes regulating the X-ray corona. By the inclusion of high-luminosity targets at lower-redshifts, we will be able to assess whether both high-z and lower-z AGN comply to the same mechanisms.

Regarding topic *b)*, we searched for bright, high-z QSOs in the most updated Chandra source catalog Release 2.1 (CSC 2.1; Evans et al. 2020) and the fourth XMM serendipitous survey (4XMM-DR12, Webb et al. 2020a), by cross-matching them with the SDSS-DR16 quasar catalog (Wu & Shen 2022). We then excluded all blazars based on the most recent Roma-BZCAT catalog (Massaro et al. 2015) and as WISE MIR colors selection (D'Abrusco et al. 2019). Lastly, we only keep radio-quiet quasars with radio loudness RL$<$10 since the hard X-rays of radio-loud quasars

might be contaminated by their jet emission (Elvis et al. 1994; Padovani et al. 2017). Our clean sample thus totals 10 high-z ($z > 1$) radio-quiet quasars that are bright enough ($f_{(2-10)} > 3 \times 10^{-13}$ erg s^{-1} cm^{-2}) to ensure good constraints on their cutoff through reasonable exposure times with *NuSTAR*. Three of such sources are those presented in Lanzuisi et al. (2019) and this thesis (Bertola et al. 2022), demonstrating the efficiency of our selection. We proposed and were granted a *NuSTAR*+XMM-*Newton* Large Program in Cycle 8 (PI: Zhao) to observe four other high-z AGN of our clean sample, and were recently awarded a second *NuSTAR*+XMM-*Newton* Large Program in Cycle 9 (PI: Zhao) to complete the X-ray coverage of such sample.

6.2 The effects of AGN on galaxy growth at cosmic noon

Regarding the second approach of this thesis, I focused on assessing the effects that AGN are expected to have on the molecular gas reservoir of galaxies (i.e., the gas phase from which stars are formed). The idea is that, if AGN influence the evolution of a galaxy as a whole, then they will reasonably impact the molecular gas reservoir first, and then SF as a consequence.

Results available in the literature are however controversial and seem to hint at a dichotomy between low-z and high-z studies. Moreover, regarding the high-z Universe alone, literature results are usually based on few, high-luminosity and heterogeneous sources, pre-selected as good candidates for hosting outflows. This was true until recently, when the KASHz and SUPER surveys were conceived to provide multi-wavelength studies of unbiased high-z AGN samples at cosmic noon, selected solely based on X-ray luminosity and redshift range, without priors regarding AGN feedback. In particular, the SUPER project managed to demonstrate that, if we include regular AGN in our samples, more representative of the whole population, then AGN host galaxies only show hints of gas depletion.

In this thesis, we updated and expanded the work of C21, capitalizing on their Bayesian framework free of the uncertainties intrinsic to conversion factors between observable and physically meaningful quantities. We collected all the available ALMA data of cosmic noon KASHz AGN, that is the sibling survey of SUPER. Since our ALMA data is archival, it is heterogeneous in target CO transition. For this reason, we selected all those ALMA observations targeting low-J transitions (CO(2-1), CO(3-2), CO(4-3)) and then assumed a reasonable CO excitation ladder to convert all of our measurements to the transition to the ground state (CO(1-0)). Other key quantites of the AGN+galaxy system were retrieved through SED fitting with the CIGALE code (Boquien et al. 2019; Yang et al. 2020), collecting the most up-to-date photometry of our sources, as provided by the deep survey projects (CANDELS/GOODS-S, COSMOS, HELP collaboration).

By merging our ALMA results with those of C21, we obtained a sample of 43

SUPER+KASHz AGN at cosmic noon, with a CO detection rate of $\simeq 50\%$. This represents a $\simeq$10% increase in detection rate and a 40% increase in sample size with respect to SUPER AGN alone.

We built a control sample of non-active galaxies, matched in z, M_*, SFR to our AGN sample, by capitalizing on the PHIBSS project (Tacconi et al. 2018, and references therein), the ASPECS survey (Boogaard et al. 2020, and references therein) and the ALMA/NOEMA survey of sub-mm galaxies in the COSMOS, UDS, and ECDFS fields by Birkin et al. (2021).

We then carried out a quantitative analysis of the differences between the SUPER+KASHz AGN sample and the control sample of non-active galaxies, applying the Bayesian framework developed by the SUPER project. We quantitatively compared the two samples in terms of *i)* $L'_{\rm CO(1-0)}$ vs. $L_{\rm FIR}$ (see Sect. 5.5.1), *ii)* $L'_{\rm CO(1-0)}$ vs. M_*, *iii)* $\log(L'_{\rm CO}/M_*)$ distribution (proxy of the gas fraction distribution), *iv)* $\log(L'_{\rm CO}/M_*)$ vs. M_*. Our results confirm those of C21 on SUPER AGN: cosmic noon AGN, selected without priors regarding AGN feedback, are indistinguishable from non-active galaxies, matched in z, M_*, SFR.

Lastly, we addressed the possibility of a correlation between $\log(L'_{\rm CO}/M_*)$ and bolometric luminosity in the AGN sample. We find hints of a negative trend between the two quantities, with decreasing $\log(L'_{\rm CO}/M_*)$ for increasing $L_{\rm bol}$. We interpret this as the possibility of a luminosity effect regulating the efficiency by which AGN might impact on galaxy growth, that we will investigate by merging the SUPER+KASHz AGN sample with high-power cosmic-noon AGN, as available in the literature.

Future perpectives The latest (and upcoming) facilities have opened (and will broaden) new windows to assess AGN feedback in the high-z Universe, both through high-spatial-resolution studies and through demographic studies of the properties of AGN-driven winds in large samples.

Regarding the first, a promising new approach would be to compare the kinematics of molecular and ionized gas components (at similar resolution) to investigate whether the activity of AGN at cosmic noon perturbs the otherwise Keplerian motions of their hosts. I would envisage a complementary observing strategy to achieve this goal in KASHz and SUPER. Some of the ALMA archival observations of KASHz AGN are resolved ($\theta_{\rm res} < 0.5''$, i.e. $\simeq$ 4 kpc), allowing to observe molecular disks in few targets. The spatial resolution in the present [OIII] data is, however, more coarse ($\theta_{\rm res} > 5$ kpc); to compare the two gas phases at a similar resolution, these ALMA data could be complemented by JWST/NIRspec/IFU observations (wavelenght coverage: $\lambda \simeq 0.9 - 5.3$ μm)). For SUPER AGN, instead, we have higher resolution ionized gas maps ($\simeq$ 2 kpc), but we tailored their ALMA coverage at measuring the total CO flux of galaxies ($\theta_{\rm res} \simeq 2''$). Nonetheless, three SUPER targets

(one of which is shared with KASHz), selected based on their prominent [OIII] outflows, will be observed by JWST/MIRI/MRS (PI: V. Mainieri; wavelenght coverage: $\lambda \simeq 6.5 - 27.9$ μm) to map the MIR ro-vibrational H_2 lines, thus completing their multi-phase characterization by measuring also the warm-ionized gas phase. We will thus be able to determine the dynamics of the molecular gas and to derive the total (ionized+molecular) mass outflow rate and kinetic energy for these outflows, some of the most difficult wind parameters to measure with accuracy, thus providing a key constrain for current models of AGN feedback (e.g., Costa et al. 2020).

One of the VLT/ERIS GTO programs (115hr, PI: G. Cresci) will open a new window in the study of high-z AGN feedback. GTO targets were selected as cosmic noon AGN with already measured total molecular gas masses, for which VLT/ERIS will provide [OIII] maps and, for some of them, also Hα maps, with a pixel size of at least half that obtained with the AO-assisted VLT/SINFONI (Kravchenko et al. 2023). By this data, we will be able to properly assess the dynamics of the gas and the entanglement of SF and AGN-driven outflows at an unprecedented resolution at these redshifts, alongside testing other effects of AGN feedback on the host galaxy properties (e.g., gas depletion in AGN hosts). Moreover, one could then apply for ALMA time to observe the VLT/ERIS GTO targets, possibly starting from a subsample of the most prominent [OIII] outflows, if any, and/or the most gas depleted, to probe molecular outflows (for instance, as traced by CO transitions with $J_{\rm up} \geq 5$) and complete the picture of kpc-scale AGN-driven outflows, in the first case, and/or to assess if molecular outflows concur in gas depleting the hosts. Even if very time-consuming (easily more than 10 hrs per target), another interesting approach would be to ask for high-resolution ALMA observations of VLT/ERIS GTO sources showing [OIII] outflows, to target the lower-J CO transitions and test if and how the dynamics of the gas phase that will power the future SF of the galaxy are perturbed by AGN-driven ionized outflows. Moreover, ERIS/GTO targets with detected [OIII] outflows could be ideal sources to be followed up with JWST/MIRI/MRS to sample the warmer molecular gas phase ($T \simeq 400$ K) through ro-vibrational H_2 lines, as we will do for SUPER AGN but with the added value of having similar spatial resolution in the [OIII] and H_2, thus allowing for a more-complete full characterization of the ISM of such AGN hosts.

A complementary approach to these spatially resolved studies would be to perform integrated spectral analysis on thousands of X-ray selected AGN to assess the incidence and properties of [OIII] AGN-driven ionized outflows as function of AGN and galaxy properties. MOONRISE will offer the unique opportunity to perform this study at cosmic noon thanks to the NIR coverage (0.65–1.8 μm) by VLT/MOONS. Since the survey will observe deep fields for which ancillary multiwavelength data are already available, we will be able to reliably characterize the targeted sources and thus investigate AGN-driven ionized outflows on a sizable sample. Moreover,

since such deep fields are the same from which the KASHz AGN were selected, MOONRISE could yield the [OIII] coverage we are lacking for those sources which we only observed in Hα.

Appendices

Appendix A

Gravitational Lensing in a nutshell

Gravitational fields can perturb the trajectories of photons traveling across the Universe. Based on the mass and size of the overdensities, we distinguish between weak and strong gravitational lensing. Weak lensing is caused by the non-homogeneous distribution of matter and produces small distortions, that can be employed to study the large-scale structure of the cosmos. Strong lensing, instead, is produced by massive foreground overdensities, such as galaxies and clusters, that create multiple images of a background source, that is other galaxies or quasars. A strong lens can generate two different sets of magnification patterns due to macro-lensing and micro-lensing effects. Macro-lensing indicates the macroscopic effect of producing multiple magnified images of the background source. Micro-lensing instead is mostly due to masses orbiting inside the strong lens (e.g., stars and planets) whose motions generate a pertubation of the lensing system and time-variable magnification patterns. The next sections summarize the fundamentals of strong lens modeling, following the review by Treu (2010).

A.1 Macrolensing

A gravitational lens system (GLS) can be broken up in three fundamental components: the source plane, the image plane, the observer position. Figure A.1 shows a sketch of a typical GLS. Let the source position be $D_{\rm s}$, the lens position be $D_{\rm d}$, and the relative distance be $D_{\rm ds}$, if the deflector size is small when compared to such lengths, we can assume the lens to be totally contained in the image plane, showing a 2D structure. In the same way, we can consider the source photons as all emitted at the same distance ($D_{\rm s}$), therefore from the source plane. These approximations to planar distributions are referred to as the *thin screen approximation*.
A source of intrinsic position $\vec{\beta}$ is observed at the apparent position $\vec{\theta}$ due to the gravitational lens. Being $\hat{\vec{\alpha}}$ the deflection angle, the relation between intrinsic and

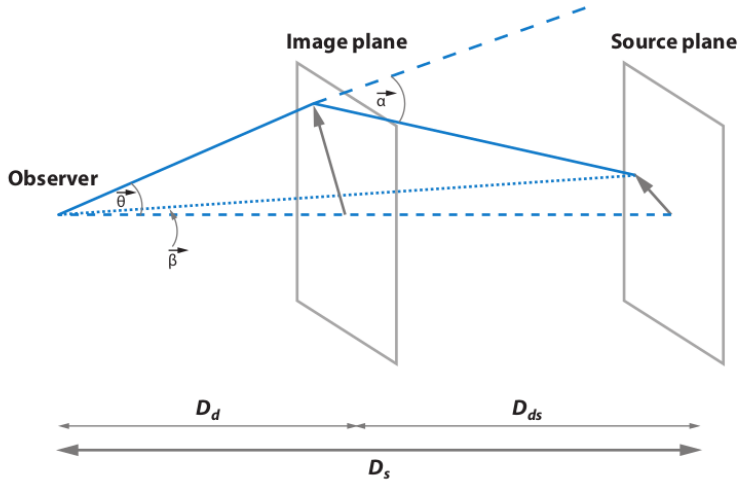

Figure A.1: Sketch of a gravitational lens system. Credit: Treu (2010).

apparent positions is given by the *lens equation*:

$$\vec{\beta} = \vec{\theta} - \vec{\alpha}(\vec{\theta}) = \vec{\theta} - \frac{D_{\rm ds}}{D_{\rm s}}\hat{\vec{\alpha}}(\vec{\theta}) \tag{A.1}$$

where $\vec{\alpha}(\vec{\theta})$ is the *reduced deflection angle*. The lens equation states that only one $\vec{\beta}$ can exist for a given $\vec{\theta}$, thus the source is uniquely determined for a given image, if the lens is known. However, solving Eq. (A.1) for $\vec{\theta}$ is not trivial, since $\hat{\vec{\alpha}}(\vec{\theta})$ is typically a highly non-linear function of $\vec{\theta}$. This implies that more than one solution can be found for $\vec{\theta}$, that is the source can be lensed into multiple images.

It can be demonstrated that the deflection induces a delay in the light travel-time from the source to the observer and that such time delay can vary between the images. The time delay Δt depends both on the position $\vec{\theta}$ in the image plane and on that in the source plane $\vec{\beta}$:

$$\Delta t = \frac{D_{\rm d} D_{\rm s}(1+z_l)}{cD_{\rm ds}}\left(\frac{1}{2}|\theta-\beta|^2 - \psi(\theta)\right) \tag{A.2}$$

where z_l is the redshift of the lens and $\psi(\theta)$ the two-dimensional lensing potential. Such potential satisfies the two-dimensional Poisson equation $\nabla^2\psi = 2\kappa$, where κ is the *convergence*, the deflector's projected surface mass density $\Sigma(\vec{\theta})$ in units of the critical density $\Sigma_{\rm cr}$:

$$\kappa(\vec{\theta}) \equiv \frac{\Sigma(\vec{\theta})}{\Sigma_{\rm cr}}, \qquad \text{where} \quad \Sigma_{\rm cr} = \frac{c^2 D_{\rm s}}{4\pi G D_{\rm d} D_{\rm ds}}. \tag{A.3}$$

A second effect of gravitational lensing is the distorsion of the images, which can be

described by the Jacobian matrix A, defined as follows

$$\mathrm{A} \equiv \frac{\partial \vec{\beta}}{\partial \vec{\theta}}; \tag{A.4}$$

it can be demonstrated that its radial and tangential eigenvalues are $\lambda_{\mathrm{r}} = 1 - \kappa + \gamma$ and $\lambda_{\mathrm{t}} = 1 - \kappa - \gamma$ respectively, where γ is the *shear* of the lens. The convergence $\kappa(\vec{\theta})$ determines the isotropic transformation of the lensed object, while the shear is responsible for anisotropic deformations, stretching the shape of the background source along privileged directions (for instance, circular sources can be mapped in elliptical images due to the shear effects).

The third effect is flux magnification. Gravitational lensing is an achromatic phenomenon thus it only affects the trajectories of photons, leaving unchanged both their number and momenta, that is the surface brightness is conserved. However, it can be demonstrated that a strong lens produces a variation in the surface angle subtended by the background object. As a consequence, gravitational lensing acts on the geometry other than on the number or energy of the photons, resulting in a flux magnification of the images. Let I_ν be the surface brightness in the image plane and I_ν^S that in the source plane, the source flux F_ν is given by the following equation

$$F_\nu = \int_I I_\nu(\vec{\theta}) d^2\theta = \int_I I_\nu^S[\vec{\beta}(\vec{\theta})] \mu_{\mathrm{L}} d^2\beta \tag{A.5}$$

where μ_{L} is the magnification factor. The latter is the determinant of the magnification tensor M, that is the coordinate-change matrix between the source and the image planes, equal to the inverse matrix of the Jacobian matrix A:

$$\mu = detM = (detA)^{-1} = \frac{1}{(1-\kappa)^2 - \gamma^2}. \tag{A.6}$$

The ensemble of points where the determinant of the lensing Jacobian vanishes are called *critical lines*. As Eq. (A.6) shows, they correspond to formally infinite magnifications. The total flux of astrophysical sources with finite size is always finite but can reach large values (up to ~ 100 or so). The corresponding lines on the source plane are called *caustics*. Sources placed near the location of caustics can be highly magnified.

Another fundamental quantity when describing a GLS is its characteristic angle, the so-called Einstein radius θ_{E}. For a circular lens, the Einstein radius defines the region where the average surface-mass density is equal to Σ_{cr}. Its size depends on the properties of the GLS: enclosed mass and redshifts of lens and source. A point-like background object placed exactly at the center of the deflector's mass distribution is lensed into the so-called *Einstein ring*, a circle whose radius corresponds to the Einstein radius.

Macro-lensing indicates the case of an extended lens that maps the background object in multiple images. In summary, the number of images, the time delays and the shape deformation of the background object are dependent on to the mass distribution of the lens and the relative position of background object and lens. Moreover, the lens mass distribution defines the actual distance among the images and their multiplicity, for instance the typical separation induced by massive galaxies is of the order of few arcseconds.

A.2 Microlensing

When the lens mass is small, we refer to the lensing phenomenon as micro-lensing. Microlensing events are extremely hard to model, especially when considering micro-lenses contained in a macro-lens, given the intricate structure of the yielded caustics. Micro-lensing events can be detected within our Galaxy and in nearby GLSs, induced by stars within the lens. The source-lens relative motion can induce temporary modifications of the source flux that can be appreciated only when the background object is contained within the Einstein ring of the micro-lens. One can thus define the micro-lensing cross section $\sigma_{\rm micro}$ as the solid angle within which a source has to be placed in order to produce a detectable microlensing signal, that is the Einstein ring itself: $\sigma_{\rm micro} = \pi\theta_E^2$. The timescale of micro-lensing events is the *Einstein crossing time* $t_{\rm E} = \theta_{\rm E}/\mu_{\rm rel}$, where $\mu_{\rm rel}$ expresses the relative motion between the source and the micro-lens. The timescale of the flux modifications therefore depends on the GLS geometry and the proper motion of the micro-lenses.

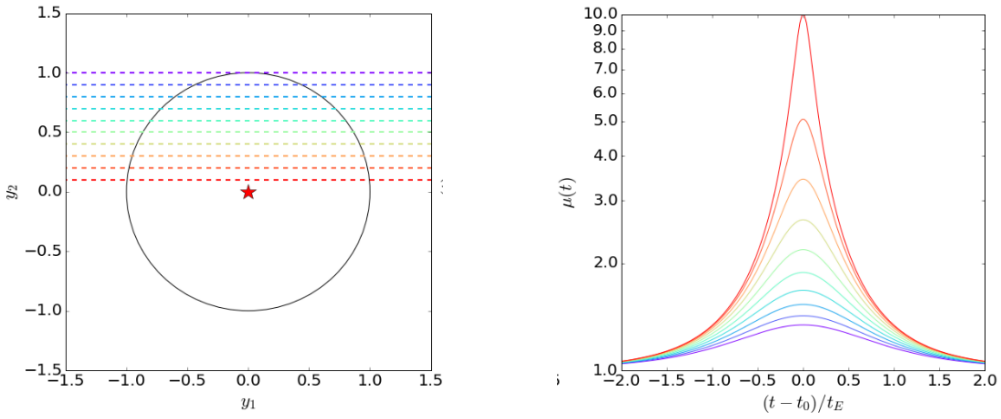

Figure A.2: *Left panel*: source trajectories projected in the image plane; the different colors correspond to different dimensionless impact parameters (source-lens projected distance in units of the Einstein radius $\theta_{\rm E}$), ranging from 0.1 (red) to 1 (purple). *Right panel*: Micro-lensing light curves color-coded as the trajectories in the left panel, time in given in units of the Einstein crossing time $t_{\rm E}$. Credit: Massimo Meneghetti, Gravitational lensing lectures (2017/2018).

Micro-lensing events manifest themselves as pertubations of the image flux, thus one way to investigate them is through the light curves of the multiple images produced by the strong lens. If we consider a galaxy as macro-lens, micro-lensing flux variations can be induced by the motion of stars within the galaxy, given the negligible displacement that the background source undergoes in the same time. To simplify the description, it is useful to treat the system as a stationary lens, ascribing all the motion to the background source only. In general, the simplest GLS to describe such phenomena is a stationary point-mass lens and a point-like background object that moves across the source plane. Figure A.2 displays the micro-lensing light curves induced by the motion of a source placed at various distances (*impact parameter*) from the lens. As shown, the peak of the induced magnification depends on the source-lens projected distance. In this simple example, the duration of a micro-lensing event is determined by the time taken by the source to cross the Einstein ring. When considering a real GLS, micro-lensing events are parameterized through the source crossing time, that is the time taken by the micro-lens to move across the emitting region of the background object. Based on the GLS structure, such time ranges between few months and years for extra-galactic sources, while among our Galaxy it is typically of the order of a few days. Lastly, given that gravitational lensing is an achromatic phenomenon, wavelength-dependent micro-lensing magnification patterns can be used to probe and compare the sizes of regions emitting at the different wavelengths.

Appendix B

Feedback-unbiased sample

Here I summarized all the targets of the high-z GLQ sample (Table B.1), then used to build the "feedback-unbiased" sample of Chapter 2, and the list of XMM-*Newton* observations, as retrieved from the archive (Table B.2).

Table B.1: List of confirmed GLQs with background source at $z_q > 1$ from from the CASTLES (Muñoz et al. 1998) and the SQLS (Inada et al. 2012) catalogs.

Name	Ra	Dec	z_Q	z_L	N_{im}	sep ($''$)
B1152+200	11:55:18.297	+19:39:42.24	1.019	0.439	2	1.59
SDSSJ0832+0404	08:32:16.997	+04:04:05.23	1.116	0.659	2	1.98
SDSSJ1226-0006	12:26:08.024	-00:06:02.29	1.126	0.517	2	1.26
B0850+054	08:52:53.58	+05:15:15.30	1.14	0.59	2E	0.68
SDSSJ1620+1203	16:20:26.146	+12:03:42.02	1.158	0.398	2	2.77
MG1549+3047	15:49:12.37	+30:47:16.6	1.17	0.11	R	1.7
SDSSJ1524+4409	15:24:45.62	+15:24:45.62	1.21	0.32	2	1.67
FBQ0951+2635	09:51:22.57	+26:35:14.1	1.246	0.24)	2	1.11
SDSSJ1055+4628	10:55:45.45	+46:28:39.4	1.249	0.388	2	1.15
B2045+265	20:47:20.35	+26:44:01.2	1.28	0.87	4	2.74
QJ0158-4325	01:58:41.44	-43:25:04.20	1.29	0.317	2	1.22
B0712+472	07:16:03.58	+47:08:50.0	1.34	0.41	4	1.46
Q1355-2257	13:55:43.434	-22:57:23.17	1.37	0.48)	2	1.23
SBS0909+532	09:13:01.05	+52:59:28.83	1.38	0.83	2	1.17
B1608+656	16:09:13.96	+65:32:29.0	1.39	0.63	4	2.27
SDSSJ1330+1810	13:30:18.64	+18:10:32.1	1.393	0.373	4	1.76
Q0957+561	10:01:20.83	+55:53:49.6	1.413	0.36	2	-
SDSSJ1455+1447	14:55:01.91	+14:47:34.8	1.424	-	2	1.73
SDSSJ1332+0347	13:32:22.627	+03:47:39.97	1.438	0.191	2	1.14
SDSSJ1527+0141	15:27:20.131	+01:41:39.60	1.439	-	2	2.58

continued.

Name	Ra	Dec	$z_{\rm Q}$	$z_{\rm L}$	$N_{\rm im}$	sep ($''$)
SDSSJ1054+2733	10:54:40.842	+27:33:06.42	1.452	-	2	1.27
Q1120+0195	11:23:20.730	+01:37:47.52	1.472	-	-	-
HS0810+2554	08:13:31.3	+25:45:03.2	1.5	-	4	0.96
SDSSJ1320+1644	13:20:59.17	+16:44:02.5	1.502	0.899]	2	8.59
SDSSJ0924+0219	09:24:55.87	+02:19:24.9	1.523	0.394	4	1.81
B1030+074	10:33:34.0242	+07:11:26.147	1.535	0.6	2	1.65
SDSSJ0806+2006	08:06:23.705	+20:06:31.89	1.538	0.573	2	1.49
SDSSJ1650+4251	16:50:43.445	+42:51:49.33	1.543	0.577]	2	1.18
HE0512-3329	05:14:10.78	-33:26:22.50	1.57	0.93)	2	0.65
SDSSJ1335+0118	13:35:34.793	+01:18:05.53	1.571	0.44	2	1.63
B1600+434	16:01:40.45	+43:16:47.8	1.589	0.41	2	1.4
SDSSJ1128+2402	11:28:18.496	+24:02:17.49	1.608	-	2	0.84
SDSSJ1353+1138	13:53:06.347	+11:38:04.72	1.624	0.3	2	1.41
WFI2033-4723	20:33:42.08	-47:23:43.0	1.66	0.66	4	2.33
HE0047-1756	00:50:27.835	-17:40:09.27	1.676	0.41	2	1.44
SDSSJ0246-0825	02:46:34.11	-08:25:36.2	1.686	0.723	2	1.09
HE0435-1223	04:38:14.9	-12:17:14.4	1.689	0.46	4	2.42
Q2237+030	22:40:30.34	+03:21:28.8	1.695	0.0395	4	1.78
SDSSJ1322+1052	13:22:36.418	+10:52:39.42	1.717	-	2	2
SDSSJ1021+4913	10:21:11.01	+49:13:30.3	1.72	0.451]	2	1.14
PG1115+080	11:18:17.00	+07:45:57.7	1.72	0.31	4	2.32
SDSSJ1349+1227	13:49:29.846	+12:27:06.94	1.722	-	2	3
SDSSJ1004+4112	10:04:34.91	+41:12:42.8	1.74	0.68	5	14.72
MG1654+1346	16:54:41.83	+13:46:22.00	1.74	0.25	R	2.1
SDSSJ1206+4332	12:06:29.64	+43:32:17.5	1.789	0.748]	2	2.9
SDSSJ1405+0959	14:05:15.42	+09:59:31.3	1.81	0.66	2	1.98
SDSSJ0904+1512	09:04:04.159	+15:12:54.55	1.826	-	2	1.13
SDSSJ1001+5027	10:01:28.61	+50:27:56.8	1.841	0.415	2	2.86
SBS1520+530	15:21:44.83	+52:54:48.6	1.855	0.72	2	1.59
SDSSJ1313+5151	13:13:39.98	+51:51:28.4	1.877	0.194	2	1.24
SDSSJ1529+1038	15:29:38.904	+10:38:03.92	1.971	-	2	1.27
SDSSJ0746+4403	07:46:53.04	+44:03:51.3	1.998	0.513	2	1.08
SDSSJ1216+3529	12:16:46.04	+35:29:41.4	2.013	-	2	1.49
SDSSJ0820+0812	08:20:16.112	+08:12:15.98	2.024	0.803	2	2.2
HE2149-2745	21:52:07.44	-27:31:50.2	2.033	0.5	2	1.7
SDSSJ1515+1511	15:15:38.59	+15:11:35.8	2.054	0.742]	2	1.95
B1938+666	19:38:25.19	+66:48:52.2	2.059	0.881	R	1
B0827+525	08:31:05.362	+52:25:20.24	2.064	-	-	-

continued.

Name	Ra	Dec	$z_{\rm Q}$	$z_{\rm L}$	$N_{\rm im}$	sep ($''$)
HST15433+5352	15:43:20.9	+53:51:52	2.092	0.497	2R	1.18
SDSSJ1406+6126	14:06:24.824	+61:26:40.96	2.135	0.271	2	1.98
HE0230-2130	02:32:33.1	-21:17:26	2.162	0.52	4	2.05
SDSSJ1304+2001	13:04:43.588	+20:01:04.26	2.175	0.373?	2	1.87
SDSSJ1029+2623	10:29:13.945	+26:23:17.98	2.199	0.58	3	22.54
PMNJ0134-0931	01:34:35.6668	-09:31:02.873	2.225	0.77	5R	0.73
WFI2026-4536	20:26:10.43	-45:36:27.1	2.23	-	4	1.34
SDSSJ1339+1310	13:39:07.138	+13:10:39.63	2.241	0.609	2	1.69
IRASF10214+472	10:24:34.561	+47:09:09.59	2.286	0.75)	2E	1.59
HE1104-1805	11:06:33.45	-18:21:24.2	2.32	0.73	2	3.19
SDSSJ1334+3315	13:34:01.398	+33:15:34.35	2.426	0.557]	2	0.83
SDSSJ1138+0314	11:38:03.70	+03:14:58.0	2.44	0.45	4	1.34
Q1017-207	10:17:23.983	-20:46:58.62	2.545	0.78)	2	0.85
H1413+117	14:15:46.40	+11:29:41.4	2.55	-	4	1.35
B1933+503	19:34:30.95	+50:25:23.6	2.63	0.76	10	1
MG0414+0534	04:14:37.73	+05:34:44.3	2.64	0.96	4E	2.4
J1004+1229	10:04:24.890	+12:29:22.28	2.681	0.95	2	1.54
SDSSJ1011+0143	10:11:29.49	+01:43:23.30	2.701	0.331	4	3.67
SDSSJ1258+1657	12:58:19.244	+16:57:17.67	2.702	0.505	2	1.28
Q0142-100	01:45:16.610	-09:45:17.31	2.738	0.49	2	2.24
LBQS1009-0252	10:12:15.71	-03:07:02.0	2.739	0.87	2	1.54
PMNJ1838-3427	18:38:28.5	-34:27:41.6	2.78	-	2R	0.99
RXJ0911+0551	09:11:27.50	+05:50:52.0	2.8	0.77	4	2.47
SDSSJ1155+6346	11:55:17.349	+63:46:22.03	2.888	0.176	2	1.83
SDSSJ1131+1915	11:31:57.729	+19:15:27.73	2.915	-	2	1.46
HS0818+1227	08:21:39.1	+12:17:29	3.115	0.39	2	2.83
MG0751+2716	07:51:41.46	+27:16:31.35	3.2	0.35	R	0.7
SDSSJ1400+3134	14:00:12.774	+31:34:54.14	3.235	-	6	1.71
MG2016+112	20:19:18.15	+11:27:08.3	3.27	1.01	2E	3.52
B1359+154	14:01:35.55	+15:13:25.60	3.317	-	2	1.74
HST14176+5526	14:17:36.51	+52:26:40	3.4	0.81	4	2.83
SDSSJ0903+5028	09:03:34.92	+50:28:19.2	3.584	0.388	2	2.84
Q0047-2808	00:49:41.89	-27:52:25.70	3.6	0.48	4ER	2.7
B1422+231	14:24:38.09	+22:56:00.6	3.62	0.34	4E	1.68
SDSSJ1254+2235	12:54:18.951	+22:35:36.59	3.626	-	2	1.56
Q1208+101	12:10:57.041	+09:54:26.96	3.822	-	2	0.48
APM08279+5255	08:31:41.59	+52:45:17.0	3.87	-	3	0.38
CY2201-3201	22:01:32.8	+32:01:44.0	3.9	0.32	2	0.83

continued.

Name	Ra	Dec	$z_{\rm Q}$	$z_{\rm L}$	$N_{\rm im}$	sep ($''$)
PSSJ2322+1944	23:22:07.2	+19:44:22.9	4.118	-	2	1.49
BRI0952-0115	09:55:00.01	-01:30:05.0	4.434	0.632	2	1
SDSSJ0946+1835	09:46:04.795	+18:35:39.72	4.799	0.388	2	3.06

Table B.2: List of XMM-*Newton* observations.

GLQ	obsID	Target	Exp.	PI	offset ($'$)
HST 15433+5352	60370101	SBS1542+541	11.4	Mathur	9.16
HST 15433+5352	60370901	SBS1542+541	34.1	Mathur	9.16
HE 2149-2745	62940401	HE2149-2745	39.4	Chartas	1.49
PG 1115+080	82340101	PG1115+080	63.2	Chartas	0.04
PG 1115+080	82340201	PG1115+080	9.6	Chartas	0.04
RX J0911.4+0551	83240201	RXJ0911.4+0551	20.7	Hjorth	0.0
APM 08279+5255	92800101	APM08279+5255	17.5	Hasinger	0.01
APM 08279+5255	92800201	APM08279+5255	102.9	Hasinger	0.01
Q 0957+561	110930201	NGC3079	25.3	Watson	14.05
SDSS 1138+0314	111970701	TLeo	12.9	Mason	9.21
SDSS 1138+0314	111971501	TLeo	7.8	Mason	9.21
H 1413+117	112250301	H1413+117	26.6	Turner	0.10
H 1413+117	112251301	H1413+117	29.6	Turner	0.10
HE 1104-1805	112630101	HE1104-1805	36.4	Turner	0.10
MG 2016+112	112960301	AXJ2019+112	15.3	Turner	0.12
MG 2016+112	112960501	AXJ2019+112	16.0	Turner	0.12
MG 2016+112	112960601	AXJ2019+112	16.3	Turner	0.12
SBS 0909+532	143150301	SBS0909+532	33.1	Reeves	0.08
SBS 0909+532	143150601	SBS0909+532	21.7	Reeves	0.08
Q 1120+0195	145750101	Q1120+0195	42.2	Chartas	0.01
Q 0957+561	147760101	SN2001ci	44.4	Pietsch	13.04
PSS J2322+1944	202140301	PSSJ2322+1944	35.9	Priddey	0.007
PG 1115+080	203560201	PG1115+080	81.9	Chartas	0.04
PG 1115+080	203560401	PG1115+080	86.5	Chartas	0.04
SDSS J1004+4112	207130201	RBS825	53.1	Lamer	0.05
APM 08279+5255	502220201	APM08279+5255	89.6	Chartas	0.0
APM 08279+5255	502220301	APM08279+5255	90.5	Chartas	0.0
APM 08279+5255	502220401	APM08279+5255	7.4	Chartas	0.0
APM 08279+5255	502220501	APM08279+5255	6.6	Chartas	0.0
SDSS J1313+5151	653530101	Abell1703	17.3	Gastaldello	12.68
SDSS J1313+5151	653530201	Abell1703	15.4	Gastaldello	12.68
SDSS J1313+5151	653530301	Abell1703	14.2	Gastaldello	12.68
SDSS J1313+5151	653530401	Abell1703	15.1	Gastaldello	12.68
SDSS J1313+5151	653530501	Abell1703	15.1	Gastaldello	12.68
SDSS J1313+5151	653530601	Abell1703	16.1	Gastaldello	12.68
SDSS J1313+5151	653530701	Abell1703	15.7	Gastaldello	12.68

continued.

GLQ	obsID	Target	Exp.	PI	offset (′)
SDSS J1313+5151	653530801	Abell1703	13.4	Gastaldello	12.68
SDSS J1313+5151	653530901	Abell1703	13.4	Gastaldello	12.68
HST 14176+5526	723860101	SDSSJ141711+522540	56.7	Lin	4.00
HS 0810+2554	728990101	HS0810+2554	56.9	Chartas	0.003
B 1422+231	744240101	B1422+231	86.2	Dadina	0.002
SDSS J1353+1138	762520101	SDSSJ1353+1138	55.0	Chartas	0.006
SDSS J15293+1038	762520201	SDSSJ15293+1038	93.6	Chartas	0.009
SDSS J09040+1512	762520301	SDSSJ09040+1512	101.3	Chartas	0.003
MG J0414+0534	781210301	MG0414+0534	85.0	Dadina	0.001
B 1422+231	795640101	B1422+231	38.0	Lanzuisi	0.007
Q 0957+561	802710101	NGC3079	22.8	Hodges-kluck	14.04
Q 0957+561	802710201	NGC3079	22.4	Hodges-kluck	14.04
Q 0957+561	802710301	NGC3079	22.4	Hodges-kluck	14.04
Q 0957+561	802710401	NGC3079	22.4	Hodges-kluck	14.04
Q 0957+561	802710501	NGC3079	22.4	Hodges-kluck	14.04
Q 0957+561	802710601	NGC3079	22.4	Hodges-kluck	14.04
Q 0957+561	802710701	NGC3079	22.4	Hodges-kluck	14.04
Q 0957+561	802710801	NGC3079	26.0	Hodges-kluck	14.04
Q 0957+561	802710901	NGC3079	22.4	Hodges-kluck	14.04
Q 0957+561	802711001	NGC3079	25.3	Hodges-kluck	14.04
B 1152+199	804680101	B1152+199	119.9	Nardini	0.004
SDSS J1128+2402	822530201	SDSSJ1128+2402	37.0	Chartas	0.004
APM 08279+5255	830480101	APM08279+5255	31.4	Lanzuisi	0.02
APM 08279+5255	830480301	APM08279+5255	33.0	Lanzuisi	0.02

Appendix C

Literature high-energy cutoff measurements

Here I summarize all the measurements of the high-energy cutoff that we collected from the literature. The values in Tables C.1–C.3 populate the graphs in Fig. 4.4.

Table C.1: Literature low-z measurements collected by L19

Source	z	$\log L_{2-10}$	$E_{\rm cut}$	Flag	References
NGC 5506	0.006	42.68	720^{+130}_{-190}	1	(a),(b)
NGC 7213	0.006	42.07	< 140	1	(a),(b)
MCG-6-30-15	0.008	43.39	< 110	1	(a),(b)
MCG 5-23-16	0.009	43.2	116^{+6}_{-5}	1	(a),(b)
SWIFT J2127.4+5654	0.014	43.0	108^{+11}_{-10}	1	(a),(b)
NGC 5548	0.018	43.3	70^{+40}_{-10}	1	(a),(b)
Mrk 335	0.026	42.51	< 174	1	(a),(b)
1H0707-495	0.041	43.06	< 63	1	(a),(b)
Fairall 9	0.047	43.98	< 242	1	(a),(b)
Cyg A	0.056	44.24	< 110	1	(a),(b)
3C 382	0.058	44.37	214^{+147}_{-63}	1	(a),(b)
IGR J0033+6122	0.105	45.28	< 52	2	(c),(a),(b)
3C 111	0.049	44.81	136^{+47}_{-29}	2	(c),(a),(b)
IGR J07597-3842	0.04	43.89	79^{+24}_{-16}	2	(c),(a),(b)
NGC 3783	0.01	43.42	98^{+79}_{-34}	2	(c),(a),(b)
NGC 4151	0.003	42.96	196^{+47}_{-32}	2	(c),(a),(b)
IGR J16558-5203	0.054	44.12	194^{+202}_{-72}	2	(c),(a),(b)
1H2251-179	0.064	44.62	138^{+38}_{-57}	2	(c),(a),(b)
MCG-02-58-022	0.047	44.29	< 510	2	(c),(a),(b)
MCG+08-11-011	0.021	44.03	163^{+53}_{-32}	1	(d),(b)
Mrk 6	0.019	43.21	120^{+51}_{-28}	1	(d),(b)
IGR J12415-5750	0.024	43.24	123^{+54}_{-47}	1	(d),(b)

continued.

Source	z	$\log L_{2-10}$	$E_{\rm cut}$	Flag	References
IC4329A	0.016	43.97	153^{+20}_{-16}	1	(d),(b)
GRS 1734-292	0.021	43.64	53^{+13}_{-9}	1	(d),(b)
3C 390.3	0.056	44.37	130^{+42}_{-32}	1	(d),(b)
NGC 6814	0.005	42.18	115^{+26}_{-18}	1	(d),(b)
4C 74.24	0.104	44.38	94^{+54}_{-26}	1	(d),(b)
S5 2116+81	0.086	44.42	< 93	1	(d),(b)
PG 1114+445	0.144	44.6	< 22	2	(e),(a),(b)
NGC 4051	0.002	40.68	< 381	2	(e),(a),(b)
PG 1202+281	0.165	44.39	< 64	2	(e),(a),(b)
NGC 4138	0.003	41.21	< 75	2	(e),(a),(b)
Mrk 766	0.013	42.38	21^{+6}_{-7}	2	(e),(a),(b)
NGC 4258	0.002	40.82	< 284	2	(e),(a),(b)
Mrk 50	0.023	43.19	< 334	2	(e),(a),(b)
NGC 4593	0.009	42.82	< 517	2	(e),(a),(b)
Mrk 1383	0.087	44.17	< 134	2	(e),(a),(b)
NGC 3998	0.0035	41.51	104^{+39}_{-22}	1	(f),(b)
NGC 4579	0.0056	41.9	414^{+146}_{-158}	1	(f),(b)
ESO 103-035	0.013	42.96	100^{+90}_{-30}	1	(g),(b)
IGR 2124	0.02	43.68	80^{+11}_{-9}	1	(g),(b)
B2202-209	0.532	45.22	152^{+103}_{-54}	1	(h),(b)
GRS 1734-292	0.021	43.72	53^{+11}_{-8}	1	(i),(b)

Notes. Col. (1): Source name; Col. (2): Redshift; Col. (3): Logarithm of the 2–10 keV luminosity (erg s^{-1}); Col. (4): High-energy cutoff (keV); Col. (5): telescope flag, 1=*NuSTAR*, 2=non-focusing; Col. (6): References: (a) Fabian et al. (2015), (b) L19, (c) Malizia et al. (2014), (d) Molina et al. (2019), (e) Vasudevan et al. (2013), (f) Younes et al. (2019), (g) Buisson et al. (2018), (h) Kammoun et al. (2017), (i) Tortosa et al. (2017).

Table C.2: Literature low-z measurements collected in this work.

Source	z	$\log L_{2-10}$	$E_{\rm cut}$	Flag	References
NGC 985	0.043	43.72	< 72	2	(j)
ESO198-G24	0.045	43.8	97^{+312}_{-58}	2	(j)
NCG 1068	0.003	42.26	< 35	2	(j)
3C 120	0.033	44.04	77^{+94}_{-30}	2	(j)
H0557	0.034	43.88	35^{+175}_{-20}	2	(j)
MCG-1-24-12	0.02	42.37	< 420	2	(j)
MCG-5-23-16	0.008	43.11	191^{+110}_{-60}	2	(j)
NGC 3516	0.009	42.83	101^{+404}_{-37}	2	(j)
NGC 4151*	0.003	42.45	56^{+14}_{-10}	2	(j)
NGC 4507	0.012	42.67	152^{+350}_{-70}	2	(j)
NGC 4945	0.002	40.51	122^{+41}_{-26}	2	(j)
Mrk 509*	0.035	43.78	60^{+71}_{-23}	2	(j)
MR 2251	0.068	44.59	132^{+130}_{-68}	2	(j)
NGC 7469	0.017	43.27	211^{+235}_{-95}	2	(j)
Ark 564	0.02468	43.59	46^{+3}_{-3}	1	(k)
MGC +8-11-11	0.0204	43.71	175^{+110}_{-50}	1	(l)
Ark 120	0.033	43.96	180^{+80}_{-40}	1	(l)
PG 1211+143	0.0809	43.54	< 124	1	(l)
1E 0754.6+3928	0.096	43.7	< 170	1	(m)
HE 1143-1810	0.0328	43.74	280^{+170}_{-80}	1	(n)
MCG-01-24-12	0.0196	43.18	70^{+21}_{-14}	1	(o)
PDS 456	0.184	44.97	51^{+11}_{-8}	1	(p)
1RXSJ034704.9	0.095	42.72	29^{+437}_{-18}	1	(q)
1RXS J174538.1	0.111	43.75	< 83	1	(q)
1RXS J213445.2	0.067	43.24	< 85	1	(q)
2MASS J19334715	0.057	43.39	< 166	1	(q)
2MASX J04372814	0.053	42.85	< 114	1	(q)
2MASX J12313717	0.028	42.34	< 84	1	(q)
2MASX J15144217	0.068	43.19	< 32	1	(q)
2MASX J15295830	0.104	43.5	< 119	1	(q)
2MASX J19301380	0.063	43.66	23^{+29}_{-9}	1	(q)
2MASX J19380437	0.04	42.85	< 105	1	(q)
2MASX J20005575	0.037	42.8	< 207	1	(q)
3C 227	0.086	43.65	< 44	1	(q)
4C +18.51	0.186	43.79	< 55	1	(q)
ESO 438-G009	0.024	42.03	< 140	1	(q)
Fairall 1146	0.031	42.81	< 184	1	(q)
Fairall 1203	0.058	42.75	< 108	1	(q)

continued.

Source	z	$\log L_{2-10}$	$E_{\rm cut}$	Flag	References
[HB89] 0241+622	0.044	43.36	< 211	1	(q)
IGR J14471-6414	0.053	42.75	< 73	1	(q)
IGR J14552-5133	0.016	41.89	< 180	1	(q)
IRAS 04392-2713	0.084	43.46	< 71	1	(q)
LCRSB 232242.2	0.036	41.95	< 51	1	(q)
Mrk 9	0.04	42.34	< 193	1	(q)
Mrk 376	0.056	42.83	< 152	1	(q)
Mrk 595	0.027	41.96	< 67	1	(q)
Mrk 732	0.029	42.5	< 173	1	(q)
Mrk 739	0.03	42.32	< 143	1	(q)
Mrk 813	0.11	43.71	< 177	1	(q)
Mrk 817	0.031	42.56	< 230	1	(q)
Mrk 841	0.036	43.05	< 179	1	(q)
Mrk 1018	0.042	42.18	< 212	1	(q)
Mrk 1044	0.016	42.02	< 214	1	(q)
Mrk 1310	0.019	42.17	< 130	1	(q)
Mrk 1393	0.054	42.48	< 19	1	(q)
NGC 0985	0.043	43.02	< 121	1	(q)
PG 0804+761	0.1	43.56	< 183	1	(q)
PKS 0558-504	0.137	44.03	< 134	1	(q)
RBS 0295	0.074	43.17	< 49	1	(q)
RBS 0770	0.032	43.05	< 267	1	(q)
RBS 1037	0.084	43.14	< 92	1	(q)
RBS 1125	0.063	42.91	< 98	1	(q)
SBS 1136+594	0.06	43.28	< 92	1	(q)
SDSS J104326.47	0.048	42.67	< 34	1	(q)
UM 614	0.033	42.58	< 106	1	(q)
WKK 1263	0.024	42.94	< 224	1	(q)
NGC 262	0.015	43.62	170^{+40}_{-30}	1	(r)
ESO 195-IG021	0.0494	43.76	< 230	1	(r)
NGC 454 E	0.0121	42.43	< 50	1	(r)
NGC 513	0.0195	42.73	< 230	1	(r)
NGC 612	0.0298	43.82	< 120	1	(r)
2MASX J0140	0.0716	44.0	70^{+40}_{-20}	1	(r)
MCG-01-05-047	0.0172	42.9	< 100	1	(r)
NGC 788	0.0136	43.18	< 100	1	(r)
ESO 416-G002	0.0591	43.53	< 480	1	(r)
NGC 1052	0.005	41.9	80^{+40}_{-20}	1	(r)

continued.

Source	z	$\log L_{2-10}$	$E_{\rm cut}$	Flag	References
2MFGC 2280	0.0152	43.33	< 50	1	(r)
NGC 1229	0.0363	42.93	< 82	1	(r)
NGC 1365	0.0055	42.0	290^{+200}_{-100}	1	(r)
2MASX J0356	0.0748	43.87	< 240	1	(r)
3C 105	0.089	44.36	< 70	1	(r)
2MASX J0423	0.045	44.05	70^{+40}_{-30}	1	(r)
MCG+03-13-001	0.0154	42.63	< 60	1	(r)
CGCG 420-015	0.0294	43.48	< 100	1	(r)
ESO 033-G002	0.0181	42.93	< 460	1	(r)
LEDA 178130	0.035	44.0	< 200	1	(r)
2MASX J0508	0.0175	42.99	160^{+200}_{-60}	1	(r)
NGC 2110	0.0078	43.73	300^{+50}_{-30}	1	(r)
ESO 005-G004	0.0062	42.03	< 140	1	(r)
Mrk 3	0.0135	43.83	150^{+60}_{-30}	1	(r)
ESO 121-IG028	0.0405	43.63	< 150	1	(r)
LEDA 549777	0.061	43.63	< 90	1	(r)
LEDA 511628	0.0469	43.53	90^{+80}_{-30}	1	(r)
MCG+06-16-028	0.0157	42.93	< 110	1	(r)
IRAS 07378-3136	0.0258	43.23	60^{+40}_{-20}	1	(r)
UGC 3995 A	0.0158	42.93	100^{+110}_{-40}	1	(r)
Mrk 1210	0.0135	42.93	90^{+40}_{-20}	1	(r)
MCG-01-22-006	0.0218	43.43	110^{+60}_{-30}	1	(r)
CGCG 150-014	0.0647	43.93	< 110	1	(r)
MCG+11-11-032	0.0363	43.63	< 140	1	(r)
2MASX J0903	0.091	43.73	< 270	1	(r)
2MASX J0911	0.0268	43.33	70^{+60}_{-20}	1	(r)
IC 2461	0.0075	41.93	< 110	1	(r)
MCG-01-24-012	0.0196	43.46	110^{+50}_{-30}	1	(r)
2MASX J0923	0.0424	43.83	40^{+90}_{-20}	1	(r)
NGC 2992	0.0077	43.03	< 380	1	(r)
NGC 3079	0.0037	42.73	40^{+20}_{-10}	1	(r)
ESO 263-G013	0.0335	43.73	< 120	1	(r)
NGC 3281	0.0107	42.53	70^{+10}_{-10}	1	(r)
MCG+12-10-067	0.0336	43.13	< 109	1	(r)
MCG+06-24-008	0.0259	42.92	< 170	1	(r)
UGC 5881	0.0206	42.53	80^{+120}_{-30}	1	(r)
NGC 3393	0.0125	43.53	< 60	1	(r)
2MASX J1136	0.014	42.33	< 350	1	(r)

continued.

Source	z	$\log L_{2-10}$	$E_{\rm cut}$	Flag	References
NGC 3822	0.0209	42.53	< 70	1	(r)
B2 1204+34	0.0791	44.09	< 280	1	(r)
IRAS 12074-4619	0.0315	42.93	< 320	1	(r)
WAS 49	0.061	43.73	60^{+60}_{-20}	1	(r)
NGC 4388	0.0084	42.87	210^{+120}_{-40}	1	(r)
NGC 4395	0.0011	40.63	120^{+50}_{-30}	1	(r)
LEDA 170194	0.0367	43.2	< 230	1	(r)
NGC 4941	0.0037	41.73	< 50	1	(r)
NGC 4992	0.0251	43.46	80^{+90}_{-30}	1	(r)
Mrk 248	0.0366	43.53	50^{+20}_{-10}	1	(r)
ESO 509-IG066	0.0446	43.63	70^{+50}_{-20}	1	(r)
NGC 5252	0.023	43.43	330^{+150}_{-100}	1	(r)
2MASX J1410	0.0339	42.93	< 80	1	(r)
NGC 5643	0.004	41.13	< 130	1	(r)
NGC 5674	0.0249	43.23	< 100	1	(r)
NGC 5728	0.0094	43.23	80^{+30}_{-20}	1	(r)
IC 4518A	0.0163	42.73	120^{+150}_{-50}	1	(r)
2MASX J1506	0.0377	42.93	< 140	1	(r)
NGC 5899	0.0086	42.23	< 340	1	(r)
MCG+11-19-006	0.044	43.43	< 60	1	(r)
MCG-01-40-001	0.0227	42.93	< 130	1	(r)
NGC 5995	0.0252	43.28	< 340	1	(r)
MCG+14-08-004	0.0239	42.81	< 120	1	(r)
Mrk 1498	0.0547	44.22	60^{+10}_{-10}	1	(r)
IRAS 16288+3929	0.0306	43.37	< 60	1	(r)
NGC 6240	0.0245	44.02	90^{+70}_{-30}	1	(r)
NGC 6300	0.0037	42.04	210^{+100}_{-50}	1	(r)
MCG+07-37-031	0.0412	43.85	< 110	1	(r)
2MASX J1824	0.067	43.83	< 110	1	(r)
IC 4709	0.0169	42.83	140^{+200}_{-60}	1	(r)
LEDA 3097193	0.022	43.34	130^{+110}_{-40}	1	(r)
ESO 103-G035	0.0133	43.25	100^{+20}_{-10}	1	(r)
ESO 231-G026	0.0625	44.12	< 250	1	(r)
2MASX J1926	0.071	43.33	< 70	1	(r)
2MASX J1947	0.0539	43.83	120^{+110}_{-40}	1	(r)
3C 403	0.059	44.03	< 110	1	(r)
2MASX J2006	0.043	43.33	< 80	1	(r)
2MASX J2018	0.0144	42.83	< 100	1	(r)

continued.

Source	z	$\log L_{2-10}$	$E_{\rm cut}$	Flag	References
2MASX J2021	0.017	42.63	< 90	1	(r)
NGC 6921	0.0145	43.13	< 100	1	(r)
MCG+04-48-002	0.0139	42.73	< 150	1	(r)
IC 5063	0.0114	43.03	< 130	1	(r)
NGC 7130	0.0162	43.53	< 100	1	(r)
MCG+06-49-019	0.0213	42.13	< 200	1	(r)
NGC 7319	0.0225	42.63	< 220	1	(r)
NGC 7582	0.0053	41.78	200^{+190}_{-80}	1	(r)
2MASX J2330	0.037	43.13	< 70	1	(r)
PKS 2331-240	0.0477	43.86	< 110	1	(r)
PKS 2356-61	0.0963	44.23	< 80	1	(r)

Notes. Col. (1): Source name; Col. (2): Redshift; Col. (3): Logarithm of the 2–10 keV luminosity (erg s^{-1}); Col. (4): High-energy cutoff (keV); Col. (5): telescope flag, 1=*NuSTAR*, 2=non-focusing; Col. (6): References: (j) Dadina (2007), (k) Kara et al. (2017), (l) Tortosa et al. (2018), (m) Middei et al. (2020), (n) Ursini et al. (2020), (o) Middei et al. (2021), (p) Reeves et al. (2021), (q) Kamraj et al. (2018), (r) Baloković et al. (2020).
*: AGN with multiple observations in Dadina (2007). Observation dates of selected measurements: 1996-12-06 for NGC 4151, 2000-11-08 for Mrk 509.

Table C.3: High-z measurements

Source	z	$\log L_{2-10}$	$E_{\rm cut}$	Flag	References
2MASSJ16	1.86	45.93	107^{+102}_{-37}	1	(b)
B1422	3.62	45.5	66^{+17}_{-12}	1	(b)
APM 08279	3.91	45.8	99^{+91}_{-35}	1	This work

Notes. Col. (1): Source name; Col. (2): Redshift; Col. (3): Logarithm of the 2–10 keV luminosity (erg s^{-1}); Col. (4): High-energy cutoff (keV); Col. (5): telescope flag, 1=*NuSTAR*, 2=non-focusing; Col. (6): References: (b) L19.

Appendix D

CO emission of KASHz AGN

I present here the velocity-integrated line maps and the respective spectra of the KASHz ALMA observations (18 detections, 11 non-detections). Those of lid_1646 are also shown in Figure 5.2 as example of the full dataset. The ALMA analysis is presented in Section 5.3. For those sources that are near the 3σ threshold in the moment 0 map, we show also the cube rms range in the spectrum (as +/-$\mathrm{rms_{cube}}$).

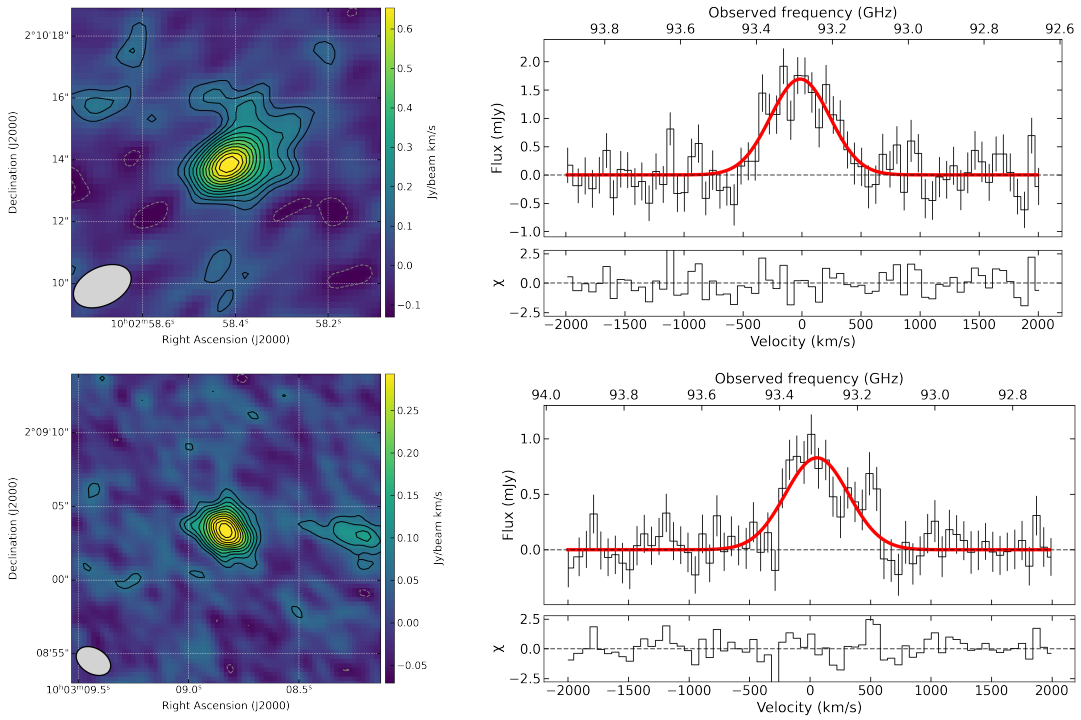

Figure D.1: CO line velocity-integrated emission map (*Left*) and spectrum (*Right*) of lid_1639 (*Top*) and lid_1646 (*Bottom*). Solid contour levels in the left panels start at 2σ. Dashed contour indicate the [-3,-2]$\times\sigma$ level. The beam of each observation is shown by the grey ellipse at the bottom-left corner of each map.

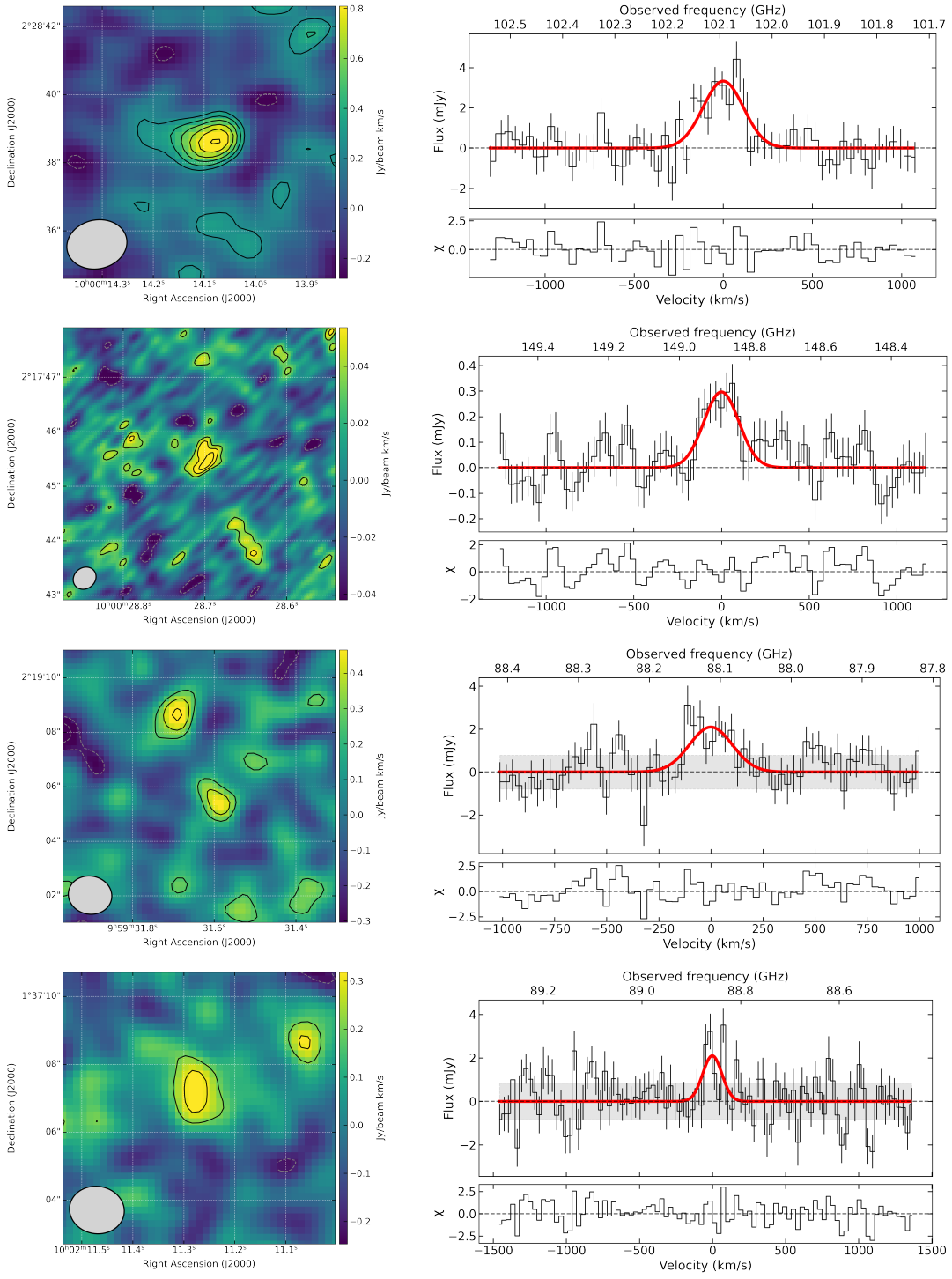

Figure D.2: CO line velocity-integrated emission map (*Left*) and spectrum (*Right*) of cid_108, cid_86, cid_864 and lid_1565, from *Top* to *Bottom*. Solid contour levels in the left panels start at 2σ. Dashed contour indicate the [-3,-2]$\times\sigma$ level. The beam of each observation is shown by the grey ellipse at the bottom-left corner of each map. The grey shaded area in the spectrum of cid_864 and lid_1565 marks the $\pm\mathrm{rms}_{\mathrm{cube}}$ range.

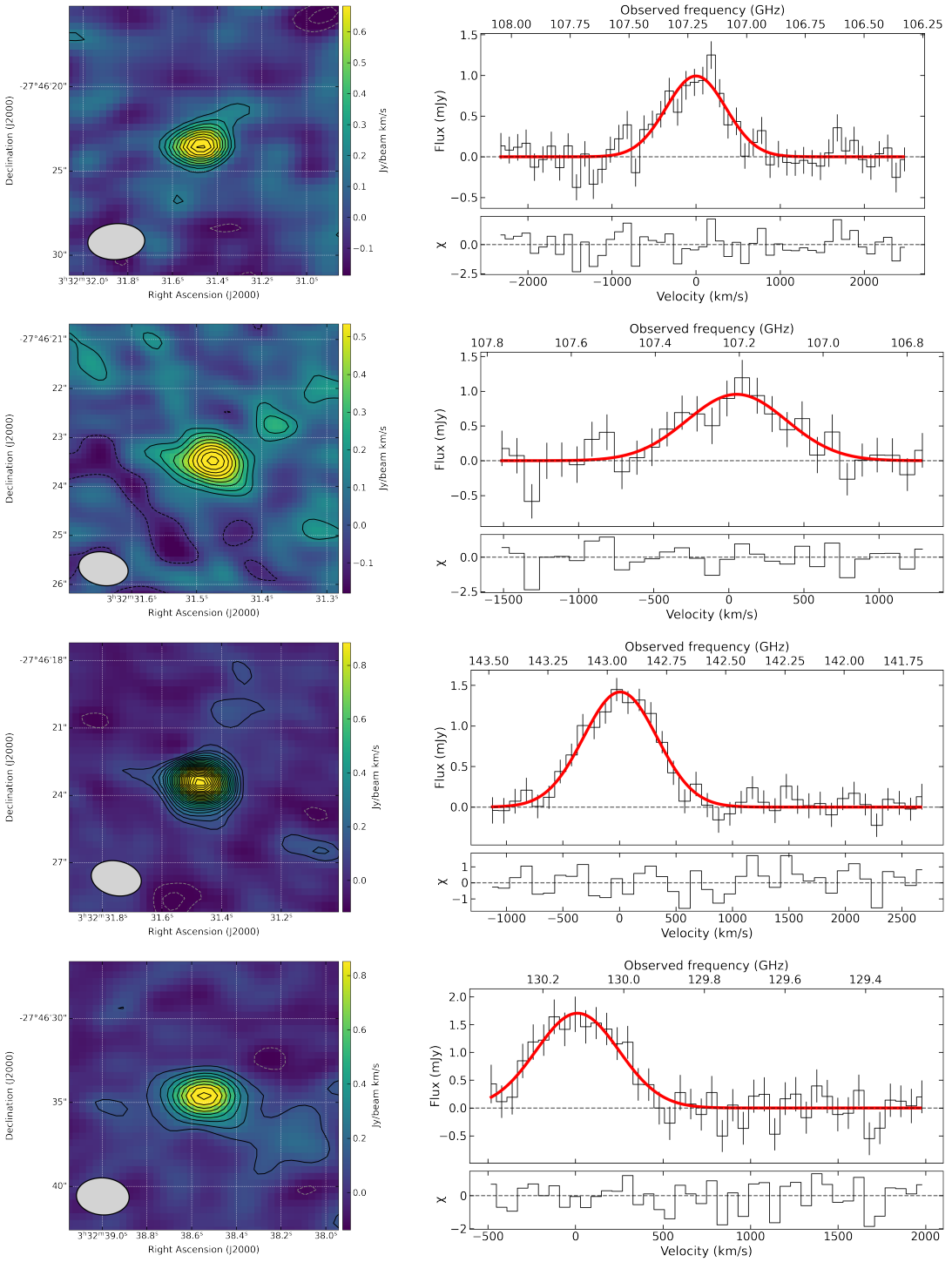

Figure D.3: CO line velocity-integrated emission map (*Left*) and spectrum (*Right*) of cdfs_587 in CO(3-2) (first and second row) and CO(4-3) (third row), and cdfs_718 (last row). Solid contour levels in the left panels start at 2σ. Dashed contour levels indicate the [-3,-2]$\times\sigma$ level. The beam of each observation is shown by the grey ellipse at the bottom-left corner of each map.

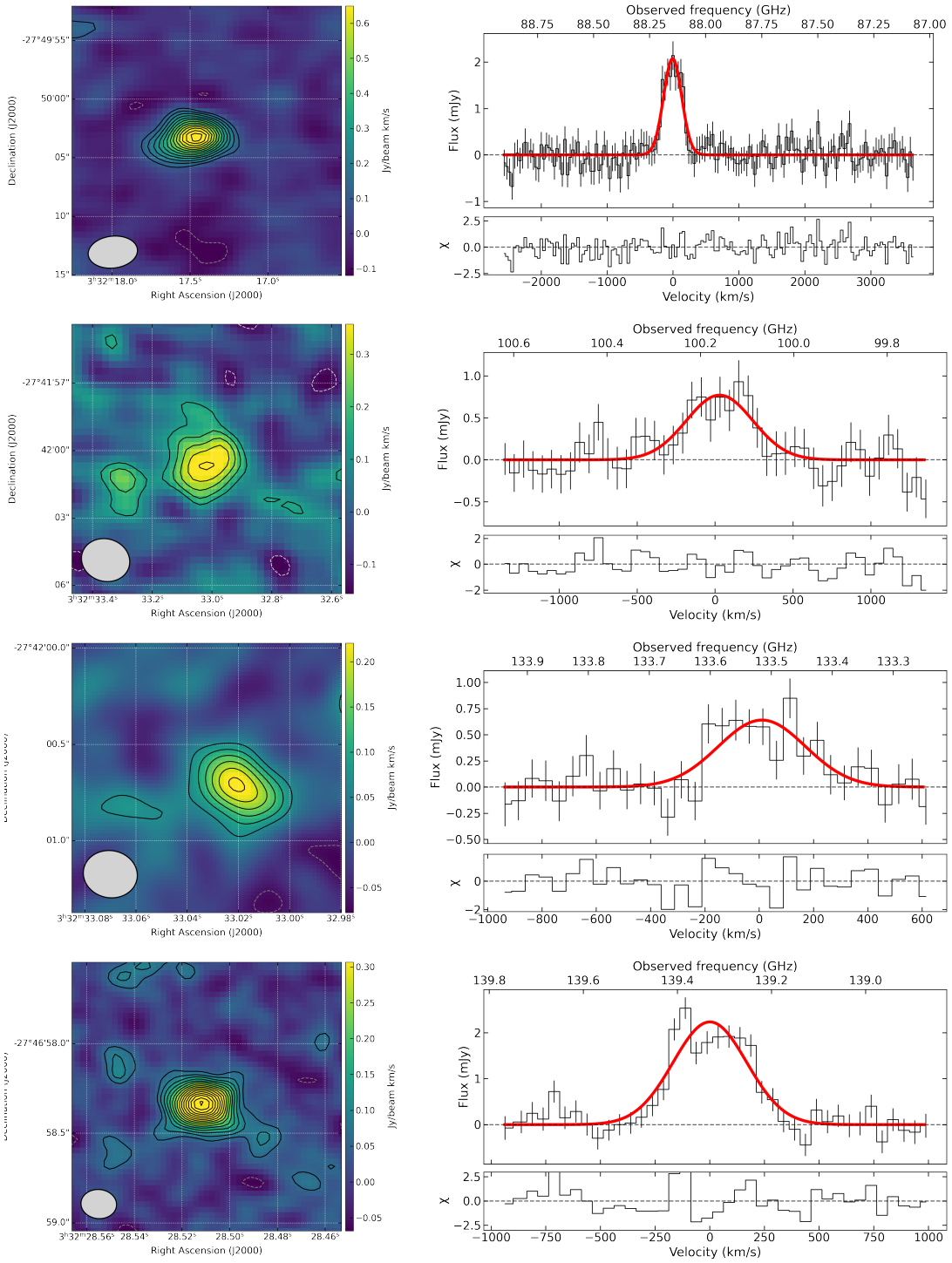

Figure D.4: CO line velocity-integrated emission map (*Left*) and spectrum (*Right*) of cdfs_313, cdfs_614 in CO(3-2) and CO(4-3) (second and third row, respectively), and cdfs_522, from *Top* to *Bottom*. Solid contour levels in the left panels start at 2σ. Dashed contour indicate the [-3,-2]$\times\sigma$ level. The beam of each observation is shown by the grey ellipse at the bottom-left corner of each map.

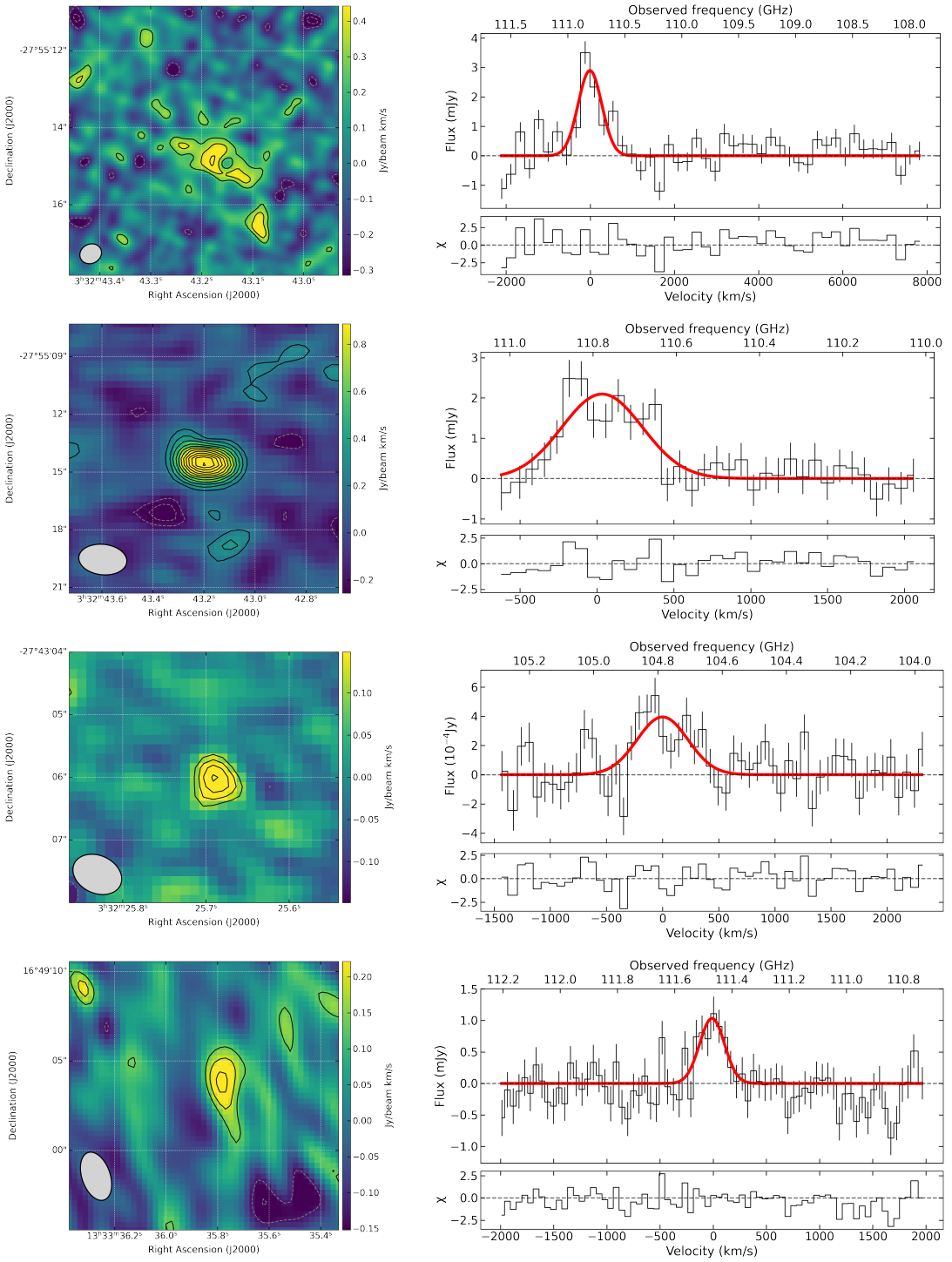

Figure D.5: CO line velocity-integrated emission map (*Left*) and spectrum (*Right*) of cdfs_794 (first and second row), cdfs_458 (third row) and J1333+1649 (fourth row). Solid contour levels in the left panels start at 2σ. Dashed contour indicate the [-3,-2]$\times\sigma$ level. The beam of each observation is shown by the grey ellipse at the bottom-left corner of each map.

Table D.1: Summary of the ALMA observations reduced and analyzed in this thesis.

ID	Band	Project code	MOUS UID
cdfs_258	3	2019.1.00678.S	uid://A001/X14d8/X3eb
cdfs_313	3	2018.1.00164.S	uid://A001/X133d/X7a8
cdfs_419	3	2019.1.00678.S	uid://A001/X14d8/X3ef
cdfs_427	3	2013.1.00092.S	uid://A001/X13f/X2e; uid://A001/X13f/X16
cdfs_427	4	2019.1.01537.S	uid://A001/X1465/X86b
cdfs_458	3	2013.1.00092.S	uid://A001/X13f/X2e; uid://A001/X13f/X16
cdfs_522	4	2016.1.00990.S	uid://A001/X87c/X9e8
cdfs_587	4	2015.1.00228.S	uid://A001/X2f6/X462
cdfs_587	3	2015.1.00228.S	uid://A001/X2f6/X45e
cdfs_587	3	2015.1.01379.S	uid://A001/X2fb/X818
cdfs_614	4	2016.1.00990.S	uid://A001/X87c/X9e0
cdfs_614	3	2019.1.00678.S	uid://A001/X14d8/X3eb
cdfs_718	4	2019.1.01528.S	uid://A001/X1465/X96a
cdfs_794	3	2013.1.00470.S	uid://A001/X12a/X3c
cdfs_794	3	2016.1.00564.S	uid://A001/X879/Xd9
cid_108	3	2016.1.00171.S	uid://A001/X879/X23f
cid_1286	3	2016.1.01001.S	uid://A001/X8c4/Xf
cid_178	3	2016.1.00171.S	uid://A001/X879/X23b
cid_499	3	2016.1.00171.S	uid://A001/X879/X233
cid_72	3	2016.1.01001.S	uid://A001/X8c4/X1b
cid_86	4	2016.1.00726.S	uid://A001/X885/X249
cid_864	3	2016.1.00171.S	uid://A001/X879/X237
lid_1565	3	2016.1.00171.S	uid://A001/X879/X237
lid_1639	3	2018.1.00251.S	uid://A001/X133d/X316
lid_1646	3	2018.1.00251.S	uid://A001/X133d/X31e
xuds_358	3	2019.1.00337.S	uid://A001/X14d7/X168
xuds_477	3	2019.1.00337.S	uid://A001/X14d7/X168
xuds_481	3	2019.1.00337.S	uid://A001/X14d7/X168

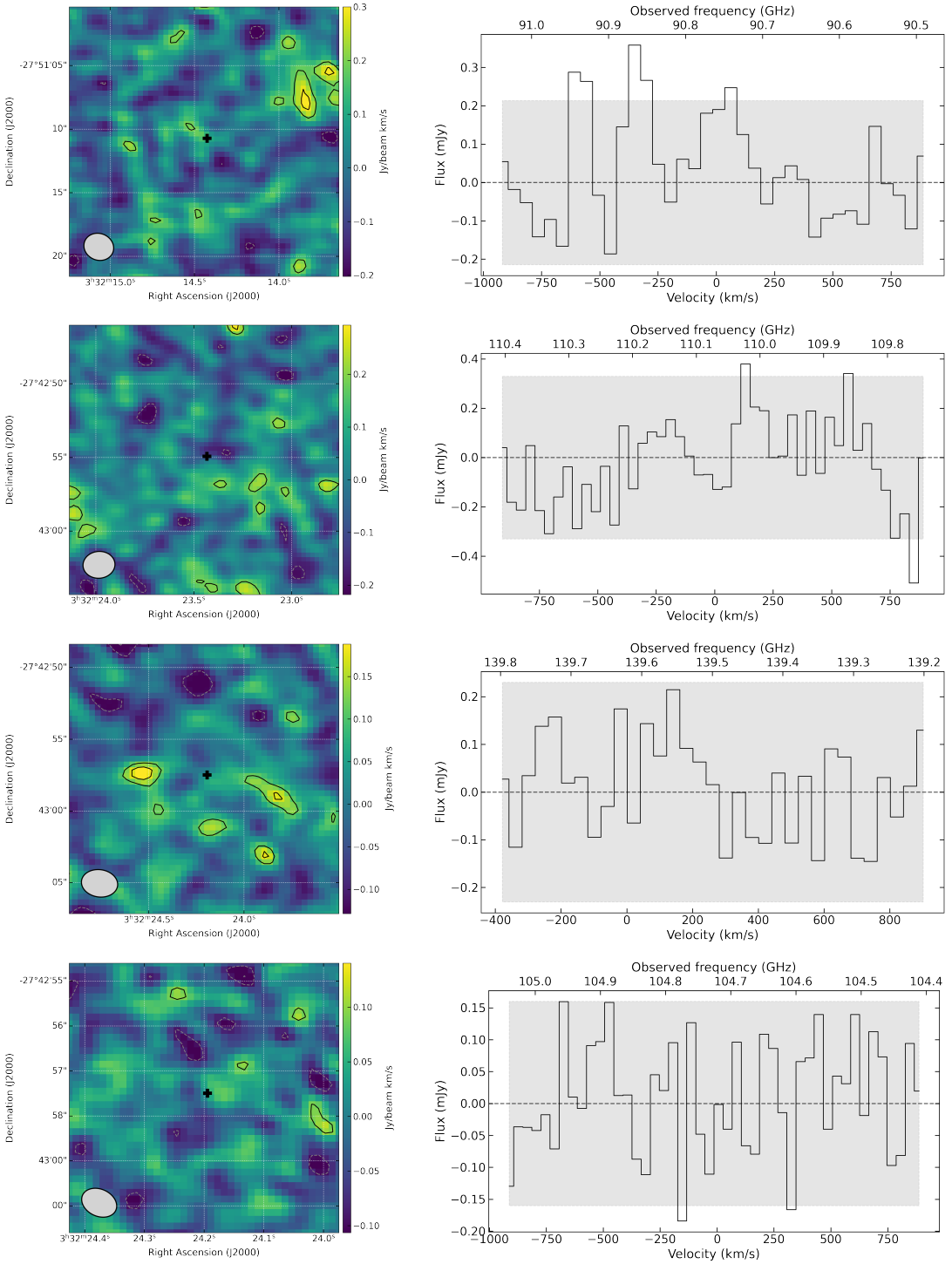

Figure D.6: CO line velocity-integrated emission map (*Left*) and spectrum (*Right*) of cdfs_258, cdfs_419, cdfs_427 CO(4-3) and CO(3-2), from *Top* to *Bottom*. Solid contour levels in the left panels start at 2σ. Dashed contour indicate the [-3,-2]$\times\sigma$ level. The black cross marks the coordinates of the undetected target. The beam of each observation is shown by the grey ellipse at the bottom-left corner of each map. The grey shaded area in the spectra marks the $\pm\mathrm{rms}_{\mathrm{cube}}$ range.

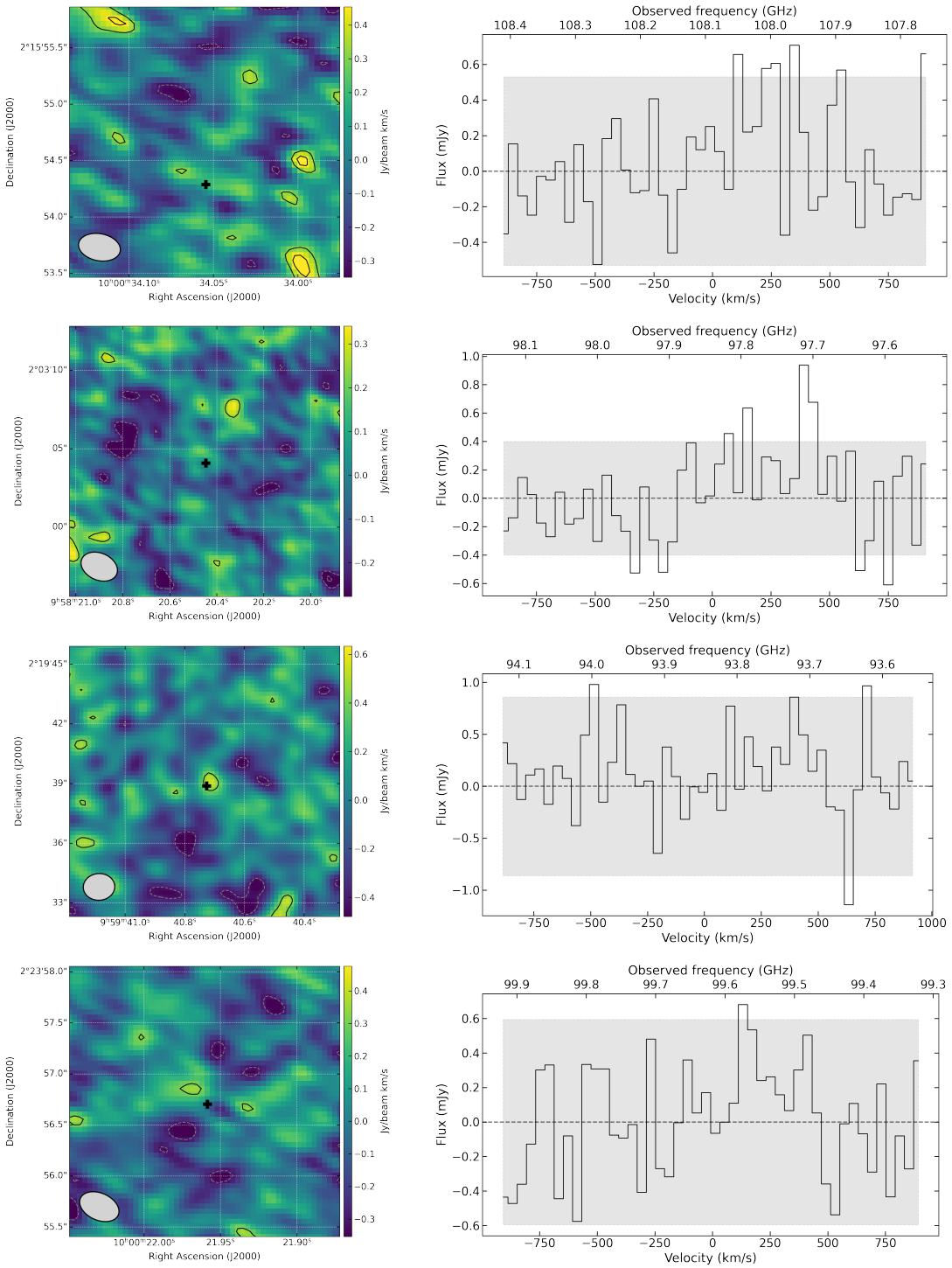

Figure D.7: CO line velocity-integrated emission map (*Left*) and spectrum (*Right*) of cid_1286, cid_178, cid_499 and cid_72, from *Top* to *Bottom*. Solid contour levels in the left panels start at 2σ. Dashed contour indicate the [-3,-2]$\times\sigma$ level. The black cross marks the coordinates of the undetected target. The beam of each observation is shown by the grey ellipse at the bottom-left corner of each map. The grey shaded area in the spectra marks the $\pm\mathrm{rms}_{\mathrm{cube}}$ range.

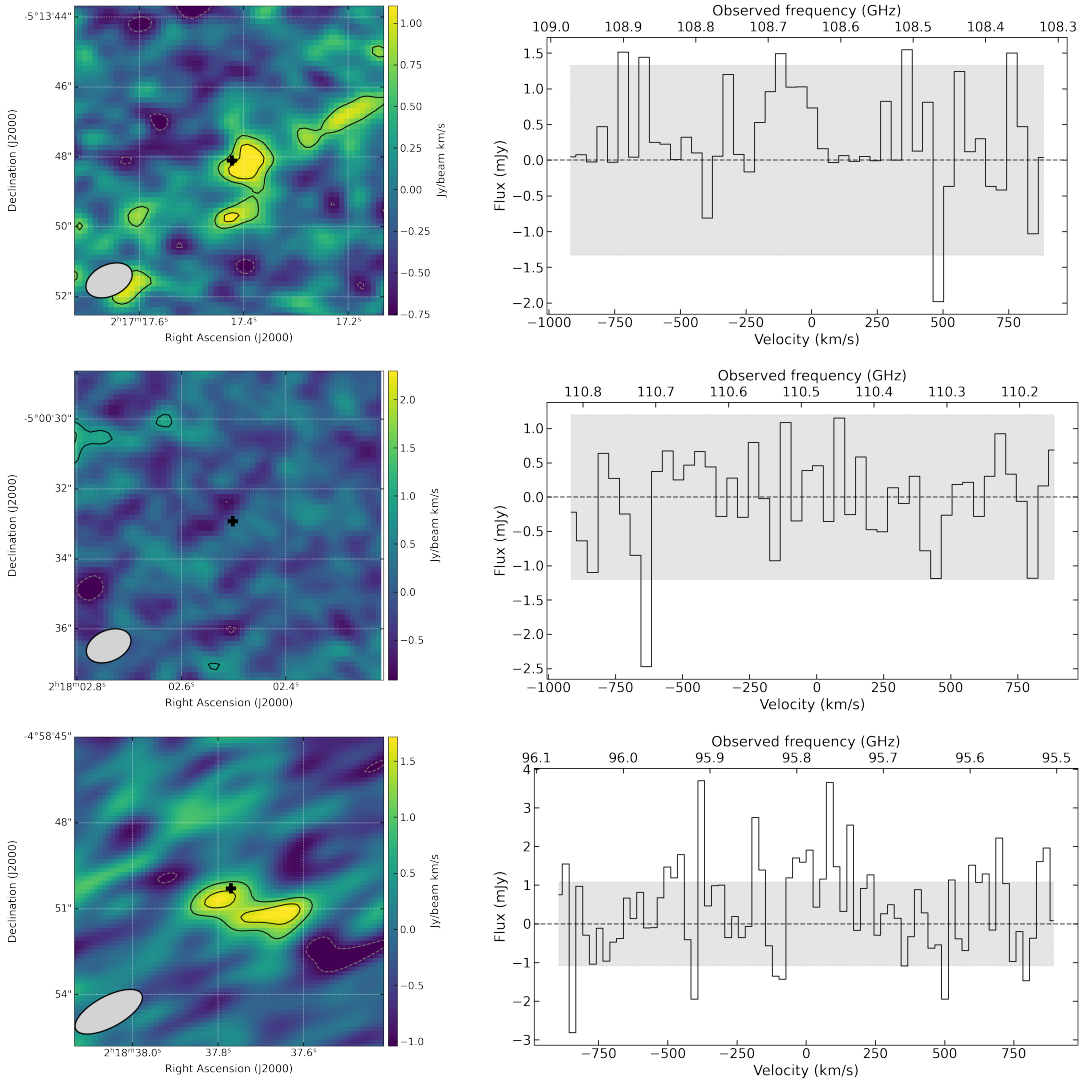

Figure D.8: CO line velocity-integrated emission map (*Left*) and spectrum (*Right*) of xuds_358, xuds_477 and xuds_481, from *Top* to *Bottom*. Solid contour levels in the left panels start at 2σ. Dashed contour indicate the [-3,-2]$\times\sigma$ level. The black cross marks the coordinates of the undetected target. The beam of each observation is shown by the grey ellipse at the bottom-left corner of each map. The grey shaded area in the spectra marks the $\pm\mathrm{rms}_{\mathrm{cube}}$ range.

Appendix E

SED fitting of KASHz AGN

We report here the best-fit SEDs of our KASHz targets, the filter setup (Table E.1), and the model parameters set in X-CIGALE (Table E.2).

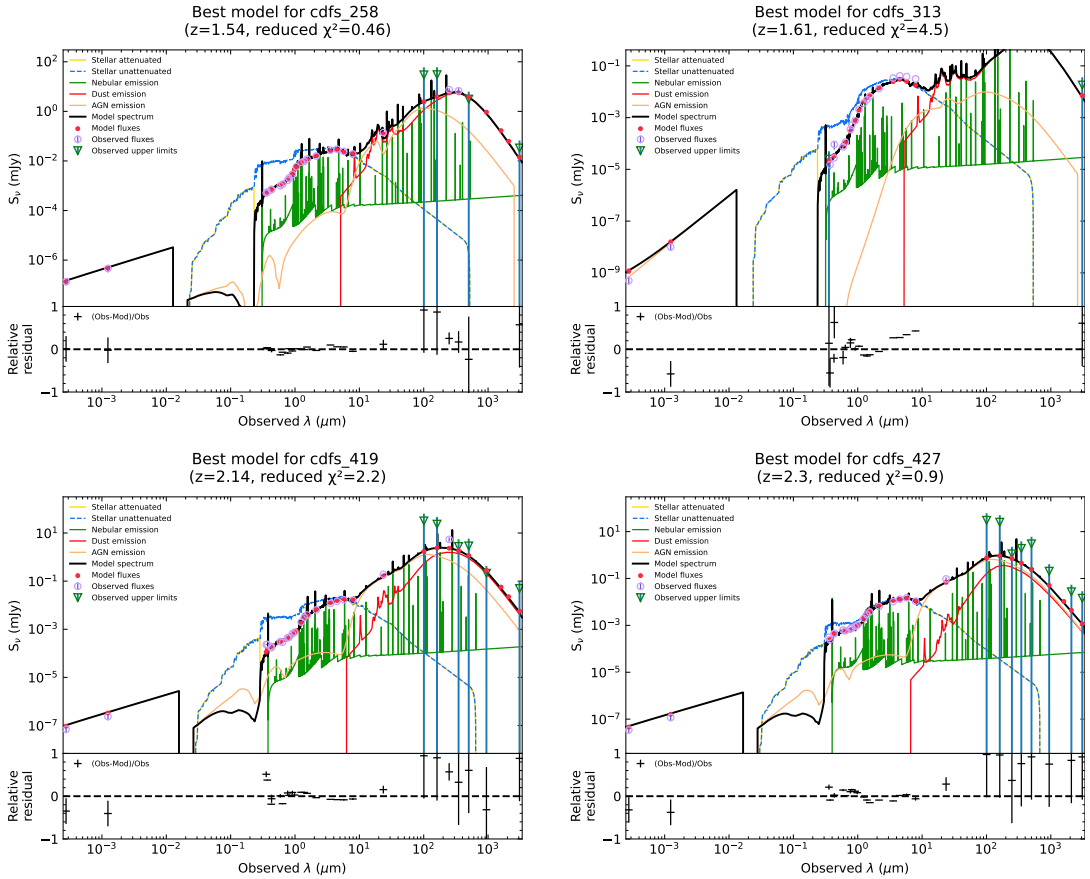

Figure E.1: Observed-frame, best-fit SED models of KASHz ALMA targets. Color-coding is as described in Figure 5.4.

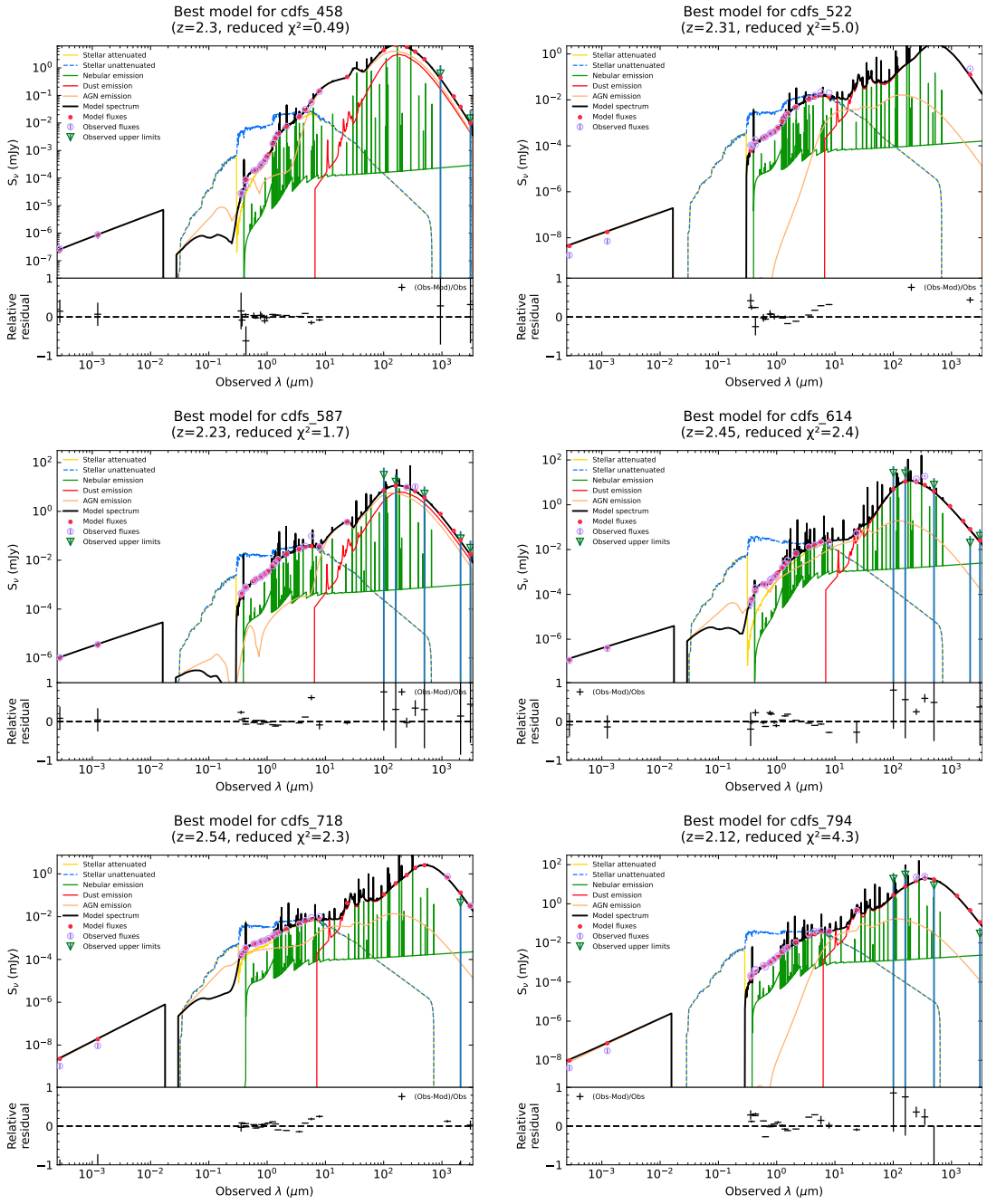

Figure E.2: Observed-frame, best-fit SED models of KASHz ALMA targets. Color-coding is as described in Figure 5.4.

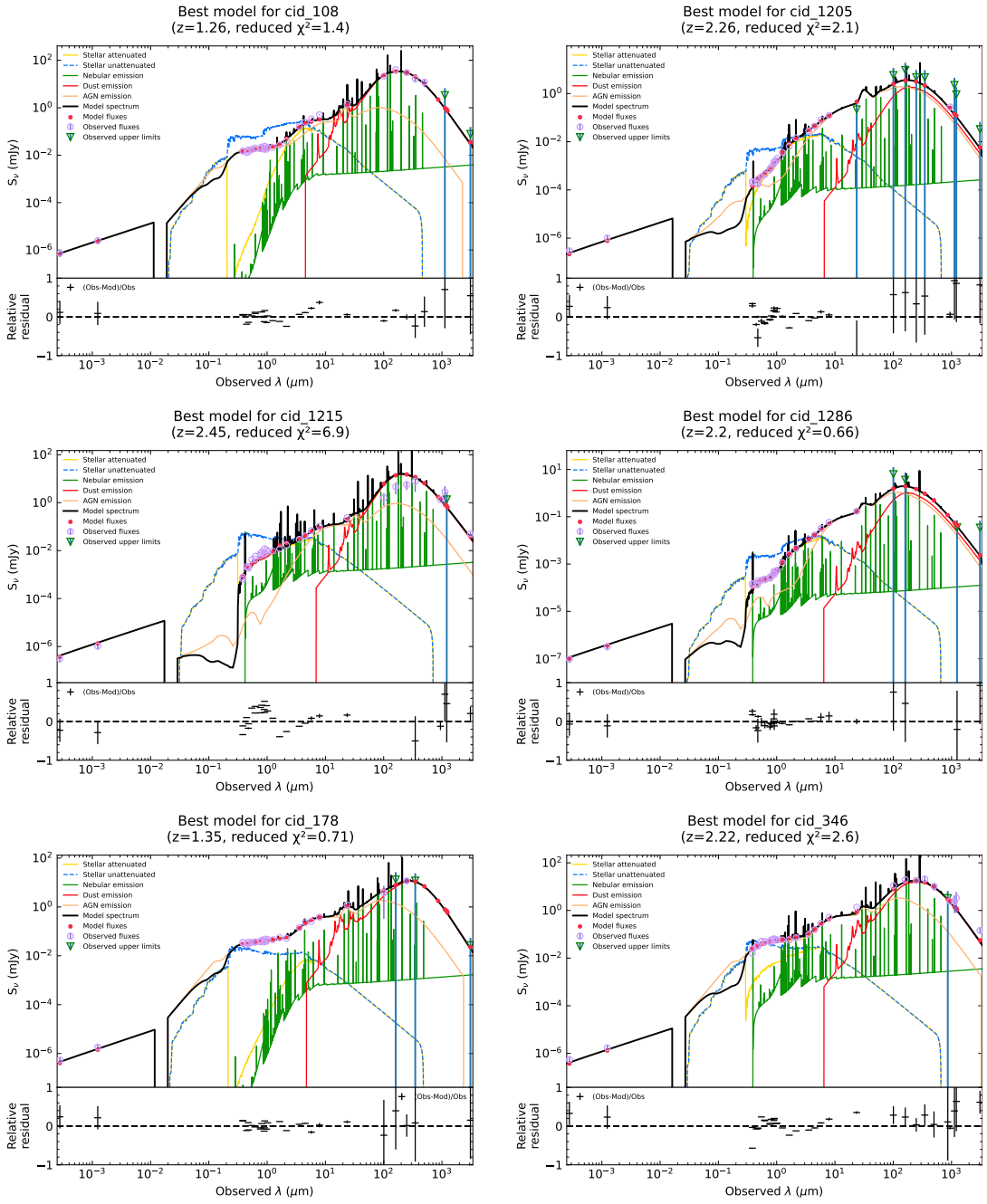

Figure E.3: Observed-frame, best-fit SED models of KASHz ALMA targets. Color-coding is as described in Figure 5.4.

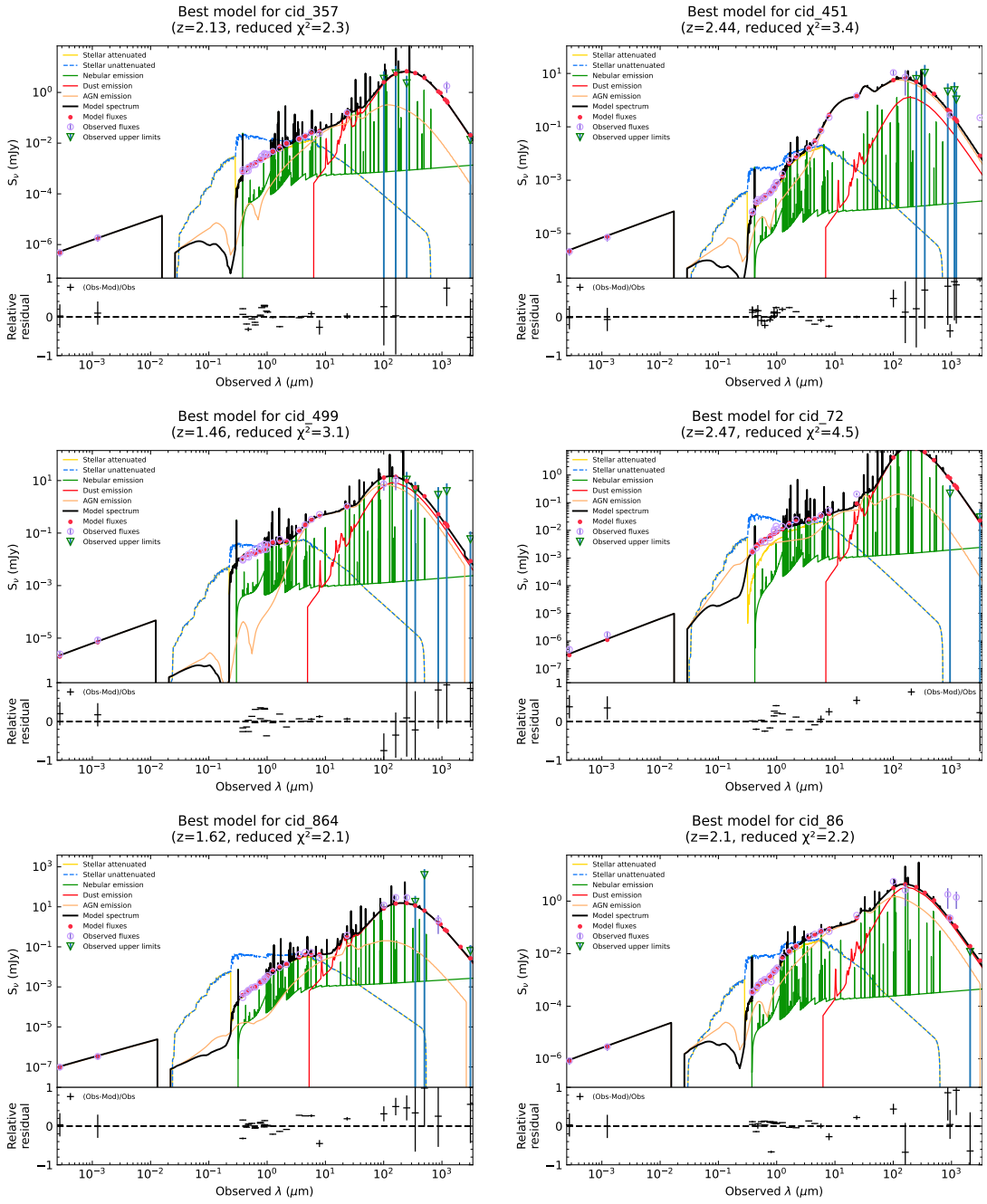

Figure E.4: Observed-frame, best-fit SED models of KASHz ALMA targets. Color-coding is as described in Figure 5.4.

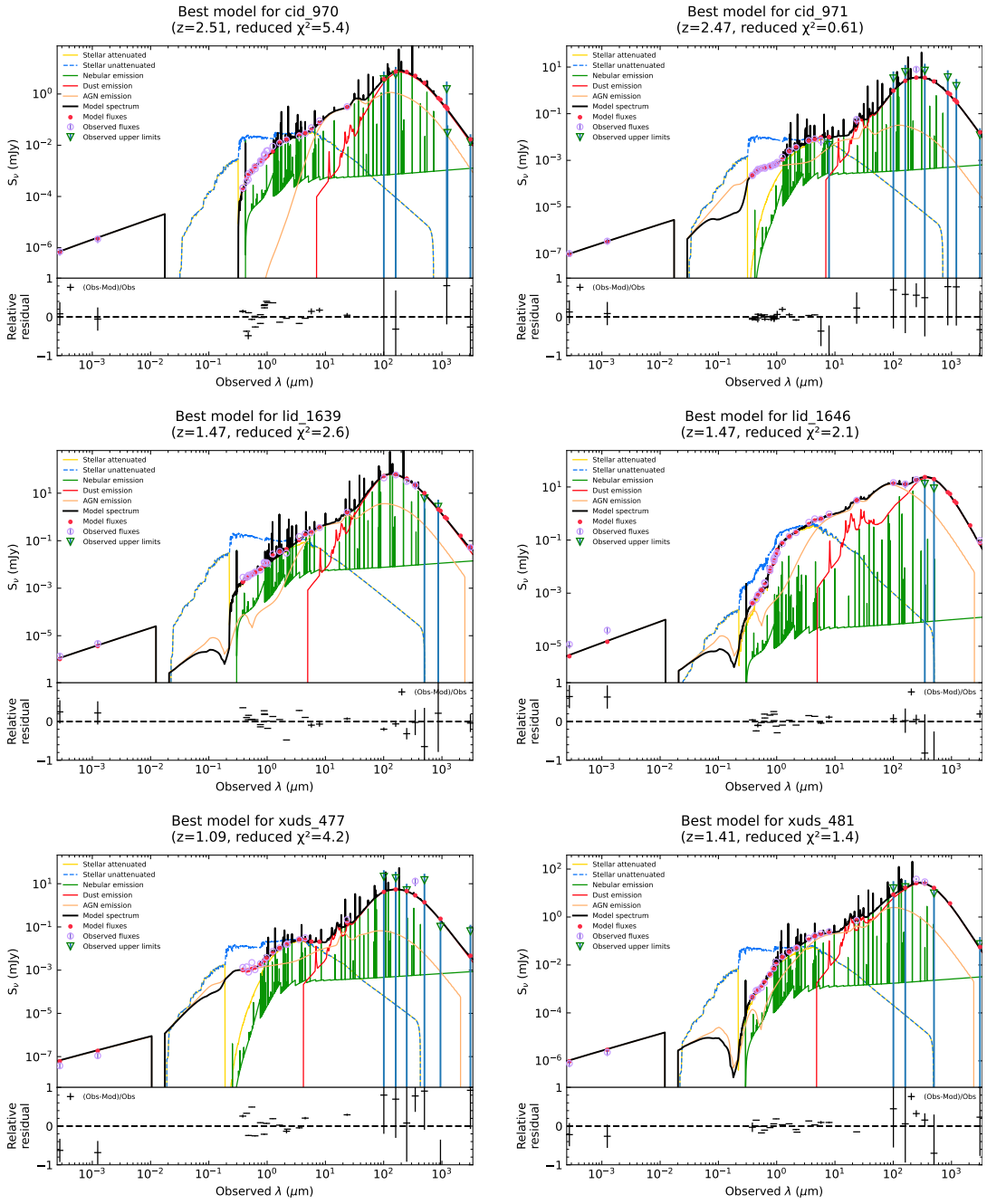

Figure E.5: Observed-frame, best-fit SED models of KASHz ALMA targets. Color-coding is as described in Figure 5.4.

Table E.1: Summary of the photometric data used for the SED-fitting modeling described in Chapter 5.

Field	λ range	Reference	Telescope/Instrument	Bands
CDF-S	UV to NIR	Merlin et al. (2021)	CTIO-Blanco/Mosaic-II	*U*
			VLT/VIMOS	*U, B, R*
			HST/ACS	F435W, F606W, F775W, F814W, F850LP
			HST/WFC3	F098M, F105W, F125W, F160W
			VLT/HAWK-I	K_S
	$3-500$ μm	Shirley et al. (2021)	*Spitzer*/IRAC	3.6, 4.5, 5.8, 8.0 μm
			Spitzer/MIPS	24 μm
			Herschel/PACS	70, 100, 160 μm
			Herschel/SPIRE	250, 350, 500 μm
	>1000 μm	Scholtz et al. (2018),	ALMA	Band 7 (800−1100 μm)
		González-López et al. (2020),		Band 6 (1100—1400 μm)
		Aravena et al. (2020)		Band 5 (1400—1800 μm)
		and this work		Band 4 (1800—2400 μm)
				Band 3 (2600−3600 μm)
COSMOS	UV to MIR	Weaver et al. (2022)	CFHT/MegaCam	*u*, u^*
			HST/ACS	F814W
			Subaru/HSC	*g, r, i, z, y*
			Subaru/Suprime-Cam	*B*, g^+, *V*, r^+, i^+, z^+, z^{++}
			VISTA/VIRCAM	*Y, J, H*, K_s
			Spitzer/IRAC	3.6, 4.5, 5.8, 8.0 μm
	$24-500$ μm [a]	Jin et al. (2018)	*Spitzer*/MIPS	24 μm
			Herschel/PACS	70, 100, 160 μm
			Herschel/SPIRE	250, 350, 500 μm
	>1000 μm	Scholtz et al. (2018),	ALMA	Band 7 (800−1100 μm)
		Circosta et al. (2021)		Band 6 (1100—1400 μm)
		and this work		Band 4 (1800—2400 μm)
				Band 3 (2600−3600 μm)
X-UDS	UV to FIR	Shirley et al. (2021)	CFHT/MegaCam	u^*
			Subaru/Suprime	*r*
			Subaru/HSC	*g, i, z, y*
			UKIDSS	*J, H, K*
			VISTA/VIRCAM	*Ks*
			Spitzer/IRAC	3.6, 4.5, 5.8, 8.0 μm
			Spitzer/MIPS	24 μm
			Herschel/PACS	70, 100, 160 μm
			Herschel/SPIRE	250, 350, 500 μm
	>1000 μm	Scholtz et al. (2018),	ALMA	Band 7 (800−1100 μm)
		and this work		Band 6 (1100—1400 μm)
				Band 5 (1400—1800 μm)
				Band 4 (1800—2400 μm)
				Band 3 (2600−3600 μm)

Notes. [a] The $24-500$ μm photometry of lid_1565, lid_1646 and cid_72 is collected from Lutz et al. (2011) and Hurley et al. (2017).

Table E.2: Input parameter values used for the SED-fitting procedure in Chapter 5.

Template	Parameter	Value and range	Description
Stellar emission	IMF	Chabrier (2003)	
	Z	0.02	Metallicity
	Separation age	10 Myr	Separation age between the young and the old stellar populations
Delayed SFH	Age	0.10, 0.25, 0.5, 1.0, 1.5, 2.0, 2.5 Gyr	Age of the oldest SSP
	τ	0.10, 0.25, 0.5, 1.0, 3.0, 5.0, 10.0 Gyr	e-folding time of the SFH
Modified Calzetti	$E(B-V)$	0.05, 0.1, 0.3, 0.5, 0.7, 0.9, 1.1, 1.3	Attenuation of the young stellar population
attenuation law	Reduction factor	0.93	Differential reddening applied to the old stellar population
	δ	-0.6, -0.4, -0.2, 0.0	Slope of the power law multiplying the Calzetti attenuation law
Dust emission	$\alpha_{\rm SF}$	0.5, 1.0, 1.5, 2.0, 2.5, 3.0	Slope of the power law combining the contribution of different dust templates
AGN emission	$R_{\rm max}/R_{\rm min}$	60	Ratio of the outer and inner radii
	$\tau_{9.7}$	0.6, 3.0, 6.0	Optical depth at 9.7 μm
	β	0.00, -0.5, -1.0	Slope of the radial coordinate
	γ	0.0, 6.0	Exponent of the angular coordinate
	Θ	100 degrees	Opening angle of the torus
	ψ	0, 10, 20, 30, 40, 50, 60, 70, 80, 90 degrees	Inclination of the observer's line of sight
	$f_{\rm AGN}$	0.05, 0.1, 0.15, 0.2, 0.25, 0.3, 0.35, 0.4, 0.45, 0.5, 0.55, 0.6, 0.65, 0.7, 0.75, 0.8, 0.85, 0.9	AGN fraction
AGN intrinsic X-ray emission	Γ	1.8, 1.9, 2.4[a], 3[a]	Intrinsic X-ray photon index
Nebular emission	U	10^{-2}	Ionization parameter
	$f_{\rm esc}$	0%	Fraction of Lyman continuum photons escaping the galaxy
	$f_{\rm dust}$	10%	Fraction of Lyman continuum photons absorbed by dust

Notes. We divided the sample in different runs of CIGALE based on the photon index value obtained from the X-ray catalogs or X-ray fits to reduce the computational time. [b] Input values used only for cdfs_313, cdfs_718, cdfs_794, which are AGN Type 1 with very steep intrinsic photon index (Luo et al. 2017).

Acknowledgements

As someone once said, research is a collective activity, that can only be done by collaborating and exchanging views with other people. Despite the COVID outbreak happened right when I was starting to see the fun in it, there are many researchers that helped me throughout these years, both in person and remotely.

First of all, I want to thank my supervisor, Prof. Vignali, for the invaluable guidance and support he has never denied me, even in his busiest times and my darkest hours. I am also very grateful to my co-supervisors, Dr. Dadina and Dr. Cappi, for their fundamental guidance since my Master's, generating reasonable (statistical) doubts every time I was too sure about my results. A special mention goes to Dr. Dadina, for granting me access to sbuccia each time I needed. I am sincerely grateful to Dr. Mainieri, Dr. Ginolfi, Dr. Calistro Rivera and all the people I collaborate with since visiting the European Southern Observatory, where significant part of the ALMA analysis took place, and for the support they provided in developing the rest of our analysis.

This thesis would not have been possible without several other people. I am grateful to Dr. Chartas, for improving my understanding of gravitational lensing and how to use it as a powerful tool to study distant quasars; to Dr. Lanzuisi, for being the first to deal with me as a peer; to Dr. Circosta, for being an inspiration since the times of the "Circosta book"; to Dr. Pensabene, for having answered each of my intricate questions, even while writing his thesis; to L. Barchiesi, for all the discussions we had in the office; to I. López, for having taught me how to handle CIGALE and JWST's ETC, and that a mate can fix (almost) anything.

Bibliography

Aird, J., Coil, A. L., Georgakakis, A., et al. 2015, MNRAS, 451, 1892

Akiyama, M., Ueda, Y., Watson, M. G., et al. 2015, PASJ, 67, 82

Akylas, A. & Georgantopoulos, I. 2021, A&A, 655, A60

Almaini, O., Foucaud, S., Lane, K., et al. 2007, in Astronomical Society of the Pacific Conference Series, Vol. 379, Cosmic Frontiers, ed. N. Metcalfe & T. Shanks, 163

Antonucci, R. 1993, Annual Review of Astronomy and Astrophysics, 31, 473

Antonucci, R. R. J. & Miller, J. S. 1985, ApJ, 297, 621

Aravena, M., Boogaard, L., Gónzalez-López, J., et al. 2020, ApJ, 901, 79

Aravena, M., Decarli, R., Gónzalez-López, J., et al. 2019, ApJ, 882, 136

Arribas, S., Colina, L., Bellocchi, E., Maiolino, R., & Villar-Martín, M. 2014, A&A, 568, A14

Assef, R. J., Denney, K. D., Kochanek, C. S., et al. 2011, ApJ, 742, 93

Baldwin, J. A. 1977, ApJ, 214, 679

Baloković, M., Harrison, F. A., Madejski, G., et al. 2020, ApJ, 905, 41

Bassani, L., Dadina, M., Maiolino, R., et al. 1999, The Astrophysical Journal Supplement Series, 121, 473

Bertola, E., Dadina, M., Cappi, M., et al. 2020, A&A, 638, A136

Bertola, E., Vignali, C., Lanzuisi, G., et al. 2022, A&A, 662, A98

Bianchi, S., Guainazzi, M., Matt, G., & Fonseca Bonilla, N. 2007, A&A, 467, L19

Bianchi, S., Guainazzi, M., Matt, G., Fonseca Bonilla, N., & Ponti, G. 2009, A&A, 495, 421

Birkin, J. E., Weiss, A., Wardlow, J. L., et al. 2021, MNRAS, 501, 3926

Bischetti, M., Feruglio, C., D'Odorico, V., et al. 2022, Nature, 605, 244

Bischetti, M., Feruglio, C., Piconcelli, E., et al. 2021, A&A, 645, A33

Bischetti, M., Fiore, F., Feruglio, C., et al. 2023, arXiv e-prints, arXiv:2301.09731

Bischetti, M., Piconcelli, E., Feruglio, C., et al. 2019, A&A, 628, A118

Bischetti, M., Piconcelli, E., Vietri, G., et al. 2017, A&A, 598, A122

Boissay-Malaquin, R., Danehkar, A., Marshall, H. L., & Nowak, M. A. 2019, ApJ, 873, 29

Bolatto, A. D., Wolfire, M., & Leroy, A. K. 2013, ARA&A, 51, 207

Bonanomi, F., Cicone, C., Severgnini, P., et al. 2023, A&A, 673, A46

Bonzini, M., Mainieri, V., Padovani, P., et al. 2015, MNRAS, 453, 1079

Boogaard, L. A., van der Werf, P., Weiss, A., et al. 2020, ApJ, 902, 109

Boquien, M., Burgarella, D., Roehlly, Y., et al. 2019, A&A, 622, A103

Bradford, C. M., Bolatto, A. D., Maloney, P. R., et al. 2011, ApJ, 741, L37

Brusa, M., Cresci, G., Daddi, E., et al. 2018, A&A, 612, A29

Brusa, M., Perna, M., Cresci, G., et al. 2016, A&A, 588, A58

Bruzual, G. & Charlot, S. 2003, MNRAS, 344, 1000

Buat, V., Mountrichas, G., Yang, G., et al. 2021, A&A, 654, A93

Buisson, D. J. K., Parker, M. L., Kara, E., et al. 2018, MNRAS, 480, 3689

Burtscher, L., Meisenheimer, K., Tristram, K. R. W., et al. 2013, A&A, 558, A149

Calistro Rivera, G., Hodge, J. A., Smail, I., et al. 2018, ApJ, 863, 56

Calzetti, D., Armus, L., Bohlin, R. C., et al. 2000, ApJ, 533, 682

Cappi, M., Panessa, F., Bassani, L., et al. 2006, A&A, 446, 459

Cappi, M., Tombesi, F., Bianchi, S., et al. 2009, A&A, 504, 401

Carilli, C. L. & Walter, F. 2013, ARA&A, 51, 105

Carniani, S., Marconi, A., Maiolino, R., et al. 2016, A&A, 591, A28

Carniani, S., Marconi, A., Maiolino, R., et al. 2017, A&A, 605, A105

Cash, W. 1979, ApJ, 228, 939

Cavaliere, A. & Morrison, P. 1980, ApJ, 238, L63

Chabrier, G. 2003, ApJ, 586, L133

Chartas, G., Agol, E., Eracleous, M., et al. 2002, ApJ, 568, 509

Chartas, G., Brandt, W. N., & Gallagher, S. C. 2003, ApJ, 595, 85

Chartas, G., Brandt, W. N., Gallagher, S. C., & Proga, D. 2007a, AJ, 133, 1849

Chartas, G., Cappi, M., Hamann, F., et al. 2016a, ApJ, 824, 53

Chartas, G., Cappi, M., Vignali, C., et al. 2021, ApJ, 920, 24

Chartas, G., Davidson, E., Brusa, M., et al. 2020, MNRAS, 496, 598

Chartas, G., Eracleous, M., Dai, X., Agol, E., & Gallagher, S. 2007b, ApJ, 661, 678

Chartas, G., Krawczynski, H., Zalesky, L., et al. 2017, ApJ, 837, 26

Chartas, G., Rhea, C., Kochanek, C., et al. 2016b, Astronomische Nachrichten, 337, 356

Chartas, G., Saez, C., Brandt, W. N., Giustini, M., & Garmire, G. P. 2009, ApJ,

706, 644
Chen, B., Dai, X., Kochanek, C. S., et al. 2011, ApJ, 740, L34
Chen, B., Dai, X., Kochanek, C. S., et al. 2012, ApJ, 755, 24
Chen, C.-C., Hodge, J. A., Smail, I., et al. 2017, ApJ, 846, 108
Cicone, C., Brusa, M., Ramos Almeida, C., et al. 2018, Nature Astronomy, 2, 176
Cicone, C., Feruglio, C., Maiolino, R., et al. 2012, A&A, 543, A99
Cicone, C., Maiolino, R., Sturm, E., et al. 2014, A&A, 562, A21
Circosta, C., Mainieri, V., Lamperti, I., et al. 2021, A&A, 646, 96
Circosta, C., Mainieri, V., Padovani, P., et al. 2018, A&A, 620, A82
Civano, F., Marchesi, S., Comastri, A., et al. 2016, ApJ, 819, 62
Costa, T., Pakmor, R., & Springel, V. 2020, MNRAS, 497, 5229
Costa, T., Rosdahl, J., Sijacki, D., & Haehnelt, M. G. 2018, MNRAS, 479, 2079
Crenshaw, D. M. & Kraemer, S. B. 2012, ApJ, 753, 75
Crenshaw, D. M., Kraemer, S. B., & George, I. M. 2003, ARA&A, 41, 117
Cresci, G., Mainieri, V., Brusa, M., et al. 2015, ApJ, 799, 82
Cresci, G. & Maiolino, R. 2018, Nature Astronomy, 2, 179
D'Abrusco, R., Álvarez Crespo, N., Massaro, F., et al. 2019, ApJS, 242, 4
Daddi, E., Elbaz, D., Walter, F., et al. 2010, ApJ, 714, L118
Dadina, M. 2007, A&A, 461, 1209
Dadina, M. 2008, A&A, 485, 417
Dadina, M., Cappi, M., Malaguti, G., Ponti, G., & de Rosa, A. 2005, A&A, 442, 461
Dadina, M., Vignali, C., Cappi, M., et al. 2016, A&A, 592, A104
Dadina, M., Vignali, C., Cappi, M., et al. 2018, A&A, 610, L13
Dai, X., Chartas, G., Agol, E., Bautz, M. W., & Garmire, G. P. 2003, ApJ, 589, 100
Dale, D. A., Helou, G., Magdis, G. E., et al. 2014, ApJ, 784, 83
D'Amato, Q., Gilli, R., Vignali, C., et al. 2020, A&A, 636, A37
Dauser, T., Garcia, J., Parker, M. L., Fabian, A. C., & Wilms, J. 2014, MNRAS, 444, L100
De Rosa, A., Panessa, F., Bassani, L., et al. 2012, MNRAS, 420, 2087
Decarli, R., Walter, F., Aravena, M., et al. 2016, ApJ, 833, 70
Decarli, R., Walter, F., Gónzalez-López, J., et al. 2019, ApJ, 882, 138
Decarli, R., Walter, F., Neri, R., et al. 2012, ApJ, 752, 2
Del Moro, A., Alexander, D. M., Aird, J. A., et al. 2017, ApJ, 849, 57
Di Matteo, T., Springel, V., & Hernquist, L. 2005, Nature, 433, 604

Downes, D., Neri, R., Wiklind, T., Wilner, D. J., & Shaver, P. A. 1999, ApJ, 513, L1

Ducourant, C., Wertz, O., Krone-Martins, A., et al. 2018, A&A, 618, A56

Duras, F., Bongiorno, A., Ricci, F., et al. 2020, A&A, 636, A73

Egami, E., Neugebauer, G., Soifer, B. T., et al. 2000, ApJ, 535, 561

Ellison, S. L., Ibata, R., Pettini, M., et al. 2004, A&A, 414, 79

Elvis, M., Wilkes, B. J., McDowell, J. C., et al. 1994, ApJS, 95, 1

Esposito, F., Vallini, L., Pozzi, F., et al. 2022, MNRAS, 512, 686

Evans, I. N., Allen, C., Anderson, C. S., et al. 2019, in AAS/High Energy Astrophysics Division, Vol. 17, AAS/High Energy Astrophysics Division, 114.01

Evans, I. N., Primini, F. A., Miller, J. B., et al. 2020, in American Astronomical Society Meeting Abstracts, Vol. 235, American Astronomical Society Meeting Abstracts #235, 154.05

Ezhikode, S. H., Dewangan, G. C., Misra, R., & Philip, N. S. 2020, MNRAS, 495, 3373

Fabbiano, G., Paggi, A., & Elvis, M. 2019, ApJ, 876, L18

Fabian, A. C. 2012, Annual Review of Astronomy and Astrophysics, 50, 455

Fabian, A. C., Lohfink, A., Kara, E., et al. 2015, MNRAS, 451, 4375

Falocco, S., Carrera, F. J., Corral, A., et al. 2013, A&A, 555, A79

Faucher-Giguère, C.-A. & Quataert, E. 2012, MNRAS, 425, 605

Fedorova, E. V., Zhdanov, V. I., Vignali, C., & Palumbo, G. G. C. 2008, A&A, 490, 989

Feltre, A., Hatziminaoglou, E., Fritz, J., & Franceschini, A. 2012, MNRAS, 426, 120

Ferrarese, L. & Ford, H. 2005, Space Sci. Rev., 116, 523

Feruglio, C., Fabbiano, G., Bischetti, M., et al. 2020, ApJ, 890, 29

Feruglio, C., Ferrara, A., Bischetti, M., et al. 2017, A&A, 608, A30

Feruglio, C., Fiore, F., Carniani, S., et al. 2015, A&A, 583, A99

Fiore, F., Feruglio, C., Shankar, F., et al. 2017, A&A, 601, A143

Flesch, E. W. 2021, arXiv e-prints, arXiv:2105.12985

Fluetsch, A., Maiolino, R., Carniani, S., et al. 2019, MNRAS, 483, 4586

Foreman-Mackey, D., Hogg, D. W., Lang, D., & Goodman, J. 2013, PASP, 125, 306

Fritz, J., Franceschini, A., & Hatziminaoglou, E. 2006, MNRAS, 366, 767

Fruscione, A., McDowell, J. C., Allen, G. E., et al. 2006, in Society of Photo-Optical Instrumentation Engineers (SPIE) Conference Series, Vol. 6270, Society of Photo-Optical Instrumentation Engineers (SPIE) Conference Series, ed. D. R. Silva & R. E. Doxsey, 62701V

Fukumura, K., Kazanas, D., Contopoulos, I., & Behar, E. 2010, ApJ, 715, 636

Fukumura, K., Tombesi, F., Kazanas, D., et al. 2014, ApJ, 780, 120

Furusawa, H., Kosugi, G., Akiyama, M., et al. 2008, ApJS, 176, 1

Gallagher, S. C. & Everett, J. E. 2007, in Astronomical Society of the Pacific Conference Series, Vol. 373, The Central Engine of Active Galactic Nuclei, ed. L. C. Ho & J. W. Wang, 305

Gallerani, S., Ferrara, A., Neri, R., & Maiolino, R. 2014, MNRAS, 445, 2848

Gandhi, P., Fabian, A. C., Suebsuwong, T., et al. 2007, MNRAS, 382, 1005

García, J., Dauser, T., Lohfink, A., et al. 2014, ApJ, 782, 76

García, J. A., Kara, E., Walton, D., et al. 2019, ApJ, 871, 88

García-Burillo, S., Alonso-Herrero, A., Ramos Almeida, C., et al. 2021, A&A, 652, A98

Gaspari, M. & Sądowski, A. 2017, ApJ, 837, 149

Gaspari, M., Tombesi, F., & Cappi, M. 2020, Nature Astronomy, 4, 10

Genzel, R., Tacconi, L. J., Lutz, D., et al. 2015, ApJ, 800, 20

Giustini, M., Cappi, M., Chartas, G., et al. 2011, A&A, 536, A49

Giustini, M. & Proga, D. 2019, A&A, 630, A94

Gofford, J., Reeves, J. N., Braito, V., et al. 2014, ApJ, 784, 77

Gofford, J., Reeves, J. N., McLaughlin, D. E., et al. 2015, MNRAS, 451, 4169

Gofford, J., Reeves, J. N., Tombesi, F., et al. 2013, MNRAS, 430, 60

González-López, J., Decarli, R., Pavesi, R., et al. 2019, ApJ, 882, 139

González-López, J., Novak, M., Decarli, R., et al. 2020, ApJ, 897, 91

Goodman, J. & Weare, J. 2010, Communications in Applied Mathematics and Computational Science, 5, 65

Gravity Collaboration, Sturm, E., Dexter, J., et al. 2018, Nature, 563, 657

Guerras, E., Dai, X., Steele, S., et al. 2017, ApJ, 836, 206

Guilbert, P. W., Fabian, A. C., & Rees, M. J. 1983, MNRAS, 205, 593

Haardt, F. & Maraschi, L. 1991, ApJ, 380, L51

Haardt, F., Maraschi, L., & Ghisellini, G. 1994, ApJ, 432, L95

Haardt, F., Maraschi, L., & Ghisellini, G. 1997, ApJ, 476, 620

Hagino, K., Done, C., Odaka, H., Watanabe, S., & Takahashi, T. 2017, MNRAS, 468, 1442

Harris, C. R., Millman, K. J., van der Walt, S. J., et al. 2020, Nature, 585, 357

Harrison, C. M. 2017, Nature Astronomy, 1, 0165

Harrison, C. M., Alexander, D. M., Mullaney, J. R., et al. 2016, MNRAS, 456, 1195

Harrison, C. M., Costa, T., Tadhunter, C. N., et al. 2018, Nature Astronomy, 2, 198

Harrison, F. A., Craig, W. W., Christensen, F. E., et al. 2013, ApJ, 770, 103

Hasinger, G., Schartel, N., & Komossa, S. 2002, ApJ, 573, L77

HI4PI Collaboration, Ben Bekhti, N., Flöer, L., et al. 2016, A&A, 594, A116

Hickox, R. C. & Alexander, D. M. 2018, ARA&A, 56, 625

Hinkle, J. T. & Mushotzky, R. 2021, MNRAS, 506, 4960

Hodge, J. A. & da Cunha, E. 2020, Royal Society Open Science, 7, 200556

Hopkins, P. F. & Elvis, M. 2010, MNRAS, 401, 7

Huchra, J., Gorenstein, M., Kent, S., et al. 1985, AJ, 90, 691

Hurley, P. D., Oliver, S., Betancourt, M., et al. 2017, MNRAS, 464, 885

Husemann, B., Davis, T. A., Jahnke, K., et al. 2017, MNRAS, 470, 1570

Ibata, R. A., Lewis, G. F., Irwin, M. J., Lehár, J., & Totten, E. J. 1999, AJ, 118, 1922

Igo, Z., Parker, M. L., Matzeu, G. A., et al. 2020, MNRAS, 493, 1088

Inada, N., Oguri, M., Rusu, C. E., Kayo, I., & Morokuma, T. 2014, AJ, 147, 153

Inada, N., Oguri, M., Shin, M.-S., et al. 2012, AJ, 143, 119

Inoue, A. K. 2011, MNRAS, 415, 2920

Irwin, M. J., Webster, R. L., Hewett, P. C., Corrigan, R. T., & Jedrzejewski, R. I. 1989, AJ, 98, 1989

Isobe, T., Feigelson, E. D., Akritas, M. G., & Babu, G. J. 1990, ApJ, 364, 104

Iwasawa, K. & Taniguchi, Y. 1993, ApJ, 413, L15

Jaffe, W., Meisenheimer, K., Röttgering, H. J. A., et al. 2004, Nature, 429, 47

Jarvis, M. E., Harrison, C. M., Mainieri, V., et al. 2020, MNRAS, 498, 1560

Jin, S., Daddi, E., Liu, D., et al. 2018, ApJ, 864, 56

Just, D. W., Brandt, W. N., Shemmer, O., et al. 2007, ApJ, 665, 1004

Kakkad, D., Mainieri, V., Brusa, M., et al. 2017, MNRAS, 468, 4205

Kakkad, D., Mainieri, V., Vietri, G., et al. 2020, A&A, 642, A147

Kalberla, P. M. W., Burton, W. B., Hartmann, D., et al. 2005, A&A, 440, 775

Kallman, T. & Bautista, M. 2001, ApJS, 133, 221

Kammoun, E. S., Risaliti, G., Stern, D., et al. 2017, MNRAS, 465, 1665

Kamraj, N., Brightman, M., Harrison, F. A., et al. 2022, ApJ, 927, 42

Kamraj, N., Harrison, F. A., Baloković, M., Lohfink, A., & Brightman, M. 2018, ApJ, 866, 124

Kang, J.-L. & Wang, J.-X. 2022, arXiv e-prints, arXiv:2203.07118

Kara, E., García, J. A., Lohfink, A., et al. 2017, MNRAS, 468, 3489

Kaspi, S., Brandt, W. N., George, I. M., et al. 2002, ApJ, 574, 643

Kellermann, K. I., Sramek, R., Schmidt, M., Shaffer, D. B., & Green, R. 1989, AJ, 98, 1195

Kennicutt, Robert C., J. 1989, ApJ, 344, 685

Kennicutt, Robert C., J. 1998, ApJ, 498, 541

King, A. 2005, ApJ, 635, L121

King, A. 2008, New Astron. Rev., 52, 253

King, A. & Pounds, K. 2015, ARA&A, 53, 115

Kirkpatrick, A., Sharon, C., Keller, E., & Pope, A. 2019, ApJ, 879, 41

Kocevski, D. D., Hasinger, G., Brightman, M., et al. 2018, ApJS, 236, 48

Kormendy, J. & Ho, L. C. 2013, ARA&A, 51, 511

Koss, M., Trakhtenbrot, B., Ricci, C., et al. 2017, ApJ, 850, 74

Koss, M. J., Strittmatter, B., Lamperti, I., et al. 2021, ApJS, 252, 29

Kravchenko, K., Dallilar, Y., Absil, O., et al. 2023, arXiv:2301.01580

Krawczynski, H. & Chartas, G. 2017, ApJ, 843, 118

Krawczynski, H., Chartas, G., & Kislat, F. 2019, ApJ, 870, 125

Krumpe, M., Lamer, G., Markowitz, A., & Corral, A. 2010, ApJ, 725, 2444

Lada, C. J., Forbrich, J., Lombardi, M., & Alves, J. F. 2012, ApJ, 745, 190

Laigle, C., McCracken, H. J., Ilbert, O., et al. 2016, ApJS, 224, 24

Lammers, C., Iyer, K. G., Ibarra-Medel, H., et al. 2022, arXiv e-prints, arXiv:2212.00762

Lamperti, I., Harrison, C. M., Mainieri, V., et al. 2021, A&A, 654, A90

Lanzuisi, G., Civano, F., Elvis, M., et al. 2013, MNRAS, 431, 978

Lanzuisi, G., Gilli, R., Cappi, M., et al. 2019, ApJ, 875, L20

Lanzuisi, G., Giustini, M., Cappi, M., et al. 2012, A&A, 544, A2

Lanzuisi, G., Perna, M., Comastri, A., et al. 2016, A&A, 590, A77

Lanzuisi, G., Ranalli, P., Georgantopoulos, I., et al. 2015, A&A, 573, A137

Lapi, A., Raimundo, S., Aversa, R., et al. 2014, ApJ, 782, 69

Laurenti, M., Luminari, A., Tombesi, F., et al. 2021, A&A, 645, A118

Lehmer, B. D., Alexander, D. M., Geach, J. E., et al. 2009, ApJ, 691, 687

Lemon, C., Auger, M. W., McMahon, R., et al. 2020, MNRAS, 494, 3491

Lemon, C. A., Auger, M. W., & McMahon, R. G. 2019, MNRAS, 483, 4242

Lemon, C. A., Auger, M. W., McMahon, R. G., & Ostrovski, F. 2018, MNRAS, 479, 5060

Leung, T. K. D., Hayward, C. C., Casey, C. M., et al. 2019, ApJ, 876, 48

Li, J., Wang, R., Riechers, D., et al. 2020, ApJ, 889, 162

Liu, T., Tozzi, P., Wang, J.-X., et al. 2017, ApJS, 232, 8

Longinotti, A. L., Vega, O., Krongold, Y., et al. 2018, ApJ, 867, L11

Luminari, A., Nicastro, F., Elvis, M., et al. 2021, A&A, 646, A111

Luminari, A., Tombesi, F., Piconcelli, E., et al. 2020, A&A, 633, A55

Luo, B., Brandt, W. N., Xue, Y. Q., et al. 2017, ApJS, 228, 2

Lusso, E. & Risaliti, G. 2016, ApJ, 819, 154

Lutz, D., Poglitsch, A., Altieri, B., et al. 2011, A&A, 532, A90

Madau, P. & Dickinson, M. 2014, ARA&A, 52, 415

Maiolino, R., Salvati, M., Bassani, L., et al. 1998, A&A, 338, 781

Makishima, K. 1986, Iron Lines from Galactic and Extragalactic X-ray Sources, ed. K. O. Mason, M. G. Watson, & N. E. White, Vol. 266, 249

Malizia, A., Molina, M., Bassani, L., et al. 2014, ApJ, 782, L25

Marasco, A., Cresci, G., Nardini, E., et al. 2020, A&A, 644, A15

Marchesi, S., Lanzuisi, G., Civano, F., et al. 2016, ApJ, 830, 100

Martocchia, S., Piconcelli, E., Zappacosta, L., et al. 2017, A&A, 608, A51

Massaro, E., Maselli, A., Leto, C., et al. 2015, Ap&SS, 357, 75

Matt, G., Fabian, A. C., Guainazzi, M., et al. 2000, MNRAS, 318, 173

Matzeu, G. A., Brusa, M., Lanzuisi, G., et al. 2022a, arXiv e-prints, arXiv:2212.02960

Matzeu, G. A., Lieu, M., Costa, M. T., et al. 2022b, MNRAS, 515, 6172

Matzeu, G. A., Reeves, J. N., Braito, V., et al. 2017, MNRAS, 472, L15

Matzeu, G. A., Reeves, J. N., Nardini, E., et al. 2016, MNRAS, 458, 1311

McConnell, N. J., Ma, C.-P., Gebhardt, K., et al. 2011, Nature, 480, 215

Mehdipour, M., Kriss, G. A., Brusa, M., et al. 2022, arXiv e-prints, arXiv:2212.02961

Merlin, E., Castellano, M., Santini, P., et al. 2021, A&A, 649, A22

Middei, R., Matzeu, G. A., Bianchi, S., et al. 2021, A&A, 647, A102

Middei, R., Tombesi, F., Vagnetti, F., et al. 2020, A&A, 635, A18

Mingozzi, M., Vallini, L., Pozzi, F., et al. 2018, MNRAS, 474, 3640

Miniutti, G. & Fabian, A. C. 2006, MNRAS, 366, 115

Mizumoto, M., Izumi, T., & Kohno, K. 2019, ApJ, 871, 156

Molina, J., Ho, L. C., Wang, R., et al. 2022a, arXiv e-prints, arXiv:2212.05295

Molina, J., Ho, L. C., Wang, R., et al. 2022b, ApJ, 935, 72

Molina, M., Bassani, L., Malizia, A., et al. 2013, MNRAS, 433, 1687

Molina, M., Bassani, L., Malizia, A., et al. 2009, MNRAS, 399, 1293

Molina, M., Malizia, A., Bassani, L., et al. 2019, MNRAS, 484, 2735

More, A., Oguri, M., Kayo, I., et al. 2016, MNRAS, 456, 1595

Morganti, R., Veilleux, S., Oosterloo, T., Teng, S. H., & Rupke, D. 2016, A&A, 593, A30

Mosquera, A. M. & Kochanek, C. S. 2011, ApJ, 738, 96

Mosquera, A. M., Kochanek, C. S., Chen, B., et al. 2013, ApJ, 769, 53

Mountrichas, G., Buat, V., Yang, G., et al. 2021, A&A, 646, A29

Muñoz, J. A., Falco, E. E., Kochanek, C. S., et al. 1998, Ap&SS, 263, 51

Nagao, T., Maiolino, R., Marconi, A., & Matsuhara, H. 2011, A&A, 526, A149

Nandra, K., George, I. M., Mushotzky, R. F., Turner, T. J., & Yaqoob, T. 1999, ApJ, 523, L17

Nandra, K. & Pounds, K. A. 1994, MNRAS, 268, 405

Nardini, E., Reeves, J. N., Gofford, J., et al. 2015, Science, 347, 860

Netzer, H. 2015, ARA&A, 53, 365

Noll, S., Burgarella, D., Giovannoli, E., et al. 2009, A&A, 507, 1793

Oliver, S. J., Bock, J., Altieri, B., et al. 2012, MNRAS, 424, 1614

Ota, N., Oguri, M., Dai, X., et al. 2012, ApJ, 758, 26

Padovani, P. 2017, Nature Astronomy, 1, 0194

Padovani, P., Alexander, D. M., Assef, R. J., et al. 2017, Astronomy and Astrophysics Review, 25, 2

Panessa, F., Barcons, X., Bassani, L., et al. 2007, A&A, 467, 519

Parker, M. L., Alston, W. N., Härer, L., et al. 2021, MNRAS, 508, 1798

Peebles, P. J. E. 1972, ApJ, 178, 371

Pensabene, A., Decarli, R., Bañados, E., et al. 2021, A&A, 652, A66

Perna, M., Brusa, M., Cresci, G., et al. 2015, A&A, 574, A82

Perna, M., Sargent, M. T., Brusa, M., et al. 2018, A&A, 619, A90

Perola, G. C., Matt, G., Cappi, M., et al. 2002, A&A, 389, 802

Peterson, B. M. 2004, in IAU Symposium, Vol. 222, The Interplay Among Black Holes, Stars and ISM in Galactic Nuclei, ed. T. Storchi-Bergmann, L. C. Ho, & H. R. Schmitt, 15–20

Petrucci, P. O., Haardt, F., Maraschi, L., et al. 2001, ApJ, 556, 716

Petrucci, P. O., Ursini, F., De Rosa, A., et al. 2018, A&A, 611, A59

Piconcelli, E., Jimenez-Bailón, E., Guainazzi, M., et al. 2005, A&A, 432, 15

Planck Collaboration, Aghanim, N., Akrami, Y., et al. 2020, A&A, 641, A6

Ponti, G., Cappi, M., Vignali, C., et al. 2009, MNRAS, 394, 1487

Ponti, G., Papadakis, I., Bianchi, S., et al. 2012, A&A, 542, A83

Popović, L. Č., Jovanović, P., Mediavilla, E., et al. 2006, ApJ, 637, 620

Popping, G., Decarli, R., Man, A. W. S., et al. 2017, A&A, 602, A11

Pounds, K. A., Nixon, C. J., Lobban, A., & King, A. R. 2018, MNRAS, 481, 1832

Pozzi, F., Vallini, L., Vignali, C., et al. 2017, MNRAS, 470, L64

Protassov, R., van Dyk, D. A., Connors, A., Kashyap, V. L., & Siemiginowska, A. 2002, ApJ, 571, 545

Puglisi, A., Rodighiero, G., Franceschini, A., et al. 2016, A&A, 586, A83

Rees, M. J. 1984, in X-ray and UV Emission from Active Galactic Nuclei, ed. W. Brinkmann & J. Truemper, 138–151

Reeves, J. N., Braito, V., Nardini, E., et al. 2018, ApJ, 867, 38

Reeves, J. N., Braito, V., Porquet, D., et al. 2021, MNRAS, 500, 1974

Reynolds, M. T., Walton, D. J., Miller, J. M., & Reis, R. C. 2014, ApJ, 792, L19

Ricci, C., Ho, L. C., Fabian, A. C., et al. 2018, MNRAS, 480, 1819

Ricci, C., Trakhtenbrot, B., Koss, M. J., et al. 2017, ApJS, 233, 17

Richards, G. T., Lacy, M., Storrie-Lombardi, L. J., et al. 2006, ApJS, 166, 470

Riechers, D. A., Boogaard, L. A., Decarli, R., et al. 2020, ApJ, 896, L21

Riechers, D. A., Walter, F., Carilli, C. L., & Lewis, G. F. 2009, ApJ, 690, 463

Risaliti, G. & Elvis, M. 2004, in Astrophysics and Space Science Library, Vol. 308, Supermassive Black Holes in the Distant Universe, ed. A. J. Barger, 187

Risaliti, G., Salvati, M., Elvis, M., et al. 2009, MNRAS, 393, L1

Rodighiero, G., Renzini, A., Daddi, E., et al. 2014, MNRAS, 443, 19

Rosario, D. J., Burtscher, L., Davies, R. I., et al. 2018, MNRAS, 473, 5658

Rosario, D. J., Togi, A., Burtscher, L., et al. 2019, ApJ, 875, L8

Ross, R. R. & Fabian, A. C. 2005, MNRAS, 358, 211

Ruszkowski, M. & Fabian, A. C. 2000, MNRAS, 315, 223

Sabatini, G., Gruppioni, C., Massardi, M., et al. 2018, MNRAS, 476, 5417

Saez, C. & Chartas, G. 2011, ApJ, 737, 91

Saez, C., Chartas, G., & Brandt, W. N. 2009, ApJ, 697, 194

Saintonge, A., Catinella, B., Tacconi, L. J., et al. 2017, ApJS, 233, 22

Salvestrini, F., Gruppioni, C., Hatziminaoglou, E., et al. 2022, A&A, 663, A28

Sargent, M. T., Daddi, E., Béthermin, M., et al. 2014, ApJ, 793, 19

Saturni, F. G., Bischetti, M., Piconcelli, E., et al. 2018, A&A, 617, A118

Saturni, F. G., Trevese, D., Vagnetti, F., Perna, M., & Dadina, M. 2016, A&A, 587, A43

Sawicki, M. 2012, PASP, 124, 1208

Schmidt, M. 1959, ApJ, 129, 243

Schmidt, R., Webster, R. L., & Lewis, G. F. 1998, MNRAS, 295, 488

Schneider, D. P., Turner, E. L., Gunn, J. E., et al. 1988, AJ, 95, 1619

Scholtz, J., Alexander, D. M., Harrison, C. M., et al. 2018, MNRAS, 475, 1288

Scholtz, J., Harrison, C. M., Rosario, D. J., et al. 2020, MNRAS, 492, 3194

Serafinelli, R., Tombesi, F., Vagnetti, F., et al. 2019, A&A, 627, A121

Shakura, N. I. & Sunyaev, R. A. 1973, A&A, 500, 33

Shangguan, J., Ho, L. C., Bauer, F. E., Wang, R., & Treister, E. 2020, ApJ, 899, 112

Shirley, R., Duncan, K., Campos Varillas, M. C., et al. 2021, MNRAS, 507, 129

Shirley, R., Roehlly, Y., Hurley, P. D., et al. 2019, MNRAS, 490, 634

Shivaei, I., Kriek, M., Reddy, N. A., et al. 2016, ApJ, 820, L23

Silk, J. & Rees, M. J. 1998, A&A, 331, L1

Sirressi, M., Cicone, C., Severgnini, P., et al. 2019, MNRAS, 489, 1927

Sądowski, A. & Gaspari, M. 2017, MNRAS, 468, 1398

Smith, R. N., Tombesi, F., Veilleux, S., Lohfink, A. M., & Luminari, A. 2019, ApJ, 887, 69

Solomon, P. M. & Vanden Bout, P. A. 2005, ARA&A, 43, 677

Somerville, R. S. & Davé, R. 2015, ARA&A, 53, 51

Somerville, R. S., Hopkins, P. F., Cox, T. J., Robertson, B. E., & Hernquist, L. 2008, MNRAS, 391, 481

Stacey, H. R., McKean, J. P., Robertson, N. C., et al. 2018, MNRAS, 476, 5075

Stalevski, M., Fritz, J., Baes, M., Nakos, T., & Popović, L. Č. 2012, MNRAS, 420, 2756

Stalevski, M., Ricci, C., Ueda, Y., et al. 2016, MNRAS, 458, 2288

Stern, B. E., Poutanen, J., Svensson, R., Sikora, M., & Begelman, M. C. 1995, ApJ, 449, L13

Strateva, I., Ivezić, Ž., Knapp, G. R., et al. 2001, AJ, 122, 1861

Tacconi, L. J., Genzel, R., Saintonge, A., et al. 2018, ApJ, 853, 179

Tacconi, L. J., Neri, R., Genzel, R., et al. 2013, ApJ, 768, 74

Talia, M., Pozzi, F., Vallini, L., et al. 2018, MNRAS, 476, 3956

Tamborra, F., Papadakis, I., Dovčiak, M., & Svoboda, J. 2018, MNRAS, 475, 2045

Tananbaum, H., Avni, Y., Branduardi, G., et al. 1979, ApJ, 234, L9

Tombesi, F., Cappi, M., Reeves, J. N., & Braito, V. 2012, MNRAS, 422, L1

Tombesi, F., Cappi, M., Reeves, J. N., et al. 2013, MNRAS, 430, 1102

Tombesi, F., Cappi, M., Reeves, J. N., et al. 2010a, A&A, 521, A57

Tombesi, F., Meléndez, M., Veilleux, S., et al. 2015, Nature, 519, 436

Tombesi, F., Sambruna, R. M., Reeves, J. N., et al. 2010b, ApJ, 719, 700

Tortosa, A., Bianchi, S., Marinucci, A., Matt, G., & Petrucci, P. O. 2018, A&A, 614, A37

Tortosa, A., Marinucci, A., Matt, G., et al. 2017, MNRAS, 466, 4193

Tortosa, A., Ricci, C., Ho, L. C., et al. 2022, arXiv:2212.06183

Tozzi, G., Cresci, G., Marasco, A., et al. 2021, A&A, 648, A99

Treu, T. 2010, Annual Review of Astronomy and Astrophysics, 48, 87

Tudorica, A., Hildebrandt, H., Tewes, M., et al. 2017, A&A, 608, A141

Ueda, Y., Watson, M. G., Stewart, I. M., et al. 2008, ApJS, 179, 124

Ulrich, M.-H., Maraschi, L., & Urry, C. M. 1997, Annual Review of Astronomy and Astrophysics, 35, 445

Ursini, F., Petrucci, P. O., Bianchi, S., et al. 2020, A&A, 634, A92

Valentino, F., Daddi, E., Puglisi, A., et al. 2021, A&A, 654, A165

Vallini, L., Tielens, A. G. G. M., Pallottini, A., et al. 2019, MNRAS, 490, 4502

van der Werf, P. P., Berciano Alba, A., Spaans, M., et al. 2011, ApJ, 741, L38

Vasudevan, R. V., Brandt, W. N., Mushotzky, R. F., et al. 2013, ApJ, 763, 111

Veilleux, S., Bolatto, A., Tombesi, F., et al. 2017, ApJ, 843, 18

Veilleux, S., Maiolino, R., Bolatto, A. D., & Aalto, S. 2020, A&ARv, 28, 2

Venturi, G., Nardini, E., Marconi, A., et al. 2018, A&A, 619, A74

Vietri, G., Piconcelli, E., Bischetti, M., et al. 2018, A&A, 617, A81

Vignali, C., Brandt, W. N., Schneider, D. P., & Kaspi, S. 2005, AJ, 129, 2519

Vignali, C., Comastri, A., Cappi, M., et al. 1999, ApJ, 516, 582

Vignali, C., Iwasawa, K., Comastri, A., et al. 2015, A&A, 583, A141

Virtanen, P., Gommers, R., Oliphant, T. E., et al. 2020, Nature Methods, 17, 261

Vito, F., Brandt, W. N., Bauer, F. E., et al. 2019, A&A, 630, A118

Vito, F., Maiolino, R., Santini, P., et al. 2014, MNRAS, 441, 1059

Wagner, A. Y., Umemura, M., & Bicknell, G. V. 2013, ApJ, 763, L18

Walter, F., Weiß, A., Downes, D., Decarli, R., & Henkel, C. 2011, ApJ, 730, 18

Walton, D. J., Nardini, E., Gallo, L. C., et al. 2019, MNRAS, 484, 2544

Wambsganss, J., Brunner, H., Schindler, S., & Falco, E. 1999, A&A, 346, L5

Ward, S. R., Harrison, C. M., Costa, T., & Mainieri, V. 2022, MNRAS, 514, 2936

Weaver, J. R., Kauffmann, O. B., Ilbert, O., et al. 2022, ApJS, 258, 11

Webb, N. A., Coriat, M., Traulsen, I., et al. 2020a, A&A, 641, A136

Webb, N. A., Coriat, M., Traulsen, I., et al. 2020b, VizieR Online Data Catalog, IX/59

Wechsler, R. H. & Tinker, J. L. 2018, ARA&A, 56, 435

Weiß, A., Downes, D., Neri, R., et al. 2007, A&A, 467, 955

Wertz, O. & Surdej, J. 2014, MNRAS, 442, 428

Wilkins, D. R., Gallo, L. C., Costantini, E., Brandt, W. N., & Blandford, R. D. 2021, Nature, 595, 657

Wu, Q. & Shen, Y. 2022, ApJS, 263, 42

Yang, G., Boquien, M., Buat, V., et al. 2020, MNRAS, 491, 740

Yee, H. K. C. 1988, AJ, 95, 1331

Younes, G., Ptak, A., Ho, L. C., et al. 2019, ApJ, 870, 73

Zappacosta, L., Comastri, A., Civano, F., et al. 2018, ApJ, 854, 33

Zappacosta, L., Piconcelli, E., Fiore, F., et al. 2023, arXiv e-prints, arXiv:2305.02347

Zubovas, K. & King, A. 2012, ApJ, 745, L34